

Journal Information

Maejo International Journal of Science and Technology (ISSN 1905-7873 © 2010), the international journal for preliminary communications in Science and Technology is the first peer-refereed scientific journal of Maejo University (www.mju.ac.th). Intended as a medium for communication, discussion, and rapid dissemination of important issues in Science and Technology, articles are initially published online in an open access format, which thereby gives authors the chance to communicate with a wide range of readers in an international community.

Publication Information

MIJST is published triannually. Articles are available online and can be accessed free of charge at <http://www.mijst.mju.ac.th>. Printed and bound copies of each volume are produced and distributed to authors and selected groups or individuals. This journal and the individual contributions contained in it are protected under the copyright by Maejo University.

Abstracting/Indexing Information

MIJST is covered and cited by Science Citation Index Expanded, SCOPUS, Journal Citation Reports/Science Edition, Zoological Record, Chemical Abstracts Service (CAS), SciFinder Scholar, Directory of Open Access Journals (DOAJ) and Google Scholar.

Contact Information

Editorial office: Maejo International Journal of Science and Technology (MIJST), 1st floor, Orchid Building, Maejo University, San Sai, Chiang Mai 50290, Thailand

Tel: +66-53-87-3880, Fax: +66-53-87-3880

E-mails: duang@mju.ac.th



MAEJO INTERNATIONAL JOURNAL OF SCIENCE AND TECHNOLOGY

Editor

Duang Buddhasukh, Maejo University, Thailand.

Associate Editors

Jatuphong Varith, Maejo University, Thailand.
Wasin Charentantanakul, Maejo University, Thailand.
Morakot Sukchotiratana, Chiang Mai University, Thailand.
Nakorn Tippayawong, Chiang Mai University, Thailand.

Editorial Assistants

James F. Maxwell, Chiang Mai University, Thailand.
Jirawan Banditpuritat, Maejo University, Thailand.

Editorial Board

Prof. Dallas E. Alston	University of Puerto Rico, USA.
Dr. Pei-Yi Chu	Changhua Christian Hospital, Taiwan, R.O.C.
Asst. Prof. Ekachai Chukeatirote	Mae Fah Luang University, Thailand.
Prof. Richard L. Deming	California State University Fullerton, Fullerton CA
Prof. Cynthia C. Divina	Central Luzon State University, Philippines.
Prof. Mary Garson	The University of Queensland, Australia.
Prof. Kate Grudpan	Chiang Mai University, Thailand.
Assoc. Prof. Duangrat Inthorn	Mahidol University, Thailand.
Prof. Minoru Isobe	Nagoya University, Japan.
Prof. Kunimitsu Kaya	Tohoku University, Japan.
Assoc. Prof. Margaret E. Kerr	Worcester State College, Worcester, MA
Dr. Ignacy Kitowski	University of Maria-Curie Sklodowska, Poland.
Asst. Prof. Andrzej Komosa	University of Maria-Curie Sklodowska, Poland.
Asst. Prof. Pradeep Kumar	Jaypee University of Information Technology, India.
Asst. Prof. Ma. Elizabeth C. Leoveras	Central Luzon State University, Philippines.
Dr. Subhash C. Mandal	Jadavpur University, India.
Prof. Amarendra N. Misra	Fakir Mohan University, Orissa, India.
Dr. Robert Molloy	Chiang Mai University, Thailand.
Prof. Mohammad A. Mottaleb	Northwest Missouri State University, USA.
Prof. Stephen G. Pyne	University of Wollongong, Australia.
Prof. Renato G. Reyes	Central Luzon State University, Philippines.
Dr. Waya Sengpracha	Silpakorn University, Thailand.
Dr. Settha Siripin	Maejo University, Thailand.
Prof. Paisarn Sithigorngul	Srinakharinwirot University, Thailand.
Prof. Anupam Srivastav	College of Engineering and Technology, India.
Prof. Maitree Suttajit	Naresuan University (Payao Campus), Thailand.
Assoc. Prof. Chatchai Tayapiwatana	Chiang Mai University, Thailand.
Emeritus Prof. Bela Ternai	La Trobe University, Australia.
Asst. Prof. Narin Tongwittaya	Maejo University, Thailand.
Asst. Prof. Jatuphong Varith	Maejo University, Thailand.
Assoc. Prof. Niwoot Whangchai	Maejo University, Thailand.

Consultants

Asst. Prof. Chamnian Yosraj, Ph.D., President of Maejo University
Assoc. Prof. Thep Phongparnich, Ed. D., Former President of Maejo University
Assoc. Prof. Chalermchai Panyadee, Ph.D., Vice-President in Research of Maejo University

MAEJO INTERNATIONAL JOURNAL OF SCIENCE AND TECHNOLOGY

*The International Journal for Preliminary Communications in Science and
Technology*



<http://www.mijst.mju.ac.th>

ISSN 1905-7873 © 2010 by Maejo University



MAEJO INTERNATIONAL JOURNAL OF SCIENCE AND TECHNOLOGY

Volume 4, Issue 3 (September - December 2010)

CONTENTS

	Page
Are we placing too much reliance on technology? <i>Editorial</i>	i
Novel analysis of Petri-net-based controllers by means of TCT implementation tool of supervisory control theory <i>Gökhan Gelen and Murat Uzam*</i>	360-396
Effects of modulus and dosage of sodium silicate on limestone flotation <i>Danda S. Rao*, Tadiparthi V. Vijayakumar, Shivakumar Angadi, Swarna Prabhakar and Guntamadugu B. Raju</i>	397-404
Segmentation and feature extraction of fluid-filled uterine fibroid–A knowledge-based approach <i>Ratha Jeyalakshmi * and Ramar Kadarkarai</i>	405-416
Effects of extender type, sperm volume, cryoprotectant concentration, cryopreservation and time duration on motility, survival and fertilisation rates of Mekong giant catfish sperm <i>Kriangsak Mengumphan*, Niwooti Whangchai and Dounporn Amornlerdpison</i>	417-427
A random number generator based on NTRU cryptosystem <i>He Debiao*, Chen Jianhua and Hu Jin</i>	428-434
Feature extraction of near-spherical fruit with partial occlusion for robotic harvesting <i>Lü Qiang, Lu Huazhu, Cai Jianrong*, Zhao Jiewen, Li YongPing and Zhou Fang</i>	435-445
Isolation and primary identification of endophytic fungi from <i>Cephalotaxus mannii</i> trees <i>Pramuan Saithong*, Wanchai Panthavee, Siriporn Stonsaovapak and Li Congfa</i>	446-453
Antiglycation and antioxidant activities of oxyresveratrol extracted from the heartwood of <i>Artocarpus lakoocha</i> Roxb. <i>Nasapon Povichit, Ampai Phrutivorapongkul, Maitree Suttajit and Pimporn Leelapornpisid*</i>	454-461

	Page
Testing the recoverability of grass DNA transferred to textiles for forensic purpose <i>Francesc Francès*, Ana Castelló and Fernando Verdú</i>	462-467
Natural convection of nanofluids in a cavity with linearly varying wall temperature <i>Sivanandam Sivasankaran*, Thangaraj Aasaithambi and Subbarayagounder Rajan</i>	468-482
Urban ecological characteristics and vascular wall flora on the Anatolian side of Istanbul, Turkey <i>Volkan Altay*, Ibrahim İ. Özyiğit and Celal Yarci</i>	483-495
EEG activity in Muslim prayer: A pilot study <i>Haider H. Alwasiti*, Ishak Aris and Adznan Jantan</i>	496-511
Free vibration analysis of symmetrically laminated composite rectangular plates using extended Kantorovich method <i>Kullasup Phongsrisuk*, Prasong Ingsuwan, Wetchayan Rangsri and Wiwat Klongpanich</i>	512-532
Variation in physical characters and evaluation of genetic diversity in <i>Acacia caesia</i> var. <i>caesia</i> (L.) Willd. in an environmental gradient in the Western Ghats of Tamil Nadu, India <i>Palanisamy Sathishkumar, Subramanian Paulsamy* and Anaimalai M. Anandakumar</i>	533-539
Antilisterial effects of ethanolic extracts of some edible Thai plants on refrigerated cooked pork <i>Siriporn Stonsaovapak* and Soithong Saiyudthong</i>	540-546
Botanical notes <i>James F. Maxwell *</i>	547-551

MAEJO INTERNATIONAL JOURNAL OF SCIENCE AND TECHNOLOGY

Volume 4, Issue 3 (September - December 2010)

Author Index

Author	Page	Author	Page
Aasaithambi T.	468	Özyiğit İ. İ.	483
Altay V.	483	Panthavee W.	446
Alwasiti H. H.	496	Paulsamy S.	533
Amornlerdpison D.	417	Phongsrisuk K.	512
Anandakumar A. M.	533	Phrutivorapongkul A.	454
Angadi S.	397	Povichit N.	454
Aris I.	496	Prabhakar S.	397
Castelló A.	462	Qiang L.	435
Congfa L.	446	Rajan S.	468
Debiao H.	428	Raju G. B.	397
Fang Z.	435	Rangsri W.	512
Francès F.	462	Rao D. S.	397
Gelen G.	360	Saithong P.	446
Huazhu L.	435	Saiyudthong S.	540
Ingsuwan P.	512	Sathishkumar P.	533
Jantan A.	496	Sivasankaran S.	468
Jeyalakshmi R.	405	Stonsaovapak S.	446, 540
Jianhua C.	428	Suttajit M.	454
Jianrong C.	435	Uzam M.	360
Jiewen Z.	435	Verdú F.	462
Jin H.	428	Vijayakumar T. V.	397
Kadarkarai R.	405	Whangchai N.	417
Klongpanich W.	512	Yarci C.	483
Leelapornpisid P.	454	YongPing L.	435
Maxwell J. F.	547		
Mengumphan K.	417		

Instructions for Authors

Manuscript Preparation

Manuscripts should be prepared in English using a word processor. MS Word for Macintosh or Windows, and .doc or .rtf files are preferred. Manuscripts may be prepared with other software provided that the full document (with figures, schemes and tables inserted into the text) is exported to a MS Word format for submission. Times or Times New Roman font is preferred. The font size should be 12 pt and the line spacing "at least" 17 pt. The printing area is 17.5 cm x 24.7cm (6.9" x 9.73"). For A4 paper, margins must be 1.5 cm on top, 2.0 cm at the bottom and 1.75 cm on both left and right sides of the paper. For US letter-sized paper, margins must be 1.5 cm (0.59") on top, 1.74 cm (0.68") at the bottom and 2.05 cm (0.8") on both left and right sides. Although our final output is in .pdf format, authors are asked NOT to send manuscripts in this format as editing them is much more complicated.

A template file may be downloaded from the *Maejo Int. J. Sci. Technol.* homepage. ([DOWNLOAD HERE](#))

Authors' full mailing addresses, homepage addresses, phone and fax numbers, and e-mail addresses homepages can be included in the title page and these will be published in the manuscripts and the Table of Contents. The corresponding author should be clearly identified. It is the corresponding author's responsibility to ensure that all co-authors are aware of and approve of the contents of a submitted manuscript.

A brief (200 word maximum) Abstract should be provided. The use in the Abstract of numbers to identify compounds should be avoided unless these compounds are also identified by names.

A list of three to five keywords must be given and placed after the Abstract. Keywords may be single words or very short phrases.

Although variations in accord with contents of a manuscript are permissible, in general all papers should have the following sections: Introduction, Materials and Methods, Results and Discussion, Conclusions, Acknowledgments (if applicable) and References.

Authors are encouraged to prepare Figures and Schemes in colour. Full colour graphics will be published free of charge.

Tables and Figures should be inserted into the main text, and numbers and titles supplied for all Tables and Figures. All table columns should have an explanatory heading. To facilitate layout of large tables, smaller fonts may be used, but in no case should these be less than 10 pt in size. Authors should use the Table option of MS Word to create tables, rather than tabs, as tab-delimited columns are often difficult to format in .pdf for final output.

Figures, tables and schemes should also be placed in numerical order in the appropriate place within the main text. Numbers, titles and legends should be provided for all tables, schemes and figures. Chemical structures and reaction schemes should be drawn using an appropriate software package designed for this purpose. As a guideline, these should be drawn to a scale such that all the details and text are clearly legible when placed in the manuscript (i.e. text should be no smaller than 8-9 pt).

For bibliographic citations, the reference numbers should be placed in square brackets, i.e. [], and placed before the punctuation, for example [4] or [1-3], and all the references should be listed separately and as the last section at the end of the manuscript.

Format for References

Journal :

1. D. Buddhasukh, J. R. Cannon, B. W. Metcalf and A. J. Power, " Synthesis of 5-n-alkylresorcinol dimethyl ethers and related compounds *via* substituted thiophens", *Aust. J. Chem.*, **1971**, *24*, 2655-2664.

Text :

2. A. I. Vogel, "A Textbook of Practical Organic Chemistry", 3rd Edn., Longmans, London, **1956**, pp. 130-132.

Chapter in an edited text :

3. W. Leistritz, "Methods of bacterial reduction in spices ", in "Spices: Flavor Chemistry and Antioxidant Properties" (Ed. S. J. Risch and C-T. Ito), American Chemical Society, Washington, DC, **1997**, Ch. 2.

Thesis / Dissertation :

4. W. phudhawong, "Isolation of glycosides by electrolytic decolourisation and synthesis of pentinomycin", *PhD. Thesis*, **2002**, Chiang Mai University, Thailand.

Patent :

5. K. Miwa, S. Maeda and Y. Murata, "Purification of stevioside by electrolysis", *Jpn. Kokai Tokkyo Koho 79 89,066* (**1979**).

Proceedings :

6. P. M. Sears, J. Peele, M. Lassauzet and P. Blackburn, "Use of antimicrobial proteins in the treatment of bovine mastitis", Proceedings of the 3rd International Mastitis Seminars, **1995**, Tel-Aviv, Israel, pp. 17-18.

Editorial

Are we placing too much reliance on technology?

Most of us are now undeniably living in a world dominated by modern technology and our lifestyle is accordingly shaped by it. For example, just think of what it would be like if we were to go without electricity for the rest of our life. Or if there were no means of such modern communications as telephone, computers, TV and radio any more. Our ancestors had in fact gone through that kind of lifestyle before and surprisingly they survived and actually did very well! For one thing, this simply shows that, in the ultimate sense, those products of modern technology that we tend to take for granted and think we cannot do without are indeed not essentials for life per se.

Having said that, it is also true that technology, when used judiciously, can help make our modern everyday life much easier and more pleasant. In fact, our ancestors also had their own technology to ease them through life, but they relied on it only for their physical comfort and conveniences and never appeared to allow it to take the place of or interfere with their moral/ethical standards or judgement on important issues.

To cite as examples—and well known ones at that, cases have been occasionally witnessed even as recently as within the lifetime of many of us still living now, in which a pledge is kept without a written and signed document (in a way, a product of technology). Obviously for these people of integrity (mostly the senior members of the common citizen), words and deeds are more important and worthier of keeping than a piece of paper. Recently also, an average couple might simply live together as man and wife and have a dozen children without a single official marriage licence (another product of technology). However, to these people, irresponsibility and unfaithfulness is out the question. Just think of how life would be if, every time a wife is pregnant and gives birth to a child, the husband and/or his folks raise their eyebrows and demand a DNA test!

Nowadays it seems we tend to place too much reliance on modern technology, the more modern the better! A patient with a simple ailment, for example, has been known to go through diagnostic tests with a battery of expensive instruments of the latest technology when sometimes all that is needed is a simple stethoscope coupled with a sound analysis and judgement by an experienced doctor to find out what is wrong. Other examples of over-reliance on technology abound in this country, where technology and its verdict is sometimes regarded as something almost sacred and not to be disputed.

Technology is fine as it is, but it should neither be allowed to control, manipulate or modify our discernment and integrity as human beings especially when and where it counts most, nor be looked upon as the final answer or cure-all to all our problems.

22 September 2010

Full Paper

Novel analysis of Petri-net-based controllers by means of TCT implementation tool of supervisory control theory

Gökhan Gelen and Murat Uzam*

Niğde Üniversitesi, Mühendislik-Mimarlık Fakültesi, Elektrik-Elektronik Mühendisliği Bölümü,
Kampüs, 51200, Niğde, Turkey

*Corresponding author, E-mail: murat_uzam@hotmail.com or murat_uzam@nigde.edu.tr ;
Tel: + 90 388 225 22 82; Fax: + 90 388 225 01 12; URL: <http://host.nigde.edu.tr/muzam/>

Received: 24 March 2010 / Accepted: 2 August 2010 / Published: 7 September 2010

Abstract: The control of discrete event systems (DES) has been widely studied in the past two decades. Finite-state automata (FSA) and Petri nets (PN) are the two principal modelling formalisms for this study. Supervisory control theory (SCT), based on language and FSA concepts, is a well established framework for the study of discrete event control systems (DECS). PN-based approaches to the control design have been considered as an alternative framework. In the PN-based control of DES, given an uncontrolled PN model of a system and a set of specifications, a PN-based controller consisting of monitors (control places) is synthesised to solve the problem. In general, forbidden-state specifications are considered. Another heavily studied specification is to obtain the live system behaviour (non-blockingness in SCT terminology) for a given PN model by computing a PN-based controller. Unfortunately, PN-based analysis tools cannot deal with uncontrollable transitions. Therefore, to date there is no general technique for the correctness analysis of the computed PN-based controllers. This paper proposes a novel and general methodology to carry out the correctness analysis for the computed PN-based controllers by using the TCT implementation tool of SCT. Three examples are considered for illustration.

Keywords: discrete event systems (DES), Petri nets (PN), finite state automata (FSA), supervisory control theory (SCT)

1. Introduction

The control of discrete event systems (DES) has been widely studied in the past two decades. There are mainly two modelling formalisms for this study: finite-state automata (FSA) and Petri nets (PN). Supervisory control theory (SCT) is based on language and FSA concepts and was originally introduced to extend control theory concepts for continuous systems to the discrete event environment [1-4]. SCT is a well established framework for the study of discrete event control systems (DECS). On the other hand, PN-based approaches to the control design have been considered as an alternative

framework [5-9]. This is mainly because the state-space representation of PN as a vector addition system can result in a compact system description, thus keeping the net structure small even though the number of possible markings may become large. PN models lend themselves not only to the systematic construction of supervisory controllers, but also to the analysis of various qualitative properties and quantitative performance evaluation. The disadvantage of the PN models is that, in general, optimal supervisors need not exist within the class of PN even though the counterpart SCT problem may be solvable in the framework of automata.

In the PN-based control of DES, an uncontrolled PN model of a system represents the open-loop system. Without any means of control, the open-loop system would not behave as requested. Given an uncontrolled PN model of a system and a set of specifications, a PN-based controller consisting of monitors or control places is synthesised to solve the problem. When the uncontrolled PN model and the computed PN-based controller are augmented, the controlled model is obtained, which also represents the closed-loop system. In general, the specifications considered are of forbidden-state ones. Another heavily studied specification is to obtain live system behaviour (non-blockingness in SCT terminology) for a given PN model by computing a PN-based controller. Unfortunately, to date there is no general technique for the correctness analysis of the computed PN-based controllers. Heuristically, this analysis can be carried out by considering the reachability graph of a given PN model [10], but when dealing with complex models this method becomes impractical due to huge reachability graphs. In addition, it is not possible to deal with uncontrollable transitions with the currently available PN analysis tools. Therefore, it is crucial to obtain a general methodology to carry out the correctness analysis for the computed PN-based controllers. This paper proposes a general methodology to carry out the correctness analysis for the computed PN-based controllers by using the TCT implementation tool [11] of SCT. TCT (Toy Control Theory) is a standard software package developed under the supervision of Professor W. N. Wonham, the founder of SCT, for carrying out all necessary computations of SCT.

In brief, the correctness analysis is carried out as follows. To start with, it is assumed that an uncontrolled PN model, the specifications, and the PN-based controller, i.e. a set of monitors (control places), are given. Then the correctness analysis is carried out based on the following three main steps: (1) Transform the given problem from the PN domain to the automata domain and solve the problem by using TCT tool based on SCT. This transformation involves the representation of both uncontrolled PN model and the specifications as automata models. The proper supervisor obtained in this step is called RWSUPER and represents the maximally permissive and non-blocking behaviour for the considered problem; (2) Represent the PN-based controller as an automaton and obtain the controlled model of the system in the automata domain by using the synchronous product of automaton representation of the PN-based controller and automaton representation of the uncontrolled PN model. The supervisor obtained in this step is called PNSUPER and represents the controlled behaviour for the considered problem that survives under the supervision of the PN-based controller; and (3) Compare RWSUPER and PNSUPER. If these two are identical, then it can be concluded that the PN-based controller is maximally permissive and non-blocking.

The transformation from the PN domain to the automata domain has already been used [12-13]. The detailed treatment of this transformation involving more general classes of PN is proposed in this paper. It is well known that PN can be transformed into automata by means of the reachability graph [14]. Some recent work can also be seen [15-18] dealing with transformation from PN to automata. Transformation from automata to PN is also possible [19]. This transformation has already been applied to the control of DES [18, 20-22].

The purpose of this paper is to propose a general methodology for carrying out the correctness analysis for the computed PN-based controllers by using the TCT implementation tool of SCT. To show the applicability of the proposed method, three examples are considered in detail.

The remainder of the paper is organised as follows. PN with weighted input, output, inhibitor and enabling arcs are defined in Section 2. FSA and SCT are briefly reviewed in Section 3. Section 4 defines and explains the proposed mappings from PN to their automata representations. In Section 5, the proposed analysis technique of PN-based controllers by using TCT is explained. In Section 6, three

examples are considered in detail to show the applicability of the proposed analysis technique. Finally, conclusions are given in Section 7.

2. PN with Weighted Input, Output, Inhibitor and Enabling Arcs

PN are widely used as a formal tool for the design, analysis and control of DES. PN were named after Carl A. Petri, a contemporary German mathematician and computer scientist, who introduced a net-like mathematical tool for the study of communication with automata [23]. For PN basics the reader is referred to Peterson [24]. A weighted-arc PN is the one in which weights are associated with arcs. The arc mappings may take values over a set of all non-negative integers. In this case, each arc is said to have *multiplicity* w , where w represents the weight of arcs. *Ordinary* PN have a multiplicity of 1. The weight of an arc is indicated by a non-negative integer assigned to the arc. Unlike a standard PN, a PN with *inhibitor arcs* has the possibility of testing whether a place is void of tokens (*zero-testing ability*). Inhibitor arcs are a well known extension for standard PN. Inhibitor arcs are well suited to model a specific condition testing as opposed to producing and consuming tokens. The addition of inhibitor arcs gives PN the same modelling power as a Turing machine [25]. In this paper, weighted inhibitor arcs are considered in addition to ordinary inhibitor arcs. The former can be used for testing whether the number of tokens in a place is less than a certain threshold number [25]. As a complement of inhibitor arc, enabling arc was introduced by Uzam and Jones [26-27]. The introduction of enabling arcs causes PN to have *one testing ability*, i.e. the ability to test whether a place has a token(s). As with inhibitor arcs, enabling arcs are also well suited to model a specific condition testing. In this paper, weighted enabling arcs are considered in addition to ordinary enabling arcs. The former can be used for testing whether the number of tokens in a place is larger than or equal to a certain threshold number [26-27].

Formally a PN with weighted input, output, inhibitor and enabling arcs can be defined as follows:

$$PN = (P, T, Pre, Post, In, En, M_0)$$

where:

- $P = \{p_1, p_2, \dots, p_n\}$ is a finite, non-empty set of places ;
- $T = \{t_1, t_2, \dots, t_m\}$ is a finite, non-empty set of transitions, $P \cup T \neq \emptyset$ and $P \cap T = \emptyset$;
- $Pre: (P \times T) \rightarrow N$ is an input function that defines weighted input arcs from places to transitions, where N is a set of non-negative integers ;
- $Post: (T \times P) \rightarrow N$ is an output function that defines weighted output arcs from transitions to places ;
- $In: (P \times T) \rightarrow N$ is an inhibitor function that defines weighted inhibitor arcs from places to transitions ;
- $En: (P \times T) \rightarrow N$ is an enabling function that defines weighted enabling arcs from places to transitions ;
- $M_0 : P \rightarrow N$ is the initial marking.

PN with weighted input, output, inhibitor and enabling arcs consist of two types of nodes called places, represented by circles (○), and transitions, represented by bars (—). There are three types of arcs used, namely ordinary (input or output) arc, represented by a directed arrow (→), inhibitor arc, represented by an arrow whose end is a circle (—○), and finally enabling arc, represented by a directed arrow whose end is empty (—►). Weighted and directed ordinary arcs connect places to transitions and vice versa, whereas weighted enabling arcs and inhibitor arcs connect only places to transitions. The number of tokens in places represents the current state of the system and transitions represent events. Each transition has a set of input and output places, which represent the pre-condition and post-condition of the transition respectively. The marking of the PN is represented by the number of tokens in each place. Tokens are represented by black dots (●). Movement of tokens between places describes the evolution of the PN and is accomplished by the firing of the enabled transitions. “Enabling rules” and “firing rules” are associated with transitions. The enabling rules state the conditions under which transitions are allowed to fire. The firing rules define the marking modification induced by the transition firing. The enabling rules define the conditions that allow a transition t to fire,

and the firing rules specify the change of state produced by the transition. Both the enabling and the firing rules are specified through arcs. In particular, the enabling rules involve input arcs, inhibitor arcs and enabling arcs, while the firing rules depend on input arcs and output arcs. Note that input arcs play a double role as they are involved both in enabling and in firing. The following enabling and firing rules are used to govern the flow of tokens.

Enabling Rules: In a PN with weighted input, output, inhibitor and enabling arcs, there are three rules which define whether a transition is enabled to fire. These pre-conditions must be satisfied for a transition to fire:

1. If an input place p of a transition t is connected to t with a weighted input arc $Pre(p,t)$, then t is said to be enabled when p contains at least the number of tokens equal to the weight of the directed input arc, i.e. $M(p) \geq Pre(p,t)$. This is shown in Figure 1(a), where $t1$ is enabled if there are two or more tokens in $p1$. Therefore, $t1$ is enabled as $p1$ contains three tokens, i.e. $M(p1) = 3$ and $Pre(p1,t1) = 2$.
2. If an input place p of a transition t is connected to t with a weighted inhibitor arc $In(p,t)$, then t is said to be enabled when p contains fewer tokens than the weight of the inhibitor arc, i.e. $M(p) < In(p,t)$. This is shown in Figure 1(b), where $t1$ is enabled provided that there are two or more tokens in $p1$ and there are fewer than three tokens in $p3$. Therefore, $t1$ is enabled as $M(p1) = 3$ with $Pre(p1,t1) = 2$, and $M(p3) = 2$ with $In(p3,t1) = 3$.
3. If an input place p of a transition t is connected to t with a weighted enabling arc $En(p,t)$, then t is said to be enabled when p contains at least a number of tokens equal to the weight of the enabling arc, i.e. $M(p) \geq En(p,t)$. This is shown in Figure 1(c), where $t1$ is enabled provided that there are two or more tokens in $p1$ and there are at least four tokens in $p3$. Therefore, $t1$ is enabled as $M(p1) = 3$ with $Pre(p1,t1) = 2$, and $M(p3) = 4$ with $En(p3,t1) = 4$.

Transition $t1$ in Figure 1(d) represents all enabling rules at the same time. It is enabled if $M(p1) \geq 2$ due to $Pre(p1,t1) = 2$, and if $M(p2) < 3$ due to $In(p2,t1) = 3$, and if $M(p3) \geq 4$ due to $En(p3,t1) = 4$. It can be seen that $t1$ is enabled with the initial marking given in Figure 1(d).

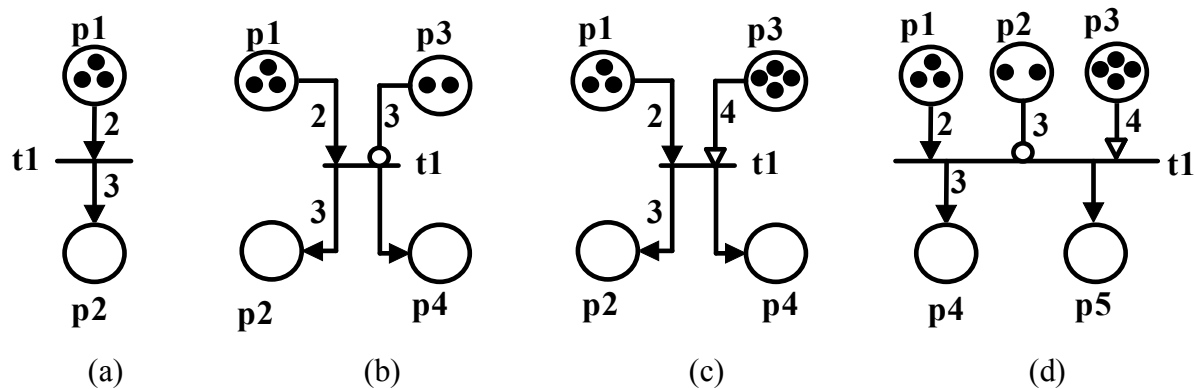


Figure 1. Illustration of enabling rules

Firing Rules: In a PN with weighted input, output, inhibitor and enabling arcs, when an enabled transition t fires, it removes $Pre(p_i,t)$ tokens from each input place p_i and deposits, at the same time, $Post(t,p_o)$ tokens in each output place p_o . The firing of an enabled transition t does not change the marking of the input places that are connected to t only by weighted enabling arcs or weighted inhibitor arcs. Firing rules can be followed from Figure 1 and Figure 2. As explained, all transitions shown in Figure 1 are enabled. When these transitions are fired the new markings are obtained as shown in Figure 2, based on the firing rules.

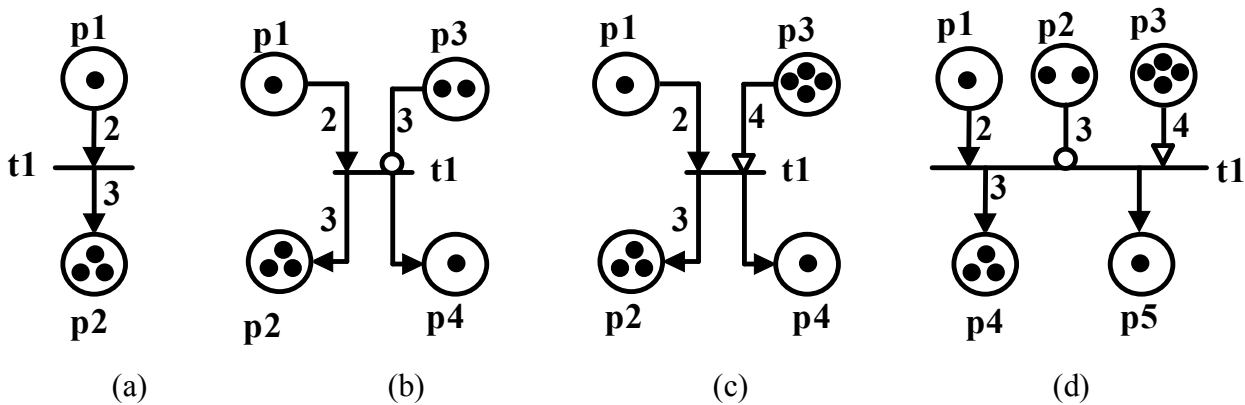


Figure 2. Illustration of firing rules

The firing of an enabled transition changes the marking, i.e. the token distribution of a PN. A marking M_i is said to be *reachable* from an initial marking M_0 if there exists a sequence of firings that can transform M_0 to M_i . A firing sequence is represented by $\sigma = t_1, t_2, t_3, \dots, t_m$. To show M_i is reachable from M_0 by σ , the following representation is used: $M_0 [\sigma > M_i$. A PN is said to be *ordinary* if the arcs are not weighted (by default the weight of an arc is 1). A PN is said to be *k-bounded* or *bounded* if the number of tokens in each place does not exceed a finite number 'k' for every marking reachable from the initial marking M_0 . A PN is said to be *safe* if all its places are safe. A place 'p' is safe if it contains no more than one token. In other words, a PN is called *safe* if it is 1-bounded. A PN is said to be *conservative* if the total number of tokens in all its places for all reachable markings is constant. A transition is said to be *live* if for all markings of the PN there is a firing sequence which takes the net to a marking, in which the transition is enabled. A PN is *live* if all its transitions are live. A live PN indicates the absence of *deadlocks* in the operation of the modelled system. A PN is said to be *reversible* if the initial marking M_0 is reachable from each marking. In this paper, bounded PN are considered. In later parts of this paper, safe and ordinary PN (SOPN) with inhibitor and enabling arcs are considered.

3. FSA and SCT

FSA are a classical tool used for many years for the study of DES. A finite automaton incorporates both principal system features, i.e. system states and system transitions in an abstract form. A FSA (or simply automaton), denoted by G , is a six-tuple $G=(Q, \Sigma, f, \Gamma, q_0, Q_m)$, where Q is the set of states, Σ is the finite event set, $f: Q \times \Sigma \rightarrow Q$ is the partial transition function, $\Gamma: q \rightarrow 2^\Sigma$ is the active event function, $\Gamma(q)$ is the set defined for every state of G and represents the feasible events of q , q_0 is the initial state and $Q_m \subseteq Q$ is the set of marked states representing the completion of a given task or operation. A simple automaton model with two states is shown in Figure 3. This automaton has two states labelled with q_0 and q_1 ; q_0 with a double arrow is the initial (and marked) state while q_1 with an exiting arrow is the marked state of the automaton. A directed arrow represents the transition functions of the automaton. Labels of transitions (e_1, e_2) correspond to events.

The language generated by G is denoted by $L(G)$ and is defined as $L(G) = \{s \in \Sigma^* : f(q_0, s) \text{ is defined}\}$. The language marked by G is denoted by $L_m(G)$ and is defined as $L_m(G) = \{s \in \Sigma^* : f(q_0, s) \in Q_m\}$. The DES modelled as automaton G is said to be non-blocking if $L(G) = L_m(G)$. DES named as A and B can be composed of a synchronous product (parallel composition) operation. The synchronous product of two automata is denoted by $A||B$ and represents the synchronous behaviour of two automata. In the resulting automaton, common events occur synchronously while the other events occur asynchronously [28-29].

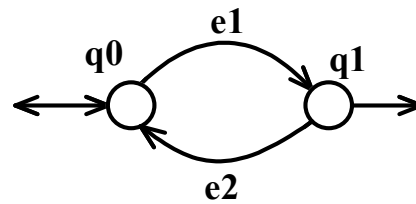


Figure 3. A simple automaton model

SCT was introduced to extend control theory concepts for continuous systems to the discrete-event environment [2, 4]. In SCT, a *forbidden state problem* [2] specifies the conditions that must be avoided, typically the simultaneous utilisation of some resource by two or more users. In addition, SCT generally requires the controlled system to be non-blocking (namely that specified target states, often just the initial state, be maintained reachable), and to be *maximally permissive*, i.e. to permit the occurrence of all events not leading to violation of the foregoing requirements. DES evolve on spontaneously occurring events. Let Σ be a finite set of events; the set of all finite concatenations of events in Σ is denoted by Σ^* . An element of this set is called a string. The number of events gives the length of the string. A string with no element is denoted by ε and is called empty string. A subset $L \subseteq \Sigma^*$ is called a language over Σ . For a string $s \in \Sigma^*$, \bar{s} denotes the prefix of s and is defined as $\bar{s} = \{s_p \in \Sigma^* \mid \exists t \in \Sigma^* (s_p t = s)\}$. Extension of this definition to language prefix closure of a language L is denoted by \bar{L} . A language L satisfying the condition $L = \bar{L}$ is said to be prefix-closed [28-29].

The SCT makes use of formal languages to model the uncontrolled behaviour of DES (plant) and specifications for the controlled behaviour. The objective is to restrict the behaviour of the system to a desired one, which is represented by the specifications. This is done by disabling some events to prevent the occurrence of some undesired strings in the system. The disabling action is accomplished by another simultaneously executing automaton called the supervisor. The system cannot be forced by the supervisor to generate new events. In SCT, events are divided into two disjoint sets, i.e. controllable events and uncontrollable events. These sets are denoted by Σ_c and Σ_{uc} respectively. The supervisor has no effect on uncontrollable events, which means that the supervisor cannot disable uncontrollable events. The existence of a supervisor is guaranteed if the desired language satisfies controllability conditions. This condition is defined as $\bar{K} \Sigma_{uc} \cap M \subseteq \bar{K}$, where \bar{K} is the language that will be generated under the control of supervisor and M is the language generated by the uncontrolled system.

The behaviour of a DES under the control of supervisor S is denoted by $L(S/G)$. A language K is called $L_m(G)$ -closed when the language satisfies condition $K = \bar{K} \cap L_m(G)$. If the desired behaviour $\bar{K} \cap L_m(G)$ is controllable and $L_m(G)$ -closed, then $\bar{K} = L(S/G) = \overline{L_m(S/G)}$, and this means that the controlled behaviour is non-blocking [29].

4. Mappings from PN to FSA

4.1 Mappings from SOPN to FSA

In this section, a set of mappings from SOPN to FSA is proposed. The mapping strategy is based on the representation of a SOPN place by an automaton with two states. The transitions between these states or self-looped transition from a state define the behaviour of the modelled SOPN. Each transition of a SOPN is represented by a transition with an associated event within its automaton counterpart. Note that the transitions considered in this section are all shown as uncontrollable, but it is also possible to consider them as controllable. In this respect there is no difference. Also note that the concurrent firing of enabled transitions is not considered and therefore at any time only one transition can fire. The conversion from a set of fundamental SOPN modules utilised in the modelling of DES to FSA is presented as follows.

4.1.1. Mapping for a single place with an input and an output transition

A single place with one input transition and one output transition is shown in Figure 4, together with its automaton representation. In Figures 4(a) and 4(b), the initial markings of p1 are $M_0(p1) = 0$ and 1 respectively. In this SOPN, t1 and t2 are labelled with ‘a’ and ‘b’ respectively to represent the respective events. In Figure 4(a), initially t1 is enabled. If it is fired, a token is deposited in p1. If p1 contains a token, then t2 is enabled to fire. When p1 contains a token and t2 is fired, the token is removed from p1. In the automaton representation of the SOPN shown in Figure 4(a), there are two states: s0 is the initial and marker state and represents the absence of a token in p1, while s1 represents the presence of a token in p1. At the initial state, if event ‘a’ occurs, then automaton changes its state from s0 to s1. When the automaton is in s1 and event ‘b’ occurs, then automaton changes its state from s1 to s0. In Figure 4(b), initially t2 is enabled. If it is fired, the token is removed from p1. When p1 is void of token, t1 is enabled to fire. When t1 is fired, a token is deposited in p1. In the automaton representation of the SOPN shown in Figure 4(b), there are two states: s0 is the initial and marker state and represents the presence of a token in p1, while s1 represents the absence of a token in p1. At the initial state, if event ‘b’ occurs, then automaton changes its state from s0 to s1. When the automaton is in s1 and event ‘a’ occurs, then automaton changes its state from s1 to s0.

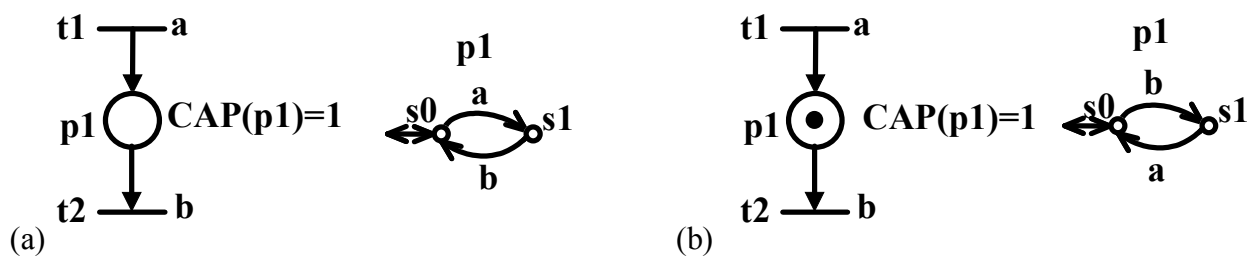


Figure 4. A single place with one input transition and one output transition and its automaton representation: (a) with the initial marking $M_0(p1) = 0$; (b) with the initial marking $M_0(p1) = 1$

4.1.2. Mapping for choice

A choice can be made between two or more activities (processes) in order to let just one of them start. To model this property in PN, a place with more than one output transition is used. A choice example is shown in Figure 5, together with its automaton representation. In Figures 5(a) and 5(b), the initial markings of p1 are $M_0(p1) = 0$ and 1 respectively. In this SOPN, t1, t2 and t3 are labelled with ‘a’, ‘b’ and ‘c’ respectively to represent the respective events. The mapping for choice is obvious from both figures and the state change from one state to another takes place based on the occurrence of the respective events as explained in the previous mappings.

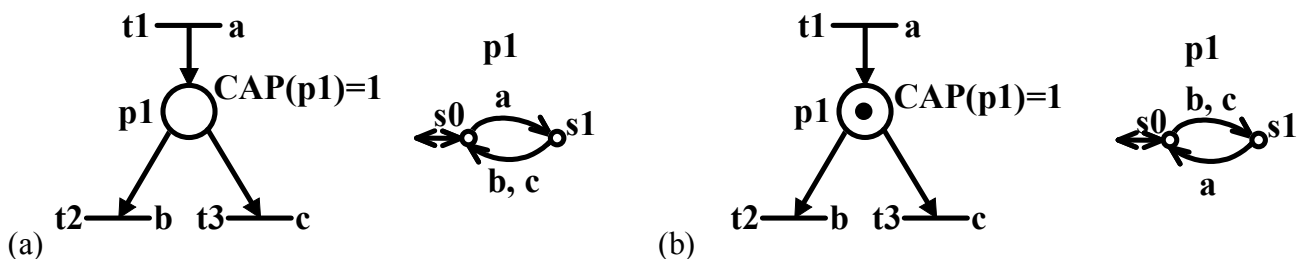


Figure 5. A choice example between transitions t2 and t3 and its automaton representation: (a) with the initial marking $M_0(p1) = 0$; (b) with the initial marking $M_0(p1) = 1$

4.1.3. Mapping for merge

Two or more activities (processes) can be merged. To model this property in PN, a place with more than one input transition is used. A merge example is shown in Figure 6, together with its automaton representation. In Figures 6(a) and 6(b), the initial markings of p1 are $M_0(p1) = 0$ and 1 respectively. In this SOPN, t1, t2 and t3 are labelled with 'a', 'b' and 'c' respectively to represent the respective events. The mapping for merge is obvious from both figures and the state change from one state to another takes place based on the occurrence of the respective events as explained in the previous mappings.

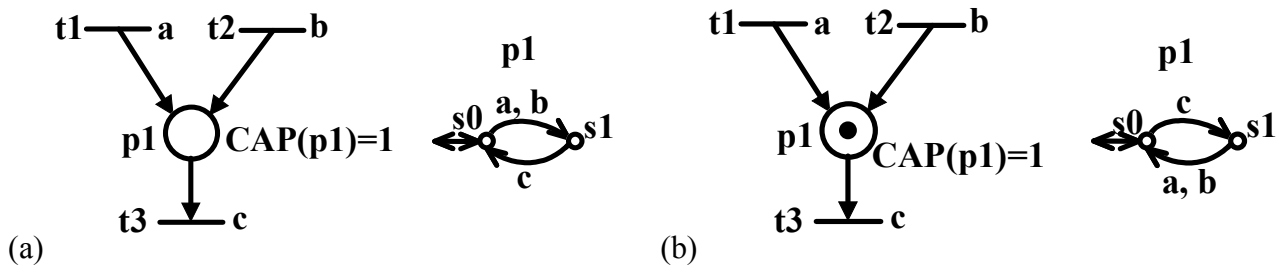


Figure 6. A merge example between transitions t2 and t3 and its automaton representation: (a) with the initial marking $M_0(p1) = 0$; (b) with the initial marking $M_0(p1) = 1$

4.1.4. Mapping for fork (concurrency)

Fork (concurrency) represents two or more concurrent processes initiated at the same time. To model this property in PN, a transition with more than one output place is used. A fork example is shown in Figure 7, together with its automaton representation. Initially, it is assumed that there are no tokens in p1 and p2. In this SOPN, t1, t2 and t3 are labelled with 'a', 'b' and 'c' respectively to represent the respective events. Initially only t1 is enabled. When there is no token in p1 and p2 and t1 is fired, then a token each is put in p1 and p2. This means that both activities represented by p1 and p2 are initiated at the same time. When there is a token in p1 (or p2), t2 (respectively t3) is enabled. When p1 (or p2) contains a token and t2 (respectively t3) is fired, the token is removed from p1 (respectively p2). Each place is represented by a two-state automaton as shown in Figure 7. Then the automaton representation of the SOPN, shown in Figure 7, is obtained by the synchronous product $p1 || p2$ of automata models p1 and p2. In the automaton model $p1 || p2$, there are four states, $Q = \{s0, s1, s2, s3\}$, representing the SOPN markings $M(p1, p2)^T = \{00, 11, 01, 10\}$ respectively. The state change from one to another takes place based on the occurrence of the respective events as explained in the previous mappings.

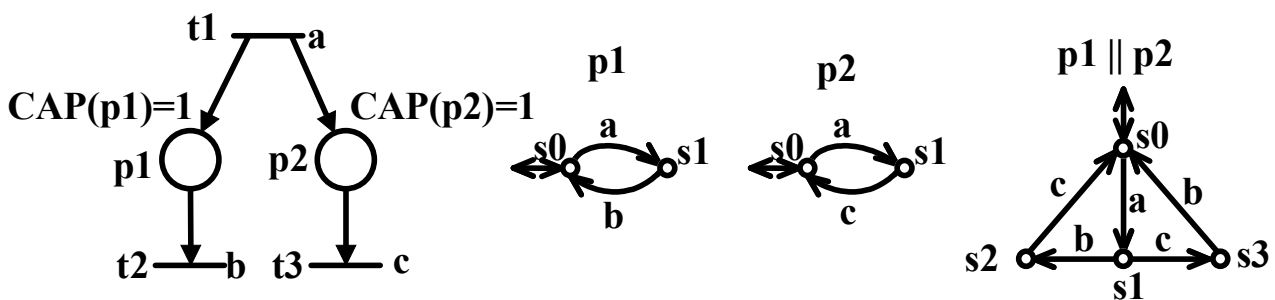


Figure 7. A fork (concurrency) example for p1 and p2 and its automaton representation

4.1.5. Mapping for join (synchronisation)

Two or more activities (processes) can be joined (synchronised). To model this property in PN, a transition with more than one input place is used. A join example is shown in Figure 8, together with its automaton representation. To represent the respective events, t_1 , t_2 and t_3 are labelled with ‘a’, ‘b’ and ‘c’ respectively. Initially both t_1 and t_2 are enabled. When there is no token in p_1 (or p_2) and t_1 (respectively t_2) is fired, then a token is put in p_1 (respectively p_2). When there is a token each in p_1 and p_2 , this means that both activities represented by p_1 and p_2 are ready to be joined (synchronised). When there is a token each in p_1 and p_2 and t_3 is fired, the tokens are removed from p_1 and p_2 and thus the two processes are joined (synchronised). Each place is represented by a two-state automaton as shown in Figure 8. Then the automaton representation of the SOPN, shown in Figure 8, is obtained by the synchronous product $p_1 || p_2$ of automata models p_1 and p_2 . In the automaton model $p_1 || p_2$, there are four states, $Q = \{s_0, s_1, s_2, s_3\}$, representing the SOPN markings $M(p_1, p_2)^T = \{00, 11, 10, 01\}$ respectively. The state change from one to another takes place based on the occurrence of the respective events as explained in the previous mappings.

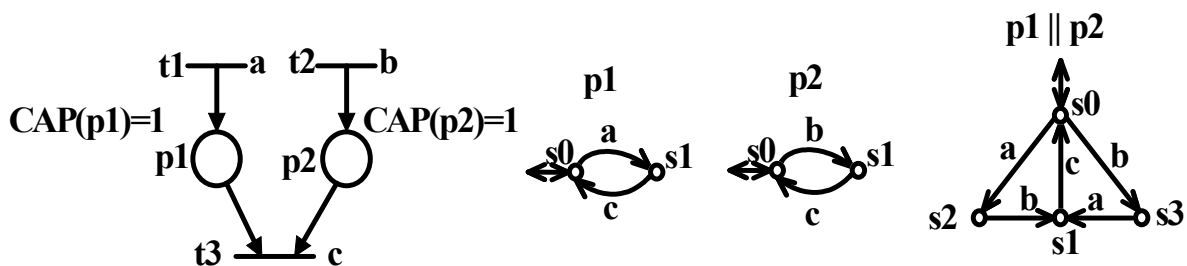


Figure 8. A join (synchronisation) example for p_1 and p_2 and its automaton representation

4.1.6. Mapping for an inhibitor arc

A single place with one input transition, one output transition and an inhibitor arc $In(p_1, t_3)$ is shown in Figure 9, together with its automaton representation. In Figures 9(a) and 9(b), the initial markings of p_1 are $M_0(p_1) = 0$ and 1 respectively. In this SOPN, t_1 , t_2 and t_3 are labelled with ‘a’, ‘b’ and ‘c’ respectively to represent the respective events. In Figure 9(a), initially both t_1 and t_3 are enabled and can fire. If t_1 is fired, a token is deposited in p_1 . If p_1 contains a token, then t_2 is enabled to fire but t_3 is not enabled and therefore cannot fire. When p_1 contains a token and t_2 is fired, the token is removed from p_1 . In brief, when there is no token in p_1 , t_3 is enabled to fire but when there is a token in p_1 , t_3 is not enabled to fire. In the automaton representation of the SOPN shown in Figure 9 (a), there are two states: s_0 is the initial and marker state and represents the absence of a token in p_1 , while s_1 represents the presence of a token in p_1 . At the initial state, the self-looped transition $[s_0, c, s_0]$ allows event ‘c’ to occur. If the automaton is in s_0 and if event ‘a’ occurs, then it changes its state from s_0 to s_1 . When the automaton is in s_1 , event ‘c’ is not allowed to occur. When the automaton is in s_1 and event ‘b’ occurs, then it changes its state from s_1 to s_0 . In Figure 9(b), initially only t_2 is enabled and since there is a token in p_1 , t_3 is not enabled. If t_2 is fired, the token is removed from p_1 . When p_1 is void of token, both t_1 and t_3 are enabled to fire. When t_1 is fired, a token is deposited in p_1 . In the automaton representation of the SOPN shown in Figure 9(b), there are two states: s_0 is the initial and marker state and represents the presence of a token in p_1 , while s_1 represents the absence of a token in p_1 . When the automaton is in s_0 , event ‘c’ is not allowed to occur. At the initial state, if event ‘b’ occurs, then the automaton changes its state from s_0 to s_1 . When the automaton is in s_1 , event ‘c’ is allowed to occur by means of the self-looped transition $[s_1, c, s_1]$. When the automaton is in s_1 and event ‘a’ occurs, then the automaton changes its state from s_1 to s_0 .

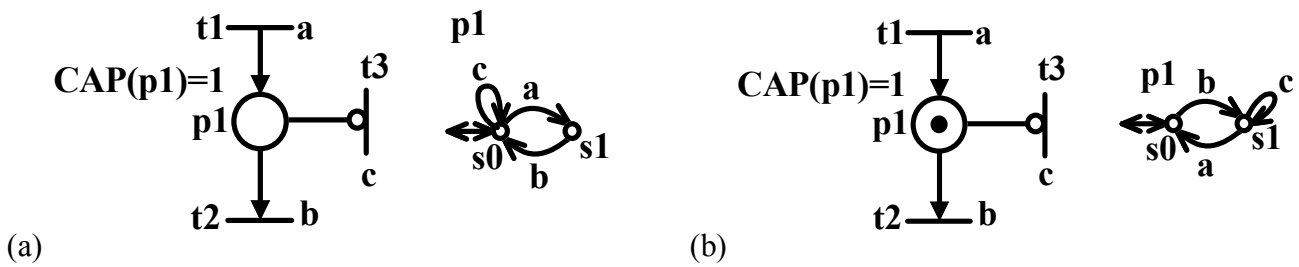


Figure 9. A place $p1$ with one input transition, one output transition and an inhibitor arc $In(p1,t3)$, and its automaton representation: a) with the initial marking $M_0(p1) = 0$; b) with the initial marking $M_0(p1) = 1$

4.1.7. Mapping for an enabling arc

A single place with one input transition, one output transition and an enabling arc $En(p1,t3)$ is shown in Figure 10, together with its automaton representation. In Figures 10(a) and 10(b), the initial markings of $p1$ are $M_0(p1) = 0$ and 1 respectively. In this SOPN, $t1$, $t2$ and $t3$ are labelled with ‘a’, ‘b’ and ‘c’ respectively to represent the respective events. In Figure 10(a), initially only $t1$ is enabled and since there is no token in $p1$, $t3$ is not enabled. If $t1$ is fired, a token is put in $p1$. When there is a token in $p1$, both $t2$ and $t3$ are enabled to fire. When there is a token in $p1$ and $t3$ is fired, the token remains in $p1$. When there is a token in $p1$ and $t1$ is fired, the token is removed from $p1$. In the automaton representation of the SOPN shown in Figure 10(a), there are two states: $s0$ is the initial and marker state and represents the absence of a token in $p1$, while $s1$ represents the presence of a token in $p1$. When the automaton is in $s0$, event ‘c’ is not allowed to occur. At the initial state, if event ‘a’ occurs, then the automaton changes its state from $s0$ to $s1$. When the automaton is in $s1$, event ‘c’ is allowed to occur by means of the self-looped transition $[s1,c,s1]$. When the automaton is in $s1$ and event ‘a’ occurs, then the automaton changes its state from $s1$ to $s0$. In Figure 10(b), initially both $t1$ and $t3$ are enabled and can fire. When there is a token in $p1$ and $t3$ is fired, the token remains in $p1$. When there is a token in $p1$ and $t1$ is fired, the token is removed from $p1$. If $p1$ contains no token, then $t1$ is enabled to fire but $t3$ is not enabled and therefore cannot fire. When $p1$ contains no token and $t1$ is fired, a token is put in $p1$. In brief, when there is a token in $p1$, $t3$ is enabled to fire, but when there is no token in $p1$, $t3$ is not enabled to fire. In the automaton representation of the SOPN shown in Figure 10(b), there are two states: $s0$ is the initial and marker state and represents the presence of a token in $p1$, while $s1$ represents the absence of a token in $p1$. At the initial state, the self-looped transition $[s0,c,s0]$ allows event ‘c’ to occur. When the automaton is in $s0$ and event ‘b’ occurs, then the automaton changes its state from $s0$ to $s1$. When the automaton is in $s1$, event ‘c’ is not allowed to occur. When the automaton is in $s1$ and event ‘a’ occurs, then the automaton changes its state from $s1$ to $s0$.

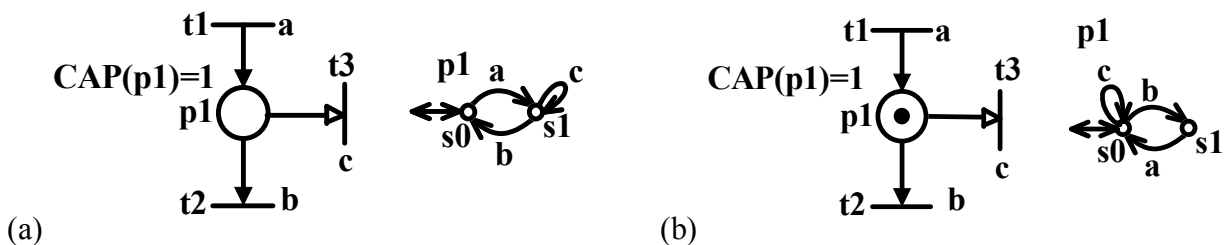


Figure 10. A place $p1$ with one input transition, one output transition and an enabling arc $En(p1,t3)$, and its automaton representation: (a) with the initial marking $M_0(p1) = 0$; (b) with the initial marking $M_0(p1) = 1$

4.1.8. Mapping for mutual exclusion

Mutual exclusion is used to avoid the simultaneous use of a common resource, examples of which include machines, robots and fixtures in the manufacturing context. There may be two or more processes trying to access the common resource at the same time. Consider a mutual exclusion example shown in Figure 11, together with its automaton representation. Initially, it is assumed that there are no tokens in p1 and p2 while there is a token in p3. In this SOPN, t1, t2, t3 and t4 are labelled with ‘a’, ‘b’, ‘c’ and ‘d’ respectively to represent the respective events. In this SOPN, p1 and p2 represent two processes using a common resource represented by a token in p3. Here, p3 ensures the following: $M(p1) + M(p2) + M(p3) = 1$. This means that at any time the sum of tokens in places p1, p2 and p3 is just 1. Initially both t1 and t3 are enabled. When there is no token in p1 (or p2) and there is a token in p3, if t1 (respectively t3) is fired, then the token is removed from p3 and a token is put in p1 (respectively p2). This means that only one activity represented by t1 or t3 can be initiated. When there is a token in p1 (or p2), t2 (respectively t4) is enabled. When p1 (or p2) contains a token and t2 (respectively t4) is fired, the token is removed from p1 (respectively p2) and a token is deposited in p3. Each place is represented by a two-state automaton as shown in Figure 11. Then, the automaton representation of the SOPN shown in Figure 11 is obtained by the synchronous product $p1||p2||p3$ of automata models p1, p2 and p3. In the automaton model $p1||p2||p3$, there are three states, $Q = \{s0, s1, s2\}$, representing the following SOPN markings: $M(p1,p2,p3)^T = \{001, 100, 010\}$ respectively. The state change from one state to another takes place based on the occurrence of the respective events as explained in the previous mappings.

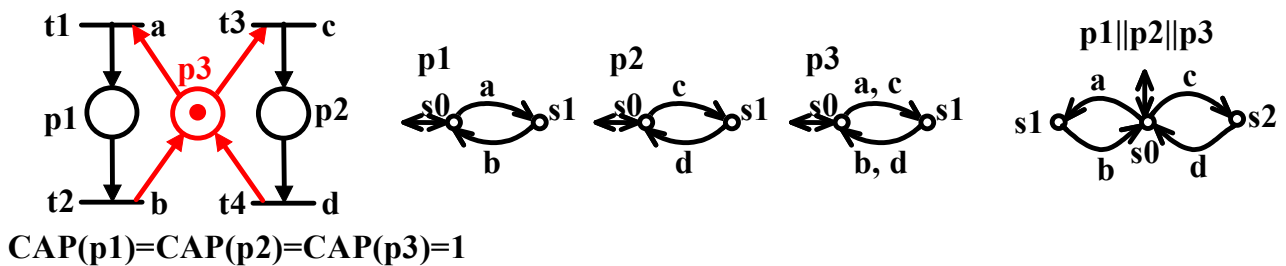


Figure 11. A mutual exclusion example in SOPN and its automaton representation

The place p3 shown in Figure 11 is called a control place or a monitor and is widely used in the literature to enforce control specifications. In this particular example the specification to be enforced is $M(p1) + M(p2) \leq 1$. This means that the sum of tokens in places p1 and p2 must be less than or equal to 1. At this point an alternative way to enforce the same specification is considered.

Consider a mutual exclusion example shown in Figure 12, together with its automaton representation. Initially, it is assumed that there are no tokens in p1 and p2. Initially both t1 and t3 are enabled, as both p1 and p2 are void of tokens. When there is no token in p1 (or p2) and t1 (respectively t3) is fired, then a token is put in p1 (respectively p2). When there is a token in p1 (respectively p2), the inhibitor arc $In(p1,t3)$ (respectively $In(p2,t1)$) inhibits t3 (respectively t1) from firing. This means that only one activity represented by t1 or t3 can be initiated. When there is a token in p1 (or p2), t2 (respectively t4) is enabled. When p1 (or p2) contains a token and t2 (respectively t4) is fired, the token is removed from p1 (respectively p2). Each place is represented by a two-state automaton as shown in Figure 12. Then the automaton representation of the SOPN shown in Figure 12 is obtained by the synchronous product $p1||p2$ of the automata models p1 and p2. In the automaton model $p1||p2$, there are three states, $Q = \{s0, s1, s2\}$, representing the following SOPN markings: $M(p1,p2)^T = \{00, 10, 01\}$ respectively. The state change from one to another takes place based on the occurrence of the respective events as explained in the previous mappings. As can be seen, the synchronous products $p1||p2||p3$ and $p1||p2$ in Figures 11 and 12 respectively are identical. In other words, these automata generate the same language and therefore the SOPN shown in Figure 11 and the one shown in Figure 12 enforce the same specification. In this respect, these two SOPN are said to be “control equivalent.”

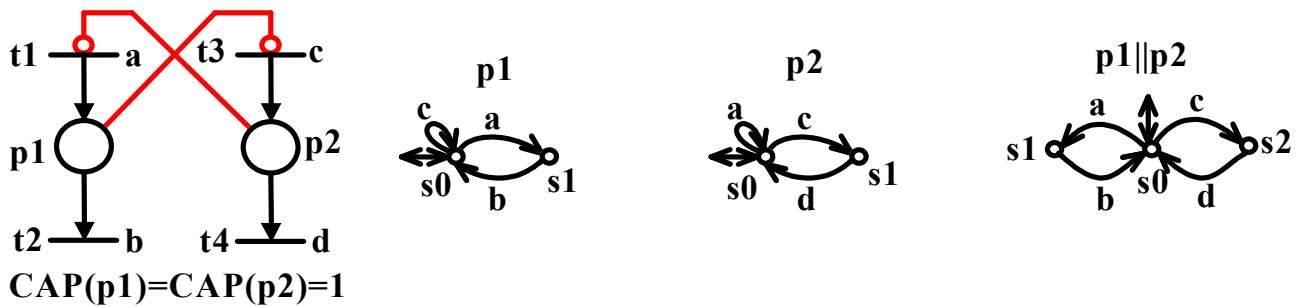


Figure 12. An alternative way to enforce the mutual exclusion specification $M(p1) + M(p2) \leq 1$ in SOPN, and its automaton representation

4.2. Mappings from PN with Weighted Arcs to FSA

In this section, a set of mappings from PN with weighted input, output, inhibitor and enabling arcs to FSA is proposed. The first requirement for mapping a PN with weighted input, output, inhibitor and enabling arcs to FSA is that the PN considered must be bounded; otherwise the mapping is not possible. The token capacity of a given place p , represented as $CAP(p)$, must be known to start the mapping. Then each place p of a given PN model is considered separately, together with its input, output, inhibitor and/or enabling arcs. If p is bounded in accordance with $CAP(p) \leq b$, for instance, then p is modelled by a buffer with capacity b (i.e. $b+1$ states). For example, if a PN place p has a token capacity of 3, i.e. $CAP(p) \leq 3$, then it can be represented by 4 states. The transitions (including the self-loops) between states of the automaton characterise the behaviour of the PN modelled. Every transition of p is represented by a transition within the automaton model of p . For the examples considered here, a label is assigned for each transition to represent the respective event. Note that the transitions considered in this section are all shown as uncontrollable, but it is also possible to consider them as controllable. In this respect, there is no difference. Also note that the concurrent firing of enabled transitions is not considered and therefore at any time only one transition can fire. In this section, some important mapping examples are considered. In these examples, only one place is considered with different arcs to show the proposed method.

4.2.1. Mapping for a single place with a token capacity $CAP(p) \leq b$

Here, two mapping examples are considered. As can be seen from Figure 13, the first example involves mapping for a single place $p1$ with a token capacity $CAP(p1) \leq 4$, together with an ordinary input arc $Pre(t1,p1) = 1$ and an ordinary output arc $Post(p1,t2) = 1$. Initially it is assumed that $p1$ is void of tokens. As long as the number of tokens in $p1$ is fewer than 4, every firing of $t1$ deposits a token in $p1$. Provided that there is a token(s) in $p1$, every firing of $t2$ removes a token from $p1$. To represent the respective events, $t1$ and $t2$ are labelled with 'a' and 'b' respectively. Since $p1$ is bounded in accordance with $CAP(p) \leq 4$, it is modelled by a buffer with capacity 5 as shown in Figure 13. State $s0$ is the initial and marker state and represents the absence of tokens in $p1$. States $s1, s2, s3$ and $s4$ represent the presence of 1, 2, 3 and 4 tokens in $p1$ respectively. In the automaton model, the occurrence of event 'a' represents both the firing of $t1$ and the depositing of a token in $p1$, while the occurrence of event 'b' represents both the firing of $t2$ and the removing of a token from $p1$.

As can be seen from Figure 14, the second example involves mapping for a single place $p1$ with a token capacity $CAP(p1) \leq 6$, together with an ordinary input arc $Pre(t1,p1) = 1$, an ordinary output arc $Post(p1,t2) = 1$, a weighted input arc $Pre(t3,p1) = 2$, and a weighted output arc $Post(p1,t4) = 3$. Initially it is assumed that $p1$ is void of tokens. As long as the number of tokens in $p1$ is fewer than 6, every firing of $t1$ deposits a token in $p1$. Similarly, if the number of tokens in $p1$ is fewer than 5, every firing of $t3$ deposits two tokens in $p1$. Provided that there is a token(s) in $p1$, every firing of $t2$ removes a token from $p1$. Similarly, if the number of tokens in $p1$ is greater than or equal to 3, every

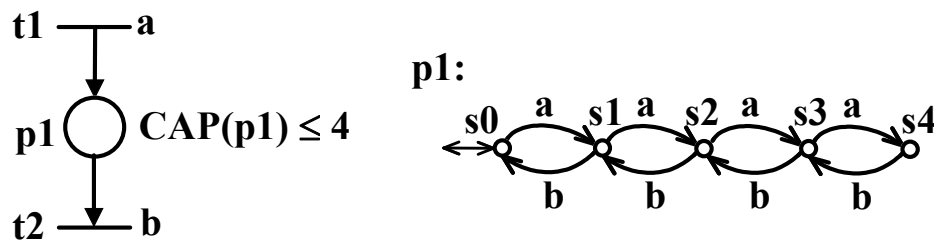


Figure 13. A single place with a token capacity $CAP(p1) \leq 4$, together with an ordinary input arc $Pre(t1,p1) = 1$ and an ordinary output arc $Post(p1,t2) = 1$, and its automaton representation

firing of $t4$ removes three tokens from $p1$. To represent the respective events, $t1$, $t2$, $t3$ and $t4$ are labelled with ‘a’, ‘b’, ‘c’ and ‘d’ respectively. Since $p1$ is bounded in accordance with $CAP(p) \leq 6$, it is modelled by a buffer with capacity 7 as shown in Figure 14. State $s0$ is the initial and marker state and represents the absence of tokens in $p1$. States $s1, s2, s3, s4, s5$ and $s6$ represent the presence of 1, 2, 3, 4, 5 and 6 tokens in $p1$ respectively. In the automaton model, the occurrence of event ‘a’ represents both the firing of $t1$ and the depositing of a token in $p1$, while the occurrence of event ‘b’ represents both the firing of $t2$ and the removing of a token from $p1$. Likewise, the occurrence of event ‘c’ represents both the firing of $t3$ and the depositing of two tokens in $p1$, while the occurrence of event ‘d’ represents both the firing of $t4$ and the removing of three tokens from $p1$.

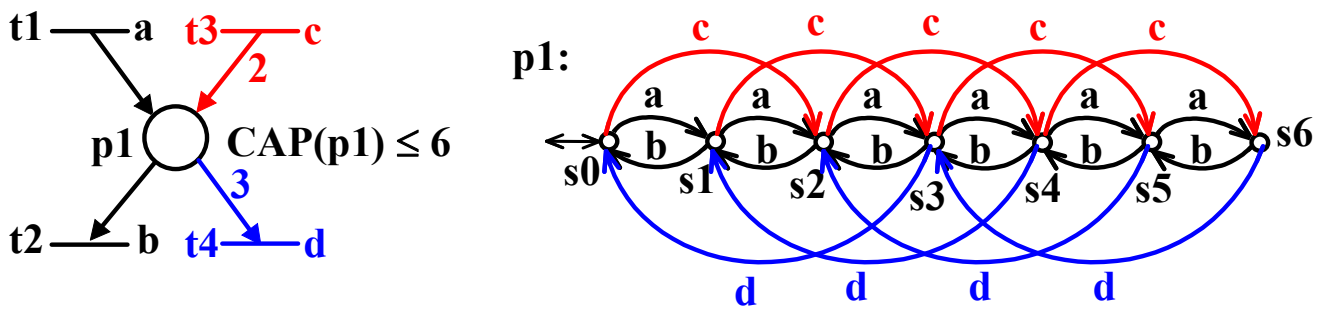


Figure 14. A single place with a token capacity $CAP(p1) \leq 6$, together with a weighted input arc $Pre(t3,p1) = 2$ and a weighted output arc $Post(p1,t4) = 3$, and its automaton representation

4.2.2. Mapping for weighted inhibitor arc

Mapping for weighted inhibitor arc is explained by means of an example in this section. As can be seen from Figure 15, this example involves mapping for a single place $p1$ with a token capacity $CAP(p1) \leq 5$, together with an ordinary input arc $Pre(t1,p1) = 1$, an ordinary output arc $Post(p1,t2) = 1$ and a weighted inhibitor arc $In(p1,t3) = 4$. Initially it is assumed that $p1$ is void of tokens. As long as the number of tokens in $p1$ is fewer than 5, every firing of $t1$ deposits a token in $p1$. Provided that there is a token(s) in $p1$, every firing of $t2$ removes a token from $p1$. As long as the number of tokens in $p1$ is fewer than 4, $t3$ is allowed to fire; otherwise it is not allowed to fire. The firing of $t3$ does not change the number of tokens present in $p1$. To represent the respective events, $t1$, $t2$, and $t3$ are labelled with ‘a’, ‘b’ and ‘c’ respectively. Since $p1$ is bounded in accordance with $CAP(p) \leq 5$, it is modelled by a buffer with capacity 6 as shown in Figure 15. State $s0$ is the initial and marker state and represents the absence of tokens in $p1$. States $s1, s2, s3, s4$ and $s5$ represent the presence of 1, 2, 3, 4 and 5 tokens in $p1$ respectively. In the automaton model, the occurrence of event ‘a’ represents both the firing of $t1$ and the depositing of a token in $p1$, while the occurrence of event ‘b’ represents both the firing of $t2$ and the removing of a token from $p1$. Self-loops $[s0,c,s0], [s1,c,s1], [s2,c,s2]$ and $[s3,c,s3]$ are added to states $s0, s1, s2$ and $s3$ respectively to represent that the occurrence of event ‘c’ is allowed in these

states. On the other hand, as there are no such self-loops assigned to states s_4 and s_5 , the occurrence of event 'c' is not allowed in these states.

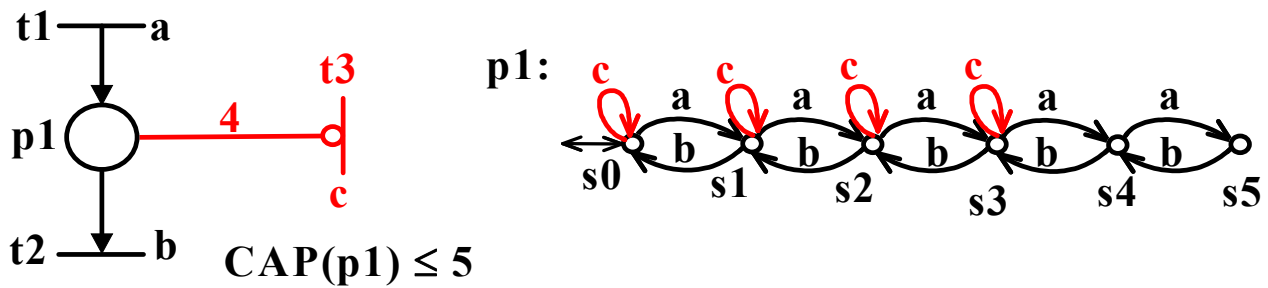


Figure 15. A single place with a token capacity $CAP(p1) \leq 5$, together with a weighted inhibitor arc $In(p1,t3) = 4$ and its automaton representation

4.2.3. Mapping for weighted enabling arc

Mapping for weighted enabling arc is explained by means of an example in this section. As can be seen from Figure 16, this example involves mapping for a single place $p1$ with a token capacity $CAP(p1) \leq 5$, together with an ordinary input arc $Pre(t1,p1) = 1$, an ordinary output arc $Post(p1,t2) = 1$ and a weighted enabling arc $En(p1,t3) = 4$. Initially it is assumed that $p1$ is void of tokens. As long as the number of tokens in $p1$ is fewer than 5, every firing of $t1$ deposits a token in $p1$. Provided that there is a token(s) in $p1$, every firing of $t2$ removes a token from $p1$. As long as the number of tokens in $p1$ is larger than or equal to 4, $t3$ is allowed to fire; otherwise it is not allowed to fire. The firing of $t3$ does not change the number of tokens present in $p1$. To represent the respective events, $t1$, $t2$ and $t3$ are labelled with 'a', 'b' and 'c' respectively. Since $p1$ is bounded in accordance with $CAP(p) \leq 5$, it is modelled by a buffer with capacity 6 as shown in Figure 16. State s_0 is the initial and marker state and represents the absence of tokens in $p1$. States s_1, s_2, s_3, s_4 and s_5 represent the presence of 1, 2, 3, 4 and 5 tokens in $p1$ respectively. In the automaton model, the occurrence of event 'a' represents both the firing of $t1$ and the depositing of a token in $p1$, while the occurrence of event 'b' represents both the firing of $t2$ and the removing of a token from $p1$. Self-loops $[s_4,c,s_4]$ and $[s_5,c,s_5]$ are added to states s_4 and s_5 respectively to represent that the occurrence of event 'c' is allowed in these states. On the other hand, as there are no such self-loops assigned to states s_0, s_1, s_2 and s_3 , the occurrence of event 'c' is not allowed in these states.

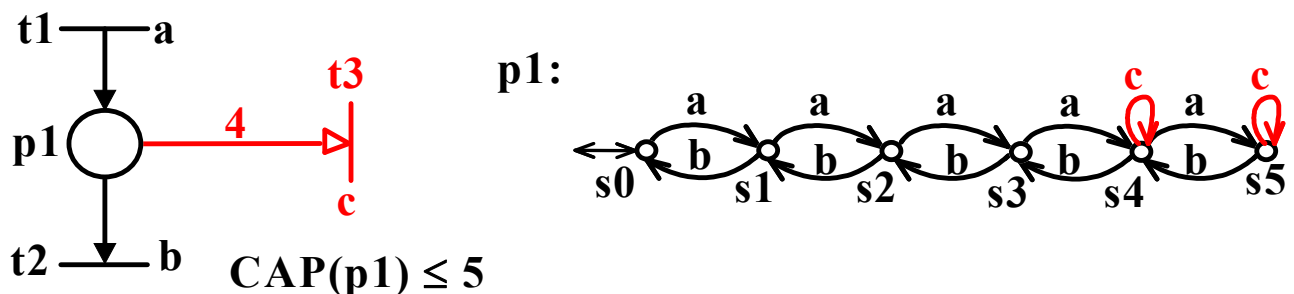


Figure 16. A single place with a token capacity $CAP(p1) \leq 5$, together with a weighted enabling arc $En(p1,t3) = 4$ and its automaton representation

5. Analysis of PN-Based Controllers by Using TCT

The proposed analysis approach based on TCT software can be summarised as follows:

1. Assume that an uncontrolled PN model (UPNM) of a DES with initial marking, feedback control elements (a set of control places) and also the related set of forbidden-state specifications are given.
2. Check that UPNM is bounded and determine explicit bounds on the place markings.
3. Convert the UPNM and the specifications into equivalent buffer models. Buffer models of UPNM and specifications are called PLANT and SPEC respectively.
4. Apply SCT to obtain a Ramadge-Wonham (RW) supervisor (RWSUPER) for a given problem by using PLANT and SPEC.
5. Convert the given feedback control elements (a set of control places) into equivalent buffer models called C1, C2, C3,
6. Obtain a controlled model called PNSUPER by using PLANT and buffer models of the given feedback control elements C1, C2, C3,
7. Compare RWSUPER and PNSUPER to see if they are identical.

In this paper, PN-based controllers enforcing forbidden-state specifications are analysed to see whether they are correct. In addition, liveness enforcing feedback control elements can also be analysed. In such problems, the specification is non-blockingness with respect to the initial state. In the literature, control places (or monitors) are very common feedback control elements with ordinary (or weighted) input and output arcs. However, in some problems it is also possible to carry out the same control action with some other type of control elements containing inhibitor arcs. The computations for the SCT can be performed by standard SCT software; in this paper the package TCT [11] is used. A quick review on some of the TCT commands used in this paper is given in the Appendix.

The boundedness computation in step 2 can be carried out with available PN tools [30] or, in simple cases, by inspection or application by hand of integer programming [29]. For step 3, to carry out the conversions, the mappings proposed in Section 4 can be used. In the conversion of UPNM into PLANT the following steps are followed. First, each place of UPNM, together with its input and output transitions (with input, output and possibly inhibitor or enabling arcs), is converted into an automaton (a buffer) model. Next, all automata models for the places are defined by using the Create() command within the TCT. Then the synchronous product command, namely Sync(), of TCT is used to obtain the PLANT automata model of UPNM. It can be shown that the PLANT model is actually isomorphic to the reachability graph of UPNM. If the problem considered is that of a forbidden-state problem, then in the conversion of specifications into SPEC, the following 3 steps are followed. First, if the specification requires more than one automaton model, namely SPEC1, SPEC2, ... SPEC_n, then they are all constructed and defined by using the Create() command within the TCT. Second, self-loops labelled with events that are possible in PLANT but not constrained by automaton model of each specification must be adjoined to one another. To accomplish this task, Selfloop() command is used. Finally, Meet() command of TCT is used to obtain the SPEC automaton model of the specifications. If the problem considered is that of a liveness enforcing problem, then the specification is non-blockingness with respect to the initial state. In this case, the non-blockingness specification is obtained by using Allevents() command: ALL = Allevents(PLANT), which results in a 1-state DES called ALL with all events of PLANT as self-loops.

If the problem considered is that of a forbidden-state problem, then step 4 is performed by supcon() command of TCT as follows: RWSUPER = Supcon(PLANT,SPEC). If the problem considered is that of a liveness enforcing problem, then step 4 is performed as follows: RWSUPER = Supcon(PLANT,ALL). Since RWSUPER is the result of a Supcon computation, it is automatically proper, i.e. trim, controllable and non-blocking with respect to PLANT. That it is maximally permissive is also a consequence of the semantics of Supcon, but maximal permissiveness is not included in the definition of "proper". This is a consequence of the semantics of Supcon, as stated explicitly by Wonham [29]. The proper RWSUPER obtained will be used as a proper supervisor reference to test the correctness of the PN-based feedback control elements.

In step 5, to carry out the conversions, the mappings proposed in Section 4 can be used. In the conversion of given feedback control elements (a set of control places) into equivalent buffer models, the following steps are followed. First, each feedback control element (a control place), together with its input and output transitions (with input, output and possibly inhibitor or enabling arcs), is converted into an automaton (buffer) model. Next, all automata models, called C_1, C_2, C_3, \dots , for the given feedback control elements are defined by using the `Create()` command within the TCT.

In step 6, a controlled model, namely `PNSUPER`, is obtained by using `PLANT` and C_1, C_2, C_3, \dots . To carry out this task, the synchronous product command, namely `Sync()`, is used. As with `RWSUPER`, `PNSUPER` obtained also represents the controlled behaviour of the `PLANT`, i.e. the subset of uncontrolled behaviour that this time survives under PN-based supervision.

In the final step, `RWSUPER` and `PNSUPER` are compared to see if they are identical (up to possible recoding of state sets). To carry out this task, the test command `Isomorph()` is used as follows: `Isomorph(PNSUPER,RWSUPER)`. If `RWSUPER` and `PNSUPER` are identical (or not identical), the outcome of this test will be 'true' (respectively 'false'). If the test result is 'true', then this proves the correctness of the PN-based feedback control elements. In that case it can be concluded that `PNSUPER` obtained by using PN-based feedback control elements is proper, i.e. maximally permissive and non-blocking. Note that when considering liveness enforcing problem, i.e. non-blockingness with respect to the initial state, if all transitions are controllable, then the trimmed plant, obtained by `Trim()` command as follows: `TPLANT = Trim(PLANT)`, will also be isomorphic to `PNSUPER` (or `RWSUPER`). To check this property, the following test is carried out by using `Isomorph()` command: `Isomorph(TPLANT,PNSUPER)`. However, when considering the liveness enforcing problem, if there are both controllable and uncontrollable transitions within the considered UPNM, then trimmed plant `TPLANT = Trim(PLANT)` may not be isomorphic to the `PNSUPER` (or `RWSUPER`). In that case, the `RWSUPER` is the supremal controllable sublanguage defining the maximally permissive and non-blocking behaviour. `Isomorph` can certainly be used to check the equality of closed and respectively marked behaviours in each of two DES, e.g. G_1 and G_2 . If `Isomorph(G1,G2) = true`, then indeed one has that $L(G_1) = L(G_2)$ and $L_m(G_1) = L_m(G_2)$. If, however, `Isomorph(G1,G2) = false`, it may still be the case that the language equalities are true. In the case of a 'false' outcome one must check, in addition, `Isomorph(MG1,MG2) = true/false`, where $MG_i = \text{Minstate}(G_i)$. If this second `Isomorph` returns 'true', then (even though the first `Isomorph` returns 'false') the language equalities do actually hold; if 'false', then one or both of the language equalities fails. This point has been made explicitly [29].

Up to now the analysis of optimal PN-based supervisors is explained. However, in the PN literature it is possible to come across suboptimal solutions to a given control problem. In order to analyse the correctness of a given suboptimal PN-based solution, RW-type supervisor `RWSUPER` can still be used as a reference for optimal controlled behaviour. Here, how this analysis is carried out is explained. The analysis steps explained above are still followed up to the last step (step 7). It is obvious that in this case the PN-based controlled model will be a sublanguage of the one generated by `RWSUPER`. Firstly, the suboptimal behaviour generated by PN-based controlled model `PNSUPER` is checked to see that it is not conflicting with the `RWSUPER` as follows: `Nonconflict(PNSUPER,RWSUPER)`. This test must result in "true". Secondly, the reachable Cartesian product of `PNSUPER` and `RWSUPER` is computed: `MRW_PN = Meet(PNSUPER,RWSUPER)`. The resulting DES `MRW_PN` must be equal to that of `PNSUPER` because in this case any suboptimal solution such as `PNSUPER` is expected to be sublanguage of the optimal solution `RWSUPER`. In short, the following result must be obtained: `true = Isomorph(MRW_PN,PNSUPER;identity)`.

6. Application Examples

In this section three examples are considered to show the applicability of the proposed analysis method. The detailed computation steps are provided in the TCT-generated log files for each example.

6.1. Example 1

The first example consists of a simple flexible manufacturing system (FMS) with deadlock (liveness enforcing) problem. Two different controllers solving the deadlock problem for this FMS are verified to be correct and “control equivalent.” Note that the PN considered in this example is in the class of SOPN unless otherwise stated. Consider the FMS shown in Figure 17 with two machines M1 and M2, each of which can process only one part at a time, and one robot, which can hold one part at a time. The parts enter the FMS through input/output buffers I/O1 and I/O2. Two parts are considered: P1 and P2. Initially it is assumed that there are no parts in the system. The production sequences are:

$$\begin{aligned} P1: & \quad M1 \rightarrow \text{Robot} \rightarrow M2 \\ P2: & \quad M2 \rightarrow \text{Robot} \rightarrow M1 \end{aligned}$$

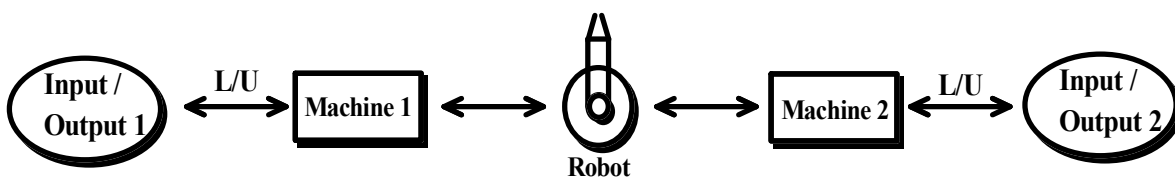


Figure 17. An example of FMS

Figure 18(a) shows the PN model (PNM) of the FMS taken from Uzam [20] for these production sequences. In this model there are eleven places, $P = \{p1, p2, \dots, p11\}$, and eight transitions, $T = \{t1, t2, \dots, t8\}$. All transitions are assumed to be controllable. Places $p2$, $p5$ and $p8$ represent the operation of M1, Robot and M2 respectively for the first production sequence. The number of tokens in $p1$, i.e. $M(p1) = 3$, represents the number of concurrent activities that can take place for P1. Similarly, places $p10$, $p7$ and $p4$ represent the operation of M2, Robot and M1 respectively for the second production sequence. The number of tokens in $p11$, i.e. $M(p11) = 3$, represents the number of concurrent activities that can take place for P2. Places $p3$, $p6$ and $p9$ denote the shared resources M1, Robot and M2 respectively. In order to have the correct system behaviour, it is desirable that each production sequence can finish. It can be shown that this system suffers from deadlock problem and for this system the specification is to obtain the live system behaviour (non-blockingness in SCT terminology). It can be shown that places $p1$ and $p11$ are redundant and therefore they can be removed from the model without any problem. When they are removed from the model, a SOPN model is obtained for the FMS as shown in Figure 18(b).

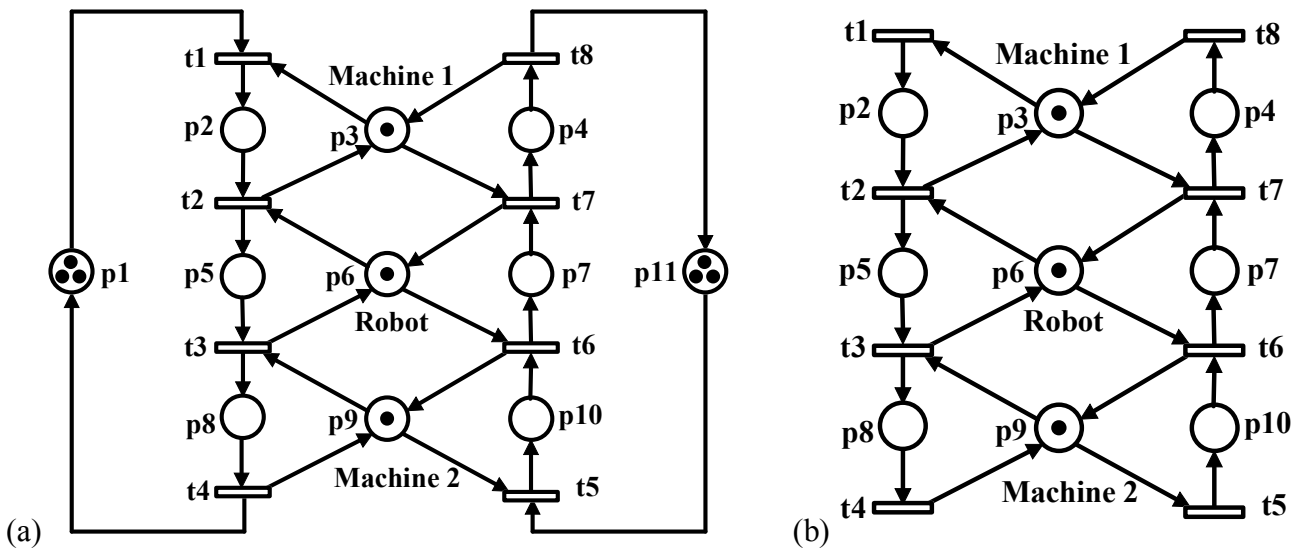


Figure 18. (a) PN model of FMS for two production sequences; (b) SOPN model for the FMS (UPNM)

It can be verified that the PN model of the FMS suffers from deadlock (the same applies to the SOPN). In the reachability graph of this model, there are 20 states, 15 of which are good states representing the optimal live behaviour and 5 of which are bad ones including 2 deadlock states. The maximally permissive controller obtained previously [20] is depicted in Figure 19(a). When the controller is augmented with the uncontrolled model (SOPN), the controlled model shown in Figure 19(b) is obtained.

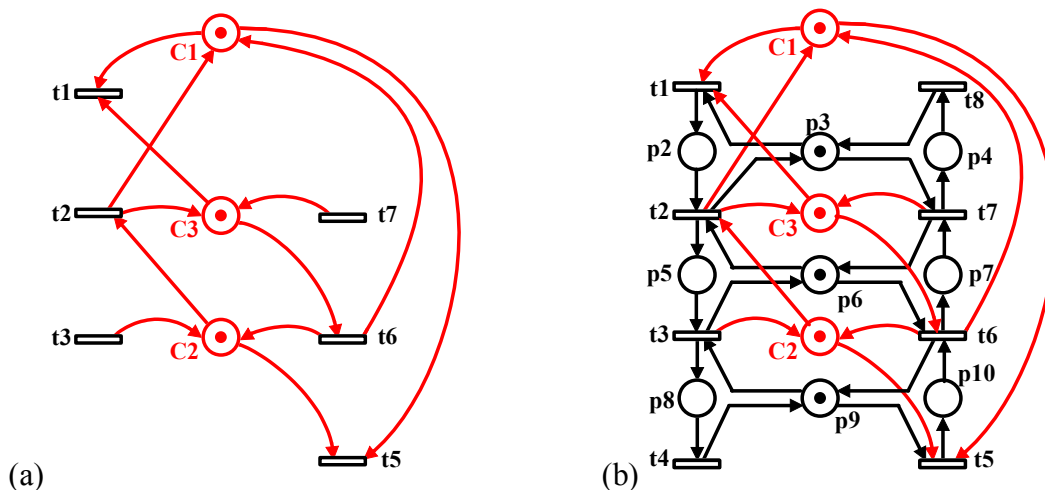


Figure 19. (a) Controller previously obtained [20] for Example 1; (b) Controlled model for the FMS

For this example the proposed analysis approach is followed as shown below.

Step 1. The UPNM is the one given in Figure 18(b); feedback control elements are three control places as depicted in Figure 19(a), and the specification for the UPNM is non-blockingness with respect to the initial state, i.e. liveness enforcing.

Step 2. It can be verified that UPNM is bounded with the place marking bounds $p2:1, p3:1, p4:1, p5:1, p6:1, p7:1, p8:1, p9:1$ and $p10:1$. It can be seen that UPNM is actually a SOPN.

Step 3. Each place of UPNM is converted into an equivalent buffer model as shown in Figure 20. The following event coding is used in the conversion process according to the TCT requirement that odd and even integers be used for controllable and uncontrollable events respectively.

Event coding for Example 1:

UPNM:	t1	t2	t3	t4	t5	t6	t7	t8
TCT:	1	3	5	7	15	13	11	9

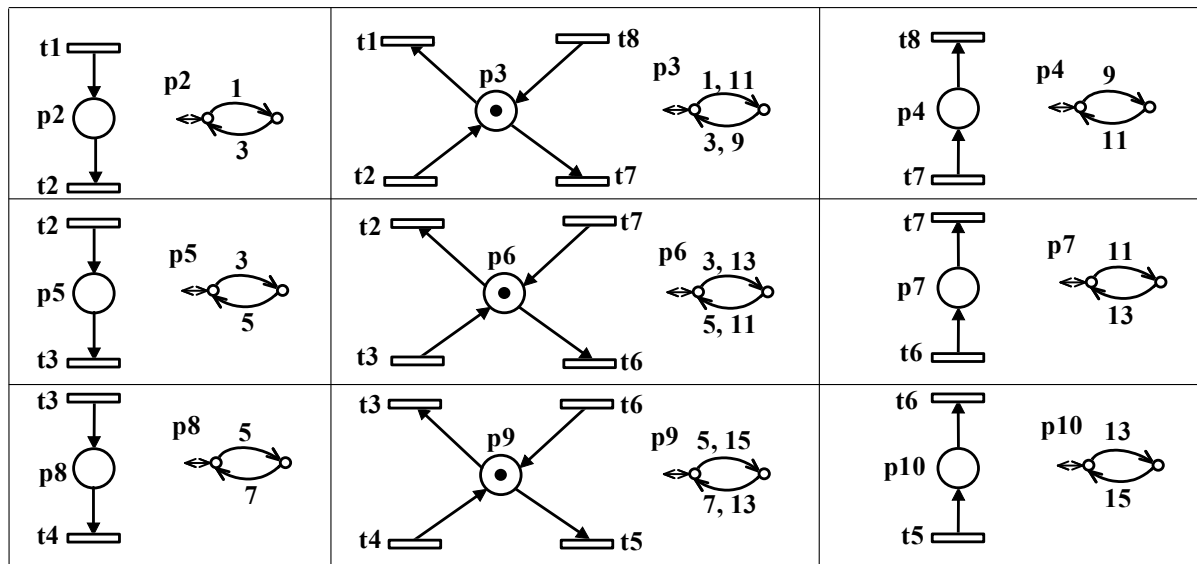


Figure 20. Mappings from UPNM to automata in Example 1

The following steps are carried out using TCT. In the following, PLANT defines automaton representation of UPNM.

First each place is created as an automaton as follows:

- p2 = Create(p2,[mark 0],[tran [0,1,1],[1,3,0]]) (2,2)
- p3 = Create(p3,[mark 0],[tran [0,1,1],[0,11,1],[1,3,0],[1,9,0]]) (2,4)
- p4 = Create(p4,[mark 0],[tran [0,11,1],[1,9,0]]) (2,2)
- p5 = Create(p5,[mark 0],[tran [0,3,1],[1,5,0]]) (2,2)
- p6 = Create(p6,[mark 0],[tran [0,3,1],[0,13,1],[1,5,0],[1,11,0]]) (2,4)
- p7 = Create(p7,[mark 0],[tran [0,13,1],[1,11,0]]) (2,2)
- p8 = Create(p8,[mark 0],[tran [0,5,1],[1,7,0]]) (2,2)
- p9 = Create(p9,[mark 0],[tran [0,5,1],[0,15,1],[1,7,0],[1,13,0]]) (2,4)
- p10 = Create(p10,[mark 0],[tran [0,15,1],[1,13,0]]) (2,2)

Then the PLANT is the synchronous product of all places, i.e. PLANT =

p2||p3||p4||p5||p6||p7||p8||p9||p10 and is obtained as follows (and depicted in Figure 21):

- PLANT = Sync(P2,P3) (4,6) Blocked_events = None
- PLANT = Sync(PLANT,P4) (3,4) Blocked_events = None
- PLANT = Sync(PLANT,P5) (6,10) Blocked_events = None
- PLANT = Sync(PLANT,P6) (12,20) Blocked_events = None
- PLANT = Sync(PLANT,P7) (8,12) Blocked_events = None
- PLANT = Sync(PLANT,P8) (16,30) Blocked_events = None
- PLANT = Sync(PLANT,P9) (32,60) Blocked_events = None
- PLANT = Sync(PLANT,P10) (20,34) Blocked_events = None

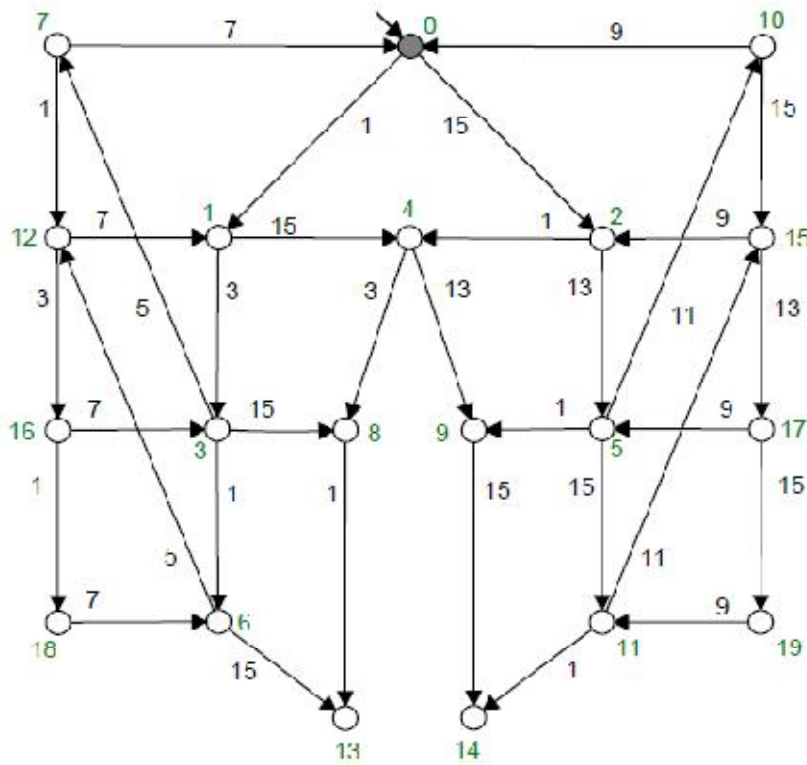


Figure 21. The automaton $PLANT = p2||p3||p4||p5||p6||p7||p8||p9||p10$ representing the uncontrolled system behaviour in Example 1

The problem considered is that of liveness enforcing. Therefore, the specification is non-blockingness with respect to the initial state and it is obtained by using `Allevvents()` command as follows: `ALL = Allevvents(PLANT) (1,8)`. In addition, the following test shows that `PLANT` will block in the absence of control: `false = Nonconflict(PLANT,ALL)`.

Step 4. A RW supervisor `RWSUPER` is obtained as follows: `RWSUPER = Supcon(PLANT,ALL) (15,24)`. The RW-type supervisor `RWSUPER` obtained is depicted in Figure 22.

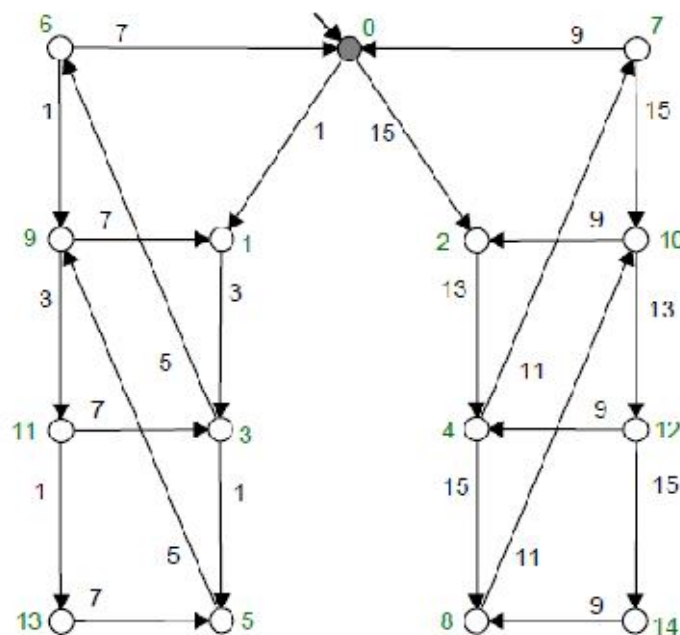


Figure 22. The supervisor `RWSUPER` computed for Example 1

Step 5. The given feedback control elements, i.e. a set of control places, are converted into equivalent buffer models as shown in Figure 23. Control places are created within TCT as follows:

$C1 = \text{Create}(C1, [\text{mark } 0], [\text{tran } [0, 1, 1], [0, 15, 1], [1, 3, 0], [1, 13, 0]])$ (2,4)

$C2 = \text{Create}(C2, [\text{mark } 0], [\text{tran } [0, 3, 1], [0, 15, 1], [1, 5, 0], [1, 13, 0]])$ (2,4)

$C3 = \text{Create}(C3, [\text{mark } 0], [\text{tran } [0, 1, 1], [0, 13, 1], [1, 3, 0], [1, 11, 0]])$ (2,4)

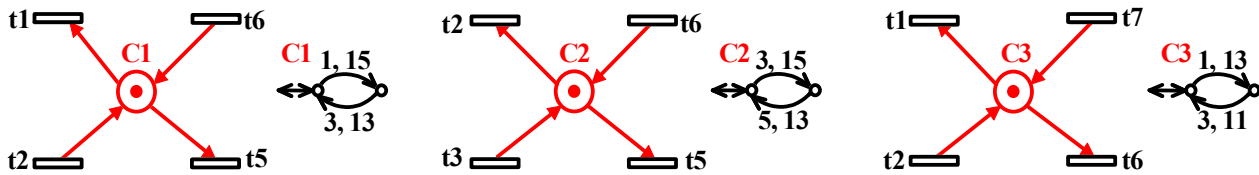


Figure 23. Mappings from given feedback control elements to automata in Example 1

Step 6. The controlled model PNSUPER (PNSUPER = PLANT||C1||C2||C3) is obtained by using PLANT and buffer models of the given feedback control elements C1, C2, and C3 as follows:

$\text{PNSUPER} = \text{Sync}(\text{PLANT}, C1)$ (17,26) Blocked_events = None

$\text{PNSUPER} = \text{Sync}(\text{PNSUPER}, C2)$ (16,25) Blocked_events = None

$\text{PNSUPER} = \text{Sync}(\text{PNSUPER}, C3)$ (15,24) Blocked_events = None

Step 7. The following test verifies that the controlled model PNSUPER obtained is isomorphic (identical) to RWSUPER: $\text{true} = \text{Isomorph}(\text{PNSUPER}, \text{RWSUPER}; \text{identity})$. This means that the controller obtained in the PN domain is also a proper supervisor, i.e. it is maximally permissive and non-blocking.

The following shows that the optimal controlled (maximally permissive and non-blocking) behaviour PNSUPER is simply the language generated by the trimmed plant as expected. This is because all transitions are controllable.

$\text{TPLANT} = \text{Trim}(\text{PLANT})$ (15,24)

$\text{true} = \text{Isomorph}(\text{TPLANT}, \text{PNSUPER}; \text{identity})$

Here, alternative feedback control elements are established and tested for Example 1. When the control places C1, C2 and C3 are examined in detail, it can be seen that these three control places implement a control mechanism in which, when there is a token in p2 or p5, t5 is not allowed to fire. This means that t5 is stopped from firing when $M(p2) = 1$ or $M(p5) = 1$. Likewise, when there is a token in p7 or p10, t1 is not allowed to fire, i.e. t1 is stopped from firing. This means that t1 is stopped from firing when $M(p7) = 1$ or $M(p10) = 1$. Actually, this control mechanism can be implemented by using the feedback control elements shown in Figure 24(a). When these feedback control elements are augmented with the uncontrolled model (SOPN), the controlled model shown in Figure 24(b) is obtained. Now the correctness of this new controller consisting of the alternative feedback control elements shown in Figure 24(a) is verified.

From this point onward the proposed analysis approach is followed for the new controller from step 5 as shown below.

Step 5. The feedback control elements shown in Figure 24(a) are converted into equivalent buffer models as shown in Figure 25. Control places are created within TCT as follows:

$\text{SP1} = \text{Create}(\text{SP1}, [\text{mark } 0], [\text{tran } [0, 1, 1], [0, 15, 0], [1, 3, 0]])$ (2,3)

$\text{SP2} = \text{Create}(\text{SP2}, [\text{mark } 0], [\text{tran } [0, 3, 1], [0, 15, 0], [1, 5, 0]])$ (2,3)

$\text{SP3} = \text{Create}(\text{SP3}, [\text{mark } 0], [\text{tran } [0, 1, 0], [0, 13, 1], [1, 11, 0]])$ (2,3)

$\text{SP4} = \text{Create}(\text{SP4}, [\text{mark } 0], [\text{tran } [0, 1, 0], [0, 15, 1], [1, 13, 0]])$ (2,3)

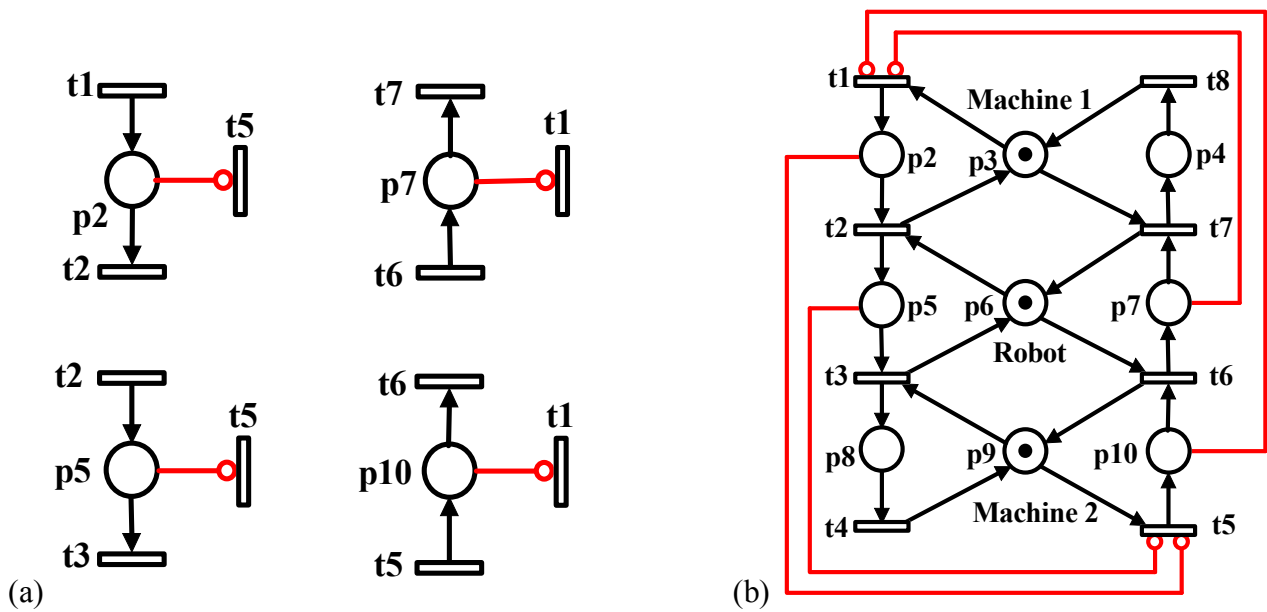


Figure 24. (a) Alternative feedback control elements constructed for Example 1; (b) Controlled model obtained by means of alternative feedback control elements

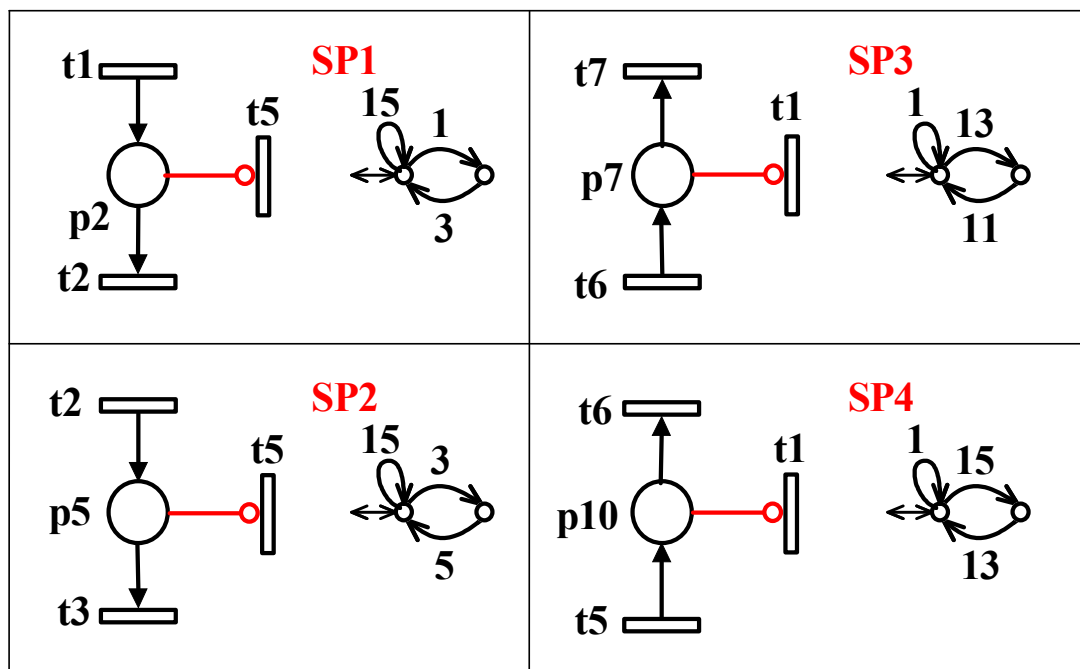


Figure 25. Mappings from PN to automata for the new controller

Step 6. The controlled model CM1 ($CM1 = PLANT || SP1 || SP2 || SP3 || SP4$) is obtained by using PLANT and buffer models of the new feedback control elements SP1, SP2, SP3 and SP3 as follows:

$CM1 = Sync(PLANT, SP1)$ (20,31) Blocked_events = None

$CM1 = Sync(CM1, SP2)$ (20,30) Blocked_events = None

$CM1 = Sync(CM1, SP3)$ (19,28) Blocked_events = None

$CM1 = Sync(CM1, SP4)$ (15,24) Blocked_events = None

Step 7. Finally, the test below verifies that the new controlled model CM1 is identical in terms of control action to that of RWSUPER, which also means that it is identical to PNSUPER. In other words, both controlled models shown in Figure 19(b) and Figure 24(b) generate the same language and

therefore they enforce the same specification. In this respect, the feedback control elements shown in Figure 23 and the ones shown in Figure 24(a) are said to be “control equivalent.”

true = Isomorph(RWSUPER,CM1;identity)

6.2. Example 2

As a second example, a generalised mutual exclusion constraint (GMEC) to be enforced on a PNM is considered. This example is taken from Basile et al. [31] and it consists of the UPNM shown in Figure 26. In the UPNM there are seven places, $P = \{p1, p2, \dots, p7\}$, and six transitions, $T = \{t1, t2, \dots, t6\}$. The initial marking is $M_0 = (0, 0, 0, 0, 0, 2, 2)^T$. It can be verified that the UPNM shown in Figure 26 is bounded, live, reversible and conservative. In the UPNM, transitions $t1, t5$ and $t6$ are controllable while transitions $t2, t3$ and $t4$ are uncontrollable. The specification, namely GMEC, to be enforced on this UPNM is $M(p1) \leq 1$, i.e. the number of tokens in place $p1$ must be fewer than or equal to 1. There are three solutions to be analysed for this example. The first two of them are two different optimal solutions and the third one is a suboptimal solution. These three solutions are considered respectively in the next three subsections.

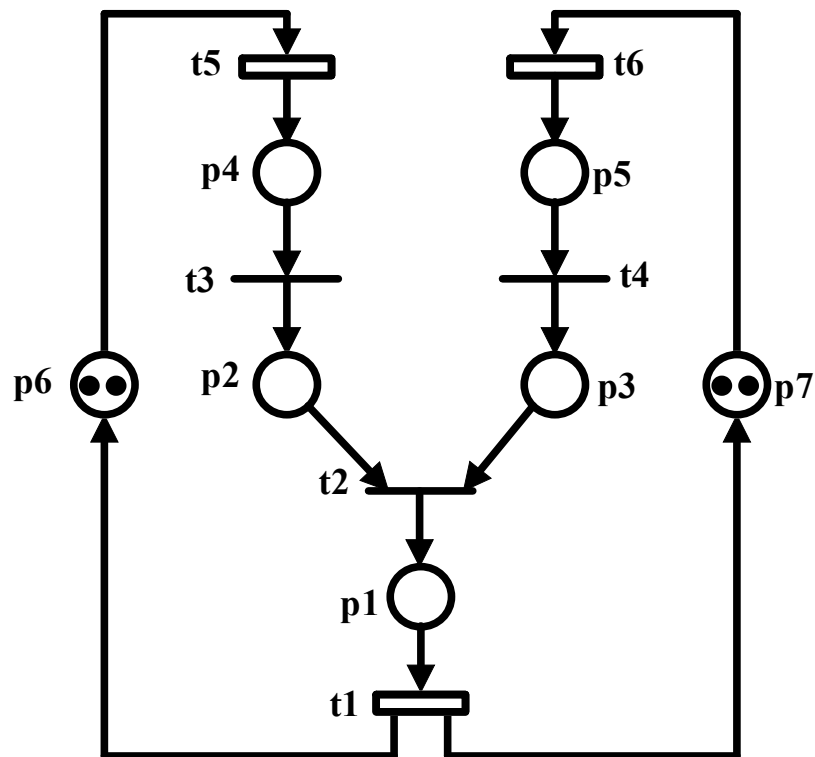


Figure 26. A PN with controllable ($t1, t5, t6$) and uncontrollable ($t2, t3, t4$) transitions [31] (without dashed arcs and places)

6.2.1. Example 2 – optimal solution 1

In order to optimally enforce GMEC $M(p1) \leq 1$ on the UPNM shown in Figure 26, the control places $C1, C2, C3$ and $C4$ in Figure 27 are provided [10]. It was shown [10] that the controlled model in Figure 28 can produce the supremal controllable sublanguage which has 32 states with 62 transitions. In short, the controlled model shown in Figure 28 is maximally permissive and non-blocking.

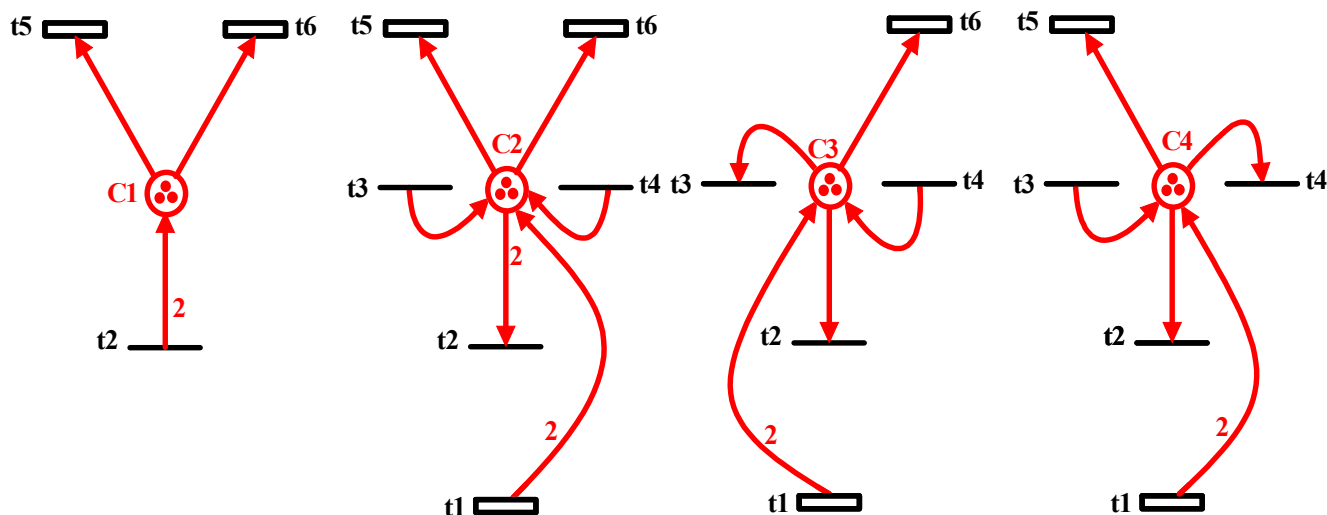


Figure 27. Four control places [10] enforcing the constraint $M(p1) \leq 1$ optimally on the PN shown in Figure 26

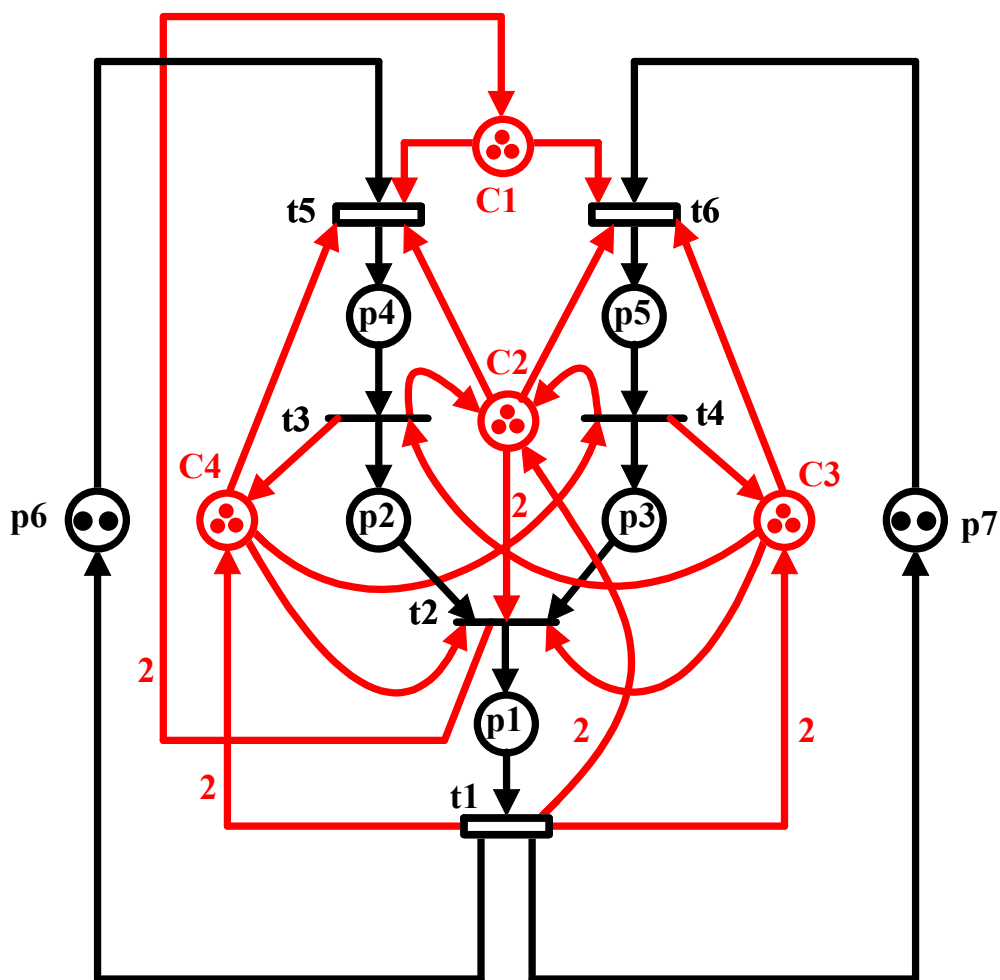


Figure 28. The controlled PN model obtained by including four control places within the PN shown in Figure 26

For this example, to verify the correctness of control places C1, C2, C3 and C4, the proposed analysis approach is followed as shown below.

Step 1. The UPNM is the one given in Figure 26; the feedback control elements are the control places as depicted in Figure 27, and the specification for the UPNM is $M(p1) \leq 1$, i.e. the number of tokens in place p1 must be less than or equal to 1.

Step 2. It can be verified that UPNM is bounded with the place marking bounds p1:2, p2:2, p3:2, p4:2, p5:2, p6:2 and p7:2.

Step 3. Each place of UPNM is converted into an equivalent buffer model as shown in Figure 29. The following event coding is used in the conversion process according to the TCT requirement that odd and even integers be used for controllable and uncontrollable events respectively.

Event coding for Example 2:

UPNM:	t1	t2	t3	t4	t5	t6
TCT:	1	2	30	4	5	61

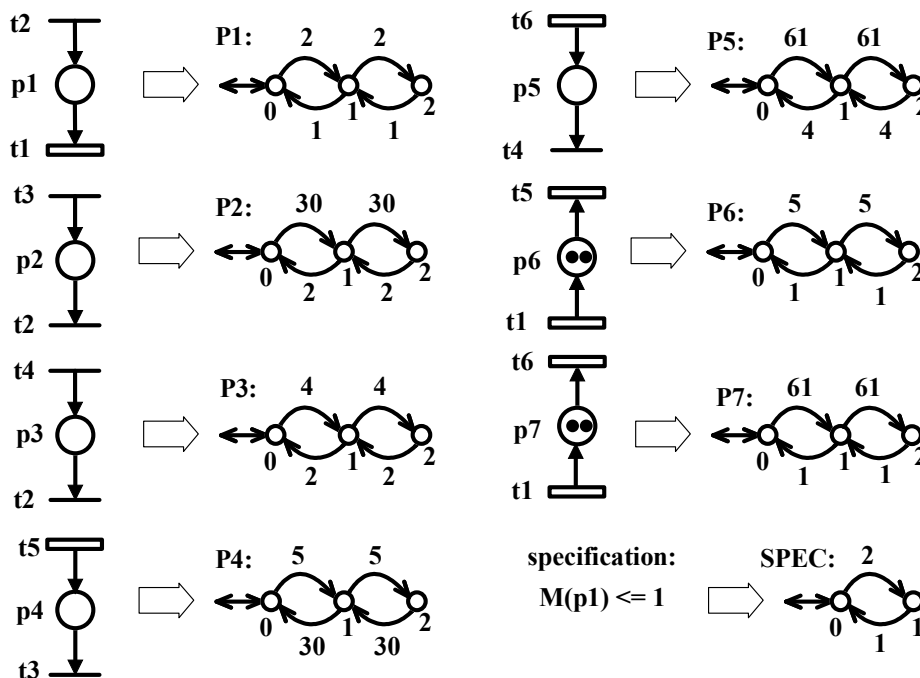


Figure 29. Mappings from UPNM to automata and specification model SPEC in Example 2

The following steps are carried out using TCT. In the following, PLANT defines automaton representation of UPNM.

First, each place is created as an automaton as follows:

- P1 = Create(P1,[mark 0],[tran [0,2,1],[1,1,0],[1,2,2],[2,1,1]]) (3,4)
- P2 = Create(P2,[mark 0],[tran [0,30,1],[1,2,0],[1,30,2],[2,2,1]]) (3,4)
- P3 = Create(P3,[mark 0],[tran [0,4,1],[1,2,0],[1,4,2],[2,2,1]]) (3,4)
- P4 = Create(P4,[mark 0],[tran [0,5,1],[1,5,2],[1,30,0],[2,30,1]]) (3,4)
- P5 = Create(P5,[mark 0],[tran [0,61,1],[1,4,0],[1,61,2],[2,4,1]]) (3,4)
- P6 = Create(P6,[mark 0],[tran [0,5,1],[1,1,0],[1,5,2],[2,1,1]]) (3,4)
- P7 = Create(P7,[mark 0],[tran [0,61,1],[1,1,0],[1,61,2],[2,1,1]]) (3,4)

Then the PLANT is the synchronous product of all places, i.e. $PLANT = P1 \parallel P2 \parallel P3 \parallel P4 \parallel P5 \parallel P6 \parallel P7$, and is obtained as follows:

PLANT = Sync(P1,P2) (9,16) Blocked_events = None
 PLANT = Sync(PLANT,P3) (27,62) Blocked_events = None
 PLANT = Sync(PLANT,P4) (81,222) Blocked_events = None
 PLANT = Sync(PLANT,P5) (243,774) Blocked_events = None
 PLANT = Sync(PLANT,P6) (90,232) Blocked_events = None
 PLANT = Sync(PLANT,P7) (46,104) Blocked_events = None

Recall that the specification is $M(p1) \leq 1$, i.e. the number of tokens in place p1 must be less than or equal to 1. This specification can be represented as a buffer automaton model as depicted in Figure 29. This specification model simply declares that once event “2” occurs, it cannot reoccur until event “1” takes place. This defines specification $M(p1) \leq 1$ as a buffer automaton model, which is defined within TCT as follows:

SPEC = Create(SPEC,[mark 0],[tran [0,2,1],[1,1,0]]) (2,2)

After this operation, self-loops labelled with events that are possible in PLANT but not constrained by the specification must be adjoined to each state. To do this, self-loops with event labels ‘4’, ‘5’, ‘30’ and ‘61’ are adjoined to each state of SPEC as follows:

SPEC = Selfloop(SPEC,[4,5,30,61]) (2,10)

Note that as there is only one specification model, it is not necessary to use Meet() command.

Step 4. A RW supervisor RWSUPER is obtained as follows:

RWSUPER = Supcon(PLANT,SPEC) (32,62)

The RW-type supervisor RWSUPER obtained is depicted in Figure 30 and is given below.

RWSUPER # states: 32 state set: 0 ... 31 initial state: 0
 marker states: 0 vocal states: none # transitions: 62

transitions:

[0,5,1][0,61,2][1,5,3][1,30,4][1,61,5][2,4,6][2,5,5][2,61,7][3,30,8][3,61,9][4,5,8][4,61,10]
 [5,4,11][5,5,9][5,30,10][5,61,12][6,5,11][6,61,13][7,4,13][7,5,12][8,30,14][8,61,15]
 [9,4,16][9,30,15][10,4,17][10,5,15][10,61,18][11,5,16][11,30,17][11,61,19][12,4,19]
 [12,30,18][13,4,20][13,5,19][14,61,21][15,4,22][15,30,21][16,30,22][17,2,23][17,5,22]
 [17,61,24][18,4,24][19,4,25][19,30,24][20,5,25][21,4,26][22,2,27][22,30,26][23,1,0]
 [23,5,27][23,61,28][24,2,28][24,4,29][5,30,29][26,2,30][27,1,1][27,30,30][28,1,2][28,4,31]
 [29,2,31][30,1,4][31,1,6]

Step 5. The given feedback control elements, i.e. control places C1, C2, C3 and C4, shown in Figure 27, are converted into equivalent buffer models as shown in Figure 31. The control places C1, C2, C3 and C4 are created within TCT as follows:

C1 = Create(C1,[mark 0], [tran [0,5,1], [0,61,1], [1,5,2], [1,61,2], [2,2,0], [2,5,3], [2,61,3], [3,2,1]]) (4,8)

C2 = Create(C2,[mark 0],[tran [0,2,2], [0,5,1], [0,61,1], [1,2,3], [1,4,0], [1,5,2], [1,30,0], [1,61,2], [2,1,0], [2,4,1], [2,5,3], [2,30,1], [2,61,3], [3,1,1], [3,4,2], [3,30,2]]) (4,16)

C3 = Create(C3,[mark 0], [tran [0,2,1], [0,30,1], [0,61,1], [1,2,2], [1,4,0], [1,30,2], [1,61,2], [2,1,0], [2,2,3], [2,4,1], [2,30,3], [2,61,3],[3,1,1],[3, 4,2]]) (4,14)

C4 = Create(C4,[mark 0], [tran [0,2,1], [0,4,1], [0,5,1], [1,2,2], [1,4,2], [1,5,2], [1,30,0], [2,1,0], [2,2,3], [2,4,3], [2,5,3], [2,30,1], [3,1,1], [3,30,2]]) (4,14)

Step 6. The controlled model PNSUPER1 ($PNSUPER1 = PLANT||C1||C2||C3||C4$) is obtained by using PLANT and buffer models C1, C2, C3 and C4 of given control places as follows:

PNSUPER1 = Sync(PLANT,C1) (37,76) Blocked_events = None

PNSUPER1 = Sync(PNSUPER1,C2) (35,69) Blocked_events = None

PNSUPER1 = Sync(PNSUPER1,C3) (34,66) Blocked_events = None

PNSUPER1 = Sync(PNSUPER1,C4) (32,62) Blocked_events = None

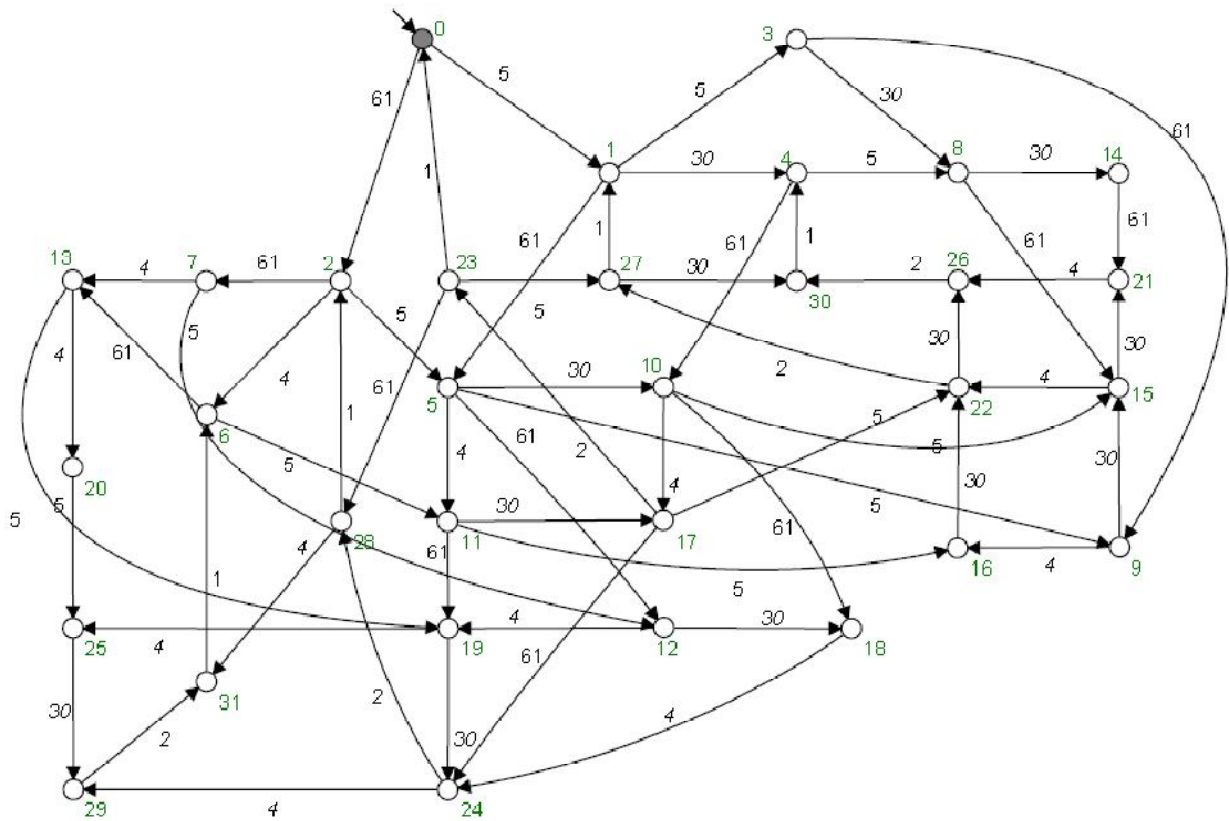


Figure 30. The supervisor RWSUPER computed for Example 2

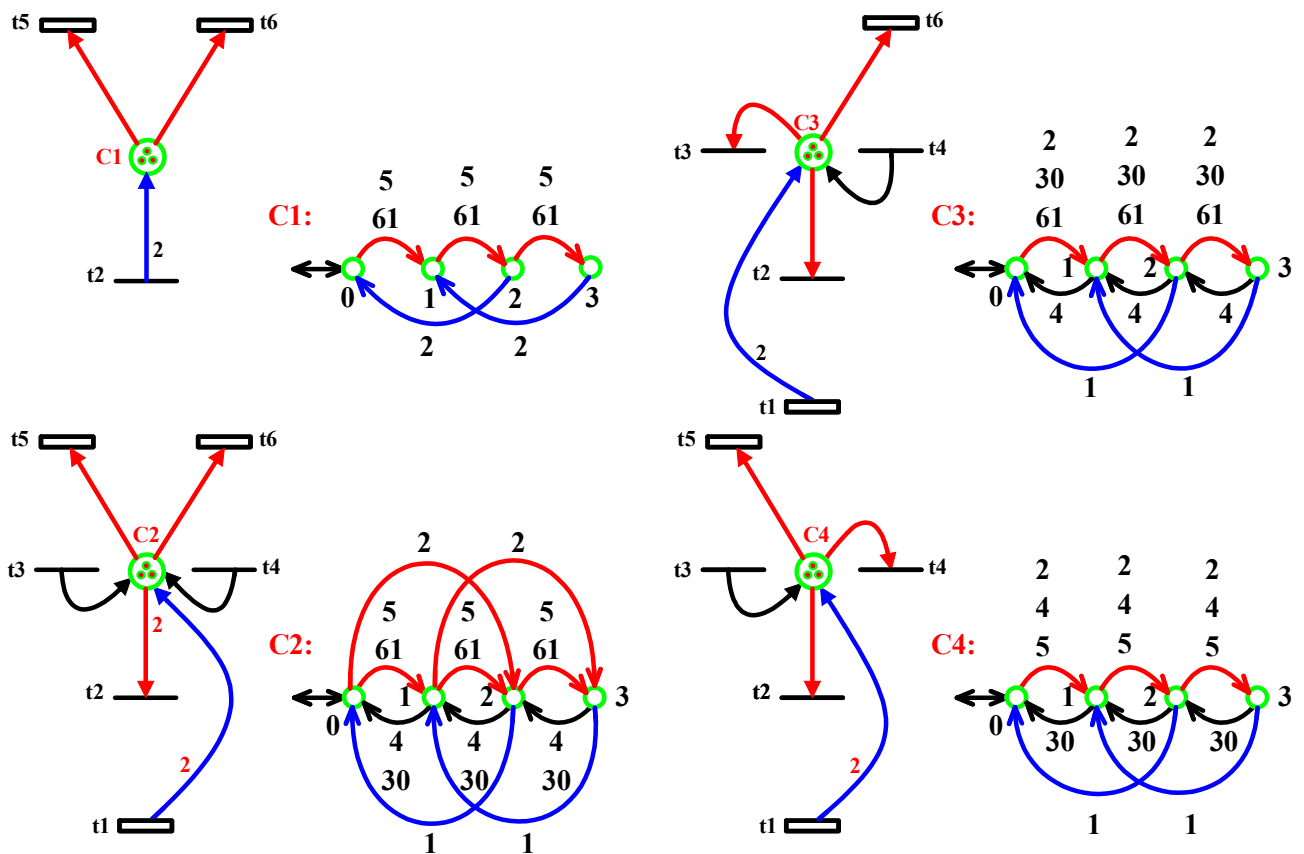


Figure 31. Mappings from control places C1, C2, C3 and C4 to automata in Example 2

Step 7. The test below verifies that the controlled model PNSUPER1 obtained is isomorphic (identical) to RWSUPER. This means that the controller obtained in the PN domain is also a proper supervisor, i.e. it is maximally permissive and non-blocking.

true = Isomorph(PNSUPER1,RWSUPER;identity)

6.2.2. Example 2 – optimal solution 2

As an alternative control mechanism to optimally enforce GMEC $M(p1) \leq 1$ on the UPNM of Figure 26, the control place C shown in Figure 32(a) is also computed [10]. It was shown [10] that the controlled model in Figure 32(b) can produce the supremal controllable sublanguage which has 32 states with 62 transitions. In short, the controlled model shown in Figure 32(b) is also maximally permissive and non-blocking.

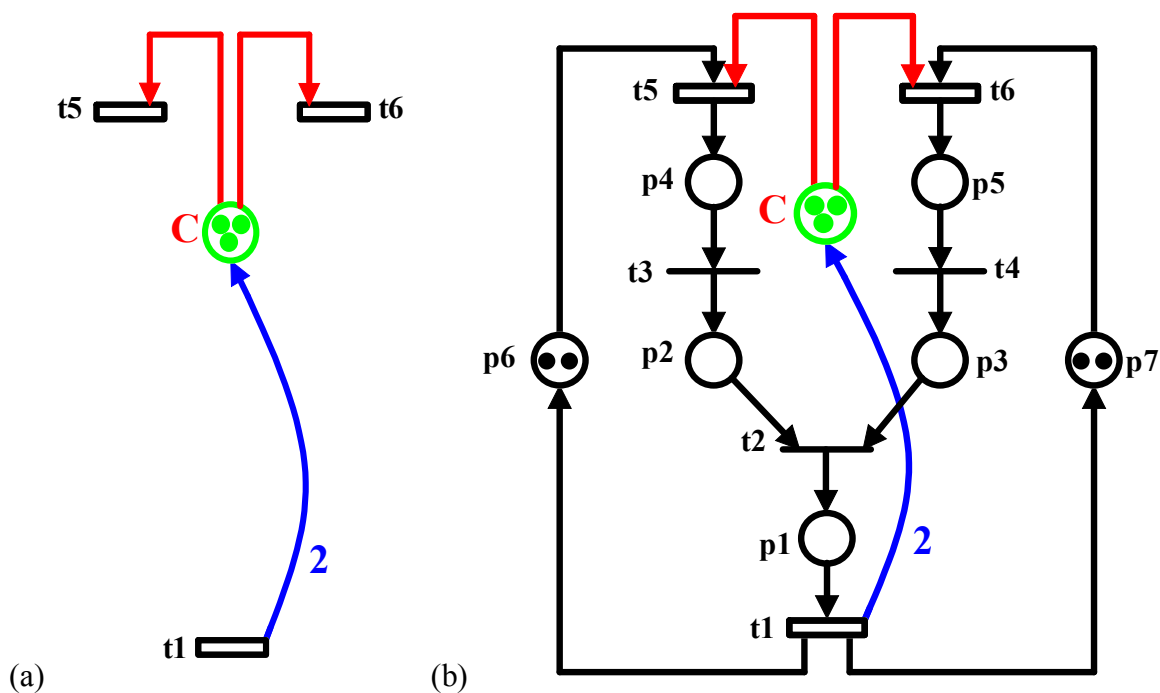


Figure 32. (a) A computed control place C [10]; (b) Controlled model

As the first four analysis steps are the same as the ones provided in the previous section, for this example, to verify the correctness of the control place C, a proposed analysis approach is followed as shown below.

Step 5. The given feedback control element, i.e. control place C shown in Figure 32(a), is converted into an equivalent buffer model as shown in Figure 33. The control place C is created within TCT as follows:

$C = \text{Create}(C, [\text{mark } 0], [\text{tran}[0,5,1], [0,61,1], [1,5,2], [1,61,2], [2,1,0], [2,5,3], [2,61,3], [3,1,1]])$ (4,8)

Step 6. The controlled model PNSUPER2 ($\text{PNSUPER2} = \text{PLANT} \parallel C$) is obtained by using PLANT and buffer model C of the given control place as follows:

$\text{PNSUPER2} = \text{Sync}(\text{PLANT}, C)$ (32,62) Blocked_events = None

Step 7. The test below verifies that the controlled model PNSUPER2 obtained is isomorphic (identical) to RWSUPER. This means that the controller obtained in the PN domain is also a proper supervisor, i.e. it is maximally permissive and non-blocking.

true = Isomorph(PNSUPER2,RWSUPER;identity)

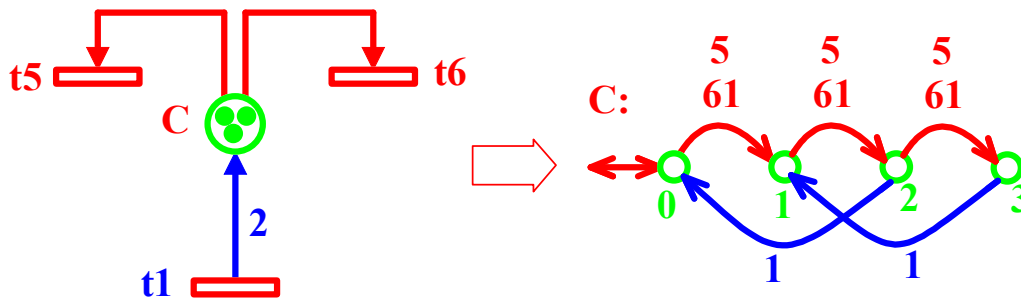


Figure 33. Mapping from control place C to automata in Example 2

6.2.3. Example 2 – suboptimal solution

In this section a suboptimal solution for enforcing $GMEC M(p1) \leq 1$ on the UPNM shown in Figure 26 is analysed. In Basile et al. [31], two suboptimal control places, namely pc1 and pc2, as shown in Figure 34(a), are computed. Only one of them is necessary to enforce the $GMEC M(p1) \leq 1$ on the UPNM shown in Figure 26. In this section the controlled model obtained by pc1 is analysed as shown in Figure 34(b).

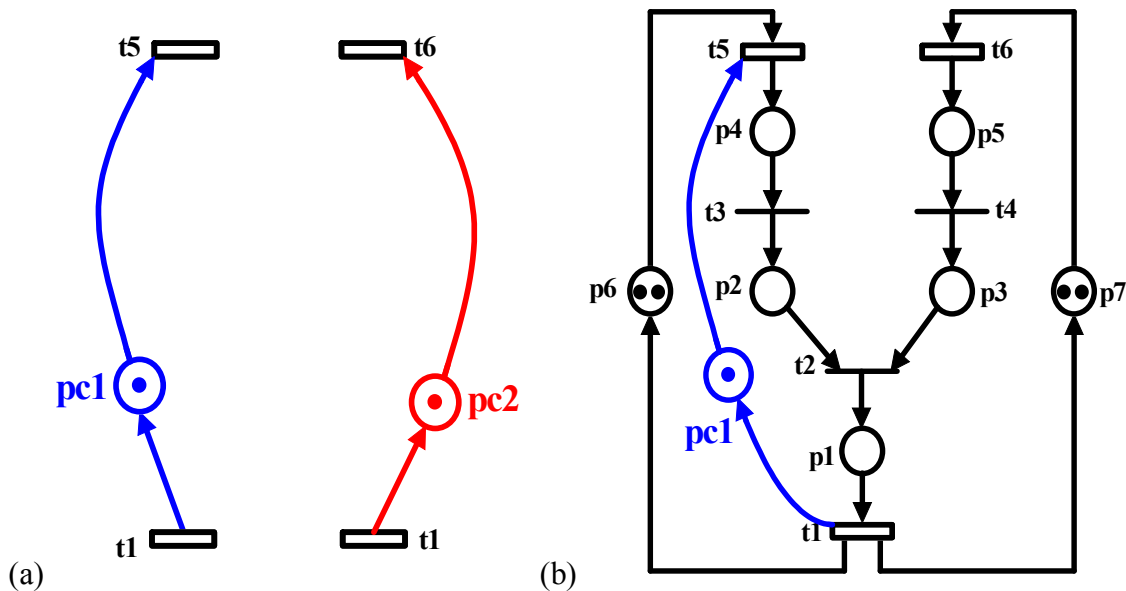


Figure 34. (a) Two computed possible control places [31] for enforcing $GMEC M(p1) \leq 1$ on the UPNM shown in Figure 26; (b) Controlled model obtained by pc1

For the suboptimal case in Example 2, the first four analysis steps are the same as the ones provided in the previous section.

Step 5. The given feedback control element pc1 is converted into an equivalent buffer model PC1 as shown in Figure 35. PC1 is created within TCT as follows:

PC1 = Create(PC1,[mark 0],[tran [0,5,1],[1,1,0]]) (2,2)

Step 6. The controlled model SPNSUPER (SPNSUPER = PLANT||PC1) is obtained by using PLANT and buffer model PC1 of the given control place as follows:

SPNSUPER = Sync(PLANT,PC1) (21,38) Blocked_events = None

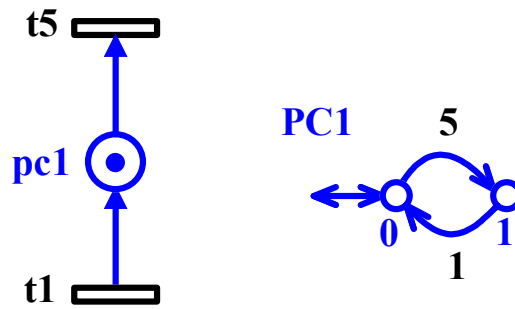


Figure 35. Mapping from pc1 to automaton model PC1 in Example 2

Step 7. The following tests verify that the controlled model SPNSUPER obtained is the sublanguage of the optimal solution RWSUPER. This means that the controller obtained in the PN domain is a suboptimal supervisor for enforcing $GMEC M(p1) \leq 1$ on the UPNM shown in Figure 26.

```
true = Nonconflict(SPNSUPER,RWSUPER)
MRW_PN = Meet(SPNSUPER,RWSUPER) (21,38)
true = Isomorph(MRW_PN,SPNSUPER;identity)
```

6.3. Example 3

In this section, an example of FMS prone to deadlock, as shown in Figure 36(a), is considered. The system is composed of two robots, namely R1 and R2, each of which can hold one part at a time, and three machines, namely M1, M2 and M3. M3 can process only one part at a time while M1 and M2 can process two parts at a time. For loading of the system, there are two loading buffers I1 and I2, and for unloading, there are three unloading buffers O1, O2 and O3. The action areas of robot R1 are I1, M1 and M3, and for robot R2, they are M1 and M2. For the sake of simplicity, it is assumed that inputting parts from I2 to M2 and outputting parts from M3 to O1, M2 to O2, and M1 to O3 are the part of machining operation. As shown in Figure 36(b), two part types are considered: P1 and P2. P1 is taken from I1 by R1 and it is either put into M3 or M1. After being processed by M3, P1 is moved to O1 by M3. When put into M1, P1 is processed by M1 and after that it is moved from M1 to M2 by R2. After being processed by M2, P1 is finally moved to O2 by M2. In the production process of P1, R1&M3 or R1&M1 and R2&M2 are used. Similarly, P2 is taken from I2 by M2, and after being processed by M2 it is moved from M2 to M1 by R2. Finally, after being processed by M1, P2 is moved to O3 by M1. In the production process of P2, M2&R2&M1 are used.

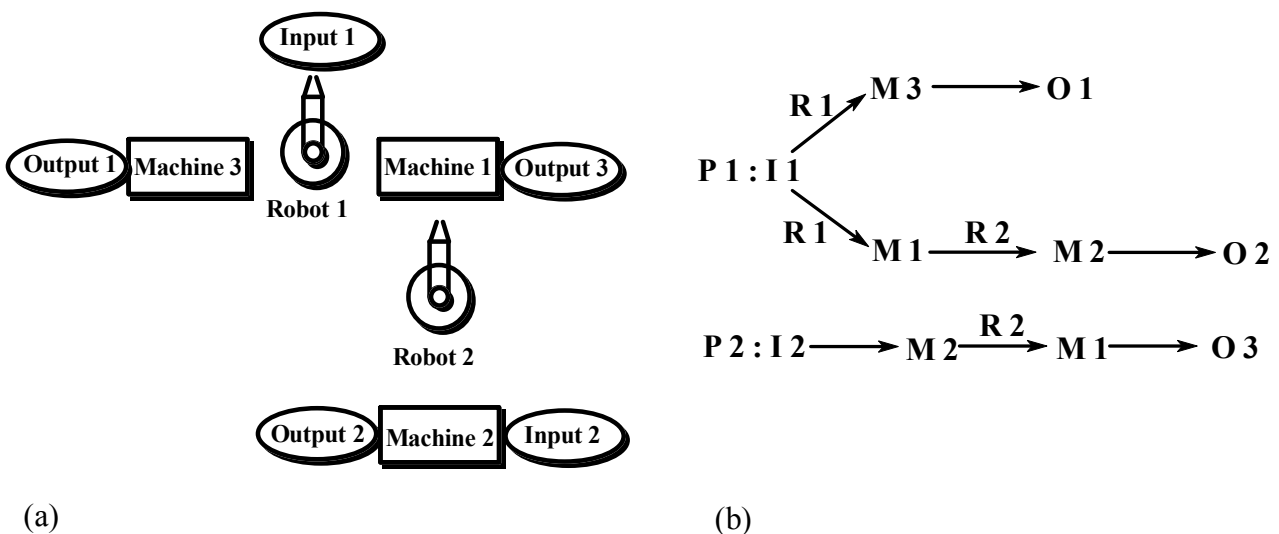


Figure 36. (a) An example of FMS; (b) The production sequences

Figure 37(a) shows the PNM of the system [18]. Initially it is assumed that there are no parts in the system. In the PNM there are fifteen places, $P = \{p1, p2, \dots, p10, R1, R2, M1, M2, M3\}$, and eleven transitions, $T = \{t0, t1, t2, \dots, t10\}$. It is assumed that once the manufacturing of the products starts, no event in the production processes can be prevented from occurring. Therefore, only transitions $t1, t2$ and $t10$ are controllable. Places $p2$ and $p3$ represent the operation of $R1$ and $M3$ respectively for the production sequence of the part type $P1$. Similarly, places $p2, p4, p5$ and $p6$ represent the operation of $R1, M1, R2$ and $M2$ respectively for production sequence of the part type $P1$. For production sequence of the part type $P2$, places $p9, p8$ and $p7$ represent the operation of $M2, R2$ and $M1$ respectively. The number of tokens in $p1$, i.e. $M(p1) = 3$, represents the number of concurrent activities that can take place for $P1$. The number of tokens in $p10$, i.e. $M(p10) = 3$, represents the number of concurrent activities that can take place for $P2$. Places $R1$ and $M3$ denote the resources robot 1 and machine 3 respectively. Places $M1, R2$ and $M2$ denote the shared resources machine 1, robot 2 and machine 2 respectively. Initial markings of places $R1, R2$ and $M3$ are all one as robots can hold one part and machine 3 can process one part at a time. Initial markings of places $M1$ and $M2$ are all two as machine 1 and machine 2 can process two parts at a time. In order to have correct system behaviour, it is desirable that each production sequence can finish. It can be shown that this system suffers from deadlock problem and for this system the specification is to obtain the live system behaviour (non-blockingness in SCT terminology). The optimal (maximally permissive and non-blocking) controller consisting of three control places, namely $pc1, pc2$ and $pc3$, obtained by Ghaffari et al.[18] is depicted in Figure 37(b). When the controller is augmented with the uncontrolled PNM, the controlled model shown in Figure 37(c) is obtained. It was reported [18] that the controlled model shown in Figure 37(c) can produce the optimal live behaviour with 215 good states.

For this example, to verify the correctness of the control places $pc1, pc2$ and $pc3$, the proposed analysis approach is followed as shown below.

Step 1. The UPNM is the one given in Figure 37(a). Feedback control elements are three control places $pc1, pc2$ and $pc3$ as depicted in Figure 37(b), and the specification for the UPNM is non-blockingness with respect to the initial state, i.e. liveness enforcing.

Step 2. It can be verified that UPNM is bounded with the place marking bounds $p1:3, p2:1, p3:1, p4:2, p5:1, p6:2, p7:2, p8:1, p9:2, p10:3, R1:1, R2:1, M1:2, M2:2$ and $M3:1$.

Step 3. Each place of UPNM is converted into an equivalent buffer model as shown in Figure 38. The following event coding is used in the conversion process according to the TCT requirement that odd and even integers be used for controllable and uncontrollable events respectively.

Event coding for Example 3:

UPNM:	t0	t1	t2	t3	t4	t5	t6	t7	t8	t9	t10
TCT:	0	1	21	30	4	50	6	70	8	90	101

The following steps are carried out using TCT. In the following, FMS defines automaton representation of UPNM

First, each place is created as an automaton as follows:

$P1 = \text{Create}(P1, [\text{mark } 0], [\text{tran } [0,0,1], [1,0,2], [1,6,0], [1,30,0], [2,0,3], [2,6,1], [2,30,1], [3,6,2], [3,30,2]])$ (4,9)

$P2 = \text{Create}(P2, [\text{mark } 0], [\text{tran } [0,0,1], [1,1,0], [1,21,0]])$ (2,3)

$P3 = \text{Create}(P3, [\text{mark } 0], [\text{tran } [0,1,1], [1,30,0]])$ (2,2)

$P4 = \text{Create}(P4, [\text{mark } 0], [\text{tran } [0,21,1], [1,4,0], [1,21,2], [2,4,1]])$ (3,4)

$P5 = \text{Create}(P5, [\text{mark } 0], [\text{tran } [0,4,1], [1,50,0]])$ (2,2)

$P6 = \text{Create}(P6, [\text{mark } 0], [\text{tran } [0,50,1], [1,6,0], [1,50,2], [2,6,1]])$ (3,4)

$P7 = \text{Create}(P7, [\text{mark } 0], [\text{tran } [0,8,1], [1,8,2], [1,70,0], [2,70,1]])$ (3,4)

$P8 = \text{Create}(P8, [\text{mark } 0], [\text{tran } [0,90,1], [1,8,0]])$ (2,2)

$P9 = \text{Create}(P9, [\text{mark } 0], [\text{tran } [0,101,1], [1,90,0], [1,101,2], [2,90,1]])$ (3,4)

$P10 = \text{Create}(P10, [\text{mark } 0], [\text{tran } [0,101,1], [1,70,0], [1,101,2], [2,70,1], [2,101,3], [3,70,2]])$ (4,6)

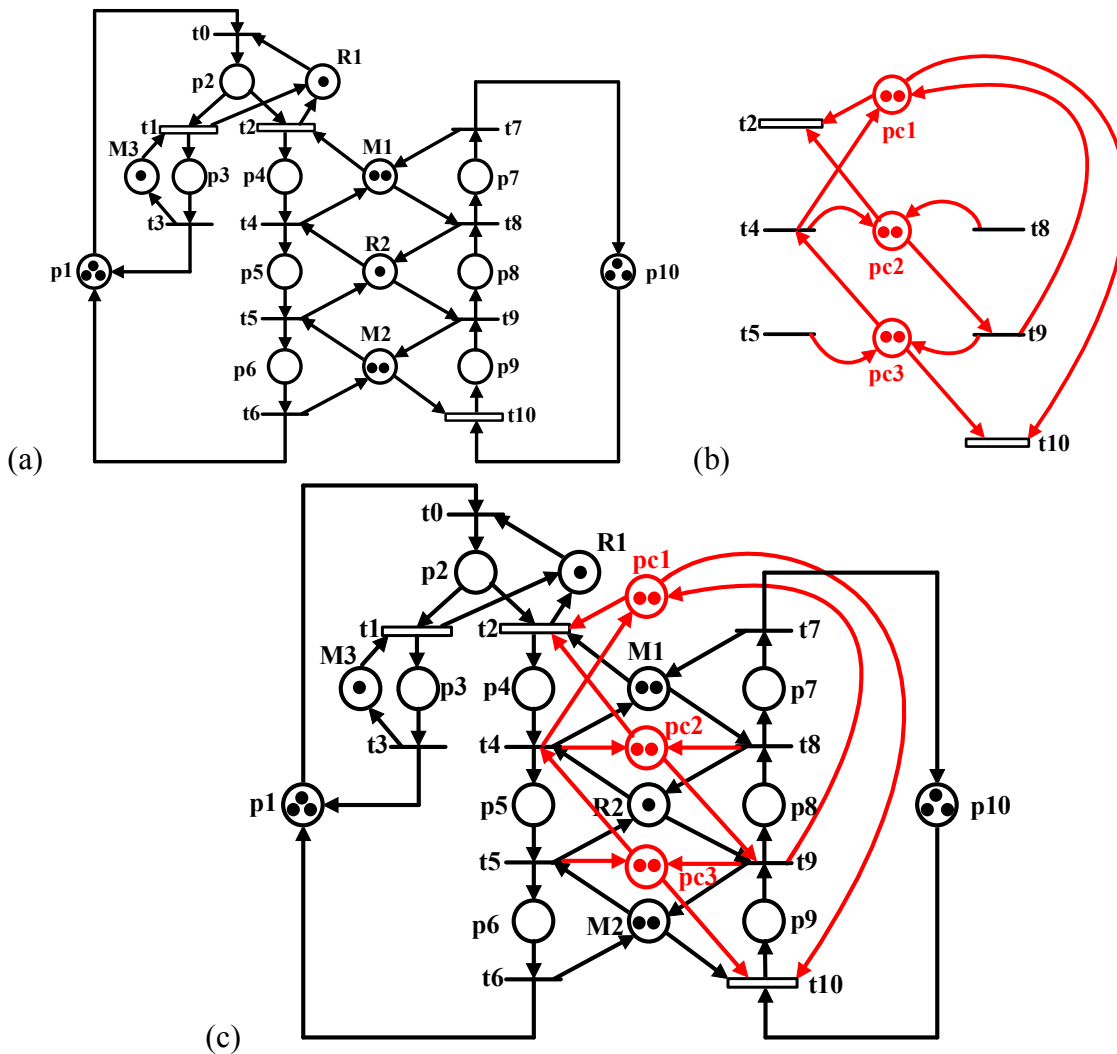


Figure 37. (a) PNM of the FMS [18]; (b) Three computed control places [18]; (c) Controlled model

$R1 = \text{Create}(R1, [\text{mark } 0], [\text{tran } [0,0,1], [1,1,0], [1,21,0]]) (2,3)$
 $R2 = \text{Create}(R2, [\text{mark } 0], [\text{tran } [0,4,1], [0,90,1], [1,8,0], [1,50,0]]) (2,4)$
 $M1 = \text{Create}(M1, [\text{mark } 0], [\text{tran } [0,8,1], [0,21,1], [1,4,0], [1,8,2], [1,21,2], [1,70,0], [2,4,1], [2,70,1]]) (3,8)$
 $M2 = \text{Create}(M2, [\text{mark } 0], [\text{tran } [0,50,1], [0,101,1], [1,6,0], [1,50,2], [1,90,0], [1,101,2], [2,6,1], [2,90,1]]) (3,8)$
 $M3 = \text{Create}(M3, [\text{mark } 0], [\text{tran } [0,1,1], [1,30,0]]) (2,2)$

Then the FMS is the synchronous product of all places, i.e. $\text{FMS} = p1 || p2 || p3 || p4 || p5 || p6 || p7 || p8 || p9 || p10 || R1 || R2 || M1 || M2 || M3$ and is obtained as follows:

$\text{FMS} = \text{Sync}(P1, P2) (8,23) \text{ Blocked_events} = \text{None}$
 $\text{FMS} = \text{Sync}(\text{FMS}, P3) (16,36) \text{ Blocked_events} = \text{None}$
 $\text{FMS} = \text{Sync}(\text{FMS}, P4) (48,132) \text{ Blocked_events} = \text{None}$
 $\text{FMS} = \text{Sync}(\text{FMS}, P5) (96,280) \text{ Blocked_events} = \text{None}$
 $\text{FMS} = \text{Sync}(\text{FMS}, P6) (36,88) \text{ Blocked_events} = \text{None}$
 $\text{FMS} = \text{Sync}(\text{FMS}, P7) (108,408) \text{ Blocked_events} = \text{None}$
 $\text{FMS} = \text{Sync}(\text{FMS}, P8) (216,852) \text{ Blocked_events} = \text{None}$
 $\text{FMS} = \text{Sync}(\text{FMS}, P9) (648,2880) \text{ Blocked_events} = \text{None}$
 $\text{FMS} = \text{Sync}(\text{FMS}, P10) (504,2168) \text{ Blocked_events} = \text{None}$
 $\text{FMS} = \text{Sync}(\text{FMS}, R1) (504,2168) \text{ Blocked_events} = \text{None}$
 $\text{FMS} = \text{Sync}(\text{FMS}, R2) (426,1696) \text{ Blocked_events} = \text{None}$
 $\text{FMS} = \text{Sync}(\text{FMS}, M1) (341,1303) \text{ Blocked_events} = \text{None}$

FMS = Sync(FMS,M2) (261,933) Blocked_events = None
 FMS = Sync(FMS,M3) (261,933) Blocked_events = None

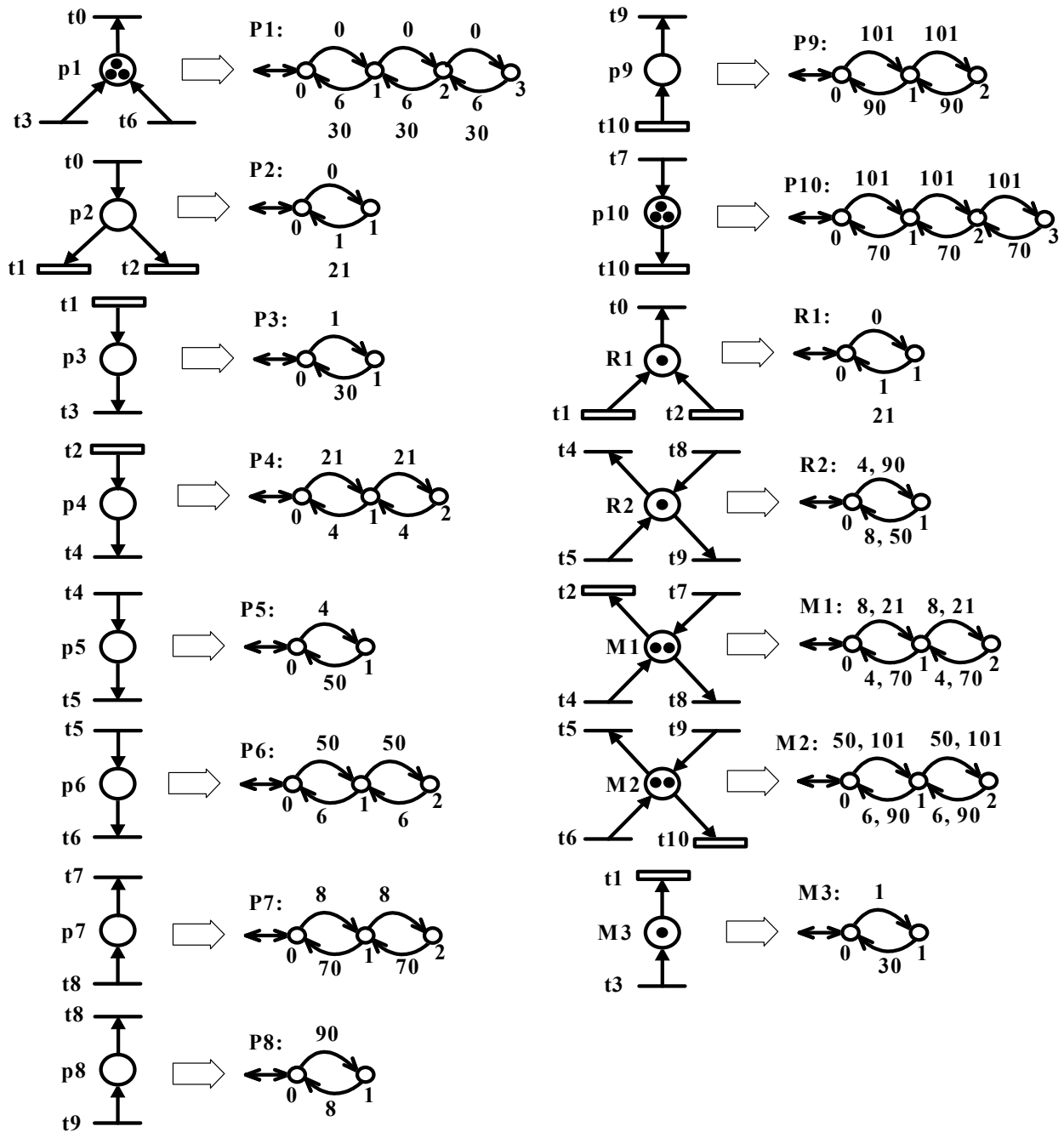


Figure 38. Mappings from UPNM to automata in Example 3

The problem considered is that of liveness enforcing problem. Therefore, the specification is non-blockingness with respect to the initial state and it is obtained by using Allevents() command as follows: ALL = Allevents(FMS) (1,11). In addition, the following test shows that FMS will block in the absence of control: false = Nonconflict(FMS,ALL).

Step 4. A RW supervisor RWSUPER is obtained as follows:
 RWSUPER = Supcon(FMS,ALL) (215,771)

Step 5. The given feedback control elements, i.e. control places pc1, pc2 and pc3, are converted into equivalent buffer models as shown in Figure 39. Control places are created within TCT as follows:

PC1 = Create(PC1,[mark 0],[tran [0,21,1], [0,101,1], [1,4,0], [1,21,2], [1,90,0], [1,101,2], [2,4,1], [2,90,1]]) (3,8)
 PC2 = Create(PC2,[mark 0],[tran [0,21,1],[0,90,1],[1,4,0],[1,8,0],[1,21,2],[1,90,2],[2,4,1], [2,8,1]]) (3,8)
 PC3 = Create(PC3,[mark 0],[tran [0,4,1], [0,101,1], [1,4,2], [1,50,0], [1,90,0], [1,101,2], [2,50,1], [2,90,1]]) (3,8)

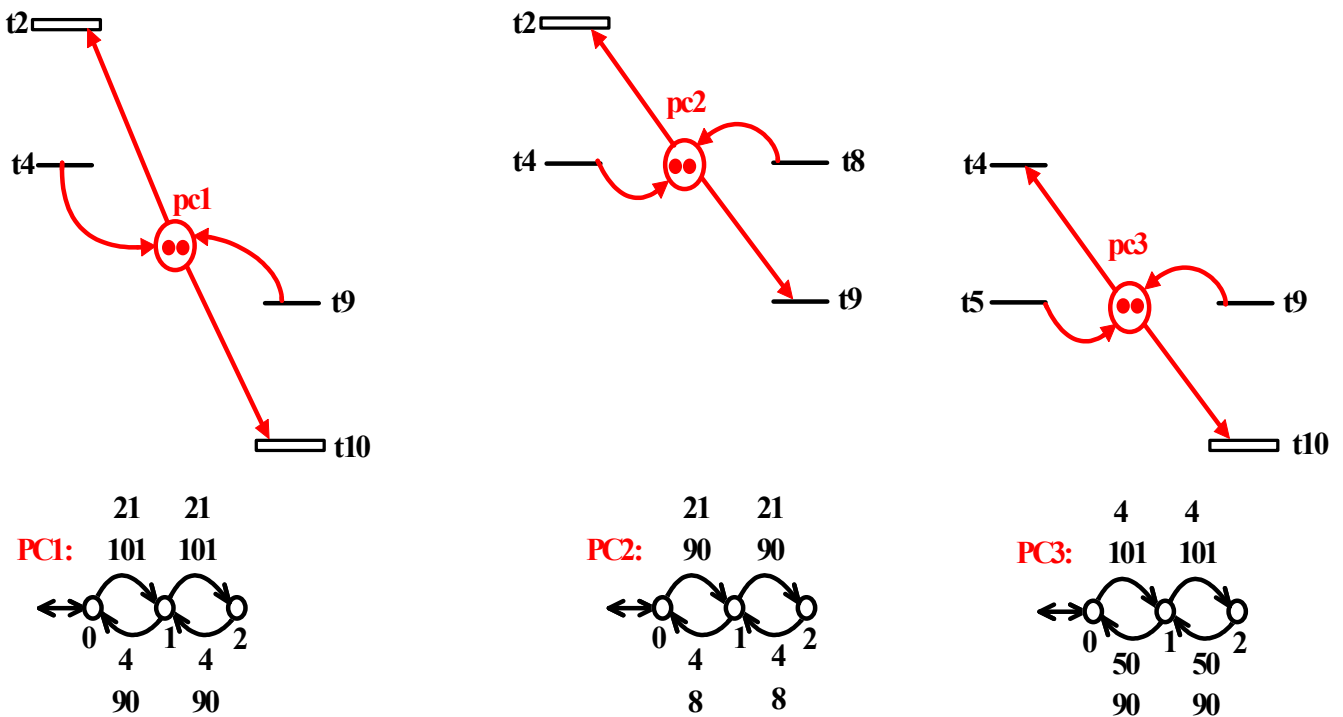


Figure 39. Mappings from control places pc1, pc2 and pc3 to automata in Example 3

Step 6. The controlled model PNSUPER (PNSUPER=FMS||PC1||PC2||PC3) is obtained by using FMS and buffer models of the given feedback control elements PC1, PC2 and PC3 as follows:

PNSUPER = Sync(FMS,PC1) (227,800) Blocked_events = None
 PNSUPER = Sync(PNSUPER,PC2) (223,793) Blocked_events = None
 PNSUPER = Sync(PNSUPER,PC3) (215,771) Blocked_events = None

Step 7. The following test verifies that the controlled model PNSUPER obtained is isomorphic (identical) to RWSUPER: true = Isomorph(RWSUPER,PNSUPER;identity). This means that the controller obtained in the PN domain is also a proper supervisor, i.e. it is maximally permissive and non-blocking.

The following shows that the optimal controlled behaviour PNSUPER (or RWSUPER) is not simply the language generated by the trimmed plant. This is because not all transitions are controllable. In this case the optimal controlled behaviour PNSUPER (or RWSUPER) is the supremal controllable sublanguage defining the maximally permissive and non-blocking behaviour.

TRIMFMS = Trim(FMS) (232,838)
 false = Isomorph(PNSUPER,TRIMFMS)

7. Conclusions

This paper has proposed a novel and general methodology for carrying out the correctness analysis for the computed PN-based controllers by using the TCT implementation tool of SCT. Assuming that an uncontrolled PN model of a system, a set of specifications, and a PN-based controller are given, the proposed analysis method provides the result as to whether the PN-based

controller enforces the specification on the uncontrolled PN model optimally. Three examples have been considered for illustration.

8. Acknowledgements

This work was supported by the research grant of the Scientific and Technological Research Council of Turkey (Türkiye Bilimsel ve Teknolojik Araştırma Kurumu - TÜBİTAK) under the project number TÜBİTAK-107E125. The authors would like to thank the editor and three anonymous referees whose comments and suggestions greatly helped us to improve the presentation and the quality of the paper.

9. References

1. P. J. Ramadge and W. M. Wonham, "Modular supervisory control of discrete event systems", *Lect. Notes Contr. Inform. Sci.*, **1986**, 83, 202-214.
2. P. J. Ramadge and W. M. Wonham, "Supervisory control of a class of discrete event processes", *SIAM J. Contr. Optim.*, **1987**, 25, 206-230.
3. P. J. Ramadge and W. M. Wonham, "The control of discrete event systems", *Proc. IEEE*, **1989**, 77, 81-98.
4. W. M. Wonham and P. J. Ramadge "On the supremal controllable sublanguage of a given language", *SIAM J. Contr. Optim.*, **1987**, 25, 637-659.
5. A. Giua, "Petri net techniques for supervisory control of discrete event systems", Proceedings of 1st International Workshop on Manufacturing and Petri Nets, **1996**, Osaka, Japan, pp. 1-21.
6. A. Giua, F. DiCesare and M. Silva, "Generalized mutual exclusion constraints on nets with uncontrollable transitions", Proceedings of IEEE International Conference on Systems, Man and Cybernetics, **1992**, Chicago, Illinois, USA, pp. 974-979.
7. K. Yamalidou, J. O. Moody, M. Lemmon and P. J. Antsaklis, "Feedback control of Petri nets based on place invariants", *Automatica*, **1996**, 32, 15-28.
8. J. O. Moody and P. J. Antsaklis, "Petri net supervisors for discrete event systems with uncontrollable and unobservable transitions", *IEEE Trans. Automat. Contr.*, **2000**, 45, 462-476.
9. R. Zurawski and M. C. Zhou, "Petri nets and industrial applications: A tutorial", *IEEE Trans. Ind. Electron.*, **1994**, 41, 567-583.
10. M. Uzam, "On suboptimal supervisory control of Petri nets in the presence of uncontrollable transitions via monitor places", *Int. J. Adv. Manufac. Technol.*, **2010**, 47, 567-579.
11. Systems Control Group, "TCT: A design software supporting supervisory control theory", www.control.utoronto.ca/DES (Accessed: **2009**).
12. M. Uzam and G. Gelen, "The real-time supervisory control of an experimental manufacturing system based on a hybrid method", *Contr. Eng. Pract.*, **2009**, 17, 1174-1189.
13. M. Uzam and W. M. Wonham, "A hybrid approach to supervisory control of discrete event systems coupling RW supervisors to Petri nets", *Int. J. Adv. Manufac. Technol.*, **2006**, 28, 747-760.
14. M. V. Iordache and P. J. Antsaklis, "Supervisory Control of Concurrent Systems, A Petri Net Structural Approach", Birkhauser, Boston, **2006**, p. 21.
15. P. Darondeau, "Equality of languages coincides with isomorphism of reachable state graphs for bounded and persistent Petri nets", *Inform. Process. Lett.*, **2005**, 94, 241-245.
16. M. Droste and R. M. Short, "From Petri nets to automata with concurrency", *Appl. Categor. Struct.*, **2002**, 10, 173-191.
17. A. Egri-Nagy and C. L. Nehaniv, "Algebraic properties of automata associated to Petri nets and applications to computation in biological systems", *BioSystems*, **2008**, 94, 135-144.
18. A. Ghaffari, N. Rezg and X. Xie, "Design of a live and maximally permissive Petri net controller using the theory of regions", *IEEE Trans. Robot. Automat.*, **2003**, 19, 137-142.
19. E. Badouel and P. Darondeau, "Theory of regions", in *Lectures on Petri Nets I: Basic Models*, Vol. 1491, Springer-Verlag, Berlin, **1998**, pp.529-586.

20. M. Uzam, "An optimal deadlock prevention policy for flexible manufacturing systems using Petri net models with resources and the theory of regions", *Int. J. Adv. Manufac. Technol.*, **2002**, 19, 192-208.
21. M. Uzam, "The use of Petri net reduction approach for an optimal deadlock prevention policy for flexible manufacturing systems", *Int. J. Adv. Manufac. Technol.*, **2004**, 23, 204-219.
22. M. Uzam, "Synthesis of feedback control elements for discrete event systems using Petri net models and theory of regions", *Int. J. Adv. Manufac. Technol.*, **2004**, 24, 48-69.
23. C. A. Petri, "Kommunikation mit automaten schriften des rheinisch", Westfalischen Inst. fur Instrumentelle Mathematik and der Universitat Bonn (translated by C. F. Green), Suppl 1 to Tech Report RADC-TR-65-337, Applied Data Research Inc., New York, **1962**.
24. J. L. Peterson, "Petri Net Theory and the Modeling of Systems", Prentice-Hall Inc., Englewood Cliffs, N.J., **1981**.
25. M. A. Marsan, G. Balbo, G. Conte, S. Donatelli and G. Franceschini, "Modelling with Generalized Stochastic Petri Nets", John Wiley and Sons Ltd., Turin, **1995**.
26. M. Uzam, "Petri-net-based supervisory control of discrete event systems and their ladder logic diagram implementations", *PhD. Thesis*, **1998**, University of Salford, UK. (Posted at URL: <http://host.nigde.edu.tr/muzam/>)
27. M. Uzam and A. H. Jones, "Discrete event control system design using automation Petri nets and their ladder diagram implementation", *Int. J. Adv. Manufac. Technol.*, **1998**, 14, 716-728.
28. C. G. Cassandras and S. Lafortune, "Introduction to Discrete Event Systems", Kluwer Academic Publishers, New York, **1999**, pp. 30, 56-57, 63, 65.
29. W. M. Wonham, "Supervisory control of discrete event systems", Section 8.2, <http://www.control.utoronto.ca/DES/> (Updated **2010**).
30. "A Petri net analysis tool" Software Version 1.0, **1987-1996**, Pedagogical University of Rzesów, Poland.
31. F. Basile, P. Chiacchio and A. Giua, "Suboptimal supervisory control of Petri nets in presence of uncontrollable transitions via monitor places", *Automatica*, **2006**, 42, 995-1004.

10. Appendix

TCT: General Information

TCT is a program for the synthesis of supervisory controls for DES. Generators and recognisers are represented as standard DES in the form of a 5-tuple:

[**Size**, **Init**, **Mark**, **Voc**, **Tran**]

Size is the number of states (the standard state set is $\{0, \dots, \text{Size}-1\}$), **Init** is the initial state (always taken to be 0), **Mark** lists the marker states, **Voc** the vocal states, and **Tran** the transitions. A vocal state is a pair $[I, V]$ representing positive integer output V at state I . A transition is a triple $[I, E, J]$ representing a transition from the exit (source) state I to the entrance (target) state J and having event label E . E is an odd or even non-negative integer, depending on whether the corresponding event is controllable or uncontrollable.

event E
exit I O----->O J entrance

All DES transition structures must be deterministic: distinct transitions from the same exit state must carry distinct labels.

TCT: Synthesis Procedures. A quick review of some of the TCT commands used in this paper:

DES = Create(DES)

is a new discrete-event system (DES). Option 1 allows fast user input via a sequence of prompts, resulting in direct creation of a .DES file. Option 2 allows user to create a text (.ADS) file with any ASCII text editor; this file can be converted to a .DES file using the TCT procedure FD.

DES2 = Selfloop(DES1,[SELF-LOOPED EVENTS])

is DES1 augmented by self-loops at each state, with common event labels listed by the user. To prevent non-determinism, this list must not contain event labels appearing in DES1.

DES3 = Sync(DES1,DES2)

is the (reachable) synchronous product of DES1 and DES2.

DES3 = Supcon(DES1,DES2)

is a trim recogniser for the supremal controllable sublanguage of the marked ("legal") language generated by DES2 with respect to the marked ("plant") generated by DES1. DES3 provides a proper supervisor for DES1.

DES2 = Trim(DES1)

is the trim (reachable and co-reachable) substructure of DES1.

DES3 = Meet(DES1,DES2)

is the meet (reachable Cartesian product) of DES1 and DES2. DES3 need not be co-reachable.

DES2 = Allevents(DES1)

is a one-state DES self-looped with all the events of DES1.

True/False = Nonconflict(DES1,DES2)

tests whether DES1 and DES2 are non-conflicting, namely whether all reachable states of the product DES are co-reachable.

True/False = Isomorph(DES1,DES2)

tests whether DES1 and DES2 are identical up to renumbering of states; if so, their state correspondence is displayed.

Full Paper

Effects of modulus and dosage of sodium silicate on limestone flotation

Danda S. Rao^{1,*}, Tadiparthi V. Vijayakumar², Shivakumar Angadi¹, Swarna Prabhakar² and Guntamadugu B. Raju²

¹ Institute of Minerals and Materials Technology, Bhubaneswar - 751 013, Orissa, India

² National Metallurgical Laboratory - Madras Centre, CSIR Madras Complex, Taramani, Chennai – 600 113, India

* Corresponding author, e-mail: dsrao@immt.res.in

Received: 15 April 2010 / Accepted: 15 September 2010 / Published: 21 September 2010

Abstract: Sodium silicates are probably one of the oldest and most widely used industrial chemicals. Among a wide variety of applications, an important one is as a depressant in flotation. In this investigation, the effectiveness of sodium silicates of different values of modulus (silica-to-soda ratio) and dosage was investigated on a low-grade siliceous limestone sample having CaO = 45.10%, SiO₂ = 15.60% and LOI = 36.03% from Jayantipuram mine of Andhra Pradesh, India. Direct flotation (flotation of carbonate minerals) was adopted to reduce the silica content and enrich CaO using laboratory-scale flotation process batch tests. The analysis of variance (ANOVA) statistical tool was used for evaluation of the influence of operating parameters, viz. the modulus and dosage of sodium silicate, on the flotation. The study indicated that a modulus of 2.19 and a dosage of 0.6 kg/ton is optimum for the flotation for the low-grade siliceous limestone sample.

Keywords: siliceous limestone, direct flotation, sodium silicate, mineral depressant

Introduction

One of the most important groups of chemicals used in mineral processing is the depressant. Most often, the flotation separation of individual minerals from ores is not possible without the use of a depressant. Depressants affect the flotation process by rendering the gangue mineral hydrophilic, thus reducing the possibility of the unwanted minerals being floated simultaneously with those substances which are to be concentrated in the froth. Substances used as gangue mineral depressants in

flotation process cover a large variety of both organic and inorganic chemicals and these are well documented in the literature. The type of depressant used largely depends on the variety of mineral substances which accompany the ore. Sodium silicate is one such chemical which is widely used as depressant in the flotation in general and non-sulphide mineral flotation in particular. Sodium silicate is a versatile, non-toxic as well as a low-cost multifaceted chemical available in many forms and for a wide range of industrial applications [1]. In the case of mineral beneficiation, sodium silicate is used as a depressant [2-6] as well as a dispersant [7-9]. In some cases, it is also used as an activator [10] because it reduces or eliminates the deleterious/depressing effects of slimes on flotation. It also helps in grinding [11] because it lowers the viscosity and/or provides finer grinding or increases throughput for the same particle sizes.

Sodium silicate is also called water glass and has a composition expressed by $m\text{Na}_2\text{O} \cdot n\text{SiO}_2$. The ratio n/m is referred to as the modulus of sodium silicate. The type frequently used in flotation has a modulus varying between 1.5-3.0 [12-13]. In flotation, the action of sodium silicate depends largely on the pH of the medium/slurry, the concentration of the depressant, the oxygen potential of the medium/slurry and the presence of other reagents. The action of the depressant also depends upon the mineral composition of the ore, its particle size and flotation parameters such as extent of conditioning, stirring and flotation time [14-15].

References on flotation employing sodium silicate are often inadequate because they failed to mention the type of sodium silicate used or its modulus. In this investigation, experiments have been conducted with three different types of sodium silicate to determine its effects of type and dosage or concentration on the recovery of a siliceous limestone sample from Jayantipuram mine of Andhra Pradesh, India. Rao et al. [16] studied a siliceous limestone sample from the same area and reported that direct flotation, in which the gangue is depressed and the useful mineral is floated, gives a better result than reverse flotation. Thus, in the present undertaking, different types of sodium silicate are studied using the same method to find out which may give rise to better results. Of course, the choice of sodium silicates is also dictated by the relative costs of the sodium silicates and other considerations.

Materials and Methods

The low-grade siliceous limestone sample used in this study was obtained from Jayantipuram mine of Andhra Pradesh, India. The bulk constituents of the sample, as analysed by conventional chemical analysis methods, was 45.10% CaO, 15.60% SiO₂ and 36.03% LOI (loss on ignition). Oleic acid and sodium hydroxide used for preparation of sodium oleate were of laboratory grade reagents. Sodium silicate and sodium oleate were used as depressant and collector respectively. Sodium silicates used were of commercial grade and procured from Kiran Pandy Chems Limited, Chennai. Table 1 gives details of the different types of sodium silicate.

The feed particle size distribution of the siliceous limestone sample obtained with a laboratory ball mill and used for the flotation experiments is presented in Table 2. It can be observed from the table that 80% of the feed material (d_{80}) was 68 microns or finer. Bench-scale conventional flotation tests were performed with a D12 Denver flotation machine (Denver Equipment Company, England). The sequence of addition of reagents was as follows:

- Tap water (1 litre, pH \approx 7.0) was added first along with the feed (500 g).
- Required dosage of sodium silicate in solution form (10% w/v) was added to the above and the mixture conditioned for 3 minutes. Then sodium oleate (0.1 g) was added to the system, which was further conditioned for another 3 minutes.
- Natural pH was maintained throughout the flotation experiment. After 10 minutes of flotation, float and non-float products were filtered, dried, weighed and analysed for CaO, SiO₂ and LOI.

Table 1. Types of sodium silicate [1]

Type	1	2	3
Specific gravity	1.56	1.56	1.49
Na ₂ O	14.76	13.82	12.04
SiO ₂	32.31	33.16	31.30
Total solid	47.09	46.98	43.34
SiO ₂ / Na ₂ O	2.19	2.49	2.60
Nature	Alkaline	Alkaline	Alkaline
Cost per ton	Rs.8750/-	Rs.8750/-	Rs.8750/-

Table 2. Size distribution of siliceous limestone sample

Size in micron	Weight (%)	Cum wt (%)
+212	1.3	98.7
-212+150	2.7	96.0
-150+106	7.3	88.7
-106+75	4.3	84.4
-75+63	5.1	79.3
-63+45	45.3	34.0
-45	34.0	0.0
	100.0	
d ₈₀ = 68 microns		

Rao et al. [16] studied the siliceous limestone sample from the same area and reported that the sodium oleate dosage of 0.2 kg/ton and water at pH 7 gives the best results. Thus, in all our experiments the pH of the flotation slurry was kept natural (\sim 7) and the sodium oleate dosage of 0.2 kg/ton was used. A series of experiments were carried out by varying the modulus of sodium silicate and its dosage at three levels as shown in Table 3.

Table 3. Experimental variables and their levels

Variable	Level 1	Level 2	Level 3
Modulus of sodium silicate	2.19	2.40	2.60
Dosage of sodium silicate (kg/ton)	0.6	1.0	1.4

Results and Discussion

A systematic approach has been made to assess the effectiveness of recovering the limestone from a low-grade siliceous ore. All experiments carried out at different values of modulus and dosage of sodium silicate are presented in Table 4.

Table 4. Flotation experimental results

Expt. no.	Modulus of sodium silicate	Dosage of sodium silicate (kg/ton)	Product	Yield (% weight)	CaO (%)	SiO ₂ (%)
1a	2.19	0.6	Froth	81.2	51.36	5.44
			Non-froth	18.8	18.06	59.48
2a	2.40		Froth	81.9	51.18	5.66
			Non-froth	18.1	17.59	60.60
3a	2.60		Froth	82.6	50.98	5.71
			Non-froth	17.4	17.26	62.42
1b	2.19	1.0	Froth	82.2	51.14	5.74
			Non-froth	17.8	17.22	61.13
2b	2.40		Froth	83.2	50.98	6.03
			Non-froth	16.8	15.98	62.99
3b	2.60		Froth	84.3	50.70	6.16
			Non-froth	15.7	15.04	66.29
1c	2.19	1.4	Froth	81.7	51.05	6.07
			Non-froth	18.3	18.54	58.15
2c	2.40		Froth	82.5	50.76	6.41
			Non-froth	17.5	18.42	58.92
3c	2.60		Froth	83.2	50.16	6.58
			Non-froth	16.8	20.04	60.28

The common indicators used for the evaluation of performance of a limestone flotation operation are yield (% weight), % CaO and % SiO₂ of the products. The flotation operation is said to be optimum when it produces a maximum yield of the froth fraction with a high CaO content and a low SiO₂ content. A change in the level of reagents is seen to affect both yield and CaO and SiO₂ contents. In the present context, the effects of sodium silicate modulus and dosage on the product yield (% weight %), % CaO and % SiO₂ are analysed.

Effects of operating variables on product yield

Table 5 presents the results of a statistical analysis of the effects of the reagent modulus and dosage on the product yield. The analysis of variance (ANOVA) shows that calculated values of 'F'

(F- ratio) for both silica-to-soda ratio (R) and dosage (D) are higher than the P values. This means that both modulus and dosage increase the yield of limestone. Further it can be inferred from the table that the effect of modulus (R) plays more prominent role than that of dosage (D) as the calculated F-ratio value for the former is higher than that for the latter.

With an increase in sodium silicate dosage, the % weight of the product concentrate (froth fraction) increases to certain level and again falls down, indicating that the unliberated calcite (with quartz) gets depressed, whereas with an increase in the reagent modulus, the % weight of the product concentrate always increases (Figure 1), although its grade (% CaO) is lowered (Table 4). The sodium silicate with a modulus of 2.19 gives the highest CaO content (51.36%) and lowest SiO₂ content (5.44%) in the froth fraction, with only 0.6 kg/ton dosage of the reagent. On the other hand, the dosage variation indicated that sodium silicate with a modulus of 2.6 gives the highest recovery of the froth fraction (84.3%) with 1.0 kg/ton dosage, but the grade of the product is lower than that obtained using sodium silicate with 2.19 modulus at 0.6 kg/ton dosage. From the economic point of view, the use of 0.6 kg/ton of the sodium silicate with 2.19 modulus should be more preferable since it gives a better grade of the product with comparable yield, while the cost of all three sodium silicate varieties is the same.

Table 5. Results of analysis of product yield (% weight) by ANOVA

Source	Sum of square	df	Mean square	F- ratio	P
R	4.167	2	2.083	56.3	19.0
D	2.687	2	1.343	36.3	19.0
Error	0.147	4	0.037		

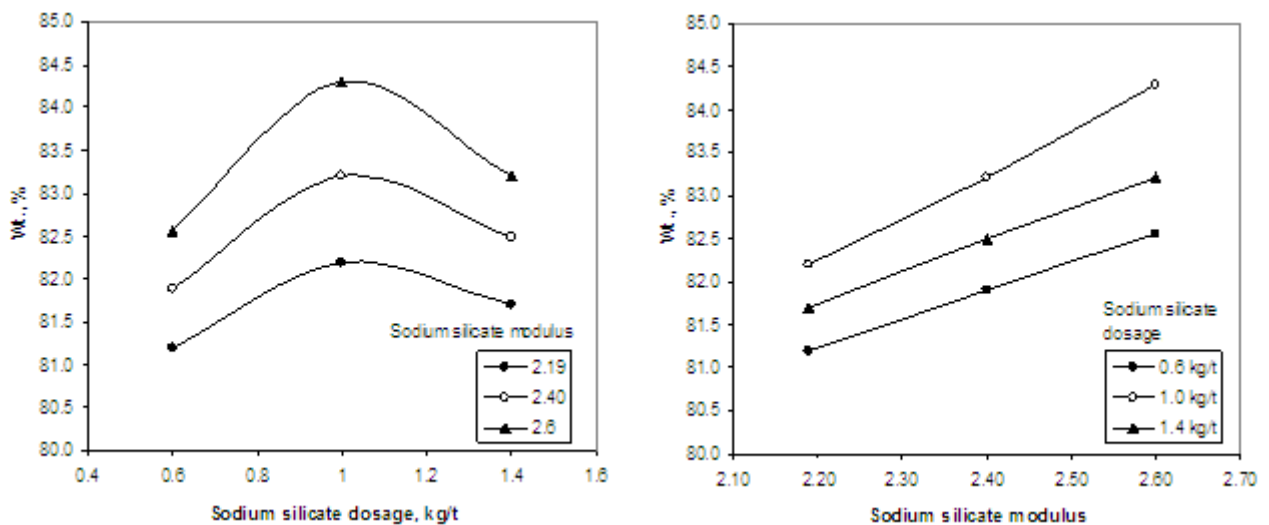


Figure 1. Influence of sodium silicate modulus and dosage on product yield (% weight)

Effects of operating variables on % CaO

Sodium silicate is used in flotation to depress and/or disperse silicate minerals, as a result of which CaO content in the froth product is enriched. In the present case, however, increase of sodium silicate dosage and modulus decreases the CaO content in the froth concentrate (Figure 2). This could be because of the association of fine silicate gangue minerals present as inclusions within the limestone minerals.

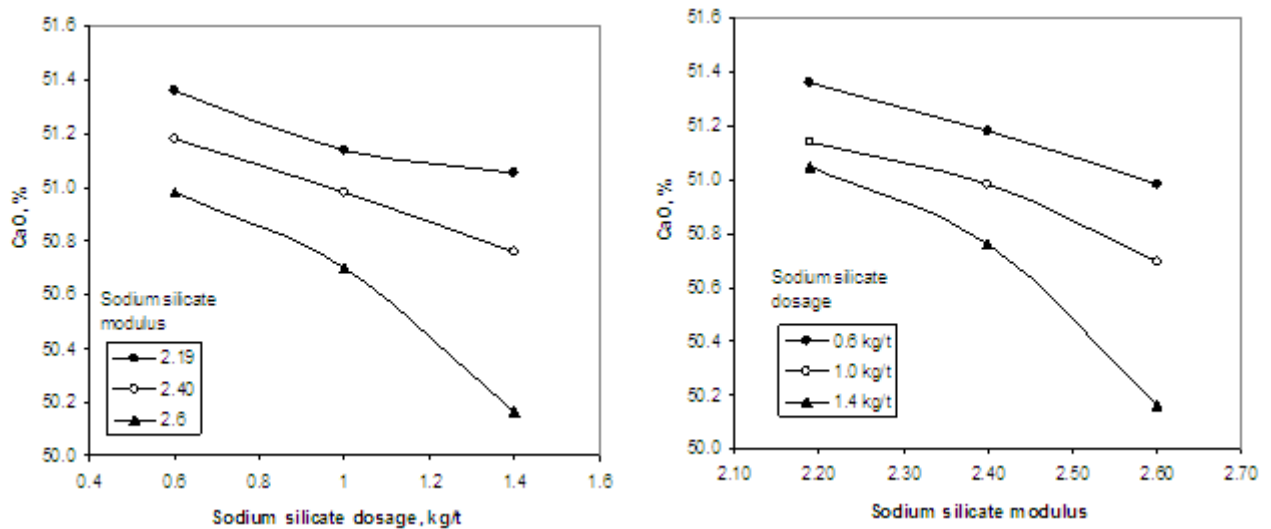


Figure 2. Influence of sodium silicate modulus and dosage on % CaO of froth concentrate

The effects of the reagent modulus and dosage on CaO content of the froth fractions were analysed statistically and the results are presented in Table 6. The analysis of variance (ANOVA) shows that calculated values of 'F' (F-ratio) for both sodium silicate modulus (R) and dosage (D) are lower than the P values. This means that neither modulus nor dosage of the reagent is prominently influencing the CaO content of the concentrate.

Table 6. Results of analysis of % CaO by ANOVA

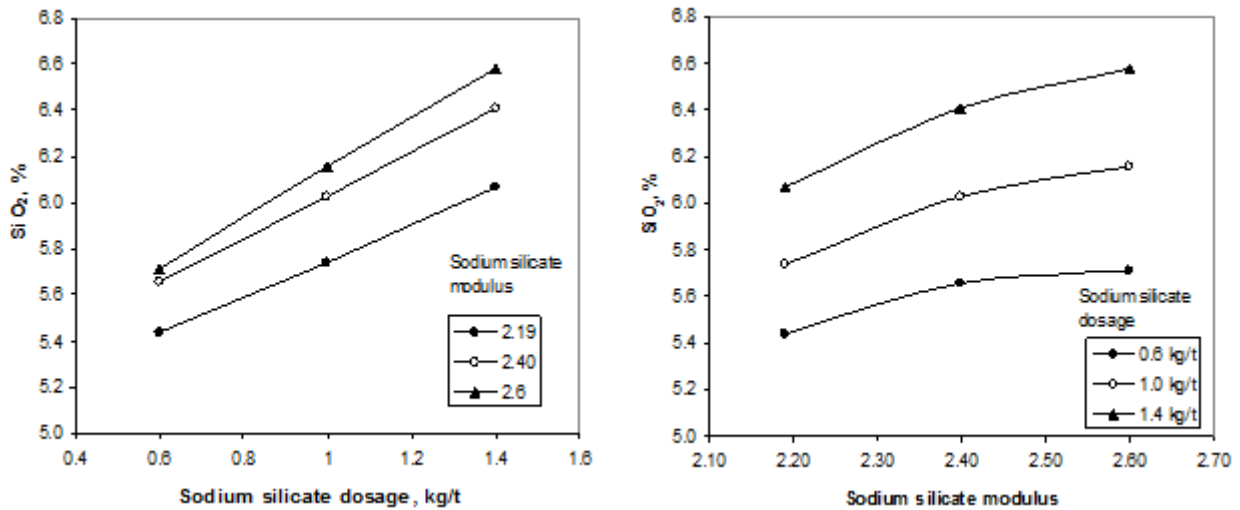
Source	Sum of square	df	Mean square	F-ratio	P
R	0.499	2	0.249	11.9	19.0
D	0.402	2	0.201	9.6	19.0
Error	0.085	4	0.021		

Effects of operating variables on % SiO₂

Similar effects of the reagent modulus and dosage on the SiO₂ content of the product were analysed statistically and the results are presented in Table 7. The analysis of variance (ANOVA) shows that calculated values of 'F' (F-ratio) for both sodium silicate modulus (R) and dosage (D) are lower than the P values. This means that neither modulus nor dosage of the reagent is prominently influencing the SiO₂ content of the concentrate (Figure 3).

Table 7. Results of analysis of % SiO₂ by ANOVA

Source	Sum of square	df	Mean square	F-ratio	P
R	0.255	2	0.127	1.7	19.0
D	0.167	2	0.084	1.1	19.0
Error	0.299	4	0.075		

**Figure 3.** Influence of sodium silicate modulus and dosage on % SiO₂ of the froth concentrate

Conclusions

This study has revealed that both the modulus and dosage of sodium silicate have an influence on the yield of the flotation product of a low-grade siliceous limestone ore. As the modulus increases, so does the yield, whereas a maximum yield occurs at an intermediate dosage of sodium silicate. As the yield increases, however, a somewhat lower grade of product is obtained.

Increase of sodium silicate modulus and dosage tends to decrease the CaO content of the flotation product while the SiO₂ content is increased. However, both of these variables were found to have less influence on the CaO and SiO₂ contents compared with that on the yield of the product.

Acknowledgements

The authors are thankful to the Director of National Metallurgical Laboratory, Jamshedpur for his valuable guidance, encouragement and permission to publish this work. The authors would also like to thank M/s. Madras Cements Limited for providing logistic support, and Chennai and Ramco Research and Development Centre, Chennai for providing chemical analysis of the limestone samples.

References

1. R. C. Merrill, "Industrial applications of the sodium silicates—some recent developments", *Ind. Eng. Chem.*, **1949**, 41, 337-345.
2. B. C. Acharya, D. S. Rao and P. S. R. Reddy, "Mineralogical and beneficiation characteristics of low grade graphite ores", *Powder Handl. Process.*, **1995**, 7, 233-237.

3. B. C. Acharya, D. S. Rao, S. Prakash, P. S. R. Reddy and S. K. Biswal, "Processing of low grade graphite ores of Orissa, India", *Miner. Eng.*, **1996**, 9, 1165-1169.
4. D. Ananth, N. N. Gothe and S. Subramanian, "Studies on beneficiation of limestone from Salem", *J. Mines Metals Fuels*, **1997**, 45, 216-219.
5. S. Rao, B. V. Narayana and S. Subramanian, "Optimization studies on limestone beneficiation", *Ind. J. Eng. Mater. Sci.*, **1997**, 4, 139-144.
6. J. R. de Wet and J. D. Singleton, "Development of a viable process for the recovery of zinc from oxide ores", *J. South Afr. Inst. Miner. Metall.*, **2008**, 108, 253-259.
7. R. Asmatulu, "Removal of the discoloring contaminants of East Georgia kaolin clay and its dewatering", *Turkish J. Eng. Env. Sci.*, **2002**, 26, 447-453.
8. J. Pauck and J. Marsh, "The role of sodium silicate in the flotation deinking of newsprint at Mondi Merebank", *Tappsa J.*, Jan. **2002**, 20-25.
9. M. O., Silvestre, C. A. Pereira, R. Galery and A. E. C. Peres, "Dispersion effect on a lead-zinc sulphide ore flotation", *Miner. Eng.*, **2009**, 22, 752-758.
10. M. C. Fuerstenau and K. N. Han, "Activators", in "Reagents in Mineral Technology: Surfactant Science Series" (Ed. P. Somusundaran and B. M. Moudgil), **1987**, 27, 411-427.
11. Y. Cebeci and O. Bayat, "Effect of flotation reagents on the wet grinding of celestite concentrate", *Ind. J. Chem. Tech.*, **2004**, 11, 382-387.
12. C. L. Sollenberger and R. B. Greenwalt, "Relative effectiveness of sodium silicates of different silica-soda ratios as gangue depressants in non-metallic flotation", *Min. Eng.*, **1958**, 10, 691-693.
13. M. C. Fuerstenau, G. Gutierrez and D. A. Elgillani, "The influence of sodium silicate in non-metallic flotation system", *AIME Trans.*, **1972**, 241, 348-352.
14. S. P. Mehrotra and P. C. Kapur, "The effects of aeration rate, particle size and pulp density on the flotation rate distributions", *Powder Technol.*, **1983**, 9, 213-219.
15. A. M. R. Botelho, C. T. O'Connar and R. C. Dunne, "The influence of various chemical, physical and mineralogical factors on the flotation of gold bearing pyrites", Proceedings of International Conference on Gold: 2. Extractive Metallurgy of Gold, **1986**, Johannesburg, South Africa, pp. 493-503.
16. D. S., Rao, T. V. Vijaya Kumar, S. Prabhakar and G. B. Raju, "Beneficiation of a siliceous limestone sample", *A. T. Min. Proc.*, **2009**, 50, 36-47.

Full Paper

Segmentation and feature extraction of fluid-filled uterine fibroid—A knowledge-based approach

Ratha Jeyalakshmi^{1,*} and Ramar Kadarkarai²

¹ Mother Teresa Women's University, Kodaikanal, Tamil Nadu, India

² Computer Science and Engineering Department, National Engineering College, Kovilpatti, Tamil Nadu, India

* Corresponding author, e-mail: radha_jeyalakshmi@yahoo.com

Received: 22 February 2010 / Accepted: 28 September 2010 / Published: 5 October 2010

Abstract: Uterine fibroids are the most common pelvic tumours in females. Ultrasound images of fibroids require image segmentation and feature extraction for analysis. This paper proposes a new method for segmenting the fluid-filled fibroid found in the uterus. It presents a fully automatic approach in which there is no need for human intervention. The method used in this paper employs a number of knowledge-based rules to locate the object and also utilises the concepts in mathematical morphology. It also extracts the necessary features of the fibroid which can be used to prepare the radiological report. The performance of this method is evaluated using area-based metrics.

Keywords: uterine fibroid, ultrasound images, mathematical morphology

INTRODUCTION

Ultrasound imaging is widely used in the field of medicine. It is used for imaging soft tissues in organs such as liver, kidney, spleen, uterus, heart and brain. Ultrasound imaging is a common modality used for detecting fibroids. The most noticeable advantages of ultrasound scanning are safety, cost effectiveness, speed, easy handling and portability. Ultrasound is based on the principle of sound wave echoes. Sound wave travels from the probe to the object, passes through it and is continuously reflected back to the probe from multiple points inside the object. Ultrasound involves sound wave of frequency in the range of megahertz; typically this ranges between 3.5-10 MHz. The reflected sound wave is converted back to electrical signals in the probe and transmitted to the processing device which displays the image on the monitor. Bright or white areas in the image represent high reflectivity

or reflective surfaces/interphases in the body. Bone, air and calcium containing lesions (e.g. stone) appear intensely bright (whiter) or hyperechoic. Blacker or low signal reflection areas are called hypoechoic. Anechoic structures are usually filled structures like blood, urine, etc. Such structures as the liver, pancreas and uterus appear in various shades of gray depending upon their echogenicity (ability to reflect ultrasound waves). If a tissue allows sound wave to be transmitted so well that no echo can be detected, it is called anechoic and it appears as a dark and uniform region on an ultrasound image because there is no echo to give the intensity and texture. Because water has a much lower acoustic impedance ($1.48 \times 10^6 \text{ kg/m}^2/\text{s}$) than an average soft tissue ($1.63 \times 10^6 \text{ kg/m}^2/\text{s}$) [1], fluid-filled collections such as cysts are often anechoic and appear as dark regions with well-defined boundaries. The echogenicity of the tissues on which the ultrasound waves fall differs with respect to the texture of the tissues.

In this paper automatic segmentation of uterine fibroids is performed. Fibroids are muscular tumours that grow in the uterus. Another medical term for fibroids is "leiomyoma" or just "myoma". Fibroids are almost always benign (not cancerous). Anyhow, the symptoms caused by a fibroid may cause certain inconvenience in women and need to be treated. The fibroid may be in different textures. There is a type of fibroid most of whose portion is filled with fluid and the remaining portion consists of soft tissues. The fluid part appears dark and all the pixels have a minimum intensity. Some fibroids may have soft tissues for the entire portion. There is another type of fibroid which sticks to the wall of the uterus which is near the urinary bladder. This can be identified by the hyperechoic part which projects into the urinary bladder. The remaining portion contains both fluid and soft tissues. In a fluid-filled fibroid, the major portion of the tumour is fluid and therefore it is anechoic. Still another type of fibroid is fully or partially calcified and found anywhere inside the uterus. The calcified part appears hyperechoic. The proposed algorithm in this paper deals with segmentation of the fluid-filled fibroids.

The quality of ultrasound images is limited by granular speckle noise. This makes it difficult to segment the images. In this paper, the image is preprocessed in order to crop it such that unnecessary portions as well as the speckle noise are removed. We use a morphological cleaning algorithm to clean the image. Then it is segmented by an algorithm which uses a collection of rules to locate the fibroid and morphological concepts to segment the image. Finally, essential features are extracted, which might be useful for treating an abnormality.

Various techniques for speckle noise removal are available in the literature [2-6]. There are many segmentation algorithms for segmenting medical images [7]. There is a survey of ultrasound image segmentation [8]. Various introduced methods for segmenting ultrasound images are fully automatic [9-12].

A hybrid segmentation method based on morphological operators and a Gaussian function constraint to delimitate the tumour search scope, both used for tumour segmentation purposes, was proposed [8]. A new automatic seed point selecting method for new region growing algorithm was proposed for breast lesions [9]. A region-based segmentation method for ultrasound images using local statistics [10] produces results that are less sensitive to the pixel location and it also allows a segmentation of the accurate homogeneous regions. An automatic process of filtering, segmenting and analysing the features of breast nodules in ultrasound images was presented [11]. Anisotropic diffusion filter to suppress speckle noise and radial derivative function to segment the breast lesion in breast

ultrasound images were presented [12]. There are a number of research work which use watershed segmentation [13-16]. To solve the over-segmentation problem associated with this method, different techniques have been used [13-14, 16, 19]. There are also research papers on the application of morphological concepts to image segmentation [17-19]. There are papers which deal with rule-based segmentation algorithm [20-22]. Only two research papers are found, which focus on uterine fibroid segmentation [23-24], but they involve work on MRI images. There is apparently no work on ultrasound images of uterine fibroid.

METHODS

Preprocessing

The preprocessing of an original ultrasound image consists of two steps, namely cropping the image and removing the speckle noise.

Cropping image

The image contains the details of the patient on the top. The left-hand side and right-hand side contain other details, viz. scale, type of scan, frequency used, diameter of tumour, etc. The view of the image is not always the same. The radiologist uses the one which shows the object of interest clearly. In some images, we found the urinary bladder occupying one quarter of the image in the upper part where the uterus was below the urinary bladder and the fibroid was on the lower part of the uterus. In such cases, the part from the upper portion of the image to the bladder should be cropped as shown in Figure 1. The uterus area should be defined from below the ending row of the urinary bladder to the end of the image.



Figure 1. (a) Original image before cropping; (b) Image after cropping

In some images, the uterus was located in the upper portion of the image and a small portion of the bladder was visible on the right-hand side of the upper portion of the image. In such cases, the fibroid could be observed in the upper half of the image. Hence, a hundred rows from the bottom of the image should be removed from the image as shown in Figure 2. These areas of the image could be cropped. The top of the image below the detailed area showed the skin and flat layer of the abdomen. So these areas could also be cropped.

Speckle noise cleaning

A modified morphological image cleaning (MMIC) algorithm was used for cleaning the image. This is the modified version of morphological image cleaning (MIC) algorithm [3]. This algorithm



Figure 2. (a) Original image where uterus is located in the upper portion; (b) Image after cropping

works as follows. Initially, we define three arbitrary structuring elements with different sizes which resemble the shape of the speckles found in the image. Using these structuring elements (shown in Figure 3), a series of operations such as opening-closing followed by closing-opening is done to remove speckle noise. The top hat and bottom hat of this filtered image is found and they are binarised separately. These two binary images are reconstructed in order to get back the features that are lost while filtering. To reconstruct the features that are lost while cleaning, grayscale opening by reconstruction and grayscale closing by reconstruction are used. These are efficient techniques for getting back the lost image features [2].

001100	000000000000	00000000000000
011111	000111100000	00001111000000
000000	011111111110	00111111110000
	011111111100	00111111111110
		01111111111110
		01111111111110
a1	a2	a3

Figure 3. Arbitrary structuring elements a1, a2 and a3

Grayscale opening by reconstruction is defined as follows using equation (1). Let I and J be two grayscale images defined on the same domain D_I such that $I \leq J$. The grayscale reconstruction by opening of I from J is obtained by iterative grayscale geodesic erosions of J above I until stability is reached.

$$\rho_I^*(J) = \bigwedge_{n \geq 1} \varepsilon_I^{(n)}(J) \quad (1)$$

where ρ^* represents the grayscale reconstruction by opening, \bigwedge represents iteration operator, ε represents the geodesic erosion, and n represents the number of iterations.

Grayscale closing by reconstruction is defined as follows using equation (2). Let I and J be two grayscale images defined on the same domain D_I such that $I \leq J$. The grayscale reconstruction by closing of I from J is obtained by iterative grayscale geodesic dilations of J under I until stability is reached.

$$\rho_I(I) = \bigvee_{n \geq 1} \delta_I^{(n)}(I) \quad (2)$$

where ρ represents grayscale closing by reconstruction, \bigvee represents the iteration operator, δ represents the geodesic dilation, and n represents the number of iterations.

The processed top hat is added to the original image and the processed bottom hat is subtracted from it. This image cleaning procedure is repeated three times with three different predefined arbitrary structuring elements. Now the input image I which is free from speckle noise and has not lost its features is obtained. Figure 4(a) shows an image with speckle noise and the cleaned image after applying the MMIC algorithm is shown in Figure 4(b), which is segmented using the proposed segmentation algorithm.



Figure 4. (a) Image before preprocessing; (b) Image after preprocessing

MMIC algorithm

Step 1. Repeat Step 2 to Step 9 three times.

Step 2. Let $X = \text{OCCO}(I, a_i)$ where I is the original image with noise and a_i is the arbitrary structure element. OCCO means a sequence of morphological operations namely opening, closing, closing and opening. X is the resulting image after applying OCCO.

Step 3. $T(x,y) = \begin{cases} I(x,y) - S(x,y) & \text{if } I(x,y) - S(x,y) > 0 \\ 0 & \text{if } I(x,y) - S(x,y) \leq 0 \end{cases} ; ;$

(x and y represents the row and column of pixels in the image.)

Step 4. Find $t(x,y)$ by thresholding $T(x,y)$ using the standard deviation of $T(x,y)$.

Step 5. Let $tcap =$ reconstruction by closing of t .

Step 6. $B(x,y) = \begin{cases} S(x,y) - I(x,y) & \text{if } S(x,y) - I(x,y) > 0 \\ 0 & \text{if } S(x,y) - I(x,y) \leq 0 \end{cases}$

Step 7. Find $b(x,y)$ by thresholding $B(x,y)$ using the standard deviation of $B(x,y)$.

Step 8. Let $bcap =$ reconstruction by opening of b .

Step 9. Modify I as $X + tcap - bcap$.

(The symbols $T, I, S, t, B, b, bcap$ and $tcap$ represent images.)

Segmentation

Segmentation is the next step applied on the preprocessed image. The segmentation component is expressed in terms of production rules, which capture the perceptual knowledge relevant to the domain. These rules will detect appropriate boundaries and pertinent regions in the image.

Outline of proposed segmentation algorithm

1. Read the original image.
2. Crop the unwanted areas from the input image.
3. Clean the image by using MMIC algorithm.
4. Find the end of the urinary bladder to locate the starting of the uterus within which the fibroid lies by fixing a threshold.
5. Make a binary image by selecting dark cluster of pixels in the range 0.005 to 0.3 which constitutes the fibroid region by applying knowledge-based rules.
6. If the number of regions is more than one, select one region by applying rules.
7. Define a diamond-shaped region in the image by dilating the region obtained in step 6.
8. Mark the pixels within the diamond-shaped area whose intensity falls in a specified range that is fixed according to the texture of the image.
9. Consider the biggest region in it and crop it to remove the extensions around it, if any.
10. Draw the contour around it.

Proposed segmentation algorithm

Step 1. Crop the original image to remove unwanted areas. The margin area is removed; only the image area is left. Clean the speckle noise in the cropped image by implementing MMIC algorithm.

Step 2. Find the starting row, starting column, ending row and ending column of the bladder by fixing a threshold obtained from the knowledge base.

Step 3. Find the uterus area within which the fibroid lies as follows.

a) Number of rows in the image > 260

i) If the ending row of the bladder is in the upper one quarter of the image or the starting column of the bladder $< \text{no. of columns}/2$, the bladder is either at the top or starts at the upper left. The uterus area is in the upper half of the image. The area starts at $(\text{no. of rows}/2-60, 70)$ and ends at $(\text{no. of rows}-30, 200)$.

ii) Otherwise, if the bladder end is in the middle of the image, the uterus area is in the middle of the image. The area starts at $(\text{no. of rows}/2-60, 70)$ and ends at $(\text{no. of rows}-30, 140)$.

b) Otherwise, if $\text{no. of rows} < 260$, the image is small and the area within which the fibroid lies is in the lower half of the image. The area starts at $(\text{no. of rows}/2, 70)$ and ends at $(\text{no. of rows}-30, 200)$.

Step 4. Search for the fibroid within the uterus area defined in Step 3 as follows.

Step 5. Find the count of pixels whose intensity is in the range 0.005-0.05. If the count is greater than 15, it could be the fibroid region; go to Step 8. Otherwise, it could not be the fibroid region and it is negligible; go to Step 6.

Step 6. Find the count of pixels whose intensity is in the range 0.005-0.155. If the count is greater than 15, it could be the fibroid region; go to Step 8. Otherwise, it could not be the fibroid region and it is negligible; go to Step 7.

Step 7. Find the count of pixels whose intensity is in the range 0.005-0.255. If the count is greater than 15, it could be the fibroid region; go to Step 8. Otherwise, it could not be the fibroid region and it is negligible; there is no fibroid and stop.

Step 8. The regions found by the steps above are displayed and the fibroid region is one among them.

Step 9. Remove the regions whose area is below 10 using morphological operation. This is because the diameter of an anechoic fibroid is not less than a centimetre.

Step 10. For each of the region do the following.

- a) Find centx_dist =difference between the x-coordinate of the centre of the image and the x-coordinate of the centroid of the region.
- b) Find centy_dist =difference between the y-coordinate of the centre of the image and the y-coordinate of the centroid of the region.
- c) Find max x1 =maximum x-coordinate of the region.
- d) Find min x1 = minimum x-coordinate of the region.
- e) If the number of rows in the image is less than 260, then the fibroid is in the lower half of the image.
 - i) If there are regions which are not near the top of the image (not within 80 rows) and whose $\text{centy_dist} \leq 75$, take it as the fibroid region.
 - ii) Otherwise, if there is any region which is not near the top with $\text{centy_dist} < 50$ and y-coordinate of the centroid < 200 with $\text{min x1} < 100$ and $\text{max x1} > 50$, take it as the fibroid region.
- f) Otherwise (if the image is not reduced much), if there are regions whose $\text{centy_dist} \leq 150$, find the biggest among them.

Step 11. Now only a part of the fibroid is found. Therefore, to find the entire fibroid region, do the following.

- a) Find the area of the fibroid region. If it is smaller than 500, a diamond-shaped structuring element enclosing the fibroid is created. The dilated region is adjusted as follows.
- b) If the y-coordinate of the centre of the dilated region is in the upper half of the image, adjust the maximum of x-coordinate such that it is not greater than 160. This is because the bladder will be at the right-hand side of the upper half.
- c) Otherwise, starting column is made as $\text{no. of columns}/2-20$. This is because when the fibroid is in the lower half of the image, the fibroid will not start at the leftmost position.

Step 12. The pixels of the original cleaned image corresponding to the pixels in the dilated region are to be considered for processing. Now the intensity of the pixels that constitute the fibroid region is determined as follows.

- a) The minimum intensity among the pixels is stored in min2 .
- b) The average of pixels in the fibroid region is found.
- c) If $\text{average} > 0.3$, set max_limit as $\text{average}-0.1$.
- d) Otherwise, if average is in the range 0.1-0.15, set max_limit as $\text{avg}+0.03$.
- e) Otherwise, if average is in the range 0.05-0.09 :
 - i) If the count of pixels is greater than 10000, set max_limit as $\text{avg}-0.01$.

ii) Otherwise, set max_limit as avg+0.05.

f) Otherwise, set max_limit as 0.05 + the first digit after the decimal point in the average.

Step 13. Pixels of the region whose intensity are in the range min2 to max_limit are marked.

Step 14. Contour of fibroid is drawn around the marked pixels.

Feature Extraction

The goal of feature extraction is to obtain representative features that can be used to determine the mode of treatment. For instance, if the size of the fibroid is very small, it can be treated by giving medicine, whereas if the size is big, it should be removed by surgery. The shape-based features, i.e. diameter, area and compactness, are the essential measures.

Diameter

It is measured and specified by the radiologist as horizontal and vertical diameters in centimetres. After segmenting the fibroid, the horizontal and vertical diameters are calculated in pixels and converted to centimetres.

Area

The area of the fibroid is the number of pixels inside the fibroid. It is used to specify the size of the fibroid. It can also be found by the formula $\pi \cdot a \cdot b / 2$, where a and b are the horizontal and vertical diameters.

Compactness

The compactness of a region is defined as the ratio of the square of the perimeter of a region to its area, i.e. $\text{compactness} = \text{perimeter}^2 / \text{area}$, where the perimeter is the distance around the boundary of the fibroid and the area is the number of pixels inside the fibroid.

Evaluation Criteria

There are two types of methods for image segmentation evaluation [25]. Analytical methods analyse and evaluate segmentation algorithms themselves by their principles and properties. Empirical evaluation methods measure the quality of segmentation results. Because empirical evaluation methods provide easy-to-interpret objective evaluations, only empirical methods are commonly used. Ideally, a segmentation result obtained from the algorithm would be compared with an expected segmentation known as the ground truth. The manual segmentations or ground truths are acquired from experts, often called gold standard.

The contour obtained from the segmentation algorithm is usually different from the one given by the expert. Every pixel in the output of the segmentation algorithm therefore belongs to one of the following classes: true positive (TP), true negative (TN), false positive (FP) or false negative (FN). These are the evaluation criteria to evaluate the performance of each algorithm. These terms are defined as follows.

TP: A recognised region that is correctly determined to be an object

FP: A recognised region that is incorrectly determined to be an object

TN: An unrecognised region that is correctly determined not to be an object

FN: An unrecognised region that is incorrectly determined not to be an object

The following evaluation measures have also been used to evaluate the performance of the proposed algorithm:

- 1) Pixel accuracy. It is defined as $(TP+TN) / (TP+TN+FP+FN) * 100 \%$. It measures the ratio of pixels/regions which are correctly identified to the total number of pixels/regions.
- 2) Specificity. It is defined as $TN / (TN + FP) * 100 \%$. This is the true negative rate. It measures the accuracy of a segmenting method in identifying all unmarked pixels/regions.
- 3) Sensitivity. It is defined as $TP / (TP+FN) * 100 \%$ and is also known as Recall. This is the true positive rate. It measures the accuracy of a segmenting method in identifying all marked pixels/regions.

RESULTS

The proposed algorithm was applied on 100 images of uterus with fluid-filled fibroids. The algorithm worked well on all images and gave good results. To evaluate the proposed segmentation algorithm, the same set of images were given to two radiologists who were asked to mark the fibroids. Figure 5(a) shows a sample output image produced by the implementation of the proposed algorithm. Figures 5(b,c) show the ground truths of the same sample image which were produced by expert 1 and expert 2 respectively. Tables 1-2 display results of performance evaluation of the proposed algorithm. The performance of the algorithm was measured using three evaluation criteria, viz. accuracy, sensitivity and specificity, by comparing the output of the proposed segmentation algorithm with the ground truths from expert 1 and expert 2 for 10 images. The performance of the algorithm was found to be very good as the average accuracy, sensitivity and specificity were above 95%.

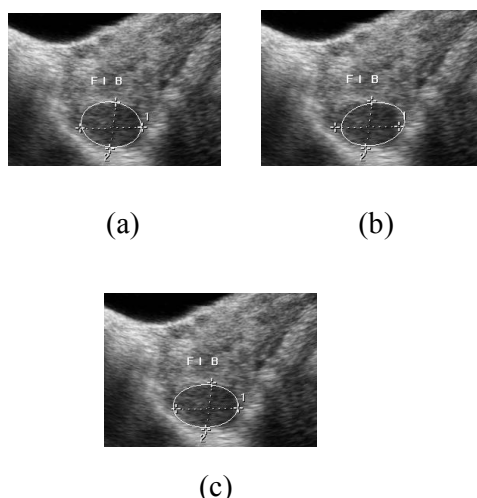


Figure 5. (a) Fibroid segmented by the algorithm; (b) Ground truth from expert 1; (c) Ground truth from expert 2

Table 1. Evaluation measures with respect to the ground truth from expert 1

Image	Accuracy (%)	Sensitivity (%)	Specificity (%)
Image1	98.02	94.16	98.16
Image2	95.55	95.40	95.56
Image3	95.76	100.00	95.64
Image4	97.89	87.55	98.09
Image5	91.75	91.98	91.73
Image6	98.89	92.42	99.12
Image7	95.87	97.14	95.81
Image8	96.86	99.07	96.74
Image9	97.73	91.85	97.97
Image10	97.06	98.05	97.01
Average	96.54	94.76	96.58

Table 2. Evaluation measures with respect to the ground truth from expert 2

Image	Accuracy (%)	Sensitivity (%)	Specificity (%)
Image1	97.83	96.86	97.86
Image2	95.55	95.40	95.56
Image3	96.27	99.65	96.15
Image4	97.86	99.49	97.83
Image5	96.42	92.19	97.05
Image6	99.00	93.08	99.22
Image7	97.42	92.53	97.76
Image8	96.86	99.07	96.74
Image9	97.73	91.85	97.97
Image10	96.92	96.88	96.93
Average	97.19	95.70	97.31

CONCLUSIONS

The subjective appearance of the output image was good. The performance of this algorithm was also very good. It was fully automatic and did not require human intervention. It was fast compared to such segmentation procedures as set methods. There was no need to give the seed point to start segmentation.

REFERENCES

1. L. Vincent, "Morphological grayscale reconstruction in image analysis applications and efficient algorithms", *IEEE Trans. Image Process.*, **1993**, 2, 176-201.

2. M. Karamam, M. Kutay and G. Bozdagi, "An adaptive speckle suppression filter for medical ultrasonic images", *IEEE Trans. Med. Imaging*, **1995**, 14, 283-292.
3. R. A. Peters II, "A new algorithm for image noise reduction using mathematical morphology", *IEEE Trans. Image Process.*, **1995**, 4, 554-568.
4. M. A. Schulze and Q. X. Wu, "Noise reduction in synthetic aperture radar imagery using a morphology-based nonlinear filter", Proceedings of Digital Image Computing: Techniques and Applications, **1995**, Brisbane, Australia, pp. 661-666.
5. P. Salembier and J. Serra, "Flat zones filtering, connected operators and filters by reconstruction", *IEEE Trans. Image Process.*, **1995**, 4, 1153-1160.
6. D. L. Pham, C. Xu and J. L. Prince, "A survey of current methods in medical image segmentation", *Annu. Rev. Biomed. Eng.*, **2000**, 2, 315-337.
7. J. A. Noble and D. Boukerroui, "Ultrasound image segmentation: A survey", *IEEE Trans. Med. Imaging*, **2006**, 25, 987-1010.
8. A. F. C. Infantosi, L. M. S. Luz, W. C. A. Periera and A. V. Alvarenga, "Breast ultrasound segmentation using morphological operators and a Gaussian function constraint", *IFMBE Proc.*, **2008**, 20, 520-523.
9. J. Shan, J. D. Cheng and Y. Wang, "A novel automatic seed point selection algorithm for breast ultrasound images", Proceedings of International Conference on Pattern Recognition, **2008**, Tampa, Finland, pp. 1-4.
10. A. Thakur and R. S. Anand, "A local statistics based region growing segmentation method for ultrasound medical images", *Int. J. Signal Process.*, **2005**, 1, 141-146.
11. M. Aleman-flores, P. Aleman-flores, L. Alvarez-leon, R. Fuentes-pavon and J. Santanamontesdeoca, "Filtering, segmentation and feature extraction in ultrasound evaluation of breast lesions", Proceedings of Image Processing for Medicine, **2008**, Berlin, Germany, pp.168-172.
12. W. Gomez, L. Leija, W. C. A. Pereria and A. F. C Infantosi, "Anisotropic diffusion filtering and average radial derivative to segment ultrasound like images", Proceedings of the XXI Brazilian Congress of Biomedical Engineering, **2008**, Salvador, Brazil, pp.1410-1413.
13. F. Meyer and S. Beucher, "Morphological segmentation", *J. Visual Commun. Image Represent.*, **1990**, 11, 21-46.
14. R. C. Gonzalez and R. E. Woods, "Digital Image Processing", 2nd Edn., Prentice Hall, Upper Saddle River, NJ, **2002**, pp. 617-624.
15. A. Bleau and L. J. Leon, "Watershed-based segmentation and region merging", *Comput. Vision Image Underst.*, **2000**, 77, 317-370.
16. I. Levner and H. Zhang, "Classification-driven watershed segmentation", *IEEE Trans. Image Process.*, **2007**, 16, 1437-1445.
17. L. Vincent, "Morphological area openings and closings for grayscale image", Proceedings of NATO Shape in Picture Workshop, **1992**, Driebergen, The Netherlands, pp. 197-208.
18. L. Vincent, "Grayscale area openings and closings, their efficient implementation and applications", Proceedings of EURASIP Workshop on Mathematical Morphology and its Applications to Signal Processing, **1993**, Barcelona, Spain, pp. 22-27.

19. H. T. Nguyen, M. Worring and R. van den Boomgaard, "Water snakes: Energy-driven watershed segmentation", *IEEE Trans. Pattern Anal.*, **2003**, 25, 330-342.
20. M. Wirth, D. Nikitenko and J. Lyon, "Segmentation of the breast region in mammograms using a rule-based fuzzy reasoning algorithm", *ICGST-GVIP J.*, **2005**, 5, 45-54.
21. E. A. Ince and S. A. Ali, "An adept segmentation algorithm and its application to the extraction of local regions containing fiducial points", *Lect. Notes Comput. Sci.*, **2006**, 4263, 553-562.
22. E. A. Ince and S. A. Ali, "Rule based segmentation and subject identification using fiducial features and subspace projection methods", *J. Comput.*, **2007**, 2, 68-75.
23. J. Yao, C. David, W. Lu and P. Ahalya, "Uterine fibroid segmentation and volume measurement on MRI", *Proceedings of SPIE on Medical Imaging 2006: Physiology, Function and Structure from Medical Images*, **2006**, 6413, 640-649.
24. J.-P. Guyon, M. Foskey, J. Kim, Z. Firat, B. Davis and S. Aylward, "Volume estimation and tracking over time: Framework and validation", *Lect. Notes Comput. Sci.*, **2003**, 2879, 142-149.
25. Y. J. Zhang, "A survey on evaluation methods for image segmentation", *Pattern Recognit.*, **1996**, 29, 1335-1346.

Full Paper

Effects of extender type, sperm volume, cryoprotectant concentration, cryopreservation and time duration on motility, survival and fertilisation rates of Mekong giant catfish sperm

Kriangsak Mengumphan*, Niwooti Whangchai and Doungporn Amornlerdpison

Faculty of Fisheries Technology and Aquatic Resources, Maejo University, Sansai, Chiang Mai, 50290, Thailand

* Corresponding author, e-mail: kriangsakm@mju.ac.th

Received: 22 March 2010 / Accepted: 7 October 2010 / Published: 14 October 2010

Abstract: The objectives of this study are to evaluate the effects of some basic factors, namely extender type, sperm volume, cryoprotectant concentration, cryopreservation and storage time, on the quality of Mekong giant catfish (MGC) sperm. The following results are obtained from conducted experiments. The sperm kept in Hanks balanced salt solution (HBSS) extender consistently produced good results in terms of motility. The highest motility grade (4.0) was observed after 12 hours of examination and still a very satisfactory grade (3.3) was observed after 48 hours. The percentage of live cells of the sperm kept in HBSS was also highest (45.3%). The optimal amount of cryoprotectant (DMSO) prior to cryopreservation was 8%, which gave the best motility grade (4.0) up to the first 72 hours of observation while at 120 hours the motility grade was 3.3. The fertilisation rate of MGC fresh sperm in HBSS (2 ml) and 1 gram eggs was 47.1% while that of cryopreserved sperm under the same conditions was 36.2%. When crossed with *P. hypophthalmus*, the fertilisation rates of a 2-week- and a 1-year-cryopreserved sperm sample were 36.2% and 30.9% respectively.

Keywords: *Pangasianodon gigas*, Mekong giant catfish, cryopreservation, cryoprotectant, sperm motility, fertilisation rate

INTRODUCTION

At present, the aquaculture industry has become a highly important sector, especially in Asia and the Mekong River region. Catfish of the families Pangasiidae and Clariidae are commercially produced throughout the region. Indigenous species include the Chao Praya catfish (*Pangasius saitwonsei*), Pla Poa (*Pangasius berguti*), Pla Swai (*Pangasius hypophthalmus*) and the Mekong giant

catfish (MGC; *Pangasinodon gigas*), which is considered to be the world's largest freshwater fish. The MGC is of considerable popularity in the Indochina region and its population has declined precipitously in recent years in the Mekong River (Figure 1). It is also listed as an endangered species in the Convention on International Trade in Endangered Species (CITES) [1].

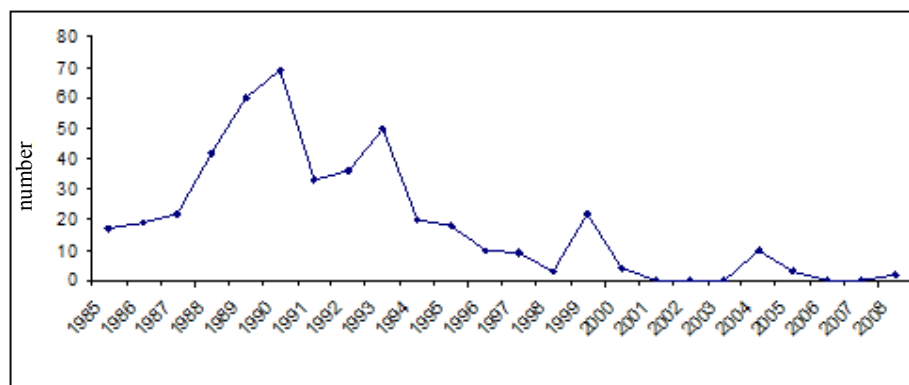


Figure 1. Annual catch of the Mekong giant catfish from the Mekong River [3].

The artificially bred MGC fingerlings have been produced from the brood stock in the Mekong River since 1983 and kept in earthen ponds in 2001-2002 by the Department of Fisheries, Maejo University. The MGC fingerlings have a fast growth in earthen ponds; they can grow to 25 kg in 3-4 years. As MGC is tasty and has a big market demand, current commercial aquaculture has been developed for both MGC and its hybrid (*P. gigas* x *P. hypophthalmus*). The demand of the MGC fingerlings is about 500,000 per year [2].

Cryopreservation is a valuable technique for artificial reproduction and genetic improvement of endangered species. The application of sperm cryopreservation to the MGC species (*P. gigas*) greatly contributes to its conservation and propagation, thereby avoiding its possible extinction in the Mekong River. The technique has also made possible the production of hybrids with striped catfish (*P. hypophthalmus*) in the event that the *P. gigas* females are not available, as well as the improvement of a hybrid of *P. hypophthalmus* [3]. This technique also makes it possible to formulate breeding programs to provide a constant supply of fingerlings for commercial purpose. However, the growth performance of the hybrid has not been better than that of the MGC [3].

The chemical composition of the extender media for cryopreserving spermatozoa varies greatly and simpler extenders contain only two or three substances with NaCl, KCl and CaCl₂ as the commonly used salts in fish spermatozoa cryopreservation studies [4]. With proper osmolality and an optimum percentage of cryoprotectant during the cryopreservation stage, a satisfactory level of post-thaw fertilisation can be achieved [5-6]. An optimum rate of decrease in temperature prior to storage at the freezing temperature has been established. With 9% DMSO mixed with the extender, the MGC sperm cryopreservation with a temperature decreasing rate of 12°C min⁻¹ has a fertilisation rate of 66% compared to 74.0% by control sample of undiluted sperm [3]. Since the availability of MGC sperm and eggs can be limited, the lowest volume possible of sperm is used to fertilise more oocytes with a satisfactory fertilisation rate. A prior study [7] achieved a fertilisation rate of 31% in common carp

(*Cyprinus carpio*) from 1-ml volume of extended cryopreserved sperm (sperm: extender = 1: 4) and one gram eggs while a yield of 83% was obtained from fresh sperm.

This study aims to find optimum conditions for pre-freezing cold storage of sperm, identify the type of extender giving the maximum duration of sperm storage, and study factors influencing the fertilisation rate of MGC cryopreserved sperm.

MATERIALS AND METHODS

Brood Stock Preparation

Prior to the collection of sperm, 2 sexually mature male specimens of MGC weighing approximately 25 kg were subjected to two weeks of conditioning and fed with individually formulated pellet feed fortified with 30% crude protein (at 5% of their body weight per day). The MGC sperm were first stripped to check for the presence of milt and then the fish were injected with a gonadotropin-releasing hormone analogue (Suprefact[®], Hoechst AG, Germany) and domperidone (Olic Limited., Thailand) at a dosage of 10 µg/kg and 5 mg/kg body weight respectively. After 8 hours after hormone injection, the MGC were stripped of milt. The collected milt was then kept at 15°C.

Effects of Extenders on Sperm Motility

The collected sperm samples kept at 15°C were treated with 4 different extenders, viz. 0.8% NaCl, Hanks balanced salt solution (HBSS), Hanks balanced salt solution-calcium free (HBSS-CF) and Kurokura. The sperm-to-extender ratio was 1:6 (v/v) and the volumes of extended sperm samples prepared were 0.5, 1.0, 2.0 and 4.0 ml. The chemical composition of each extender is shown in Table 1. The osmolality of each extender was determined using an osmometer (Osmomat 030, Gonotec, Germany).

The motility grades of all treatments were then obtained after 12, 24, 48 and 72 hours of storage by adding a drop of water to 0.1 ml of each sperm sample for motility activation and then estimating the motile sperm activity in a forward direction under the microscope at 40x magnification and interpreting the results following the grading guide for MGC sperm motility rate as shown in Table 2. A control was performed using fresh sperm.

Effects of Cryoprotective Agent

The effects of cryoprotectant (DMSO) on sperm were studied. Samples from the collected sperm were prepared and mixed with HBSS extender at a ratio of 1:6 v/v (sperm: extender). Different amounts of DMSO (5, 8 and 10 %) were then added and the mixture kept at 15°C. The motility grade was then examined after 12, 24, 48, 72, 96 and 120 hours.

Table 1. Composition of sperm extenders

	0.8%NaCl (mM)	HBSS (mM)	HBSS-CF (mM)	Kurokura (mM)
NaCl	136.89	136.89	136.89	61.60
KCl	-	5.37	5.37	-
CaCl ₂ H ₂ O	-	1.24	-	1.71
MgCl ₂	-	-	-	0.84
MgSO ₄ .7H ₂ O	-	0.81	0.81	-
Na ₂ HPO ₄ .7H ₂ O	-	0.45	0.45	-
KH ₂ PO ₄	-	0.44	0.44	-
NaHCO ₃	-	4.17	4.17	2.38
Glucose	-	5.55	5.55	-
Osmotic pressure (mosm/kg)	270	233	258	297

Table 2. Grading guide for examining motility rate of MGC sperm [2]

Motility grade	Motility (%)	Period movement after activation (sec)
0	0	0
1	1-25	10
2	25-50	20
3	50-75	30
4	75-100	40

Cryopreservation Method

Immediately after milking, the sperm sample was subjected to a low temperature (15°C) and was diluted with the prepared extenders (0.8%NaCl, HBSS, HBSS-CF and Kurokura). Samples of the extended sperm were then placed in cryovials at different volumes (0.5, 1.0, 2.0 and 4.0 ml). All samples were placed in a cryochamber and plunged into the cryobath with liquid nitrogen at 10-cm depth. A computer program (Cryogenesis V5, Australia) was then run to attain a constant cooling rate of 10°C per minute until the target temperature of -80°C was achieved. The samples were then kept in a liquid nitrogen tank.

Live Sperm Cells Determination

The two-week-cryopreserved sperm samples in the four extenders were thawed in warm water (40°C) for one minute and stained with eosin-negrosin dye (Merck) for a determination of the percentage of both living and dead sperm. A small drop each of an extended sperm sample and eosin-negrosin dye solution (0.2 g eosin, 1 g nigrosin, 0.3 g sodium citrate dehydrate and 20 ml distilled water) were placed on the slide, mixed together and distributed evenly. The stain was dried and the

numbers of dead and living sperm were examined under the microscope (100x). The live sperm that did not absorb the dye appeared somewhat clear while the dead sperm absorbed the dye and appeared pink or purple in colour. Forty sperm cells, living and dead, from five different points were separately counted.

Fertilisation Test

Fertilisation experiments were performed to compare the fertilisation rate of frozen sperm and fresh sperm. In the first experiment, artificial fertilisation was performed by placing 1 or 2 ml of HBSS-extended fresh MGC sperm (sperm-to-extender ratio = 1:6 v/v) and eggs (1 gram) in a Petri dish and mixing for 2 minutes using a rooster's tail feather and 50 ml of distilled water was then added. The mixture was placed in a small fine net enclosure (6"x6"x6"). Aeration was provided in a nursery concrete pond. After approximately 24 hours, the fertilisation rate was determined by observing the fertilised eggs (somite stage) under a dissecting microscope.

In the second experiment, the above procedure was repeated with one-year-cryopreserved MGC sperm in place of fresh sperm. In addition, 2 ml of the HBSS-extended cryopreserved MGC sperm were used to fertilise one gram of *P. hypophthalmus* eggs. A control was performed using fresh sperm.

In the third experiment, different volumes (0.5, 1.0, 2.0 and 4.0 ml) of two-week-cryopreserved MGC sperm samples in different extenders (0.8%NaCl, HBSS, HBSS-CF and Kurokura) with the same sperm-to-extender ratio as above were used to fertilise one gram of *P. hypophthalmus* eggs. A control was performed using fresh sperm.

Statistical Analysis

Every experiment was performed in triplicate. Data of living sperm cells (%) and fertilisation rate (%) were normalised by arcsine transformation. One-way analysis of variance (ANOVA) was used to analyse significant differences between treatments ($p < 0.05$). Duncan's multiple range test was used to compare the means of significant difference of each treatment using SPSS software.

RESULTS AND DISCUSSION

Motility of MGC Sperm in Different Extenders

In evaluating the potential of some extenders for use in MGC sperm cold storage, it was observed that the highest motility grade (4.0) was found at all volumes of HBSS that were examined after 12 hours of refrigeration, and a satisfactory motility grade (3.3) was observed up to 48 hours of refrigeration (Figure 2). This was followed by that obtained with HBSS-CF (3.3-4.0) and Kurokura (3.0-4.0) in that order, where satisfactory motility grades were observed up to 24 hours of refrigeration. The motility grade results in 0.8%NaCl and undiluted sperm were the least satisfactory (3.0-4.0 and 2.7-4.0 respectively for the first 24 hours). From the results in Figure 2(c-d), sperm with extenders have more satisfactory motility grades than fresh sperm within 48 hours. Sperm with motility grade of 0.5-1 cannot be used for artificial fertilisation. Thus, the storage time for fresh sperm and sperm with extenders in the refrigerator (15°C) seems to be a maximum of 48 hours.

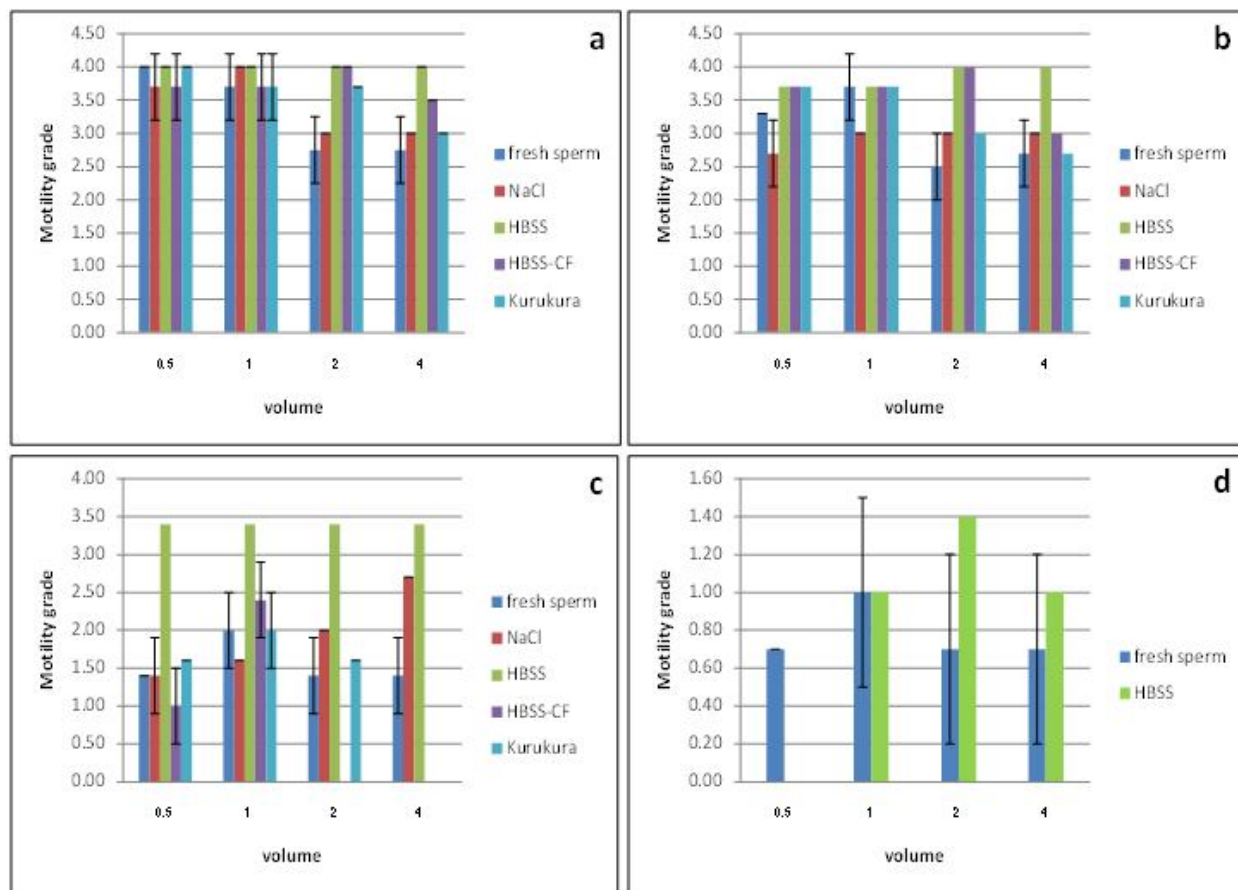


Figure 2. Motility grades of MGC fresh and frozen sperm kept at 15°C after 12 hrs (a), 24 hrs (b), 48 hrs (c) and 72 hrs (d) in different extenders

Previous studies have established the need for appropriate diluents for cool storage of sperm [5, 8]. Moreover, storage of sperm in diluents with optimal constituents prolongs their lives compared to undiluted sperm. Morisawa and Suzuki [9] determined the factors whereby the motility of teleost spermatozoa is initiated, i.e. the decrease or increase in osmolality of the environment. The composition of the diluent as well as its osmolality also has a significant influence on the success of storage. Mongkonpanya et al. [3] concluded that a suitable extender should have an osmolality level near the range of that of fresh sperm. The finding seems to agree with the data in this study, i.e. the HBSS osmolality value of 233 mOsmo/kg was almost the same as that of the fresh sperm (206 mOsmo/kg), but quite different from those of NaCl and Kurukura (270 and 297 mOsmo/kg respectively).

Since HBSS extender at all volumes (0.5, 1, 2 and 4 ml) gave the best result from the first part of the study (Figure 3), it was used to check the motility grade of MGC sperm in different levels of DMSO (a cryoprotectant usually used in sperm cryopreservation).

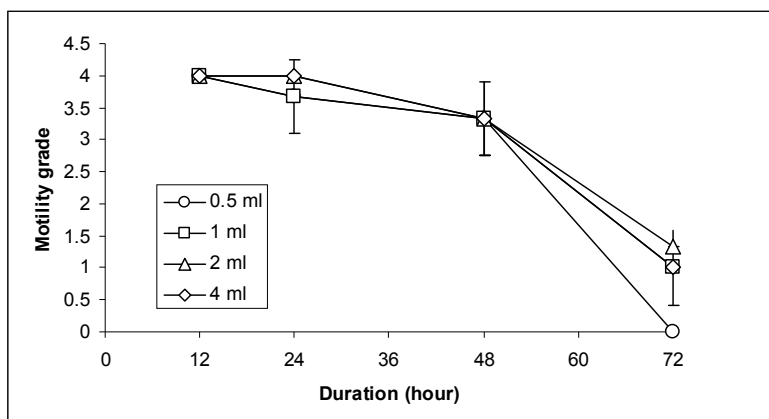


Figure 3. Sperm motility at different duration and volumes in HBSS

Effects of DMSO on Post-thaw Sperm Motility

After 12 hours of refrigeration, the sperm motility grade was 4.0 in all levels of DMSO. Mongkonpunya et al. [6] observed similar patterns when they added DMSO (5 and 9%) to a diluent (bicarbonate buffer) to diluted MGC sperm. They concluded that the use of DMSO at higher percentages than 10% could be toxic to the MGC sperm but that DMSO at 5% was not as effective as 9%. In this study, the sperm extended with 8% DMSO exhibits the highest motility grade of 4 for up to 72 hours of refrigeration. It then declines to 3.7 and 3.3 at 96 and 120 hours respectively (Figure 4). This finding agrees with a study on the cryopreservation of sperm of red snapper, which indicated that the DMSO cryoprotectant of 10% yields the highest post-thaw motility [11].

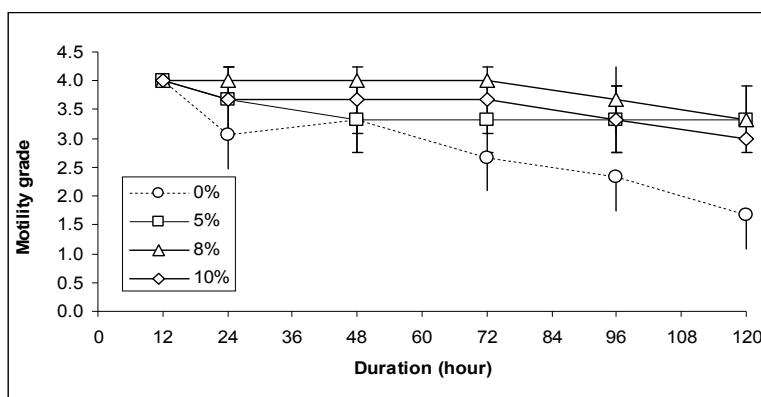


Figure 4. Motility grade of MGC sperm kept at 15°C in HBSS with different percentages of DMSO

Survival of Sperm Cells

The highest percentage of live sperm was observed in HBSS-extended sperm (45.3%), which is statistically comparable with those in Kurokura (29.3%) and HBSS-CF (28.9%), but significantly different ($p < 0.05$) from that in 0.8%NaCl-extended sperm (22.4%) (Table 3).

Table 3. Percentage of live cells in cryopreserved MGC sperm in different extenders

Extender	Viability (%)
0.8%NaCl	22.4±4.8 ^a
HBSS	45.3±6.0 ^b
HBSS-CF	28.9±4.7 ^{ab}
Kurokura	29.3±4.3 ^{ab}

Note: Data are expressed as mean±S.E. (from 3 replicates).

Means that do not share the same superscript are statistically significant ($p<0.05$).

Fertilisation Efficiency of MGC Sperm

The results of fertilisation rate of MGC sperm in HBSS extender are shown in Table 4. This result suggests that the higher the sperm volume of MGC is, the greater the fertilisation yield is achievable. From Table 4, an extended sperm volume of at least 2 ml is needed to achieve a satisfactory fertilisation. The decrease in sperm quality and consequent reduction in fertilisability of cryopreserved sperm was also observed in *Cyprinus carpio* [12] and *Misgurnus anguillicaudatus* [13]. However, Ding et al. [14] showed that the fertilisation rate and hatching rate of Mandarin fish (*Siniperca chuatsi*) by sperm cryopreserved for 1 week or even 1 year in liquid nitrogen were similar to those obtained when fresh sperm was used. Thus, this cryopreservation technique should be further improved to get a better fertilisation rate for MGC sperm.

Table 4. Fertilisation rate of MGC sperm in HBSS with 1 g MGC eggs

MGC sperm	Volume (ml)	
	1	2
Fresh sperm (control)	30.3±8.9 ^{Ba}	47.1±5.1 ^{Bb}
One-year-cryopreserved sperm	16.8±0.3 ^{Aa}	36.2±9.9 ^{Ab}

Note: Data are expressed as mean±S.E. (from 3 replicates).

Means that do not share the same superscript in the same column (capital letters) and row (small letters) are statistically significant ($p<0.05$).

For hybrid artificial breeding in different extenders, the best fertilisation rate (89.7%) of MGC sperm with *P. hypophthalmus* eggs was observed with 2 ml of the control (fresh sperm) in HBSS. This was followed by the 2-week-cryopreserved sperm in HBSS at 2 ml (36.2%), while at 0.5 ml volume no fertilisation was observed (Figure 5). An unsatisfactory rate was obtained at 1.0 ml while at 2-ml volume, fertilisation rate was highest among all treatments including fresh sperm. In a similar study involving interspecific fertilisation, a fertilisation rate of 26-45% from MGC sperm and *P. hypophthalmus* oocytes was obtained [3].

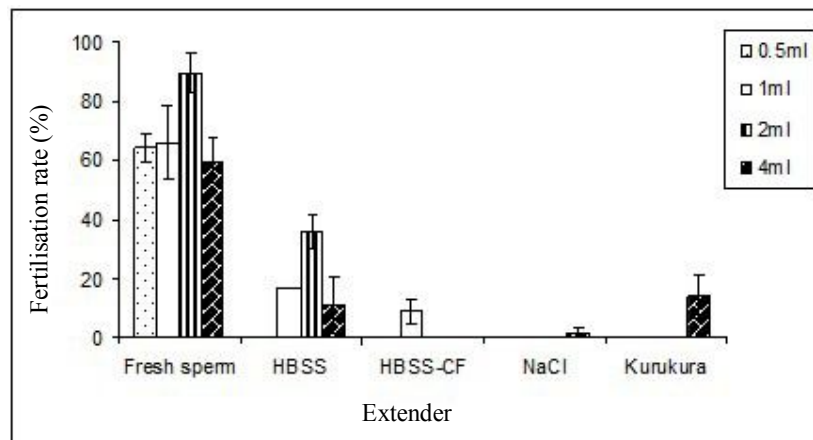


Figure 5. Fertilisation rate of fresh and cryopreserved MGC sperm in different extenders of different volumes with *P. hypophthalmus* eggs

The fertilisation rate of 30.9% by one-year-old cryopreserved MGC sperm and fresh *P. hypophthalmus* eggs proved to be satisfactory (Table 5). This finding confirms all previous experiments involving the suitability of HBSS extender for MGC sperm cryopreservation. Theoretically, extended sperm can be kept for many years and according to the findings of this study, cryopreserving for a period of one year can be considered suitable for achieving a reasonable rate of fertilisation. The availability of cryopreserved MGC sperm can now be increased since the viability of preserved sperm can be maintained for a considerably long period. More consideration should be given to the mass application of the cryopreservation process for endangered species. However, cryopreservation technique still needs to be improved in a further study to increase the fertilisation rate. Moreover, the proper ratio of cryopreserved sperms and eggs will also be evaluated in the further study.

Table 5. Fertilisation rate of 1-year-cryopreserved MGC sperm in HBSS and *P. hypophthalmus* eggs

Sperm	Fertilisation rate (%)
Fresh sperm (control)	76.6 ± 3.5^b
Cryopreserved sperm	30.9 ± 4.1^a

Note: Data expressed as mean±S.E. (from 3 replicates)

Means which do not share the same letter superscript are statistically significant ($p < 0.05$).

CONCLUSIONS

The motility, survival and fertilisation rates of Mekong giant catfish sperm were found to depend on a number of factors, i.e. type of extender, sperm volume, cryoprotectant concentration, cryopreservation and storage time. HBSS appeared to be the best extender for the fish sperm which, when present in 1:6 (sperm:extender) ratio, gave the highest motility grades (3.3-4.0) and the highest fertilisation rates at 2-ml volume. The percentage of live cells of the sperm kept in HBSS was also

highest (45.3%). A cryoprotectant (DMSO) concentration of 8% of the extended sperm was found to be optimum. The highest fertilisation rate of MGC fresh sperm and MGC eggs was 47.1% while that of one-year-cryopreserved sperm under the same conditions was 36.2%. Sperm cryopreserved for 2 weeks and 1 year gave a satisfactory fertilisation rates of 36.2 and 30.9% respectively with *P. hypophthalmus* eggs.

ACKNOWLEDGEMENTS

The authors would like to thank the Royal Thai Government for providing the needed funding. The Faculty of Fisheries Technology and Aquatic Resources of Maejo University and the Pla Buk Research Integration Project (PRIP) are thanked for allowing the use of facilities and staff. We also thank Assoc. Prof. Dr. Amarit N. Bart and Assoc. Prof. Dr. Eric Danell of Uppsala University for coordination and correction of the manuscript.

REFERENCES

1. K. Mongkonpunya, T. Pupipat and T. R. Tiersch, "Cryopreservation of sperm of Asian catfish including the endangered Mekong giant catfish", Proceedings of Conference on Cryopreservation in Aquatic Species, **2000**, Baton Rouge, Louisiana, pp.108-116.
2. K. Mengumphan, J. Promya, A. Manosoi and J. Manosoi, "The study of Mekong giant catfish *Pangasinodon gigas* (Chevy) brood stock production for conservation and commercial aquaculture", Final Report, Thailand Research Fund, **2003**, p.154.
3. K. Mongkonpunya, T. Pupipat, S. Pholprasith, M. Chantrasut, R. Rittaporn, S. Pimolboot, S. Wiwatcharakoses and M. Chaengki, "Sperm cryopreservation of Mekong giant catfish *Pangasinodon gigas* (Chevy)", Proceedings of a Network Meeting on Aquaculture, National Academy Press, **1992**, Washington D.C., USA, pp.56-60.
4. B. J. McAndrew, K. J. Rana and D. J. Penman, "Conservation and preservation of genetic variation in aquatic organisms", in "Recent Advances in Aquaculture" (Ed. J. F. Muir and R. J. Roberts), Vol. IV, Blackwell Scientific Publications, Oxford, **1993**, pp.295-336.
5. H. Ohta and T. Izawa, "Diluent for cool storage of the Japanese eel (*Anguila japonica*) spermatozoa", *Aquaculture*, **1996**, *142*, 107-118.
6. K. Mongkonpunya, T. Pupipat, S. Pholprasith, M. Chantrasut, R. Rittaporn, S. Pimolboot, S. Wiwatcharakoses and M. Chaengki, "Cryopreservation of Mekong giant catfish sperm", *Asian Fish. Sci.*, **1995**, *8*, 211-221.
7. H. Kurokura, R. Hirono and M. Tomita, "Cryopreservation of carp sperm", *Aquaculture*, **1984**, *37*, 267-273.
8. J. Stoss, "Fish gamete preservation and spermatozoan physiology", in "Fish Physiology" Volume IX, Part B: Behavior and Fertility Control (Ed. W. S. Hoar, D. J. Randall and E. M. Donaldson), Academic Press, New York, **1984**, pp.305-350.
9. M. Morisawa and K. Suzuki, "Osmolality and potassium ion: Their roles in initiation of sperm motility in teleosts", *Science*, **1980**, *210*, 1145-1147.

10. R. Billard and M. P. Cosson, "Measurement of sperm motility in trout and carp", in "Aquaculture: A Biotechnology in Progress" (Ed. N. de Pauw, E. Jaspers, H. Ackefors and N. Wilkins), European Aquaculture Society, Bredene (Belgium), **1989**, pp.449-503.
11. K. Riley, C. Holladay, E. Chesney and T. Tiersch, "Cryopreservation of sperm of red snapper (*Lutjanus campechanus*)", *Aquaculture*, **2004**, 238, 183-194.
12. D. Warnecke and J. Pluta, "Motility and fertilizing capacity of frozen/thawed common carp (*Cyprinus carpio* L.) sperm using dimethyl-acetamide as the main cryoprotectant", *Aquaculture*, **2003**, 215, 167-185.
13. G. Yasui, L. Arias-Rodriguez, T. Fujimoto and K. Arai, "A sperm cryopreservation protocol for the loach *Misgurnus anguillicaudatus* and its applicability for other related species", *Anim. Reprod. Sci.*, **2009**, 116, 335-345.
14. S. Ding, J. Ge, C. Hao, M. Zhang, W. Yan, Z. Xu, J. Pan, S. Chen, Y. Tian and Y. Huang, "Long-term cryopreservation of sperm from Mandarin fish *Siniperca chuatsi*", *Anim. Reprod. Sci.*, **2009**, 113, 229-235.

Communication

A random number generator based on NTRU cryptosystem

He Debiao*, Chen Jianhua and Hu Jin

School of Mathematics and Statistics, Wuhan University, Wuhan, China

* Corresponding author, e-mail: hedebiao@163.com

Received: 23 February 2010 / Accepted: 11 October 2010 / Published: 16 October 2010

Abstract: A random number generator based on the operation of the NTRU cryptosystem is proposed. By using the proposed generator together with the NTRU cryptosystem, we can save hardware and software components. Theoretical analyses show that periods of the proposed random number generator are sufficiently long. Moreover, the generated sequences have passed the U.S. NIST statistical test.

Keywords: random number generator, public-key cryptosystem, NTRU cryptosystem, polynomial ring

INTRODUCTION

The NTRU (Number Theory Research Unit) cryptosystem [1-3], patented by the company NTRU, is one of the fastest public-key encryption schemes known. Although this may not be a decisive advantage compared to the hybrid encryption with RSA for example, NTRU has attracted considerable interest and is being considered by the efficient embedded security standards [4] and the IEEE P1363 study group for future public-key cryptography standards [5].

On the other hand, the security of most cryptographic systems depends upon the generation of unpredictable quantities that must be of sufficient size and randomness. Taking NTRU cryptosystem as example, we need to generate random bits in order to create random polynomial. This implies that we usually need to implement a random number generator in a cryptographic system. A number of random number generators have been proposed [6-11]. However, they are usually not designed together with the cryptographic system and so extra design and implementation effort are required. If both the tasks of random number generation and encryption can be done by using the same software or hardware module, we can save hardware cost, memory space and design time. This is especially important in developing applications in an environment with limited resources such as smart cards.

With this goal, we propose a random number generator that makes use of the basic operations required in NTRU.

The organisation of the rest of the paper is as follows. The background of NTRU cryptosystem is first introduced. The proposed random number generator is then described. Periods of the proposed generator are subsequently analysed and the test results reported.

NTRU PUBLIC KEY CRYPTOSYSTEM

NTRU cryptosystem is a polynomial ring-based public-key cryptosystem that was fully introduced in 1998 [1]. The scheme is set up by three integers, viz. N , p , q , such that:

- N is prime;
- p and q are relatively prime, $\gcd(p, q)=1$;
- q is much larger than p .

NTRU cryptosystem is based on polynomial additions and multiplications in the ring $R = Z[x]/(x^N - 1)$. We use $*$ to denote a polynomial multiplication in R , which is the cyclic convolution of two polynomials. After completion of a polynomial multiplication or addition, the coefficients of the resulting polynomial need to be reduced either modulo q or p . As a side note, the key creation process also requires two polynomial inversions, which can be computed using the extended Euclidean algorithm. NTRU cryptosystem requires approximately $o(N^2)$ operations and a key length of $o(N)$.

More information on NTRU cryptosystem has been described [1-3]. We briefly outline the procedures below.

Key Generation. To generate the public key, the user must:

- Choose a secret key, a random polynomial $f \in R$, where coefficients are in $(-\frac{p}{2}, \frac{p}{2})$;
- Choose a random polynomial, $g \in R$, where coefficients are in $(-\frac{p}{2}, \frac{p}{2})$;
- Compute the inverse polynomial F_q of the secret key f modulo q .

Once the above has been completed, the public key, h , is found as

$$h = F_q * g \pmod{q} \quad (1)$$

Encryption. The encrypted message is computed as

$$e = pr * h + m \pmod{q} \quad (2)$$

where the message, $m \in R$, and the random polynomial, $r \in R$, have coefficients reduced modulo p .

Decryption. The decryption procedure requires three steps:

- $a = f * e \pmod{q}$;
- Shift coefficients of a to the range $(-\frac{q}{2}, \frac{q}{2})$;
- $d = F_p * a \pmod{p}$.

The last step of decryption requires the user to compute the inverse polynomial F_p of the secret key f modulo p . The decryption process outlined above will recover the original message.

THE PROPOSED RANDOM NUMBER GENERATOR

In this paper we use the encryption progress of NTRU cryptosystem to generate the random sequence, the parameters being as follows:

- N is prime;
- q is prime and is large enough;
- h is an element of the ring $R = Z[x]/(x^N - 1)$ and is randomly selected.

Let f be an element of the ring $R = Z[x]/(x^N - 1)$, then f can be represented as

$$f = \sum_{i=0}^{N-1} f_i x^i, f_i \in Z, i = 0, 1, \dots, N-1. \quad (3)$$

The representation is denoted by $f = [f_0, f_1, \dots, f_{N-1}]$.

A block diagram of the proposed random number generator is shown in Figure 1, where \oplus denotes the operation of XOR. It is easy to see that when these operations are done recursively, a sequence of bits can be obtained by collecting the x_n .

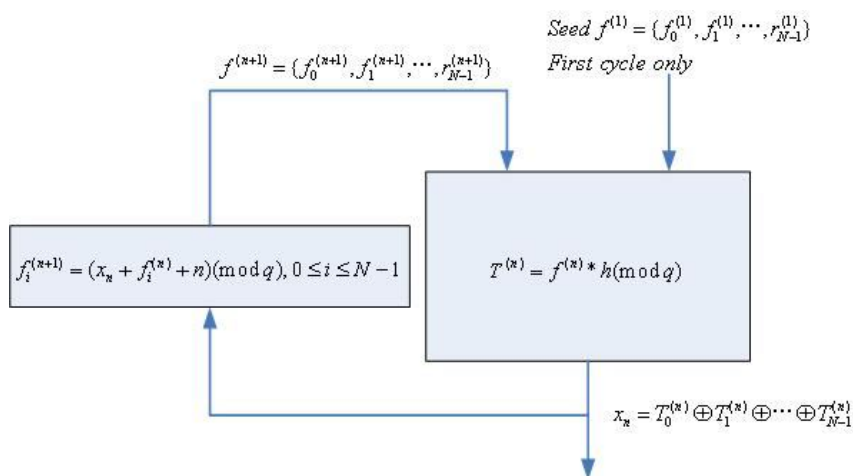


Figure 1. Block diagram of the proposed random number generator

PERIOD ANALYSIS

The purpose of setting $f_i^{(n+1)} = (x_n + f_i^{(n)} + n)(\text{mod } q), 0 \leq i \leq N-1$ is to increase the period of the generator. If n is not added, the bit sequence depends solely on the output of the $T^{(n)} = f^{(n)} * h(\text{mod } q)$ operation and the period may be very small.

In the s^{th} cycle,

$$f_i^{(s+1)} = (x_s + f_i^{(s)} + s)(\text{mod } q), 0 \leq i \leq N-1 \quad (4)$$

where x_s denotes the output of the proposed random number generator, shown in Figure 1.

In the t^{th} cycle,

$$f_i^{(t+1)} = (x_t + f_i^{(t)} + t)(\text{mod } q), 0 \leq i \leq N-1 \quad (5)$$

where x_t denotes the output of the proposed random number generator, shown in Figure 1.

Suppose that the output of the proposed random number generator in the t^{th} cycle is the same as that in the s^{th} cycle, i.e.

$$x_t = x_s \quad (6)$$

If the output of the module of the $(t+1)^{th}$ cycle is also equal to that of the $(s+1)^{th}$ cycle, then

$$f_i^{(t+1)} \equiv f_i^{(s+1)} \pmod{q}, f_i^{(t)} \equiv f_i^{(s)} \pmod{q}, 0 \leq i \leq N-1. \quad (7)$$

By equations (4), (5) and (7), we have

$$x_t + t = x_s + s \quad (8)$$

By equations (6) and (8), we can get that

$$s \equiv t \pmod{q} \quad (9)$$

Since $t > s$, we have $t = s + m q$, where m is a nonzero positive integer. Hence, the output pattern will repeat only after q cycles.

TEST RESULTS

The U.S. NIST statistical test suite [12] is used to test the randomness of the generated bits. It includes 15 statistical tests and each of them is formulated to test a null hypothesis that the sequence being tested is random. There is also an alternative hypothesis which states that the sequence is not random. For each test, there is an associated reference distribution (typically normal distribution or χ^2 distribution), based on which a P_value is computed from the binary sequence. If this value is greater than a pre-defined threshold α (0.01 in default), the sequence passes the test. The two approaches that NIST has adopted are the examination of: (1) proportion of sequences that pass a statistical test, and (2) uniformity of the distribution of those P_values .

According to NIST [12], if m sequences were tested, the proportion of sequences that passed a specific statistical test should lie above p_α :

$$p_\alpha = (1 - \alpha) - 3\sqrt{\frac{\alpha(1 - \alpha)}{m}} \quad (10)$$

In our experiment, $m = 1000$, $\alpha = 0.01$ and $p_\alpha = 98.05\%$.

To check the distribution of P_values , the interval between 0 and 1 is divided into 10 sub-intervals. The number of P_values in each sub-interval is counted, based on which a $P_valuesT$ is calculated. If $P_valuesT > 0.0001$ holds, the sequences are considered to be uniformly distributed.

The NIST statistical test suite contains 15 tests (the Lempel-Ziv complexity test having been removed from the test suite since Version 1.7) [12]. Some tests such as FT, FBT, RT, ST, AET and CST require only 100 bits for each sequence. Other tests, however, require more bits. Specially, the PTMT, LZCT, RET and REVT tests need about $1M$ for each sequence.

In our experiment, a 100-bit sequence is generated for each two parameters (N, q) by using 100 pairs of the randomly-selected initial $h, f^{(1)}$. Because the expression of the element of the ring $R = Z[x]/(x^N - 1)$ is very complicated, we just list one case here for reference. The parameters are

- $N=107$
- $q=0xCC137071797457130CFCF2CC51406B442E15EEA463F80F3C085C3ECC381BF01B$
- $h = x^{106} + x^{105} + \dots + x + 1$
- $f^{(1)} = x^{106} - 1$

In the test of P_values uniformity for FT and CST, each sequence is set to 1024 bits by concatenating the output of the proposed random generator. Otherwise, the number of different P_values will not be sufficient to carry out the uniformity test. As for other tests which require more

than 100 bits for each sequence, we collect the first 256 bits for different initial $h, f^{(1)}$. The test results can be found in Table 1.

It can be observed from Table 1 that the proposed random number generator passes all the statistical tests, i.e. the passing proportions are greater than 98.05% and P_valueT greater than 0.0001. According to NIST [12], we can conclude that the data generated by these two approaches are random.

Table 1. Test results for the random number generator

Test name	Proportion	P_valueT
FT	0.9901	0.1624
FBT	0.9852	0.3781
CST*	0.9863	0.1639
RT	0.9942	0.1498
LROBT	0.9875	0.1397
AET	0.9846	0.4153
ST*	0.9811	0.5741
RBMRT	0.9973	0.1542
DFTT	0.9918	0.3681
ATMT*	0.9857	0.2456
PTMT	0.9961	0.1572
MUST	0.9921	0.3660
RET*	0.9836	0.2718
REVT*	0.9918	0.2249
LCT	0.9826	0.1152

DISCUSSION

Choice of Parameters

By simply changing the seed f and the initial polynomial h , a different bit sequence can be generated. These two parameters should be kept secret for security. Basically, h can be any polynomial in the finite field F_q .

The NTRU system just requires that p and q be relatively prime. However, if q in our system is not prime, the period of the output of the generator may be a divisor of q . Then our system requires that q is prime. In general, the random number generator is secure if its period is about 2^{256} .

Implementation

Various types of implementation of NTRU cryptosystem have been proposed [13-16] and our proposed random number generator is based on the core operations of NTRU cryptosystem, so the proposed random generator can be designed and implemented efficiently using the existing components, and thus the cost of the implementation can be reduced.

The equation of our random number generator looks different from that of the NTRU cryptosystem. Actually, we just replace the polynomial $p * h$ with another polynomial h' . In the process of generating random numbers using existing components, we just let p be one.

CONCLUSIONS

In this paper, a new approach for constructing a random number generator using the operation of NTRU cryptosystem is presented. Periods of the generator are analysed theoretically. The test results indicate that all the random number sequences pass the U.S. NIST statistical test. Therefore, the proposed generator can be accepted as a reliable random number generator for integrating with the NTRU system to generate the dynamic private keys.

ACKNOWLEDGEMENTS

The authors thank the anonymous reviewers and Dr. Duang Buddhasukh for their valuable comments. This research was supported by the Fundamental Research Funds for the Central Universities under Grants 201275786.

REFERENCES

1. J. Hoffstein, J. Pipher and J. H. Silverman. "NTRU: a ring based public key cryptosystem", Proceedings of Algorithmic Number Theory: Third International Symposium, **1998**, Portland, USA, pp. 267-288.
2. J. Hoffstein and J. H. Silverman, "Optimizations for NTRU", http://www.sisecure.com/cryptolab/pdf/TECH_ARTICLE_OPT.pdf. (Accessed: 1 December **2009**)
3. C. O'Rourke and B. Sunar, "Achieving NTRU with Montgomery multiplication", *IEEE Trans. Comput.*, **2003**, 52, 440-448.
4. EESS: Consortium for Efficient Embedded Security, "Efficient embedded security standards #1: Implementation aspects of NTRU and NSS", Draft Version 3.0, available from <http://www.cesstandards.org>, July **2001**.
5. IEEE Standard 1363, "Standard specifications for public key cryptography", available from <http://grouper.ieee.org/groups/1363>, August **2000**.
6. D. Knuth, "The Art of Computer Programming, Vol. II: Seminumerical Algorithms", 3rd Edn., Addison-Wesley, New York, **1998**, pp. 95-100.
7. M. Blum and S. Micali, "How to generate cryptographically strong sequences of pseudo-random bits", *SIAM J. Comput.*, **1984**, 13, 850-863.
8. O. Goldreich, S. Goldwasser and S. Micali, "How to construct random functions", *J. Assoc. Comput. Mach.*, **1986**, 33, 792-807.
9. J. A. Gonzalez and R. Pino, "A random number generator based on unpredictable chaotic functions", *Comput. Phys. Commun.* **1999**, 120, 109-144.
10. M. Orlov, "Optimized random number generation in an interval", *Inf. Process. Lett.*, **2009**, 109, 722-725.

11. H. Shi, S. Jiang and Z. Qin, "More efficient DDH pseudorandom generators", *Designs Codes Cryptogr.*, **2010**, 55, 45–64.
12. National Institute of Standards and Technology (NIST), "A statistical test suite for random and pseudo-random number generators for cryptographic applications", <http://csrc.nist.gov/rng/rng2.html>, 2001. (Accessed: 1 November 2009).
13. C. O'Rourke and B. Sunar, "Achieving NTRU with Montgomery multiplication", *IEEE Trans. Comput.*, **2003**, 52, 440-448.
14. J. H. Silverman, "Commutative NTRU: Pseudo-code implementation", <http://citeseerx.ist.psu.edu/viewdoc/summary?doi=10.1.1.44.3682> (Accessed: 1 November 2009).
15. D. V. Bailey, "Daniel coffin, NTRU in constrained services", <http://citeseerx.ist.psu.edu/viewdoc/summary?doi=10.1.1.11.9174> (Accessed: 1 November 2009).
16. M.-K. Lee, J. W. Kim, J. E. Song and K. Park, "Sliding window method for NTRU", Proceedings of the 5th International Conference on Applied Cryptography and Network Security, **2007**, Zhuhai, China, pp. 432-442.

Communication

Feature extraction of near-spherical fruit with partial occlusion for robotic harvesting

Lü Qiang^{1,2}, Lu Huazhu¹, Cai Jianrong^{1,*}, Zhao Jiewen¹, Li YongPing³ and Zhou Fang¹

¹ School of Food and Biological Engineering, Jiangsu University, Zhenjiang, Jiangsu, 212013, China

² School of Information Science and Engineering, Henan University of Technology, Zhengzhou, 450001, China

³ School of Art Education, Jiangsu University, Zhenjiang, 212013, China

* Correspondence author, e-mail: lvqiang1111@gmail.com

Received: 2 December 2009 / Accepted: 12 October 2010 / Published: 20 October 2010

Abstract: For a fruit-picking robot in natural scenes, feature extraction of fruits occluded by leaves and branches based on machine vision is a key problem. In this study, the cluster barycentre (CB), edge barycentre (EB), circular Hough transform (CHT) and least square circle fitting (LSCF) are used to extract the features of fruit. The results indicate that the first two methods cannot accurately determine the circle in the presence of partial occlusion. The objects extracted by the CHT method include false targets in addition to longer time and larger memory required. The LSCF method, on the other hand, can accurately extract the features in a real-time mode. When the occluded area ratio is less than 52%, or the occlusion angle is less than 216°, the accuracy of feature extraction using LSCF can meet the requirements of the robot operation.

Keywords: near-spherical fruits, machine vision, least square circle fitting (LSCF), feature extraction, robotic harvesting

INTRODUCTION

Owing to labour shortage and high labour cost, the cost of manual harvesting accounts for over 40% of the total cost in citrus production [1]. Mechanical mass harvesting is unsuitable for fresh agricultural products for it usually damages the fruits and trees. Robotic selective harvesting is an effective way to cope with labour shortage and rise of production cost, and to meet the need of harvesting fresh agricultural products.

The use of robots to pick tree fruits was proposed by Schertz and Brown in a review of citrus mechanical harvesting system in 1968 [2]. In the past forty years, studies on robotic harvesting of oranges [3-5], apples [6-7], strawberry [8-9], tomatoes [10-12] and other fruits were reported. The increasing computational power and the availability of advanced sensors and robotic technology have facilitated the development of robotic harvesting technology. However, robotic harvesting is not yet commercially available. The challenges for robotic selective harvesting as suggested by Sarig [13] are the vision system for fruit recognition and location, the end-effector for fruit removal and the coordination of these two components.

Fruit recognition and location are the priority of harvesting robot. Machine vision, thermal imaging and laser ranging techniques were used to realise these operations by some researchers [14-15]. Considering the working efficiency, machine vision has become preferred. In general, the machine vision system of a harvesting robot is composed of a binocular camera which acquires images in the scene and a computer programmed to recognise and locate the desired objects through image segmentation, feature extraction, stereo match, and three-dimensional measurement techniques.

A fruit can be segmented from the background in the scene where significant colour contrast exists between the fruit (such as apples, oranges and tomatoes) and the canopy. However, the existence of overlapping of objects and the occlusion by branches and leaves in the unstructured natural scenes make it difficult to segment complete fruit region. All of these result in the deviation in feature extraction and spatial location. An appropriate method which can accurately extract features from incomplete target images has become one of the key research targets of harvesting robot. For positioning of near-spherical fruit, spatial features such as the centre coordinate and radius must be extracted. In a 2D image, the fitting circle of fruit contour can be used to present the object, where the centre and radius of the circle are the features.

The simplest solution to circle fitting is to compute the barycentre of the cluster of object region pixels (cluster barycentre method, CB) [16-18]. In this simple approach, the radius of the circle can be estimated as the maximum distance of the pixels from the barycentre. To reduce the calculation, the edge barycentre method (EB) was proposed, which only considers the boundary pixels, and the radius is computed as the mean distance of the boundary pixels from the estimated centre [16-18]. These approaches, however, do not take full advantage of our knowledge of a circle's shape and more refined parametric approaches have been proposed. The circular Hough transform (CHT) and its modification were used to locate centres of objects based on their contours and do not require the full outline of the objects [19-21]. Using both the edge and the directional images, a modified CHT was applied to detect circular arcs that should correspond to tomato contours [19]. The obtained results were very sensitive to the user-specified threshold value and the best result for a 99% threshold value was 68% correct detection and 42% false detection. The contour of the leaves was one of the major problems since the analysis algorithm interpreted them as possible fruits. Grasso and Recce [22] used CHT to estimate the locations of centres based on the citrus edges in natural scenes. The authors reported problem when oranges were partially occluded by leaves. Cai et al. [21] used modified CHT to extract the centre coordinates and radii and recover the shapes of citrus without occlusion or with slight occlusion.

Although CHT is a simple approach to detect near-spherical fruit, it is a computationally intensive approach with respect to time and memory. The main alternative method for the detection and analysis of near-circular features is the least-square circle fitting (LSCF). Researches in which least-

square fitting of circles has been used in astronomy, physics, biology, quality control and metrology can be found reported in the literature [17, 23-26]. The main objectives of this investigation are: 1) to find a suitable method to fit circles and extract features that can represent the near-spherical fruit (citrus, apples, pears, tomatoes, etc.), and 2) to analyse the impact of the extent of occlusion or overlapping on feature extraction.

MATERIALS AND METHODS

Materials

The near-spherical citrus tested in this study was planted in Jiangxinzhou, Zhenjiang City, China. The fruit (commonly called Miyagawa) are primarily sold in the fresh market. Therefore, selective harvesting is the best way to maximise the market value of the fruit. The equatorial or long diameter of the harvested fruit ranges between 60-78 mm. The equatorial diameter and height (short diameter) of the single fruit used for this laboratory analysis were 71.2 mm and 64.6 mm respectively.

Image Acquisition

Citrus images were obtained in a self-made image acquisition device composed of a light box with diffuse illumination, a charge coupled device and a host computer. Diffusers were installed in the light box wall as well as the dome. Multiple internal reflection caused the light to show no preferred direction. There was no shadow or strong reflection in the images. The camera of the charge coupled device was a LU075C (Lumenera Corporation, Canada). The main controlling computer had a Pentium IV CPU (3.0 GHz) and a memory of 1.5 G. All images were digitised into $640 \times 480 \times 24$ -bit colour bitmap images in RGB (red, green, blue) colour space.

The sample citrus was fixed at the centre of a white bottom, the citrus equator being perpendicular to the floor. A total of 56 images of the citrus were obtained in the laboratory, the first one being that of the unoccluded fruit and the rest, those of the fruit occluded with leaves (Figure 1). The occluded area ranged from 0 to 94% and the occluded contour angle ranged from 0 to 320° . Only one fruit sample was used to capture all the 56 images and during the image acquisition, the citrus fruit was not moved to ensure that its central location was unchanged.

An image for the validation test was captured in October of 2008 in a natural scene of an orchard using the same camera and computer.

Software

In this work, the images were captured and processed by a self-developed software based on Visual C++ 2008 (Microsoft Co., USA), LuCam SDK V4.2 (Lumenera Corporation, Canada) and MVTec Halcon 8.0 (MVTec Software GmbH, Germany) software platforms.

Image Segmentation

Segmentation separates the object (fruit) of interest from the background, which is the first step for object recognition. Its performance is critical to fruit detection since the segmentation output serves

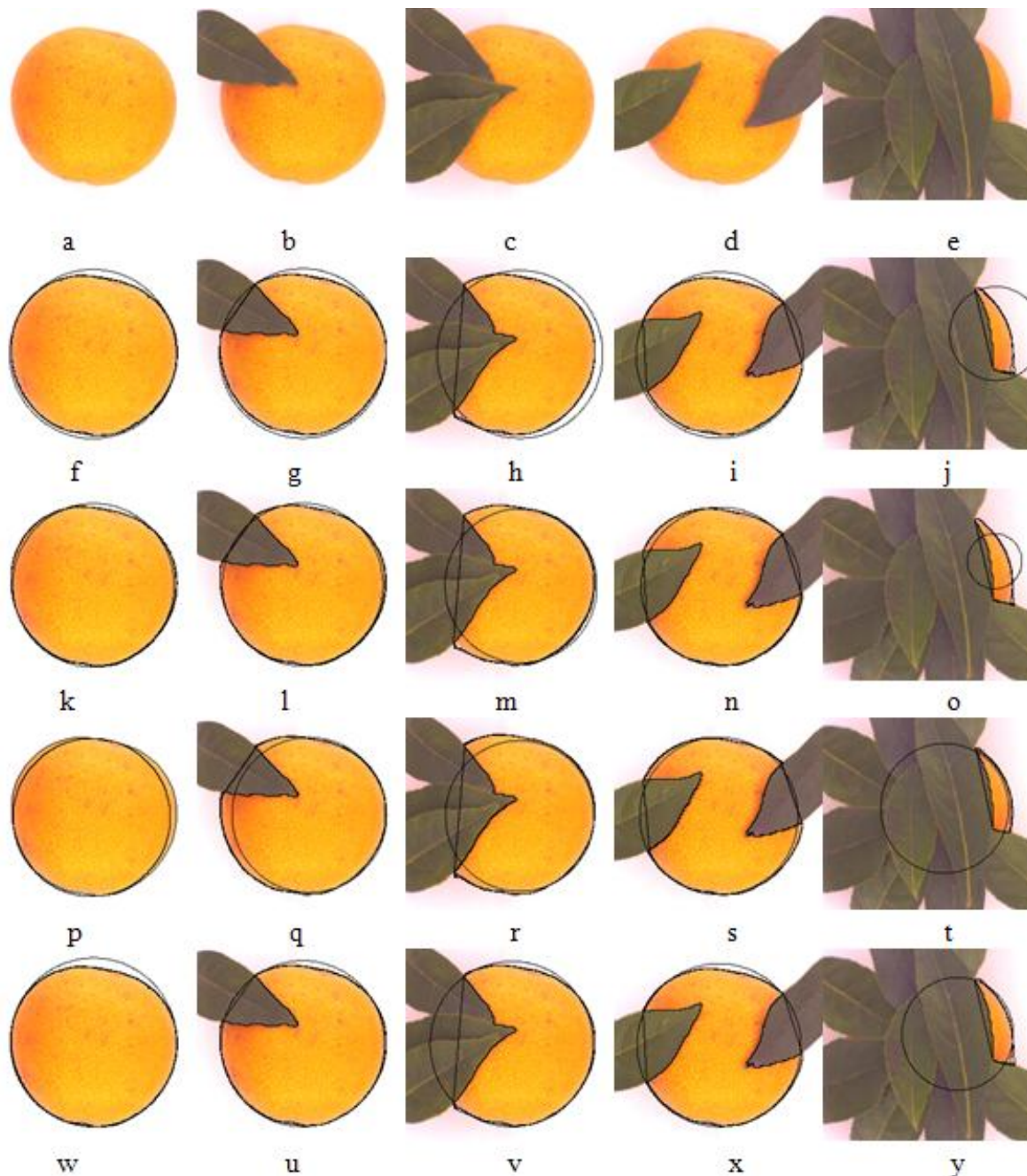


Figure 1. Fitting circles of five images using different methods. In the first row (a-e), the original images are shown. The images shown in 2nd, 3rd, 4th and 5th rows are fitted using CB, EB, CHT and LSCF respectively.

as input to succeeding processes. In occluded citrus images obtained in the lab, object (foreground) segmentation from the background (leaves and white paper) was simple. In this study, all the images were decomposed into R, G and B (red, green and blue) component images at first. By analysing the grey values and grey histograms of the component images and colour difference images, it was found that there was an obvious difference between citrus and background in the G-B colour difference images, and this difference did not exist in other component images. In computer vision, Otsu algorithm [27] was used to automatically perform histogram-shape-based image thresholding. The citrus

(foreground) regions were segmented using Otsu method. Then the holes in the fruit region were filled using hole filling.

The next step was the removing of the regions which did not correspond to the physical citrus in the binary image. The regions can have several properties and an important one is the area. This property can remove any region that is too small to be an object. So the regions were removed using size filtering and the citrus binary images were then obtained.

Due to occlusion by leaves and branches, many citrus images were incomplete, and there were different degrees of concave, which had a great impact on the circle fitting. Convex hull operation [28-29] was used to eliminate concaves and reduce their impact for fitting.

Feature Extraction

To locate a near-spherical fruit in a 2-D image, the coordinate of its centre and its radius can be accessed through circle fitting of the fruit region. In this paper, all the four approaches (CB, EB, CHT and LSCF) were used to extract the fruit's features.

In CB method, the fruit centre was the barycentre of the object cluster and the radius could be estimated as the maximum distance of the pixels from the barycentre. So the features could be computed using the citrus binary images. The results of CB are shown in Figure 1(f-j).

The other three approaches for feature extraction needed citrus contours. The contours could be obtained using edge detection. In EB method, only the boundary pixels could be considered. The centre was the barycentre of the boundary and the radius was computed as the mean distance of the border pixels from the estimated centre. The results of EB are shown in Figure 1(k-o).

Circular Hough transformation (CHT)

In image processing, CHT is widely adopted as a circle can be defined by a triplet of values, i.e. (pc, Rc) , where $pc = (x_c, y_c)$ is the circle's centre and Rc is its radius. Then the (pc, Rc) space can be discretised into a finite number of accumulation cells, each corresponding to a specific circle, and a counter is linked with it. In this method, the whole edge pixels are extracted firstly from the image: $\{P_i\}_{i=1...N}$. Then for each P_i , the counters of all those cells (pc, Rc) that are compatible with P_i are increased by one. When all the points have been considered, the most probable circle centre and radius are included in the accumulation cell with the highest count. However, this is not easy to implement, and the CHT method is very slow. Moreover, it needs a large room for memory to reach a relatively high accuracy since accuracy is proportional to the size of the discretised cells [30-31]. The results of CHT are shown in Figure 1(p-t).

Least-square circle fitting (LSCF)

To fit a circle through all points $\{P_i(x_i, y_i)\}_{i=1...N}$ of the contour, an error is defined for each point P_i as the distance between P_i and the circumference. The cost function is defined as:

$$E = \sum_{i=1}^N (\rho_i - R_c)^2 \quad (1)$$

$$\text{where } \rho_i = \|P_i - P_c\| = \sqrt{(x_i - x_c)^2 + (y_i - y_c)^2} \quad (2)$$

is the distance of a generic point from the circle's centre. P_c is the centre of the fitting circle and R_c is its radius. The cost function minimisation leads to a non-linear optimisation which can be solved iteratively using non-linear optimisation techniques [32].

The LSCF is not robust to large outliers since points that lie far from the circle have a very large weight in the optimisation because of the squared distance. To reduce the influence of distant points, we can introduce a weight function for the points. The Huber weight function and Tukey weight function are usually used [32]. In this study, we used Tukey weight function, which is given by:

$$\omega(\delta_i) = \begin{cases} [1 - (\delta_i / \tau)^2]^2 & (|\delta_i| \leq \tau) \\ 0 & (|\delta_i| > \tau) \end{cases} \quad (3)$$

where τ is the clipping factor and δ_i is the distance of the points to the circle. The cost function becomes:

$$E = \sum_{i=1}^N \omega_i (\rho_i - R_c)^2 \quad (4)$$

The object circle can be gained through minimising iterations of the functions. The results of LSCF are shown in Figure 1(w-y).

Measurement of Occlusion

Different kinds and degrees of occlusion partially hiding the citrus fruit can lead to the reducing of visible area and incomplete extraction of the original contour of the citrus. As the occlusion degrees vary, the feature extraction accuracy also does. For each image obtained in the lab, the occluded area ratio (R_{oa}) and the occluded angle (θ_o) were defined to represent the occlusion level of the object. R_{oa} was defined as:

$$R_{oa} = \left(1 - \frac{Area_v}{Area_u}\right) \times 100\% \quad (5)$$

where $Area_u$ is the area of the unoccluded citrus computable from the first image, and $Area_v$ is the visible area of the citrus with various degrees of occlusion. Occluded contours may have only one paragraph or more paragraphs (Figure 1d and Figure 2). θ_o is defined as the sum of every occluded angle (Figure 2), which can be computed by the following formula:

$$\theta_o = \sum_1^N \theta_i \quad (6)$$

where N is the number of occluded paragraphs of fruit contour, θ_i is the angle of occluded paragraph No. i , which can be obtained through the law of cosines. By calculation, R_{oa} ranged from 0 to 94%, and θ_o ranged from 0 to 320° in this experiment.

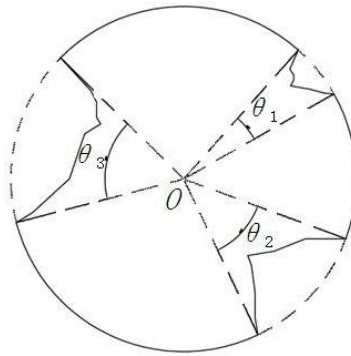


Figure 2. Diagram of occluded angles of fruit

RESULTS AND DISCUSSION

Analysis for Simulation Examples

The proposed algorithms were tested by the images obtained both in the laboratory and in the field, and the relationship between feature extraction accuracy and occlusion was analysed. For all methods, the higher the occlusion level was, the stronger the impact on the feature extraction became (Figure 1). The following indicators, viz. radius ratio (r_r) and ratio of centre offset (r_c), were used to evaluate the feature extraction accuracy. They were defined as:

$$r_r = \frac{r_o}{r_u} \quad (7)$$

where r_u is the radius of fruit without occlusion and r_o is the radius of fruit with occlusion; and

$$r_c = \frac{D}{r_u} \quad (8)$$

where D is the distance between the centres of the citrus with and without occlusion. From Figure 1(f, k, p and w), it could be found that r_u and the centres were different with different methods.

The performance of the feature extraction using CB, EB, CHT and LSCF was compared quantitatively and the results are shown in Figures 1 and 3. To position accurately the objects on the tree, the criteria of the feature extraction were set so that the radius ratio (r_r) was not less than 90% and the ratio of centre offset (r_c) was not more than 10%. Results of the feature extraction using different algorithms under different occluded area ratios and angles are shown in Figure 3. In order to meet the demand of the feature extraction, the thresholds of R_{oa} and θ_o for different methods, shown in Table 1, were applied.

From Figure 3 and Table 1, it was found that the impacts of occlusion on the feature extraction for CB and EB were greater than those for CHT and LSCF. To meet the criteria of the feature extraction, the occluded area ratios (R_{oa}) when using CB, EB, CHT and LSCF algorithm, were to be less than 25%, 27%, 54% and 52% respectively, or the occlusion angles (θ_o) less than 95°, 100°, 222° and 216° respectively.

With the increase of occlusion degree, the error of the feature extracted rose. The impact of contour occlusion on the feature extraction was greater than that of area occlusion. The curvature

stability and continuity of the remaining contour had a great influence on the feature extraction. If the contour curvature remained relatively stable, when occlusion angle reached up to 268°, the centres and radii were better extracted using CHT or LSCF. When the visible areas were equal in different occlusion, the longer the remaining contour was, the higher the extraction accuracy became.

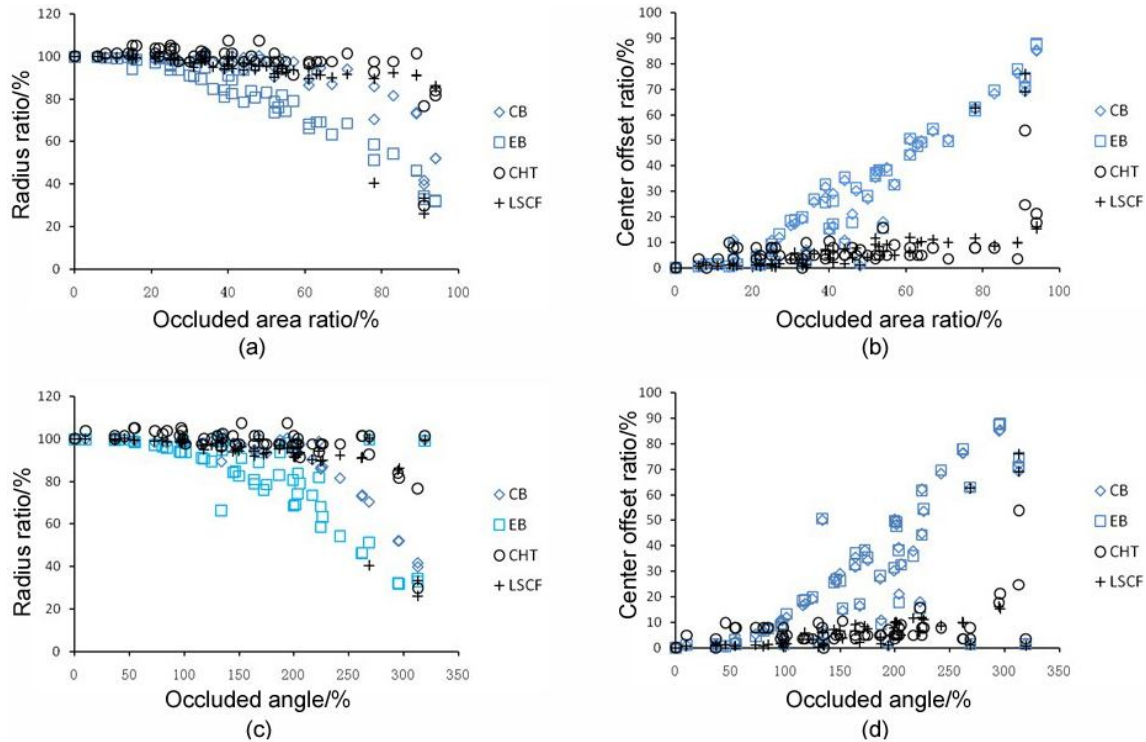


Figure 3. Distribution of feature extraction measurement: (a) radius ratio vs. occluded area ratio; (b) centre offset ratio vs. occluded area ratio; (c) radius ratio vs. occluded angle; (d) centre offset ratio vs. occluded angle

Table 1. Thresholds to meet the requirements of feature extraction using different methods

	$r_r \geq 90\%$		$r_c \leq 10\%$		$r_r \geq 90\% \& r_c \leq 10\%$	
	R_{oa} (%)	θ_o (°)	R_{oa} (%)	θ_o (°)	R_{oa} (%)	θ_o (°)
CB	<60	<224	<25	<95	<25	<95
EB	<33	<124	<27	<100	<27	<100
CHT	<90	<290	<54	<222	<54	<222
LSCF	<70	<268	<52	<216	<52	<216

Due to occlusion, the precision of extraction inevitably declined for lack of the original contour. In this study, convex hull operation was used to reduce the impact of occlusion concaves by repairing the occlusion to a certain extent.

The CB and EB apparently could not effectively extract the features. The reasons were the poor performance by using the barycentre of the cluster or edge as the fruit centre and by calculating the maximum or mean distance of the boundary pixels from the centre as the radius. The CHT and LSCF, on the other hand, worked well and could be used to extract the features of near-spherical fruit.

However, the accuracy of the CHT was limited when the accumulation cells discretised. Decreasing the size of the accumulation cells drastically increased computation time, making the CHT practically useless for many applications, especially ones that required real-time processing.

Analysis in Natural Scenes

In a natural scene, images of multiple objects are captured by the fruit-picking robot. The features of the fruit with different sizes require a suitable algorithm for real-time extraction. There are 22 fruits in the image shown in Figure 4(a); 18 of them were segmented using Otsu algorithm on G-B, size filtering, hole filling, watershed segmentation employing distance transform, convex hull operation and roundness filtering.

The features of all the 18 fruits could be extracted using LSCF as shown in Figure 4(b). By CHT, 18 objects were gained including 2 false objects and 2 fruit had not been extracted (Figure 4(c)). In the feature extraction of these 18 objects in this image, LSCF required 44.60 ms while CHT required 92.91 ms (more than twice as long as for LSCF). Moreover, comparing Figures 4(b) and 4(c), the features obtained by LSCF were more accurate in presenting objects than those obtained by CHT.

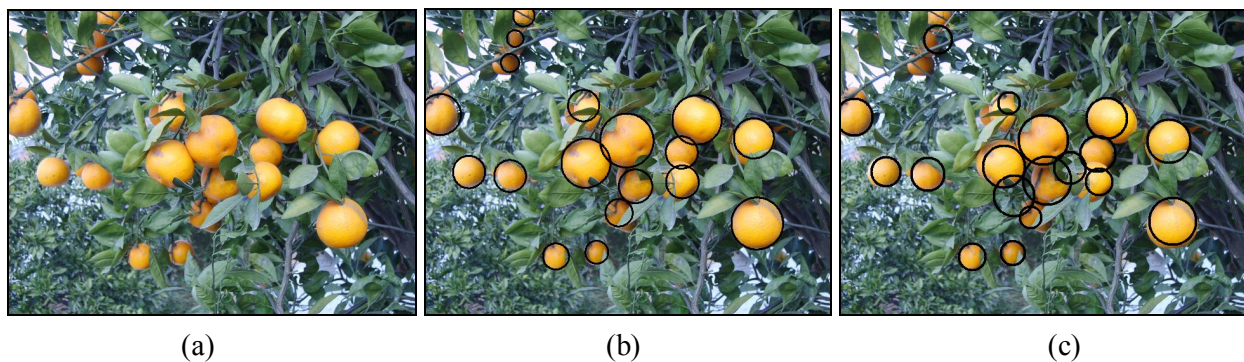


Figure 4. Feature extraction of images obtained in a natural scene: (a) original image; (b) feature extraction using LSCF; (c) feature extraction using CHT

CONCLUSIONS

The CB, EB, CHT and LSCF methods were presented and used to extract the features of near-spherical fruit in 2-D images. It was also shown with simulation and real examples that the LSCF could locate the centre and estimate the radius of the fruit accurately, reliably and in a real-time mode, even in the presence of partial occlusion. If the occlusion area ratio was less than 52% or the occlusion angle was less than 216° , the object could be located accurately, suggesting that this algorithm can be used for designing the fruit-picking robot in natural scenes.

ACKNOWLEDGEMENTS

This work has been financially supported by the National High Technology Research and Development Program of China (Project No. 2006AA10Z263) and the National Natural Science Foundation of China (Project No. 30771243).

REFERENCES

1. G. K. Brown, "Mechanical harvesting system for the Florida citrus juice industry", ASAE Paper No. 021108, ASAE Annual International Meeting, **2002**, St. Joseph, Michigan, USA.
2. C. E. Schertz and G. K. Brown, "Basic considerations in mechanizing citrus harvest", *Trans. ASAE*, **1968**, *11*, 343-346.
3. R. C. Harrell, P. D. Adist, T. A. Pool and R. Hoffman, "The Florida robotic grove-lab", *Trans. ASAE*, **1990**, *33*, 391-399.
4. G. Rabatel, A. Bourely, F. Sevilla and F. Juste, "Robotic harvesting of citrus: State-of-art and development of the French Spanish Eureka project", Proceedings of the International Conference on Harvest and Post-harvest Technologies for Fresh Fruits and Vegetables, **1995**, Michigan, USA, pp. 232-239.
5. M. Hannan, T. F. Burks and D. M. Bulanon, "A real-time machine vision algorithm for robotic citrus harvesting", ASABE Paper No. 073125, ASABE Annual International Meeting, **2007**, Minneapolis, Minnesota, USA.
6. A. G. D'Esnon, G. Rabatel and R. Pellenc, "A self-propelled robot to pick apples", ASAE Paper No.87-1037, ASAE Annual International Meeting, **1987**, St. Joseph, Michigan, USA.
7. Z. X. Liu and G. Liu, "Apple maturity discrimination and positioning system in an apple harvesting robot", *New Zealand J. Agr. Res.*, **2007**, *50*, 1103-1113.
8. S. Arima, N. Kondo and M. Monta, "Strawberry harvesting robot on table-top culture", ASAE/CSAE Paper No.043089, ASAE/CSAE Annual International Meeting, **2004**, Ottawa, Canada.
9. T. Shiigi, N. Kondo, M. Kurita, K. Ninomiya, J. Kamata, S. Hayashi, K. Kobayashi, K. Shigematsu and Y. Kohno, "Strawberry harvesting robot for fruits grown on table top culture", ASABE Paper No.084046, ASABE Annual International Meeting, **2008**, Providence, Rhode Island, USA.
10. M. Monta, N. Kondo and K. C. Ting, "End-effectors for tomato harvesting robot", *Artif. Intell. Rev.*, **1998**, *12*, 11-25.
11. P. Ling, R. Ehsani, K. C. Ting, N. Ramalingam, M. H. Klingman, Y. Chi and C. Draper, "Sensing and end-effector for a robotic tomato harvester", ASAE/CSAE Paper No.043088, ASAE/CSAE Annual International Meeting, **2004**, Ottawa, Canada.
12. N. Kondo and K. C. Ting, "Robotic for bioproduction systems", America Society of Agricultural Engineering Publisher, Michigan, **1998**, pp.195-212.
13. Y. Sarig, "Robotics of fruit harvesting: A state-of-the-art review", *J. Agr. Eng. Res.*, **1993**, *54*, 265-280.
14. A. R. Jiménez, A. K. Jain, R. Ceres and J. L. Pons, "Automatic fruit recognition: a survey and new results using range/attenuation images", *Patt. Recogn.*, **1999**, *32*, 1719-1736.
15. A. R. Jiménez, R. Ceres and J. L. Pons, "A vision system based on a laser range-finder applied to robotic fruit harvesting", *Mach. Vision Appl.*, **2000**, *11*, 321-329.
16. M. S. Shafiq, S. T. Tümer and H. C. Güler, "Marker detection and trajectory generation algorithms for a multicamera based gait analysis system", *Mechatronics*, **2001**, *11*, 409-437.
17. M. Berman. "Large sample bias in least squares estimators of a circular arc centre and its radius", *Comput. Graph. Image Process.*, **1989**, *45*, 126-128.

18. I. Frosio and N. A. Borghese, "Real-time accurate circle fitting with occlusions", *Patt. Recog.*, **2008**, *41*, 1041-1055.
19. A. D. Whittaker, G. E. Miles, O. R. Mitchell and L. D. Gaultney, "Fruit location in a partially occluded image", *Trans. ASAE*, **1987**, *30*, 591-596.
20. J. Illingworth and J. Kittler, "A survey of the Hough transform", *Comput. Vision Graph. Image Process.*, **1988**, *44*, 87-116.
21. J. R. Cai, X. J. Zhou, Y. L. Li and J. Fan, "Recognition of mature oranges in natural scene based on machine vision", *Trans. Chinese Soc. Agri. Eng.*, **2008**, *24*, 175-178 (in Chinese).
22. G. M. Grasso and M. Recce, "Scene analysis for an orange picking robot", Proceedings of the 6th International Congress for Computer Technology in Agriculture, **1996**, Wageningen, The Netherlands, pp. 275-280.
23. S. J. Ahn, W. Rauh and H. J. Warnecke, "Least-squares orthogonal distances fitting of circle, sphere, ellipse, hyperbola, and parabola", *Patt. Recog.*, **2001**, *34*, 2283-2303.
24. L. Moura and R. Kitney, "A direct method for least-squares circle fitting", *Comput. Physics Commun.*, **1991**, *64*, 57-63.
25. W. Gander, G. H. Golub and R. Strebler, "Least-squares fitting of circles and ellipses", *BIT Numer. Math.*, **1994**, *34*, 558-578.
26. N. Chernov and C. Lesort, "Least squares fitting of circles", *J. Math. Imag. Vision*, **2005**, *23*, 239-252.
27. N. Otsu, "A threshold selection method from gray-level histograms", *IEEE Trans. Syst. Man Cybern.*, **1979**, *9*, 62-66.
28. I. Barany, T. van Roy and L. Wolsey. "Uncapacitated lot-sizing: The convex hull of solutions", *Math. Program. Studies*, **1984**, *22*, 32-43.
29. A. Melkman. "On-line construction of the convex hull of simple polygon", *Inform. Process. Lett.*, **1987**, *25*, 11-12.
30. P. V. C. Hough, "Method and means for recognizing complex patterns", *US Patent*, 3069654 (**1962**).
31. I. Frosio and N. A. Borghese, "Real-time accurate circle fitting with occlusions", *Patt. Recog.*, **2008**, *41*, 1041-1055.
32. C. Steger, M. Ulrich and C. Wiedemann, "Machine Vision Algorithms and Applications", Tsinghua University Press, Beijing, **2008**, pp.238-247.

Communication

Isolation and primary identification of endophytic fungi from *Cephalotaxus mannii* trees

Pramuan Saithong^{1,*}, Wanchai Panthavee¹, Siriporn Stonsaovapak¹ and Li Congfa²

¹ Department of Applied Microbiology, Institute of Food Research and Product Development, Kasetsart University, 50 Phaholyothin Rd., Chatuchak, Bangkok 10900, Thailand

² Department of Food Science and Engineering, College of Science and Engineering, South China University of Tropical Agriculture (SCUTA), Hainan, China

* Corresponding author, e-mail: ifrpmst@ku.ac.th

Received: 13 May 2010 / Accepted: 29 October 2010 / Published: 2 November 2010

Abstract: Fifty-two isolates of endophytic fungi were collected from the bark of *Cephalotaxus mannii* (plum-yew) trees located in the north of Thailand and the south of China. All isolates were identified based on colony morphology and examination of spores and fruiting bodies using stereo and light microscopes. Thirty-five isolates (67.3%) belonging to 13 genera were recorded, viz. *Cladosporium* sp., *Acremonium* sp., *Trichoderma* sp., *Monilia* sp., *Fusarium* sp., *Spicaria* sp., *Humicola* sp., *Rhizoctonia* sp., *Cephalosporium* sp., *Botrytis* sp., *Penicillium* sp., *Chalaropsis* sp. and *Geotrichum* sp., while 17 strains (32.7%) were unidentified. The dominant genera found both in northern Thailand and southern China were *Acremonium* sp., *Monilia* sp. and *Fusarium* sp. *Cladosporium* sp. and *Trichoderma* sp. were found only in southern China, whereas *Spicaria* sp., *Humicola* sp., *Rhizoctonia* sp., *Botrytis* sp., *Penicillium* sp., *Geotrichum* sp., *Chalaropsis* sp. and *Cephalosporium* sp. were found only in northern Thailand. Thus, there seemed to be a significant difference in the genera of endophytic fungi from *Cephalotaxus mannii* trees of different sources.

Keywords: *Cephalotaxus mannii*, endophytic fungi, primary identification of fungi

INTRODUCTION

Endophytic fungi are found on all kinds of plants, i.e. trees, grasses, algae and herbaceous plants. Endophytic fungi live within a plant's tissue without causing any symptoms or apparent injury to the host. The colonisation of plant tissues by endophytic fungi occurs in a manner similar to those of plant pathogens and mycorrhizae [1]. Colonisation comprises a sequence of steps involving host recognition by the fungus, spore germination, penetration of the epidermis, and tissue colonisation.

Most endophytic fungi belong to ascomycetes and fungi imperfecti [2]. The equilibrium between the host and the fungi seems to be controlled in part by chemical factors, for example herbicidal natural products produced by the fungi versus antifungal metabolites synthesised by the host plants [2]. There are also reports demonstrating that many antitumour agents such as taxol [3-4] as well as antimicrobial agents [5-7] can be produced by these endophytic fungi. The genus *Acremonium* sp. was reported by Jeamjitt et al. [8] to be especially capable of producing secondary metabolites. These substances may have applications outside the host plant in which they normally reside. Endophytic fungi have been primarily studied in temperate regions; tropical endophytic fungi are less well understood. Fungi from this unique habitat have been shown to be the sources of new species, possibly containing new bioactive compounds.

Endophytic fungi of tropical plants have been widely researched in Thailand [8-14]. These previous studies are exemplified in Table 1. However, endophytic fungi from *Cephalotaxus mannii* have not been well researched in Thailand. *Cephalotaxus mannii* is a kind of pharmaceutical plant and is well known as a rich source of endophytic fungi. It is mainly distributed in South-East Asia and China, especially in northern Thailand [15]. Five alkaloids, namely harringtonine, isoharringtonine, homoharringtonine, dexoharringtonine and cephalozomines have been isolated from *Cephalotaxus mannii*, *C. sinensis*, *C. hainanensis*, *C. oliveri* and *C. harringtonia* var. *nana* respectively, and have been developed as clinical medicines for hospital treatment of leukemia patients [2, 6, 16].

Studies of useful endophytic fungi from such pharmaceutical plants will be of great value to ecology and pharmacology. The present study focuses on screening and identification of endophytic fungi isolated from *Cephalotaxus mannii* collected from two regions: northern Thailand (Chiang Mai and Chiang Rai provinces) and southern China (Hainan Island).

Table 1. Some studies on endophytes in Thailand [1]

Host	Number of taxa	Reference
<i>Amomum siamense</i>	33	[17]
<i>Bambusa</i> spp.	96	[18]
<i>Musa</i> sp. (banana)	61	[19]
Palms	39	[20]
<i>Dimocarpus longan</i> (longan)	18	[21]

MATERIALS AND METHODS

Sources of Endophytic Fungi

Bark samples of *Cephalotaxus mannii* were gathered from tropical rainforest complexes which have high tree species diversity during the rainy season in three locations in northern Thailand (Doi Tung, Chiang Rai province, and Doi Inthanon and Doi Suthep-Pui, Chiang Mai province) and from Hainan Island, off the southern coast of China. All samples were collected at an altitude of approximately 800 metres above sea level. Table 2 shows the numbers of samples and the locations where they were collected. These bark samples were cross-sectioned at different parts of the trees (low,

middle and high) using sterilised knives to obtain pieces of 2.0-3.0×1.5-2.0×0.3-0.5 cm (length×width×thickness). The samples were then sealed with Parafilm[®], a flexible thermoplastic film, to prevent drying during transport and maintained at 4°C until further processing.

Isolation of Endophytic Fungi

Endophytic fungi isolation was carried out under aseptic condition. The outer bark of each sample was detached with a sterilised sharp blade, cleaned by washing with running tap water several times and soaked in 70% (v/v) ethanol for 10-20 min. It was then washed several times with sterilised water, dipped into 0.1% HgCl₂ for 1-2 min, again washed with sterilised water 3-5 times and then put into a beaker of sterilised distilled water. The bark sample was then cut into small pieces, each piece put on a plate of potato dextrose agar (PDA) medium supplemented with chloramphenicol (30 µg/ml) and streptomycin (30 µg/ml), and the plate cultivated at 30°C to promote fungal growth and sporulation. Individual hyphal tips of the fungus were then picked up from each plate, inoculated onto another PDA medium plate, and incubated at 30°C for at least 1 week. Each fungal culture was checked for purity and transferred to another agar plate using the hyphal tips. The purified fungal isolates were numbered, transferred separately to PDA slants, and kept at 4°C.

Table 2. Bark samples of *Cephalotaxus mannii* trees collected from various places

Location	Number of samples	Place
Near a canal on the mountain	1	Doi Suthep-Pui National Park, Chiang Mai, Thailand
Top of the mountain	} 3	Doi Tung (Wat Phra That Doi Tung) Chiang Rai, Thailand
Near a roadside in the park		
Near a roadside in the park	} 11	Doi Inthanon National Park, Chiang Mai, Thailand
On a hillside in the forest		
Deep in the forest		
Top of the mountain	} 2	Diao Luo Mountain, Hainan Island, China
Top of the mountain		
Foot of the mountain	2	Qi Xian Ling Mountain, Hainan Island, China
Top of the mountain	1	Jian Feng Ling Mountain, Hainan Island, China

Identification of Endophytic Fungi

For characterisation of the morphology of fungal isolates, slides prepared from cultures were stained with bromothymol blue reagent and examined with a bright-field and phase-contrast microscope. Identification was based on morphological characteristics such as growth pattern, hyphae, colour of colony and medium, surface texture, margin character, aerial mycelium, mechanism of spore production and characteristics of the spore [22]. An Olympus BH-2 with Nomarski interference contrast was employed for examination by light microscopy.

RESULTS

Fifty-two isolates of endophytic fungi were collected from 20 samples (Table 2). All endophytic fungi could be cultivated on artificial media and maintained as a pure culture. They exhibited characteristic colony and microscopic morphology that could be used to differentiate them. Most of them belonged to ascomycetes and fungi imperfecti, as shown in Table 3. Some results of characterisation of colony and microscopic morphological study are shown in Figures 1 and 2 respectively. All isolates were identified as belonging to 13 genera, namely *Cladosporium* sp., *Acremonium* sp., *Trichoderma* sp., *Monilia* sp., *Fusarium* sp., *Spicaria* sp., *Humicola* sp., *Rhizoctonia* sp., *Cephalosporium* sp., *Botrytis* sp., *Penicillium* sp., *Chalaropsis* sp. and *Geotrichum* sp. (Table 3). The dominant genus found in the north of Thailand was *Geotrichum* sp. (7 isolates, 20.0%) while *Trichoderma* sp. was the dominant genus found in the south of China (4 isolates, 23.5%). *Cladosporium* sp. and *Trichoderma* sp. were found only in the south of China while *Spicaria* sp., *Humicola* sp., *Rhizoctonia* sp., *Botrytis* sp., *Penicillium* sp., *Geotrichum* sp., *Chalaropsis* sp. and *Cephalosporium* sp. were found only in the north of Thailand. Genera common to northern Thailand and southern China consisted of *Acremonium* sp., *Monilia* sp. and *Fusarium* sp. Some fungal isolates belonged to rare genera, i.e. *Spicaria* sp., *Humicola* sp. and *Acremonium* sp. Some fungi, viz. 5 isolates (29.4%) from southern China and 12 isolates (34.3%) from northern Thailand, could not be identified due to lack of spore formation. These results indicated that there are significant difference in the genera of endophytic fungi from *Cephalotaxus mannii* trees of different locations.

Huang et al. [2] reported that endophytic fungi can produce antitumour or antifungal activities. These fungi were isolated from the inner bark of three kinds of pharmaceutical plants including *Cephalotaxus* sp., and were identified as belonging to six genera, namely *Paecilomyces* sp., *Cephalosporium* sp., *Mortierella* sp., *Mucor* sp., *Trichoderma* sp. and *Cladosporium* sp.

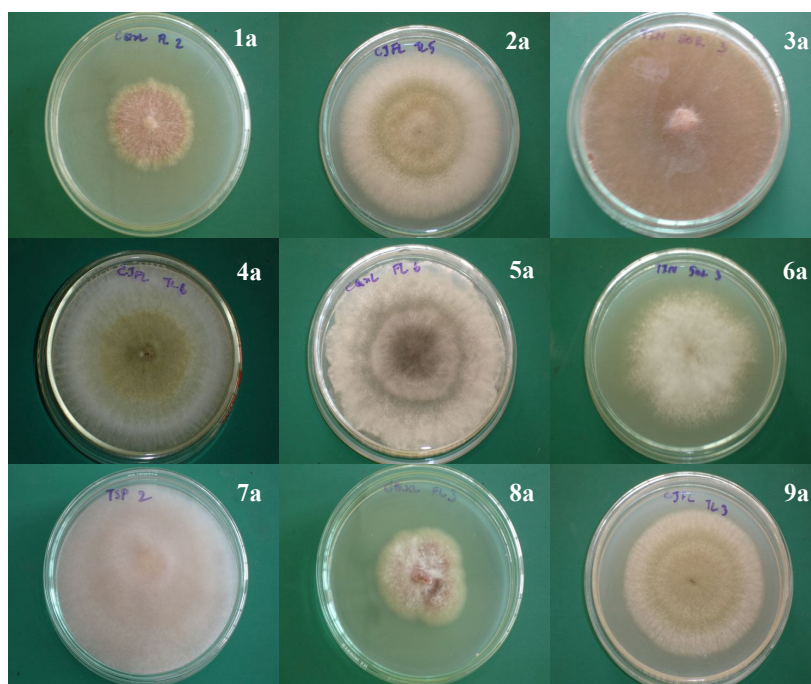


Figure 1. Colour variation among colonies on PDA medium plates at 3 days: (1a) unidentified strains; (2a) *Botrytis* sp.; (3a) *Geotrichum* sp.; (4a) *Botrytis* sp.; (5a) *Acremonium* sp.; (6a) unidentified strains; (7a) *Geotrichum* sp.; (8a) *Fusarium* sp.; (9a) *Botrytis* sp.

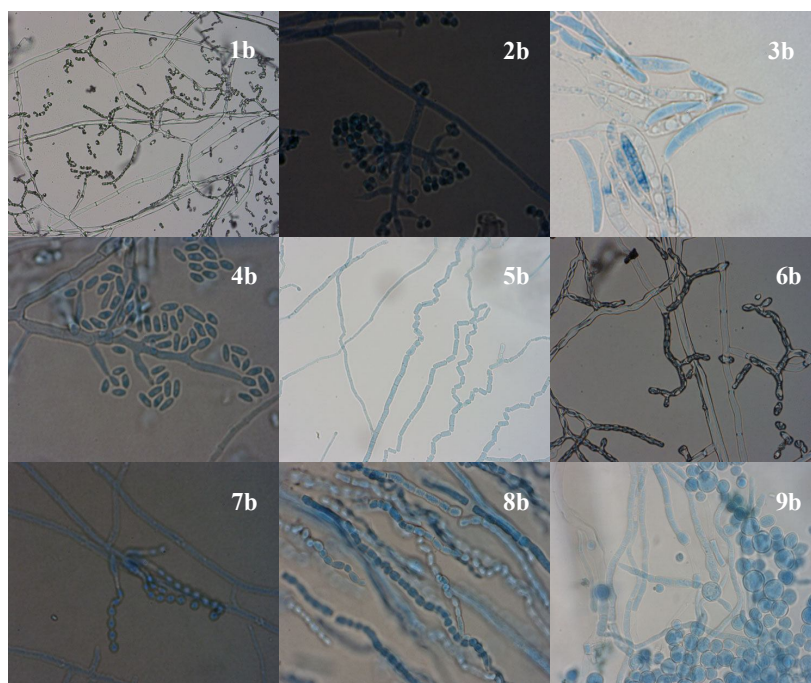


Figure 2. Light microscopic observation of fungi: (1b) *Monilia* sp.; (2b) *Trichoderma* sp.; (3b) *Fusarium* sp.; (4b) *Cephalosporium* sp.; (5b) *Geotrichum* sp.; (6b) *Monilia* sp.; (7b) *Spicaria* sp.; (8b) *Geotrichum* sp.; (9b) unidentified strain

Table 3. Genera of isolated endophytic fungi

Genus	Number of endophytes from <i>Cephalotaxus</i> sp. trees at different locations			
	Doi Tung	Doi Inthanon	Doi Suthep-Pui	Hainan Island
<i>Cladosporium</i> sp.				1
<i>Acremonium</i> sp.	2			3
<i>Trichoderma</i> sp.				4
<i>Monilia</i> sp.	1	1		1
<i>Fusarium</i> sp.		1		3
<i>Spicaria</i> sp.	1			
<i>Humicola</i> sp.	2	1		
<i>Rhizoctonia</i> sp.		1		
<i>Cephalosporium</i> sp.		1		
<i>Geotrichum</i> sp.		5	2	
<i>Botrytis</i> sp.		2		
<i>Penicillium</i> sp.		2		
<i>Chalaropsis</i> sp.		1		
unidentified strains	4	8		5

CONCLUSIONS

Endophytic fungi from the *Cephalotaxus mannii* trees were isolated and identified by their morphology and spore characteristics. From twenty samples from northern Thailand and southern China were obtained 52 isolates, which were identified as belonging to 13 genera with some unidentified strains. *Geotrichum* sp. and *Trichoderma* sp. were found to be the dominant genera in northern Thailand and southern China respectively. Bark samples from Doi Inthanon (northern Thailand) had the highest number of fungi (15 isolates and 8 unidentified, 44.2%) while those from Doi Suthep-Pui (northern Thailand) had the fewest (2 isolates, 3.8%). *Cladosporium* sp. and *Trichoderma* sp. were found only in the south of China while *Spicaria* sp., *Humicola* sp., *Rhizoctonia* sp., *Botrytis* sp., *Penicillium* sp., *Geotrichum* sp., *Chalaropsis* sp. and *Cephalosporium* sp. were found only in the north of Thailand. Some isolates belonged to the rare genera, namely *Spicaria* sp., *Humicola* sp. and *Acremonium* sp. However, these results should be considered as those of an initial study. Further investigation, e.g. 18S rDNA sequence comparisons (molecular techniques), is required to confirm the classification of these isolates.

ACKNOWLEDGEMENTS

We are grateful to the Thailand International Development Cooperation Agency (TICA) and the Ministry of Science and Technology (MOST), China, for the financial support of this research.

REFERENCES

1. S. Lumyong, P. Lumyong and K. D. Hyde, "Endophytes", in "Thai Fungal Diversity" (Ed. E. B. G. Jones, M. Tanticharoen and K. D. Hyde), National Center for Genetic Engineering and Biotechnology, Pathum Thani, Thailand, **2004**, pp. 197-205.
2. Y. Huang, J. Wang, G. Li, Z. Zheng and W. Su. "Antitumor and antifungal activities in endophytic fungi isolated from pharmaceutical plants *Taxus mairei*, *Cephalotaxus fortunei* and *Torreya grandis*", *FEMS Immunol. Med. Microbiol.*, **2001**, *31*, 163-167.
3. G. Strobel, X. Yang, J. Sears, R. Kramer, R. S. Sidhu and W. M. Hess, "Taxol from *Pestalotiopsis microspora*, an endophytic fungus of *Taxus wallachiana*", *Microbiol.*, **1996**, *142*, 435-440.
4. J. Wang, G. Li, H. Lu, Z. Zheng, Y. Huang and W. Su, "Taxol from *Tubercularia* sp. strain TF5, an endophytic fungus of *Taxus mairei*", *FEMS Microbiol. Lett.*, **2000**, *193*, 249-253.
5. X. X. Gao, H. Zhou, D. Y. Xu, C. H. Yu, Y. Q. Chen and L. H. Qu, "High diversity of endophytic fungi from the pharmaceutical plant, *Heterosmilax japonica* Kunth revealed by cultivation-independent approach", *FEMS Microbiol. Lett.*, **2005**, *249*, 255-266.
6. J. Y. Liu, Y. C. Song, Z. Zhang, L. Wang, Z. J. Guo, W. X. Zou and R. X. Tan, "*Aspergillus fumigatus* CY018, an endophytic fungus in *Cynodon dactylon* as a versatile producer of new and bioactive metabolites", *J. Biotechnol.*, **2004**, *114*, 279-287.
7. J. D. Hill, N. W. Duncan-Gould, N. A. Siddiqi, J. N. Kelly, L. A. Hoferlin, S. J. Morrison and J. K. Wyatt, "Cytosporone E: racemic synthesis and preliminary antibacterial testing", *Bioorg. Med. Chem.*, **2005**, *13*, 1409-1413.
8. O. Jeamjitt, L. Manoch, N. Visarathanonth and C. Chamswarng, "Diversity and distribution of hyphomycetes from dung in Thailand", *Kasetsart J. (Nat. Sci.)*, **2006**, *40*, 890-901.
9. S. Wiyakrutta, N. Sriubolmas, W. Panphut, N. Thongon, K. Danwiset-kanjana, N. Ruangrunsi and V. Meevootisom, "Endophytic fungi with anti-microbial, anti-cancer and anti-malarial activities isolated from Thai medicinal plants", *World J. Microbiol. Biotechnol.*, **2004**, *20*, 265-272.
10. S. Lumyong, S. Thongkantha, P. Lumyong and F. Tomita, "Mannanase production by endophytic fungi, *Fusarium* sp. GnCMU384", *Annu. Reports IC Biotech.*, **1998**, *21*, 1015-1023.
11. T. Permpoolsombat, "Screening L-asparaginase producing endophytic fungi", *MS Thesis*, **1999**, Chiang Mai University, Thailand.
12. N. Boontim, S. Lumyong, S. Thongkantha and S. Boontim, "Study of endophytic fungi from native Thai bamboo capable of antibiotic production", *J. Multidisc. Res.*, **2001**, *14*, 34-39.
13. C. Urairuj, C. Khanongnuch and S. Lumyong, "Ligninolytic enzymes from tropical endophytic *Xylariaceae*", *Fungal Diver.*, **2003**, *13*, 209-219.
14. W. Photita, S. Lumyong, P. Lumyong and K. D. Hyde, "Endophytic fungi of wild banana (*Musa acuminata*) at Doi Suthep Pui National Park, Thailand", *Mycol. Res.*, **2001**, *105*, 1508-1513.
15. R. Y. Yang, C. Y. Li, Y. C. Lin, G. T. Peng, Z. G. She and S. N. Zhou, "Lactones from a brown alga endophytic fungus (NO. ZZ36) from the South China Sea and their antimicrobial activities", *Bioorg. Med. Chem. Lett.*, **2006**, *16*, 4205-4208.
16. H. Morita, M. Yoshinaga and J. Kobayashi, "Cephalezomines G, H, J, K, L and M, new alkaloids from *Cephalotaxus harringtonia* var *nana*", *Tetrahedron*, **2002**, *58*, 5489-5495.

17. B. Bussaban, S. Lumyong, P. Lumyong, E. H. C. McKenzie and K. D. Hyde, "Endophytic fungi from *Amomum siamense*", *Can. J. Microbiol.*, **2001**, 47, 943-948.
18. S. Lumyong, S. Thongkantha, P. Lumyong and F. Tomita, "Endophytic fungi from 13 bamboo species in Thailand", *Biotechnol. Sustain. Util. Biol. Resour. Trop.*, **2000**, 14, 96-101.
19. W. Photita, "Survey and isolation of endophytic and saprobic fungi on wild banana in Doi Suthep-Pui National Park", *PhD Thesis*, **2003**, Chiang Mai University, Thailand.
20. W. Techa, "Isolation and collection of endophytic and saprobic fungi from two species of palms in Doi Suthep-Pui National Park", *MS Thesis*, **2001**, Chiang Mai University, Thailand.
21. V. Sardud, C. Sittigul, U. Sardud, P. Chantrasri and S. Promin, "Endophytic fungi in longan", in "Disease Control and Storage Life Extension in Fruit", (Ed. L.M. Coates, P. J. Hofman and G. I. Johnson), Australian Centre for International Agriculture Research (ACIAR), Canberra ACT, **1998**, pp. 147-152.
22. H. L. Barnett and B. B. Hunter, "Illustrated Genera of Imperfect Fungi", 2nd Edn., Burgess Publishing, Minneapolis, MN, **1956**, p. 218.

Communication

Antiglycation and antioxidant activities of oxyresveratrol extracted from the heartwood of *Artocarpus lakoocha* Roxb.

Nasapon Povichit¹, Ampai Phrutivorapongkul¹, Maitree Suttajit² and Pimporn Leelapornpisid^{1,*}

¹ Department of Pharmaceutical Sciences, Faculty of Pharmacy Chiang Mai University, Chiang Mai, 50200, Thailand

² School of Science and Technology, Naresuan University, Phayao Campus, Phayao 60000, Thailand

* Corresponding author, e-mail: pim_leela@hotmail.com

Received: 20 May 2010 / Accepted: 13 September 2010 / Published: 11 November 2010

Abstract: From the heartwood of *Artocarpus lakoocha*, oxyresveratrol was isolated with a yield of 10%. The isolated oxyresveratrol showed strong antiglycation and antioxidant activities. The IC₅₀ value for antiglycation was 2.0±0.03 µg/ml (five times higher than that of aminoguanidine), and the IC₅₀ values for antioxidation were 0.1±0.01 mg/ml (DPPH method) and 0.43±0.03 mg/ml (TBARS method), which were nearly twice as strong as those of resveratrol.

Keywords: *Artocarpus lakoocha*, antioxidant, antiglycation, oxyresveratrol

INTRODUCTION

The *Artocarpus* species are rich in phenolic compounds including flavonoids, stilbenoids and arylbenzofurans [1]. *Artocarpus lakoocha* Roxb. has been known for its high content of stilbenoids such as pinostilbene, desoxyrhapontigenin, pterostilbene, resveratrol and oxyresveratrol [2-10].

In our previous study [11], fifteen medicinal plant extracts were investigated for total phenolic content, free radical scavenging activities by DPPH and ABTS methods, anti-lipid peroxidation activity by TBARS, and antiglycation activity. We found that the ethanolic extract of Thai *A. lakoocha* shows high antiglycation and antioxidant activities. Glycation is a reaction that takes place when the reducing monosaccharides such as fructose or glucose bind to the proteins or lipids without the involvement of an enzyme and result in the formation of rogue molecules known as advanced glycation endproducts (AGEs).

A. lakoocha, an indigenous plant known in Thai as ‘Mahaad’, has been used in Thai traditional medicine for centuries. However, there has been no report dealing with antiglycation compounds in *A.*

lakoocha. This fact has inspired us to undertake this study, which has been designed to isolate and characterise the constituent(s) which shows both the antiglycation and radical scavenging activities in *A. lakoocha*.

MATERIALS AND METHODS

Plant Material

The heartwood of *A. lakoocha* was bought from Thai Lanna Herbal Industry Company Ltd. (52/2 Tambol Maehorphra, Maetang District, Chiang Mai) in August, 2006. The pieces of the sample were compared under microscope with the specimens of *A. lakoocha* from the herbarium of the Faculty of Pharmacy, Chiang Mai University and the authenticity of the plant was established.

Chemicals

The highest grades of all chemicals were used. Absolute ethanol, acetic acid and methanol were purchased from Lab-scan Ltd., Ireland. Aminoguanidine, bovine serum albumin (BSA), acetone, 1-butanol, 2,2-diphenyl-1-picryl hydrazyl (DPPH), D-glucose, ethyl acetate, n-hexane, 2-thiobarbituric acid (TBA), t-octylphenoxypolyethoxyethanol (Triton X-100), sodium sulphate anhydrous and quercetin were purchased from Sigma-Aldrich Chemical Co. Ltd, USA. Chloroform, D-fructose and sulfuric acid were purchased from Merck, Germany. 2,2'-Azobis-2-methyl-propanimidamide dihydrochloride (AAPH), butylated hydroxytoluene (BHT) and cholesterol (from lanolin) were purchased from Wako Pure Chemical Industries, Japan, Parchem Trading Ltd., USA, and Fluka Chemie GmbH., Japan respectively. OxyResvenox (oxyresveratrol), resveratrol and phosphatidylcholine were purchased from Sabinsa Co. Ltd, Germany, Calbiochem, Darmstadt, Germany and Epikulon 200, Degussa, Germany respectively.

Protein Glycation Assay

Protein glycation was assayed according to the method of Kim and Kim [12]. The test substance dissolved in 95% ethanol to make up an appropriate concentration was added to a solution consisting of bovine serum albumin (20 mg/ml), D-fructose (235 mM) and D-glucose (235 mM) in potassium phosphate buffer (200 mM, pH 7.4). The mixture was filtered through Whatman no.4 filter paper and incubated at 60°C for 30 hr. The fluorescence intensity was measured by a multimode detector spectrofluorometer (Model DTX 880, Beckman Coulter, Inc., USA) at an excitation wavelength of 370 nm and an emission wavelength of 440 nm. Aminoguanidine dissolved in 95% ethanol was used as a standard inhibitor [13].

Radical Scavenging Activity (DPPH Method)

The experiment was carried out according to the method of Liu et al. [14] with slight modification. Briefly, 20 µl of the test substance solution in 95% ethanol was mixed with 180 µl of 167 µM DPPH in methanol. The mixture was incubated at 37°C for 30 min and the absorbance was measured at 540 nm against reagent blank. The percentage of DPPH radical scavenging activity of the

test sample was determined at five sample concentrations within the range of 10–90% reduction in absorbance and calculated as follows:

$$\% \text{ DPPH radical-scavenging activity} = \frac{[(\text{absorbance of control} - \text{absorbance of sample}) \times 100]}{\text{absorbance of control}}$$

where 150.3 μM DPPH solution in 95% ethanol was used as control.

Lipid Peroxidation Inhibitory Activity (TBARS Method)

Lipid peroxidation assay was carried out according to thiobarbituric acid-reactive substance (TBARS) method reported by Chung et al. [15] with slight modification. A solution of soybean phosphatidylcholine (247.36 mg) and cholesterol (30.92 mg) in chloroform was dried under reduced pressure in a rotary evaporator below 50°C to give a thin homogenous film, which was placed in a desiccator for 24 hr. The film was then dispersed in phosphate buffer saline (PBS, 0.2 M, pH 7.2, 20 ml) in a water bath at 50°C. The mixture was sonicated to give a homogeneous suspension of liposome and then the test sample solution was added to the liposome suspension. In the following steps, AAPH, TBA, Triton X-100 and BHT dissolved in 95% ethanol were used. Lipid peroxidation was initiated by adding 60 μl AAPH solution (0.07 M) to the liposome in PBS solution (600 μl). The mixture was incubated at 50°C for 24 hr. After incubation, 250 μl of TBA solution (0.6% w/v) and 100 μl of Triton X-100 (3% v/v) were added, and 500 μl of BHT solution (20% v/v) was then added to terminate the reaction. The samples were then heated at 90°C for 30 min, cooled and the absorbance of the upper organic layer was measured against reagent blank at 540 nm.

Thin-Layer Chromatography (TLC)

Silica gel 60 F₂₅₄ plates (Merck) were used. The developing solvent was hexane/ethyl acetate/acetone (2:2:1 v/v/v). The spots were detected by UV irradiation (256 and 365 nm) and by heating after spraying with 20% sulfuric acid solution in 70% aqueous ethanol.

Isolation of Oxyresveratrol

The heartwood of *A. lakoocha* (2 kg.), which had been dried at 50°C in an air oven for 24 hr, was ground to powder and macerated for 6 hr in 95% ethanol three times. The alcoholic extracts were pooled and evaporated under reduced pressure below 45°C, whereupon 538 g of a crude extract was obtained. The crude extract (15.1 g) was suspended in 20% methanol (150 ml) and extracted with chloroform (300 ml). The aqueous layer was further extracted with ethyl acetate (3x300 ml). The ethyl acetate layer was evaporated to dryness below 45°C, whereupon 12.8 g of a powder was obtained. The powder (8 g) was dissolved in a small portion of ethyl acetate, silica gel (20g) was added and the mixture was dried under reduced pressure. The dried mixture was loaded onto a dry-packed silica gel column (7.5 cm i.d.×5.5cm) and developed successively using a solvent system of n-hexane/ethyl acetate/methanol (50:50:1.25 ; 48.75:48.75:2.5 ; 48.25:48.25:3.5 ; 46:46:8 ; 44:44:12). All the fractions were monitored by TLC and the fractions which showed similar TLC patterns were combined. A small portion of each combined fraction was tested for antiglycation and antioxidant activities. The fraction which showed highest activities was evaporated to dryness, whereupon 5.2 g of a powder was obtained. It was further purified by a silica gel column (4.5 cm i.d.×15 cm) using a solvent system of hexane/ethyl

acetate/methanol (2:2:0.05 v/v/v), whereupon a pure solid (AE5-3) was obtained (3.6 g, 10.3% overall from heartwood).

High Performance Liquid Chromatography (HPLC)

A reverse phase HPLC of the crude extract, the final pure solid (AE5-3) and standard oxyresveratrol was performed on HP HPLC series 1100 (Hewlett Packard, Waldbronn, Germany) equipped with Chem Station software, a degasser G1322A, a binary detection system G1314A, an Alltech Altima C18 column (250×4.6 mm i.d., 5 μm) and a C₁₈ guard column (Phenomenex 40×3.0 mm). The chromatographic separation was carried out using a linear gradient of mobile phase A (water) and mobile phase B (1% acetic acid in 35% MeOH). The elution profile was used as follows: 10%-55% B (50 min), 55%-100% B (10 min), and 100%-10% B (5 min). The flow rate was 1.0 ml/min. The eluate was on-line detected at 280 nm and monitored for 65 min. The column temperature was controlled at 25°C throughout the experiment.

Spectroscopic Studies

IR spectra (KBr tablet) were recorded on a Nicolet Nexus 470 FT-IR instrument (International Equipment Trading Ltd., USA). ¹H-NMR (400 MHz) and ¹³C-NMR (100 MHz) spectra were recorded on a Bruker Avance using TMS (for ¹H-NMR) and acetone-d₆ (for ¹³C-NMR) as an internal standards at 25°C. The studied sample was dissolved in acetone-d₆.

RESULTS AND DISCUSSION

Characterisation and Quantitation of Product Isolated from *A. lakoocha*

As shown in Figure 1, the ethanolic crude extract of *A. lakoocha*, the final pure solid isolated (AE5-3), and standard oxyresveratrol showed the same retention time at 3.5 min, suggesting that AE5-3 was oxyresveratrol. The IR spectrum of AE5-3 also matched that of the authentic oxyresveratrol. The ¹H-NMR and ¹³C-NMR spectral patterns of AE5-3 were in good agreement with those of standard oxyresveratrol (Figure 2) and also with those reported in the literature [16-17]. The signals of ¹H-NMR and ¹³C-NMR of AE5-3 were assigned as follows: δ (ppm) 7.38 (1H, d, J=8.5Hz, H-6), 7.31 (1H, d, J=16.5Hz, H-α), 6.86 (1H, d, J=16.5Hz, H-β), 6.50 (2H, s, H-2', H-6'), 6.40 (1H, d, J=2.4Hz, H-3), 6.38 (1H, dd, J=8.5, 2.4Hz, H-5), 6.22 (1H, s, H-4'). 159.0 (C-5' or C-3'), 158.9 (C-5' or C-3'), 158.6 (C-4), 156.4 (C-2), 141.1 (C-1'), 127.8 (C-6), 125.8 (olefinic C-β), 124.0 (olefinic C-α), 116.8 (C-1), 107.5 (C-5), 105.0 (C-6' or C-2'), 105.0 (C-6' or C-2'), 103.1 (C-3), 101.8 (C-4').

From the yield of the crude product and content of oxyresveratrol (AE5-3) in the crude product as determined by HPLC and a calibration curve, the oxyresveratrol content in the heartwood of *A. lakoocha* used in this study was found to be approximately 15% w/w.

Antioxidative and Antiglycation Activities

The antioxidant activity of AE5-3 was compared to those of quercetin and resveratrol by DPPH and TBARS methods. As shown in Figure 3, AE5-3 showed a strong DPPH radical scavenging activity (IC₅₀ = 0.10 ± 0.01 mg/ml) and lipid peroxydation inhibitory activity (IC₅₀ = 0.43 ± 0.03 mg/ml). These

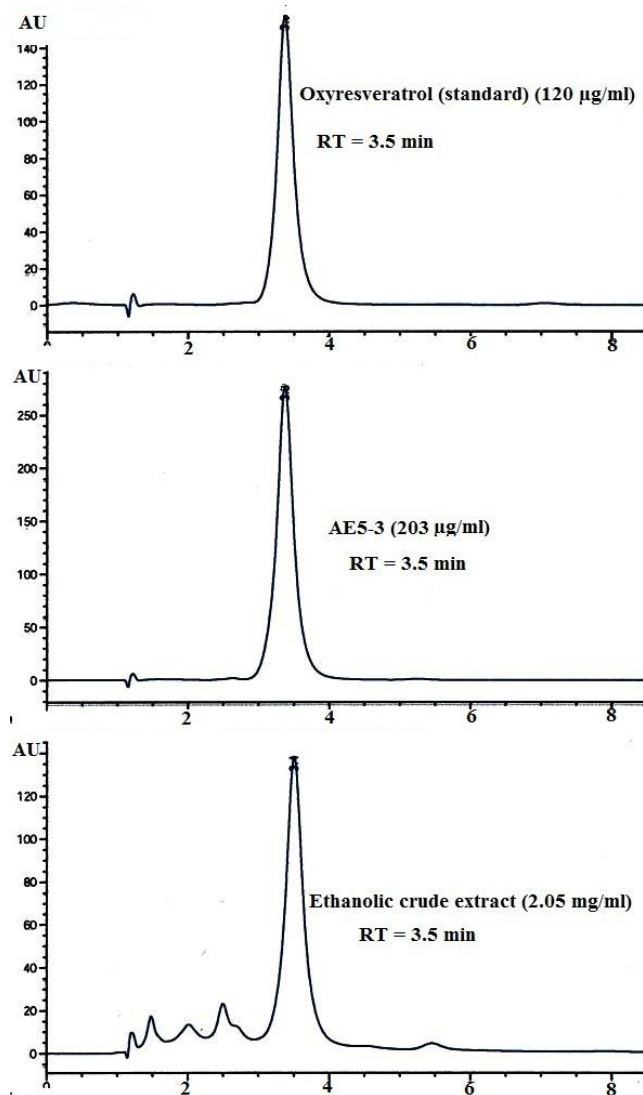


Figure 1. HPLC profile of oxyresveratrol, AE5-3 and ethanolic crude extract of *A. lakoocha*

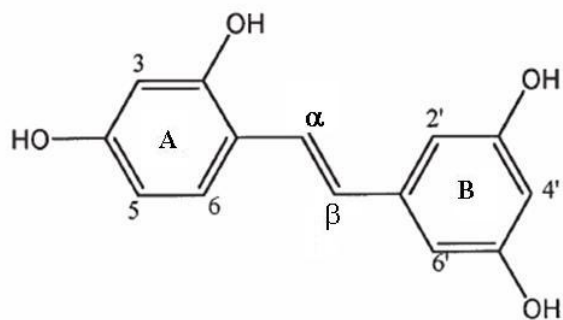


Figure 2. Chemical structure of oxyresveratrol

activities were comparable with those of quercetin. However, they were nearly twice as high as those of resveratrol ($p < 0.05$).

As shown in Figure 4, AE5-3 showed a strong antiglycation activity ($IC_{50} = 2.0 \pm 0.03 \mu\text{g/ml}$), which was 5-fold stronger than that of aminoguanidine, a hydrazine-like compound that blocks the formation of advanced glycation end products (AGEs) by interacting with amadori-derived products [13]. It is a prototype compound for the prevention of AGEs formation [18].

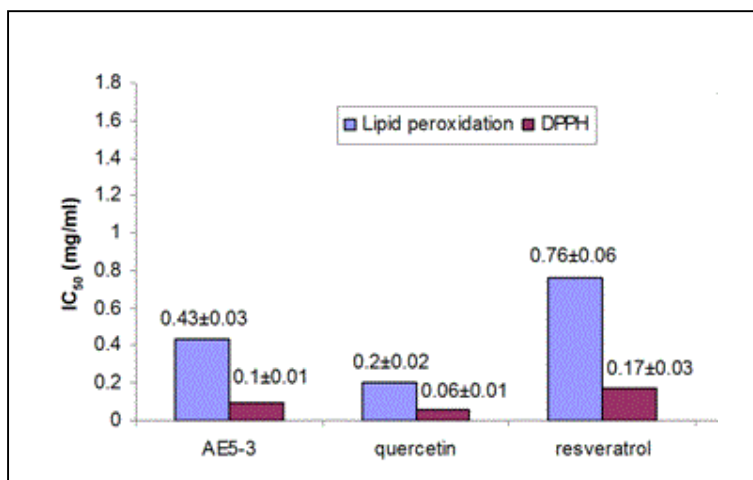


Figure 3. Antioxidant activity of AE5-3 and other antioxidant compounds. Figures in the graph were IC_{50} values (mean \pm SD).

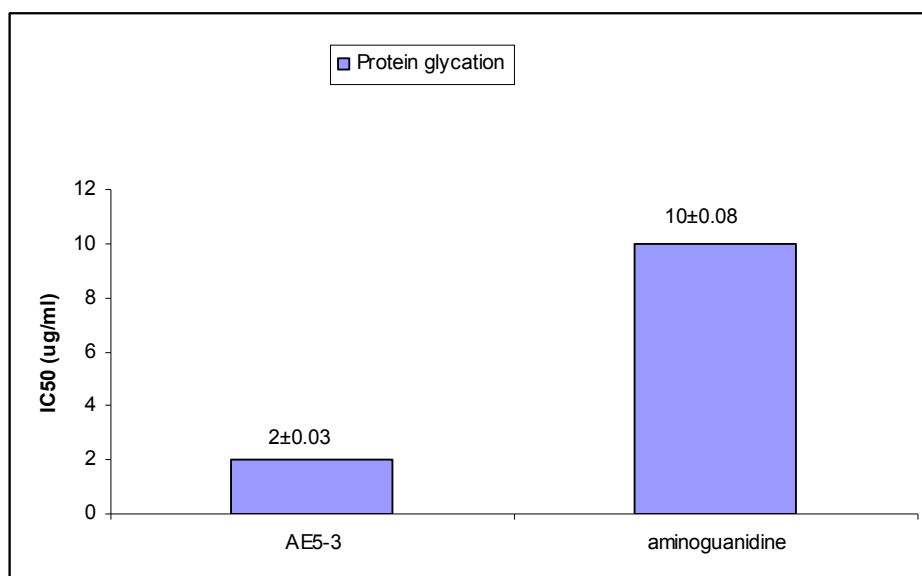


Figure 4. Antiglycation activity of AE5-3 and aminoguanidine. Figures in the graph were IC_{50} values (mean \pm SD).

Thus, in the present study, we have shown that oxyresveratrol, a compound present in a considerably large quantity in the heartwood of *Artocarpus lakoocha*, accounts for the strong antiglycation activity of its crude extract [11]. Protein glycation and oxidative stress are regarded as one of the critical factors that cause diabetes mellitus. Therefore, oxyresveratrol might prove to be another useful antidiabetic agent. Besides, this study also shows that the antioxidant activities of oxyresveratrol are about twice as strong as those of resveratrol. Several studies have shown that resveratrol can help in preventing cardiovascular diseases, cancer, inflammation and Alzheimer [19-22]. Thus, *Artocarpus lakoocha* with a high amount of oxyresveratrol may be expected to be another promising medicinal herb for these ailments.

ACKNOWLEDGEMENTS

The authors thank the Department of Pharmaceutical Sciences, Faculty of Pharmacy, Chiang Mai University for financial support.

REFERENCES

1. E. H. Hakim, S. A. Achmad and L. D. Juliawaty, "Prenylated flavonoids and related compounds of the Indonesian *Artocarpus (Moraceae)*", *J. Nat. Med.*, **2006**, *60*, 161-184.
2. K. Venkataraman, "Wood phenolics in the chemotaxonomy of the Moraceae", *Phytochem.*, **1972**, *11*, 1571-1586.
3. J. S. Chauhan and G. Kumari, "A new glycoflavonol from the root bark of *Artocarpus lakoocha*", *Planta Med.*, **1979**, *37*, 86-88.
4. J. Parao and V. Reutrakul, "New flavones in *Artocarpus lakoocha*". *Mahidol Univ. J. Pharm. Sci.*, **1976**, *3*, 161-166.
5. R. S. Kapil and S. S. Joshi, "Chemical constituents of *Artocarpus lakoocha* Roxb.", *J. Sci. Ind. Res.*, **1960**, *19B*, 498 (through *Chem. Abstr.*, *55*, 15536a).
6. G. Pavanadasivam, M. U. S. Sultanbawa and R. Mageswaran, "Cycloartenyl acetate, cycloartenol and cycloartenone in the bark of *Artocarpus* species", *Phytochem.*, **1973**, *12*, 2725-2726.
7. J. S. Chauhan and G. Kumari, "A new glycoflavonol from the root bark of *Artocarpus lakoocha*", *Planta Med.*, **1979**, *37*, 86-88.
8. J. S. Arora, R. S. Sandhu, S. S. Kamboj and S. K. Chopra, "Occurrence and characterization of lympho-agglutinins in Indian plants", *Vox Sang.*, **1987**, *52*, 134-137.
9. S. Mongkolsuk, A. Robertson and R. Towers, "2,4,3',5'-Tetrahydroxystilbene from *Artocarpus lakoocha*", *J. Chem. Soc.*, **1957**, 2231-2233.
10. P. Wetwitayaklung, "Chemical constituents from the heartwood of *Artocarpus lakoocha* Roxb.", *MS Thesis*, **1994**, Chulalongkorn University, Thailand.
11. N. Povichit, A. Phrutivorapongkul, M. Suttajit, C. Chaiyasut and P. Leelapornpisid, "Phenolic content and in vitro inhibitory effects on oxidation and protein glycation of some Thai medicinal plants", *Pakistan J. Pharm. Sci.*, **2010**, *23*, 403-408.
12. H. Y. Kim and K. Kim, "Protein glycation inhibitory and antioxidative activities of some plant extracts in vitro", *J. Agric. Food Chem.*, **2003**, *51*, 1586-1591.

13. J. L. Wilkinson-Berka, D. J. Kelly, S. M. Koerner, K. Jaworski, B. Davis, V. Thallas and M. E. Cooper, "ALT-946 and aminoguanidine, inhibitors of advanced glycation, improve severe nephropathy in the diabetic transgenic (mREN-2)27 rat", *Diabetes*, **2002**, *51*, 3283-3289.
14. D. Liu, J. Shi, A. C. Ibarra, Y. Kakuda, S. J. Xue, "The scavenging capacity and synergistic effects of lycopene, vitamin E, vitamin C, and β -carotene mixtures on the DPPH free radical", *LWT-Food Sci. Technol.*, **2008**, *41*, 1344-1349.
15. Y-C. Chung, C-T. Chien, K-Y. Teng and S-T. Chou, "Antioxidative and mutagenic properties of *Zanthoxylum ailanthoides* Sieb & Zucc", *Food Chem.*, **2006**, *97*, 418-425.
16. Z. Zhang, J. Jin and L. Shi, "Protective function of cis-mulberroside A and oxyresveratrol from *Ramulus mori* against ethanol-induced hepatic damage", *Environ. Toxicol. Pharmacol.*, **2008**, *26*, 325-330.
17. T. Kanchanapoom, K. Suga, R. Kasai, K. Yamasaki, M. S. Kamel and M. H. Mohamed, "Stilbene and 2-arylbenzofuran glucosides from the rhizomes of *Schoenocaulon officinale*", *Chem. Pharm. Bull.*, **2002**, *50*, 863-865.
18. P. J. Thornalley, "Use of aminoguanidine (Pimagedine) to prevent the formation of advanced glycation end products", *Arch. Biochem. Biophys.*, **2003**, *419*, 31-40.
19. P. Saiko, A. Szakmary, W. Jaeger and T. Szekeres, "Resveratrol and its analogs: Defense against cancer, coronary disease and neurodegenerative maladies or just a fad?", *Mut. Res.*, **2008**, *658*, 68-94.
20. F. Zhang, J. Liu and J. S. Shi, "Anti-inflammatory activities of resveratrol in the brain: Role of resveratrol in microglial activation", *Eur. J. Pharmacol.*, **2010**, *636*, 1-7.
21. F. Z. Marques, M. A. Markus and B. J. Morris, "Resveratrol: Cellular actions of a potent natural chemical that confers a diversity of health benefits", *Int. J. Biochem. Cell Biol.*, **2009**, *41*, 2125-2128.
22. S. Sánchez-Fidalgo, A. Cárdeno, I. Villegas, E. Talero and C. A. de la Lastra, "Dietary supplementation of resveratrol attenuates chronic colonic inflammation in mice", *Eur. J. Pharmacol.*, **2010**, *633*, 78-84.

Full Paper

Testing the recoverability of grass DNA transferred to textiles for forensic purpose

Francesc Francès*, Ana Castelló and Fernando Verdú

Department of Legal Medicine, School of Medicine, University of València, València, Spain

* Corresponding author, e-mail: francesc.frances@uv.es

Received: 1 July 2010 / Accepted: 15 November 2010 / Published: 19 November 2010

Abstract: Botanical evidence such as grass stains on textiles is sometimes present in the crime scene and can allow investigators to establish an association between persons linked to the criminal event and the crime scene. In this study, extraction of grass DNA from stains on textiles was undertaken. DNA extraction was performed on four grass species conserved both indoors and outdoors for 7, 14 and 30 days after staining. Once the extracted DNA was quantified, a polymerase chain reaction (PCR) amplifying a fragment of the internal transcribed spacer was performed.

DNA extraction was successful in 97.5% of samples. No significant differences in the amount of extracted DNA were detected among species or stain ages. However, one grass species (*Cynodon dactylon*) showed a significant diminution in the mean DNA concentration between indoor and outdoor samples (439.9 ± 137 ng/ μ L vs. 318.9 ± 177 ng/ μ L respectively; $p=0.041$). PCR was successful in 89.2% of samples.

This study has thus demonstrated the recoverability of grass DNA from stains on cloths and its stability in the first month after staining in both outdoor and indoor environments, as well as its suitability for PCR amplification that could allow correct species identification.

Keywords: grass DNA, forensic DNA analysis, forensic science

INTRODUCTION

Criminal investigation involves the recovery and processing of evidence from different origins and of different characteristics. Among this wide range of supporting data, forensic investigation often involves botanical traces that can potentially be useful for establishing links between individuals involved in a criminal event or at the scene of the crime. Among the huge variety of plants that could be

used as forensic evidence, grass species are of great importance as they are commonly present in both urban and rural areas and because traces of them can be transferred to several objects such as clothes and shoes.

Thus, efforts have been directed at setting up reliable, reproducible and standardised protocols and techniques of DNA analysis to correctly identify the vegetal species potentially useful as evidence. These techniques have been successfully applied to several plant samples, grass species among them [1]. For this species identification, the study of genetic sequences as internal transcribed spacer (ITS) has been proposed [2]. This study utilises leaf fragments as problem samples without considering the possibility that the plant, and specifically grass traces, may be present as textile stains, this latter case being commonly observed in daily forensic casework.

In the case of grass stains, morphological identification is obviously impossible, so DNA techniques are crucial to achieve species identification. To our knowledge, grass stains have not been evaluated for possible DNA recovery, nor has it been known whether the quantity and quality of recovered DNA (in the event of extraction being possible) will allow investigators to perform a successful polymerase chain reaction (PCR). Thus, the aim of this study is to evaluate these possibilities.

MATERIALS AND METHODS

Grass Species

Stains obtained from four grass species that are very common in the Iberian peninsula and other Mediterranean regions were tested. Three of these species (*Festuca arundinacea*, *Zoysia japonica* and *Stenotaphrum secundatum*) are frequently found in garden areas. The fourth, *Cynodon dactylon*, is used as ornamental grass in gardens, but it is also present as a ubiquitous Mediterranean wild grass, commonly found in natural environments and uncultivated fields. Species identification was done by morphological methods (quantitative and qualitative).

Sample Preparation

Grass stains were obtained by rubbing leaf samples against a white piece of cotton fabric. The rubbing was made with moderate pressing until a visible green stain was produced. From each grass species, ten stained pieces of fabric were made; five of them were kept in an indoor environment while the other five were placed outdoors. The outdoor samples received direct sunlight 3 hours a day. No rain fell in the month of the experiment so water was sprayed on the samples twice in order to compensate for this.

At the end of the 7th day, a 1×1 cm stained sample was cut from each of the 10 stained pieces of the fabric and DNA extraction was performed on each sample. The process was repeated at the end of day 14 and day 30. Thus, a total number of 30 samples for each grass species were extracted for DNA.

DNA Extraction

DNA extraction was performed according to Ahmed et al. [3]. All reagents were provided by Sigma-Aldrich, USA. A 1×1 cm piece of grass-stained fabric was placed in a reaction tube. An extraction buffer (400 µL: composed of 100 mM EDTA, 250 mM NaCl and 100 mM Tris-HCL) were

added, together with 10 μ L of dithiotreitol, 10 μ L of proteinase K (10 μ g/ μ L), 8 μ L of 98% 2-mercaptoethanol and 10 μ L of 20% sodium dodecyl sulphate. After being gently mixed in a vortex for one minute, the mixture was incubated overnight at 65°C.

After incubation, the textile piece was eliminated from the tube. Phenol-chloroform-isoamyl alcohol (25:24:1, 400 μ L) was added to the remaining liquid phase and the two phases gently mixed for 20 seconds. The tube was then centrifuged at 15000 rpm for 5 minutes and the upper phase was collected and poured into a Microcon filter (100- μ pore diameter, Millipore Inc., USA) that had been previously hydrated with 100 μ L of doubly distilled water. After centrifugation at 3000 rpm for 25 minutes, the filter was placed in another reaction tube and 200 μ L of doubly distilled water were added and the tube centrifuged again at 3000 rpm for 25 minutes in order to wash the filter. Finally, 60 μ L of doubly distilled water were added to the filter before placing it in inverted position in a new tube. A final centrifugation at 4000 rpm for 5 minutes allowed the recovery of DNA from the filter.

The DNA concentrate was automatically quantified by spectrophotometry using a Nanophotometer™ (Implen GmbH, Germany). Absorbance at 260 nm was used. The function describing the absorbance-to-concentration relation was a modification of the Lambert-Beer equation: $c_{\text{nuc}} = A_{260} * \text{factor nuc} * \text{dilution factor}$, where c_{nuc} is nucleic acid concentration (ng/ μ l); A_{260} is absorbance (AU) of nucleic acids; and factor nuc is substance specific factor for nucleic acids (ng * cm/ μ l), which equals 50 in the case of double-stranded DNA.

PCR Testing

In order to check for the PCR suitability of the stain-derived grass DNA, an explorative PCR was performed on all samples. A pair of angiosperm universal primers was selected for this purpose [4]. These oligonucleotides amplify an inter-species constant fragment of the ITS, thus generating a constant 589-bp amplicon.

The PCR conditions and reagents were as follows. DNA was amplified in a 96-plate thermocycler (Eppendorf, Germany). The reaction mixture used in the PCR consisted of 10 ng of genomic DNA, 0.2 μ M of each primer (Roche Diagnostics GmbH, Germany), 0.6 unit of Go Taq polymerase (Promega Inc., USA), 2.5 mM of MgCl₂, 10 mM of Tris-HCl (10x), 50 mM of potassium chloride, and 200 μ M of deoxynucleotide triphosphate (Roche Diagnostics GmbH, Germany), in a total volume of 25 μ L. After an initial denaturation at 94°C for 6 minutes, 30 PCR cycles were performed with 45 seconds of denaturation at 94°C, 45 seconds of annealing at 58°C, and an extension for 45 seconds at 72°C. Finally, a single extensional step at 72°C for 10 minutes was performed.

Amplified products were separated by horizontal electrophoresis (80-100 mA) in a 2% agarose gel (Sigma-Aldrich, USA) and diluted in TAE buffer (2 M Tris-acetate and 100 mM sodium EDTA, National Diagnostics, USA). After a 10-minute exposure to ethidium bromide solution (0.5 μ g/mL, Sigma-Aldrich, USA), amplified DNA fragments were visualised with UV light (254 nm).

Statistical Analysis

All statistical analyses were performed by using the SPSS software package (SPSS Inc., Chicago, Illinois). The Kolmogorov-Smirnov test [5] was undertaken in order to assess the normality of the DNA concentration value distribution. ANOVA and t Student tests were performed in order to

study mean DNA concentration differences between groups. Statistical significance was defined as $p < 0.05$.

RESULTS AND DISCUSSION

Table 1 shows mean DNA concentrations obtained from each grass species in both indoor and outdoor environments at different analysis times. In three cases (2.5%), no DNA was obtained. Eight samples (6.7%) gave DNA concentrations under 20 ng/ μ L.

Table 1. Mean DNA concentration values obtained for each grass species under different conditions

	Indoor condition			<i>p</i>	Outdoor condition			<i>p</i> *
	Day 7	Day 14	Day 30		Day 7	Day 14	Day 30	
<i>Cynodon dactylon</i> Mean \pm SD(ng/ μ L)	412.6 \pm 78.8	458.2 \pm 160.9	448.0 \pm 152.1	0.856	324.2 \pm 129.0	303.3 \pm 178.0	329.0 \pm 248.5	0.976
<i>Stenotaphrum secundatum</i> Mean \pm SD(ng/ μ L)	363.6 \pm 309.9	511.2 \pm 246.7	561.8 \pm 367.8	0.606	317.8 \pm 157.7	455.8 \pm 139.9	406.8 \pm 338.7	0.181
<i>Zoysia japonica</i> Mean \pm SD(ng/ μ L)	540.2 \pm 171.5	419.6 \pm 280.8	422.6 \pm 330.9	0.728	340.4 \pm 166.3	367.0 \pm 225.9	554.6 \pm 330.2	0.368
<i>Festuca arundinacea</i> Mean \pm SD(ng/ μ L)	459.8 \pm 196.6	562.0 \pm 322.8	360.4 \pm 344.7	0.574	427.8 \pm 107.6	547.2 \pm 378.1	390.2 \pm 275.2	0.655

Note: *p* and *p** are significance values of the comparison between means obtained at the three different times for indoor and outdoor samples respectively.

After the normal distribution of DNA concentration values had been confirmed, the difference between indoor and outdoor mean concentrations for each species was assessed. DNA concentrations from *C. dactylon* showed significantly lower values in outdoor samples (318.9 \pm 177 ng/ μ L vs. 439.9 \pm 137 ng/ μ L; $p=0.041$). The other three species did not show significant differences between mean outdoor and indoor values (*S. secundatum*: 386.8 \pm 158.2 ng/ μ L vs. 472.9 \pm 295.0 ng/ μ L, $p=0.411$; *Z. japonica*: 420.7 \pm 251.7 ng/ μ L vs. 460.5 \pm 256.1 ng/ μ L, $p=0.608$; *F. arundinacea*: 455.1 \pm 285.7 ng/ μ L vs. 460.7 \pm 286.4 ng/ μ L, $p=0.956$). When the indoor-outdoor comparison was undertaken taking the sample age separately (7days, 14days and 30days), no differences were found in any of the four species. (Means are displayed in Table 1 with the following *p* values: *C. dactylon* - 0.227, 0.188 and 0.385; *S. secundatum* - 0.776, 0.674 and 0.417; *Z. japonica* - 0.098, 0.753 and 0.545; *F. arundinacea* - 0.758, 0.949 and 0.884 respectively). Furthermore, when DNA values for the four species were taken together, neither indoor nor outdoor means showed significant difference (458.3 \pm 243.3 ng/ μ L for indoor samples vs. 396.1 \pm 223.4 ng/ μ L for outdoor samples, $p=0.159$).

When the possible effect of storage time in both environments was assessed, it was found that none of the grasses showed significant difference in the final DNA concentrations of samples at different ages (data shown in Table 1). Also, there was no statistical difference in the mean amounts of extracted DNA between the species, either for indoor or outdoor samples ($p=0.987$ and $p=0.395$ respectively).

The first PCR assay was successful in 107 samples (89.2%). After further repeating the PCR twice, seven samples still did not provide any PCR product. Three of them had previously shown no DNA in the spectrometric measurement while the four remaining samples, despite containing an appropriate DNA concentration, repeatedly failed in the PCR assay. In all other cases, the PCR product had the expected 589-bp size.

In forensic investigation, DNA extraction from biological stains is of great importance. In the case of samples of human origin, protocols and techniques are well defined and characterised. However, little attention has been paid to DNA extraction from plant-originated stains. In the case of grass species, friction between plant and textile or other materials usually results in the transfer of biological traces to these items and species identification can often provide some evidence owing to the restricted and specific geographic distribution of each kind of grasses. Short tandem repeats (STR) and single nucleotide polymorphisms (SNP) have been proposed as useful techniques for species identification [6]. DNA barcoding [7], however, is the most commonly reported species identification technique in recent researches [8-9]. Grasses have also been successfully tested with this new technique [1]. However, these studies employed leaves or leaf fragments as samples and have not taken into account the possibility that plant material may be present in stain form. This possibility is especially frequent in the case of grass samples that have been transferred by friction with clothes, shoes or other materials. In contrast to intact leaves, stain production may hypothetically alter cell walls and membranes and thus lead to greater DNA exposure to degrading agents in the environment, which may affect its recoverability and integrity.

In the present investigation, we set out from the hypothesis that friction between grass leaves and textiles can be considered analogous to the grinding of leaf fragments with a pestle performed in standard plant DNA extraction protocols. Thus, following this hypothesis, we used a standard extraction buffer with very good results as in only three cases did the DNA extraction register a complete failure. DNA from both indoor and outdoor samples was successfully extracted in nearly all samples and in all species at all three storage periods. We did find a decrease in the mean extracted DNA concentration for outdoor samples in all four species. However, only in the case of *C. dactylon* did the decrease reach statistical significance. The causes of this phenomenon could possibly be attributed, apart from the characteristics of this particular species, to slight variation in the amount of plant material attached to the fabric when the stain was made, the intensity of received sunlight, and the level of humidity applied to the samples.

Another aspect that should be had in mind is the suitability of extracted DNA for amplifying moderately heavy DNA fragments. In old stains or outdoor conditions, the possibility of DNA degradation must not be underestimated. In these cases, amplification of heavy DNA fragments may fail and species identification will have to be achieved by using lighter amplicons. In all tested environments,

species and stain ages, the PCR of a moderately heavy product was successful in nearly all samples, thus suggesting that no significant degradation occurred in these samples.

CONCLUSIONS

The recoverability of grass DNA from cloth stains has been demonstrated, which shows the stability of this DNA during the first month after the stain was made in both outdoor and indoor environments, and also its suitability for PCR amplification of relatively heavy DNA fragments that could allow correct species identification.

ACKNOWLEDGEMENT

We gratefully acknowledge F. Gimenez-Fernández for laboratory assistance.

REFERENCES

1. J. Ward, S. R. Gilmore, J. Robertson and R. Peakall, "A grass molecular identification system for forensic botany: a critical evaluation of the strengths and limitations", *J. Forensic Sci.*, **2009**, 54, 1254-1260.
2. M. Wesselink and I. Kuiper, "Species identification of botanical trace evidence using molecular markers", *Forensic Sci. Int. Genet. Suppl. Series*, **2008**, 1, 630-632.
3. I. Ahmed, M. Islam, W. Arshad, A. Mannan, W. Ahmad and B. Mirza, "High-quality plant DNA extraction for PCR: An easy approach", *J. Appl. Genet.*, **2009**, 50, 105-107.
4. T. J. White, T. Bruns, S. Lee and J. W. Taylor, "Amplification and direct sequencing of fungal ribosomal RNA genes for phylogenetics", in "PCR Protocols: A Guide to Methods and Applications" (Ed. M. A. Innis, D. H. Gelfand, J. J. Sninsky and T. J. White), Academic Press, New York, **1990**.
5. F. J. Massey, "The Kolmogorov-Smirnov test for goodness of fit", *J. Amer. Stat. Assoc.*, **1951**, 46, 68-78.
6. J. C. Fowler, J. M. Kijas and M. R. Thomas, "Current molecular methods for plant genome identification", *Australas Biotechnol.*, **1994**, 4, 153-157.
7. P. D. Hebert, A. Cywinska, S. L. Ball and J. R. deWaard, "Biological identifications through DNA barcodes", *Proc. Biol. Sci.*, **2003**, 270, 313-321.
8. G. Ferri, M. Alù, B. Corradini and G. Beduschi, "Forensic botany: Species identification of botanical trace evidence using a multigene barcoding approach", *Int. J. Legal Med.*, **2009**, 123, 395-401.
9. W. J. Kress, D. L. Erickson, F. A. Jones, N. G. Swenson, R. Perez, O. Sanjur and E. Bermingham, "Plant DNA barcodes and a community phylogeny of a tropical forest dynamics plot in Panama", *Proc. Natl. Acad. Sci. USA*, **2009**, 106, 18621-18626.

Full Paper

Natural convection of nanofluids in a cavity with linearly varying wall temperature

Sivanandam Sivasankaran^{1,*}, Thangaraj Aasaithambi² and Subbarayagounder Rajan³

¹ University College, Sungkyunkwan University, Suwon 440-746, South Korea

² Department of Mathematics, Sengunthar Engineering College, Tiruchengode – 637205, India

³ Department of Mathematics, Erode Arts and Science College, Erode – 638 009, Tamilnadu, India

* Corresponding author, e-mail: sd.siva@yahoo.com

Received: 28 April 2010 / Accepted: 16 July 2010 / Published: 26 November 2010

Abstract: The aim of the present numerical study is to investigate the convective flow and heat transfer behaviour of nanofluids with different nano-particles in a square cavity. The hot left wall temperature of the cavity is varied linearly with height whereas the cold right wall temperature is kept constant. The finite volume method is used to discretise the transport equations, which are solved by iterative method. Numerical simulations are carried out for different combinations of pertinent parameters involved in the study. It is found that the heat transfer rate increases on increasing the volume fraction of the nanofluid for all types of nanoparticles considered. The increment in average Nusselt number is strongly dependent on the nanoparticle chosen.

Keywords: convective heat transfer, nanofluid, linearly varying wall temperature

Nomenclature

c_p	specific heat, J/(kg·K)
F_o	dimensionless time
g	acceleration due to gravity, m/s ²
h	heat transfer coefficient
k	thermal conductivity, W/(m·K)
L	size of enclosure, m
Nu	local Nusselt number
\overline{Nu}	average Nusselt number
Pr	Prandtl number, ν_f/α_f

p	Pressure, Pa
Ra	Rayleigh number, $\frac{g\beta_f(\theta_h - \theta_c)L^3}{\nu_f\alpha_f}$
T	dimensionless temperature
t	time, s
u, v	velocity components, m/s
U, V	dimensionless velocity components
x, y	Cartesian coordinates
X, Y	dimensionless coordinates

Greek symbols

α	thermal diffusivity, m^2/s
β	volumetric coefficient of thermal expansion, 1/K
ε	heat transfer coefficient ratio
ϕ	volume fraction of nanofluid
μ	dynamic viscosity, Pa·s
ν	kinematic viscosity, μ_f/ρ_f
ρ	density, kg/m^3
θ	temperature, K
ψ	dimensionless stream function

Subscripts

c	cold wall
e	effective
h	hot wall
f	base fluid
n	nanofluid
p	nanoparticle

Superscript

*	property ratio
---	----------------

INTRODUCTION

Convective heat-transfer cooling enhancement technique has been a major problem in engineering and technological applications due to thermal management of small devices. The efficacy of such cooling process is restricted by poor thermal properties of the working medium. A better heat transfer medium is needed for the convective heat transfer technique to overcome this limitation. Recently, fluids with nanometre-sized particles suspended in them, called nanofluids, first termed by Choi and Eastman [1], have been considered. Much work has been conducted to study the physical properties of nano-particles but little studied is the convective heat transfer of nanofluids in enclosures [2-5]. Before using nanofluids in practical applications, an investigation on convective heat transfer

technique is needed in detail. In the present work, a numerical study is conducted to investigate the heat transfer and fluid flow characteristics of nanofluids inside an enclosure.

Some researchers analysed the convective heat transfer of nanofluids by considering different models of nanofluid properties in an enclosure. Khanafer et al. [6] numerically investigated the buoyancy-driven convection in a two-dimensional enclosure filled with nanofluids. They found that the heat transfer rate increases with an increase in the nanoparticle volume fraction. Jou and Tzeng [7] performed a numerical study on the effect of small aspect ratio on the natural convection of nanofluids in a rectangular enclosure. They found that the average Nusselt number at the hot wall increases as the aspect ratio decreases. Wen and Ding [8] made an experimental study on heat transfer using titanium-dioxide-based nanofluid. The results showed that the presence of the nanoparticles decreases the convective heat transfer rate. Hwang et al. [9] studied theoretically the thermal characteristics of natural convective heat transfer of water-based Al_2O_3 nanofluid in a rectangular cavity. They used two different models to calculate the effective viscosity of the nanofluid and compare the results obtained from these models. They showed that the ratio of the heat transfer coefficient of the nanofluid to that of the base fluid decreases as the size of the nanoparticles increases.

Ho et al. [10] numerically studied the effects of uncertainty in the effective viscosity and thermal conductivity of nanofluids on convection in an enclosure. They concluded that the effective dynamic viscosity should be taken into account when studying the heat transfer efficacy of natural convection in enclosures. Abu-Nada et al. [11] studied natural convection in horizontal concentric annuli filled with nanofluids containing various nanoparticles. Similar investigation in a partially heated rectangular enclosure was numerically studied by Oztop and Abu-Nada [12]. They found that the enhancement of the heat transfer is more pronounced at low aspect ratio than at high aspect one. Santra et al. [13] numerically studied natural convection of nanofluids in a differentially heated square cavity. They treated the nanofluids as non-Newtonian. Ghasemi and Aminossadati [14] showed that the heat transfer rate is maximised at a specific inclination angle depending on the Rayleigh number and the volume fraction of nanoparticles when studying the convection in an inclined enclosure filled with water-CuO nanofluid.

In most of the numerical or experimental studies on convective heat transfer of nanofluids, researchers have considered the cavity with either isothermal or isoflux thermal boundary conditions for vertical walls. However, these thermal boundary conditions are not suitable in many applications such as heat exchangers, injection moldings and solidification processes. We need the knowledge of the effect of variable wall temperature for some applications. Hossain and Wilson [15] performed a numerical study to investigate the natural convection in a porous enclosure with internal heat generation under linearly varying temperature boundary condition. Laminar natural convection in a two-dimensional square cavity with non-uniform side-wall temperature was studied numerically by Saeid and Yaacob [16]. They found that the average Nusselt number varies based on the hot-wall temperature. Sathiyamoorthy et al. [17] numerically investigated natural convection flow in a square cavity with linearly heated vertical walls and uniformly heated bottom wall. Dare and Petinrin [18] studied the natural convective flow along isothermal plates and in channels using diffusion velocity method. They found that as the wall temperature increases while keeping the mainstream fluid temperature constant, the thermal boundary layer thickness increases.

The above-mentioned studies are concerned with convection in enclosures with fluids or fluid-saturated porous medium with variable boundary conditions. No work seems to have been carried out on convective flow of nanofluids for such thermal boundary conditions. Therefore, the present study aims to investigate the effect of natural convective heat transfer and fluid flow characteristics in a square cavity with linearly varying hot-wall temperature utilising nanofluids.

MATHEMATICAL ANALYSIS

Consider a two-dimensional square cavity of size L filled with water-based nanofluid containing nanoparticles as shown in Figure 1. The left vertical wall of the cavity is heated linearly with height while the right vertical wall is cooled at a constant temperature and the horizontal walls are insulated. The nanofluid in the enclosure is a solid-liquid mixture with uniform volume fraction ϕ , shape and size of nanoparticles dispersed in base fluid water. Various nanoparticles, viz. Al_2O_3 , Cu, Ag and TiO_2 , are used in the study. The flow is assumed to be incompressible and laminar. It is also assumed that both the nanoparticles and the base fluid are in thermally equilibrium. The Boussinesq approximation is valid for the buoyancy term and all other thermophysical properties are assumed to be constant. In addition, the viscous dissipation is assumed to be negligible.

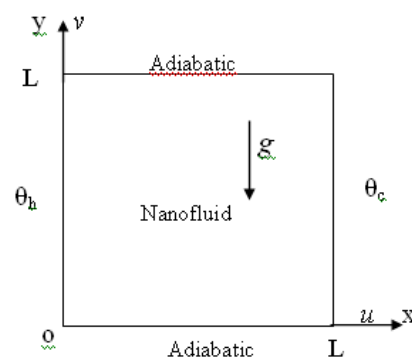


Figure 1. Physical configuration and coordinate system of a two-dimensional square cavity

The mathematical model for fluid flow and heat transfer for the above-mentioned geometrical and physical conditions and assumptions in non-dimensional form can be written as follows.

$$\frac{\partial U}{\partial X} + \frac{\partial V}{\partial Y} = 0 \quad (1)$$

$$\frac{\partial U}{\partial Fo} + U \frac{\partial U}{\partial X} + V \frac{\partial U}{\partial Y} = -\frac{\partial P}{\partial X} + \text{Pr}_f \left(\frac{C_{p,nf}^* \mu_{nf}^*}{k_{nf}^*} \right) \left[\frac{\partial^2 U}{\partial X^2} + \frac{\partial^2 U}{\partial Y^2} \right] \quad (2)$$

$$\frac{\partial V}{\partial Fo} + U \frac{\partial V}{\partial X} + V \frac{\partial V}{\partial Y} = -\frac{\partial P}{\partial Y} + \text{Pr}_f \left(\frac{C_{p,nf}^* \mu_{nf}^*}{k_{nf}^*} \right) \left[\frac{\partial^2 V}{\partial X^2} + \frac{\partial^2 V}{\partial Y^2} \right] + Ra_f \text{Pr}_f \beta_{nf}^* \left(\frac{\rho_{nf}^* C_{p,nf}^*}{k_{nf}^*} \right)^2 T \quad (3)$$

$$\frac{\partial T}{\partial Fo} + U \frac{\partial T}{\partial X} + V \frac{\partial T}{\partial Y} = \left[\frac{\partial}{\partial X} \left(k_{en}^* \frac{\partial T}{\partial X} \right) + \frac{\partial}{\partial Y} \left(k_{en}^* \frac{\partial T}{\partial Y} \right) \right] \quad (4)$$

The physical property ratios present in equations (2-4) are as follows: $k_{nf}^* = \frac{k_n}{k_f}$, $k_{en}^* = \frac{k_e}{k_n}$, $\mu_{nf}^* = \frac{\mu_n}{\mu_f}$, $c_{p,nf}^* = \frac{c_{p,n}}{c_{p,f}}$, $\rho_{nf}^* = \frac{\rho_n}{\rho_f}$ and $\beta_{nf}^* = \frac{\beta_n}{\beta_f}$, where the subscripts n and f denote, respectively, the nanofluid and the base fluid. Moreover, k_e denotes the effective thermal conductivity associated with possible heat transfer enhancement mechanisms of the nanofluid such as Brownian motion, liquid layering at liquid/particle interface, and phonon movement in nanoparticles. The effective thermophysical properties of a nanofluid can be evaluated using various formulae available in the literature. The formulae selected for the thermophysical properties of the nanofluid in the present study are as follows [10], and the thermophysical properties of the base fluid (water) and various nanoparticles are presented in Table 1.

$$\text{Density:} \quad \rho_n = (1-\phi)\rho_f + \phi\rho_p \quad (5)$$

$$\text{Thermal expansion coefficient:} \quad \beta_n = \frac{1}{\rho_n} [(1-\phi)\rho_f\beta_f + \phi\rho_p\beta_p] \quad (6)$$

$$\text{Specific heat:} \quad c_{p,n} = (1-\phi)c_{p,f} + \phi c_{p,p} \quad (7)$$

Thermal conductivity: This is evaluated from the well-known Maxwell formula [10] as

$$k_n = k_f \left[\frac{2 + k_{pf}^* + 2\phi(k_{pf}^* - 1)}{2 + k_{pf}^* - \phi(k_{pf}^* - 1)} \right] \quad (8)$$

$$\text{with } k_{pf}^* = \frac{k_p}{k_f}.$$

Dynamic viscosity: The Brinkman's formula [19] is used for the effective dynamic viscosity of a nanofluid, which is expressed as

$$\mu_n = \mu_f(1-\phi)^{-2.5} \quad (9)$$

The initial and boundary conditions in the dimensionless form are:

$$F_0 = 0; \quad U=V=T=0 \quad \text{at} \quad 0 \leq X \leq 1 \text{ and } 0 \leq Y \leq 1$$

$$F_0 > 0; \quad U=V=0, \quad \frac{\partial T}{\partial Y} = 0 \quad \text{at} \quad Y = 0 \text{ and } 1$$

$$U=V=0, T=Y \quad \text{at} \quad X=0 \text{ and } 0 \leq Y \leq 1$$

$$U=V=0, T=0 \quad \text{at} \quad X=1 \text{ and } 0 \leq Y \leq 1$$

Table 1. Thermophysical properties of base fluid (water) and various nanoparticles [10-11]

Property	Base fluid	Nanoparticles			
	Water	Alumina (Al ₂ O ₃)	Copper (Cu)	Silver (Ag)	Titanium oxide (TiO ₂)
Density (ρ)	997.1	3970	8933	10500	4250
Specific heat (Cp)	4179	765	385	235	686.2
Thermal conductivity (k)	0.613	40	401	429	8.9538
Coefficient of thermal expansion ($\beta \times 10^{-5}$)	21	0.85	1.67	1.89	0.9
Thermal diffusivity ($\alpha \times 10^7$)	1.47	131.7	1163.1	1738.6	30.7

The following non-dimensional variables are used: $(X, Y) = (x, y)/L$, $(U, V) = (u, v)L/\alpha_n$, $Fo = t\alpha_n/L^2$, $P = \rho L^2/(\rho_n \alpha_n^2)$ and $T = (\theta - \theta_c)/(\theta_h - \theta_c)$. The non-dimensional numbers appearing in the above equations are: Ra (Rayleigh number) = $\frac{g\beta_f(\theta_h - \theta_c)L^3}{\nu_f \alpha_f}$ and Pr (Prandtl number) = ν_f/α_f . The stream

function is calculated using $U = \frac{\partial \Psi}{\partial Y}$ and $V = -\frac{\partial \Psi}{\partial X}$. The heat transfer rate at the hot wall of the cavity is presented by means of the Nusselt number, which is evaluated as follows:
 $Nu_h = \frac{h_n L}{k_f} = -k_{nf}^* \frac{\partial T}{\partial Y} \Big|_{X=0}$. The average Nusselt number along the hot wall is obtained by integrating

the local Nusselt number over the hot wall:

$$\overline{Nu} = \int_0^1 Nu_h dY. \quad (10)$$

In addition, it is also important to quantify the heat transfer efficacy of the nanofluid compared to that of the base fluid. The ratio of the average heat transfer coefficient of the nanofluid at the hot wall to that of the base fluid, ε_h , is calculated as

$$\varepsilon_h = \frac{\overline{h_n}}{h_f}. \quad (11)$$

METHOD OF SOLUTION

Numerical Method

The non-dimensional governing equations, together with boundary conditions, are discretised by implicit finite volume method, which is explained by Patankar [20]. The QUICK scheme is used for the convection terms and the central difference scheme is used for diffusion terms. The velocity and pressure are coupled by SIMPLE algorithm [20]. The solution domain is discretised with non-uniform mesh in both X and Y directions [10]. The grids are clustering towards the walls of the cavity. The effect of grid size is tested to select the appropriate grid density among a range from 41×41 to 161×161

for $Ra = 10^6$, $Pr = 6.7$ and constant fluid properties; see Figure 2. It is observed from the grid independence test that an 81×81 grid is enough to investigate the problem. The time step is chosen to be uniform, $\nabla F_0 = 10^{-5}$. The resulting algebraic equations are solved by iterative method. The iterations are stopped when the convergence criterion $\left| \frac{\varphi_{(n+1)}(i,j) - \varphi_{(n)}(i,j)}{\varphi_{(n+1)}(i,j)} \right| \leq 10^{-6}$ is met for all variables $\varphi (= U, V, T)$.

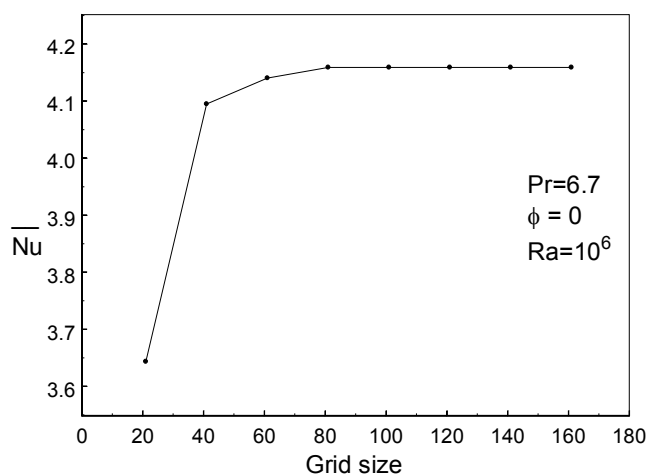


Figure 2. Grid independent test

Code Validation

The validation of present computational code for this study is verified against the existing results available in the literature. Simulations are carried out for natural convection in a differentially heated square cavity with isothermal walls for Rayleigh number ranging from 10^3 to 10^6 to validate the present code. The results obtained from the present code are compared with those by Khanafer et al. [6], Ho et al. [10], de Vahl Davis [21], Hadjisophocleous et al. [22], Fusegi et al. [23] and Barakos et al. [24] (Table 2). It is clearly seen from the table that the computed results are in good agreement with the solutions available in the literature.

Table 2. Comparison of present results (average Nusselt number) with existing ones available in the literature

Ra	\overline{Nu}						
	Present	Khanafer et al. [6]	Ho et al. [10]	Davis [21]	Hadjisophocleous et al. [22]	Fusegi et al. [23]	Barakos et al. [24]
10^3	1.118	1.118	1.118	1.118	1.141	1.106	1.114
10^4	2.281	2.245	2.246	2.238	2.290	2.302	2.245
10^5	4.728	4.522	4.522	4.509	4.964	4.646	4.510
10^6	8.959	8.826	8.825	8.817	10.390	9.012	8.806

RESULTS AND DISCUSSION

A numerical study is performed to investigate the natural convective flow and heat transfer characteristics of water-based nanofluids with various nanoparticles of different volume fractions in a cavity. The value of Prandtl number for the base fluid (water) is taken to be 6.7. Computations are carried out for the Rayleigh number ranging from 10^3 to 10^6 , and the volume fraction ϕ of nanoparticles between 0-4%. The results obtained are discussed under different combinations of pertinent parameters involved in the study. Figure 3 shows a comparison of average Nusselt number of isothermal and linearly varying hot walls using pure fluid and Al_2O_3 nanofluid with volume fraction $\phi=0.04$. It is clearly seen from the figure that there is much difference in the heat transfer rate of the linearly varying hot wall and the isothermal wall. The difference in the average Nusselt number between the two boundary conditions increases with increasing Rayleigh number.

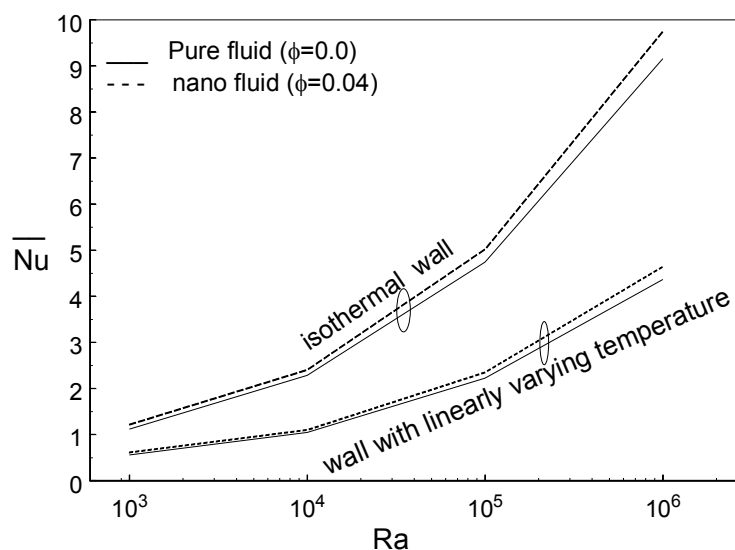


Figure 3. Average Nusselt number of isothermal wall and linearly varying hot wall using pure fluid and Al_2O_3 nanofluid with $\phi=0.04$

Though four types of nanoparticles are used, the illustrated figures for isotherms and streamlines with different values of Rayleigh number are provided only for Al_2O_3 nanofluid for brevity of the paper. Figure 4 shows fluid flow and heat transfer characteristics of Al_2O_3 nanofluid and pure fluid (water) for different values of Rayleigh number. The flow pattern consists of a single cell occupying the whole cavity. The core region of the cell is at the middle of the enclosure when $Ra \leq 10^4$. The isotherms are distributed almost equally throughout the enclosure. Here, convection is weakened and conduction is the dominant mode of heat transfer. The core region of the nanofluid is reduced compared to pure fluid for all values of Rayleigh number. When the Rayleigh number increases, the core region of the cell moves towards the cold wall and elongates. The corresponding isotherms show a vertical temperature stratification in the core region of the cavity. The core region moves towards the top-right corner of the enclosure when $Ra \geq 10^5$. The isotherms cluster along the thermally active walls and form thermal boundary layers.

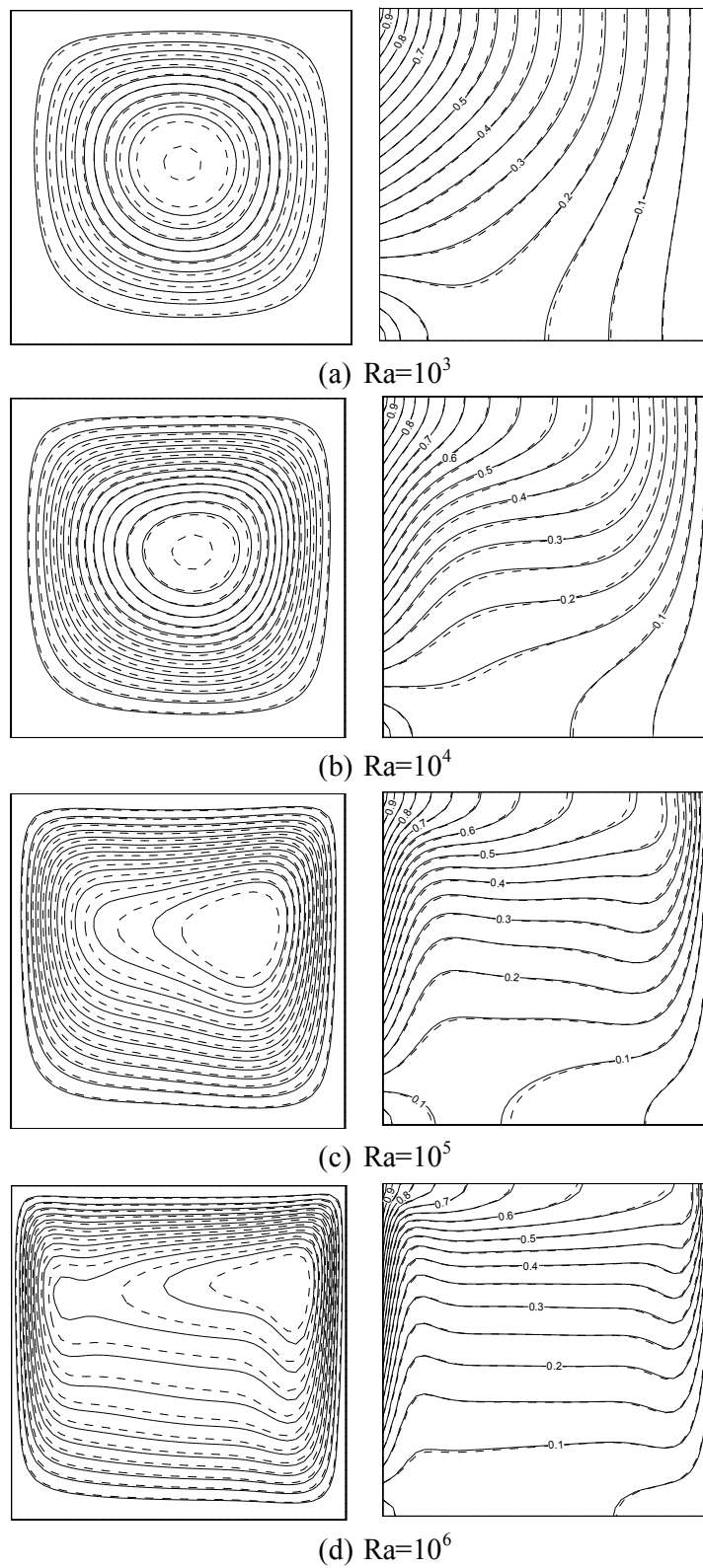


Figure 4. Streamlines (left) and isotherms (right) for different values of Rayleigh number (solid lines for pure fluid; dash lines for Al_2O_3 nanofluid:) with $\phi=0.04$

The fluid flow pattern for different nanofluids are depicted in Figure 5 for $Ra=10^6$. It is clearly seen from these figures that nanofluids with oxide nanoparticles have similar behaviour and nanofluids with metal particles have very similar flow patterns. Figure 6 shows the isotherm contours for different nanofluids with $Ra=10^6$ and $\phi=4\%$. The isotherms cluster near the thermally active walls and resemble the convection-dominated mode of heat transfer. On further scrutiny of these figures, there is not much difference in the heat distribution among the different nanofluids. The mid-height velocity profiles for different nanofluids are displayed in Figure 7 with $Ra=10^6$ and $\phi=4\%$. The velocity profiles show almost the same pattern for all type of nanofluids.

The effects of different nanofluids on the heat transfer rate are displayed in Figure 8. The figure obviously shows that the nanofluids provide higher rates of heat transfer than the pure fluid for all values of Rayleigh number. It is also observed that a better heat transfer rate is obtained upon using Ag nanofluid. A further scrutiny of the curves in Figure 8 reveals that the highest values of local Nusselt number are attained at $Y=0.75$ for $Ra=10^6$, i.e. $\frac{3}{4}$ from the bottom of the hot wall. In comparing isothermal wall and wall with linearly varying temperature, very different behaviour is observed. The highest local heat transfer rate is attained at the bottom portion of the hot wall for isothermal wall. However, the highest value of local Nusselt number is not attained at the bottom of the wall for wall with linearly varying temperature.

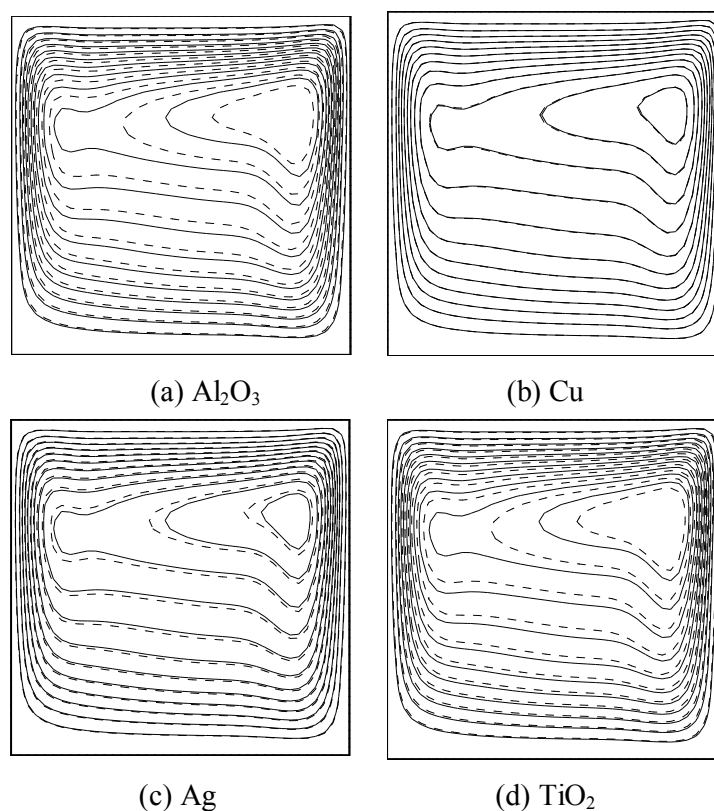


Figure 5. Streamlines for pure fluid and different nanofluids (solid lines for pure fluid; dash lines for nanofluid) with $Ra=10^6$

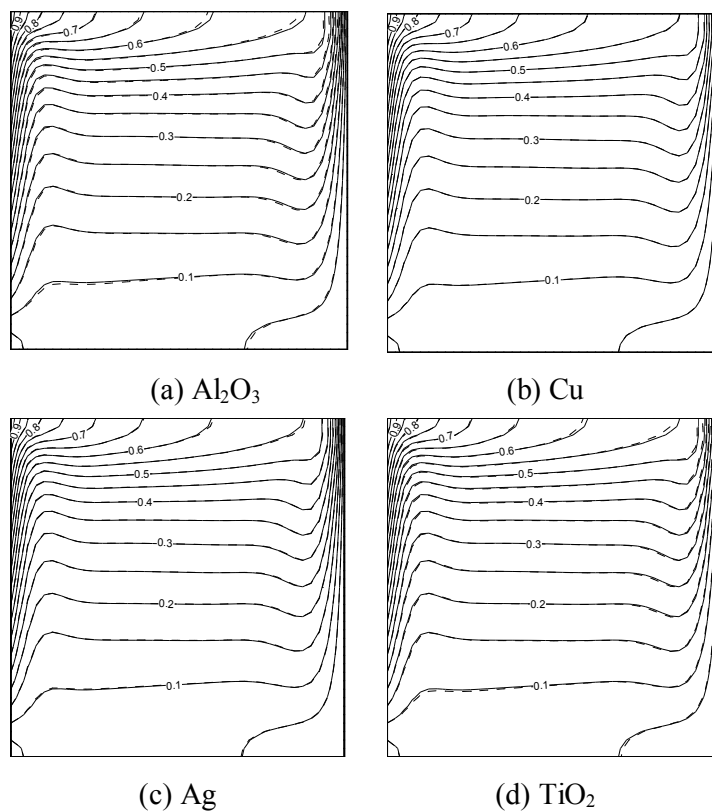


Figure 6. Isotherms for pure fluid and different nanofluids (solid lines for pure fluid; dash lines for nanofluid) with $Ra=10^6$

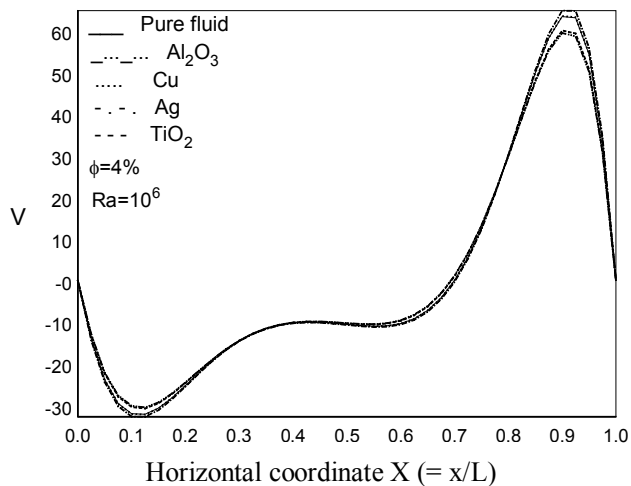


Figure 7. Mid-height velocity profiles for different nanofluids with $Ra=10^6$ and $\phi=4\%$

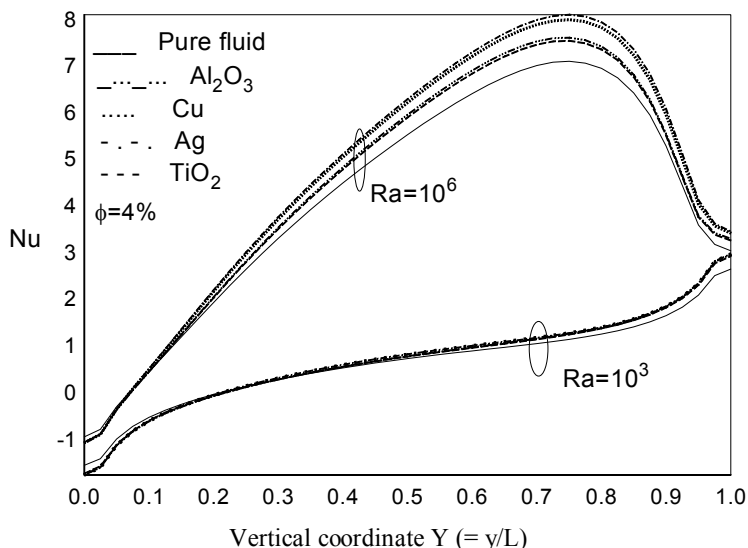


Figure 8. Local Nusselt number for different nanofluids with $\phi=4\%$

In order to find the effect of total heat transfer rate across the cavity among the different nanofluids, the average Nusselt number is plotted against the volume fraction of the nanoparticles for different values of Rayleigh number in Figure 9. The beneficial effects of the particle fraction on the average Nusselt number can be seen evidently with increasing the particle fraction. An increase in the average Nusselt number can be seen for all values of Rayleigh number. It is found that a maximum heat transfer rate is observed with Ag nanoparticles. When increasing the volume fraction of nanofluids, the difference in the heat transfer rate among the various nanofluids also increases. The difference among various nanoparticles provides a major effect on the convective heat transfer rate, which is clearly seen in Figure 9.

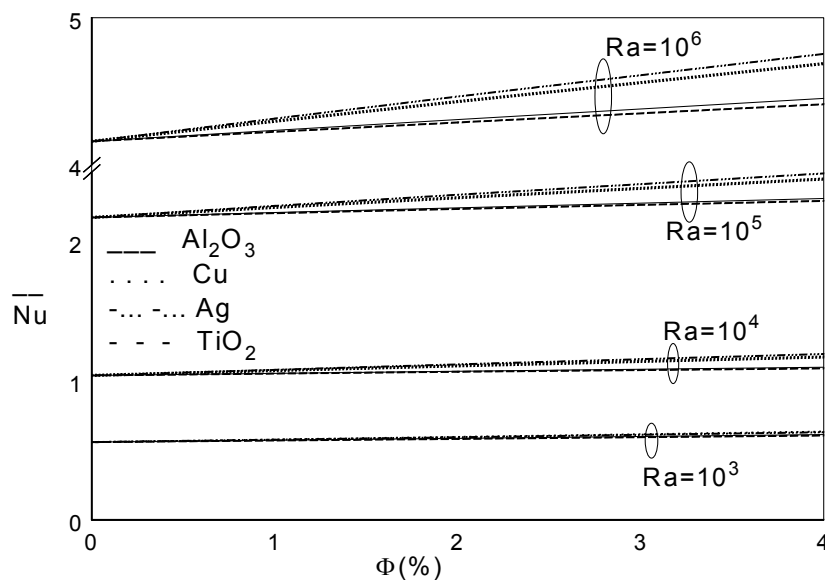


Figure 9. Average Nusselt number for different nanofluids and volume fractions

Figure 10, which plots the heat transfer coefficient ratio (ϵ_h) against the Rayleigh number for different volume fractions of the nanoparticles, demonstrates the heat transfer efficacy of the nanofluids at different volume fractions of the nanoparticles. The heat transfer coefficient ratios of the oxide nanofluids (Al_2O_3 and TiO_2) reach a minimum when $\text{Ra}=10^4$. However, the opposite behaviour is observed when using metal particles (Cu and Ag)—a maximum heat transfer ratio is attained at $\text{Ra}=10^4$. It is also found that the heat transfer coefficient ratio is always above unity. The highest values of the heat transfer coefficient ratio for the oxide nanofluids are obtained for $\text{Ra}=10^3$, whereas those for the metal nanofluids are obtained for $\text{Ra}=10^4$.

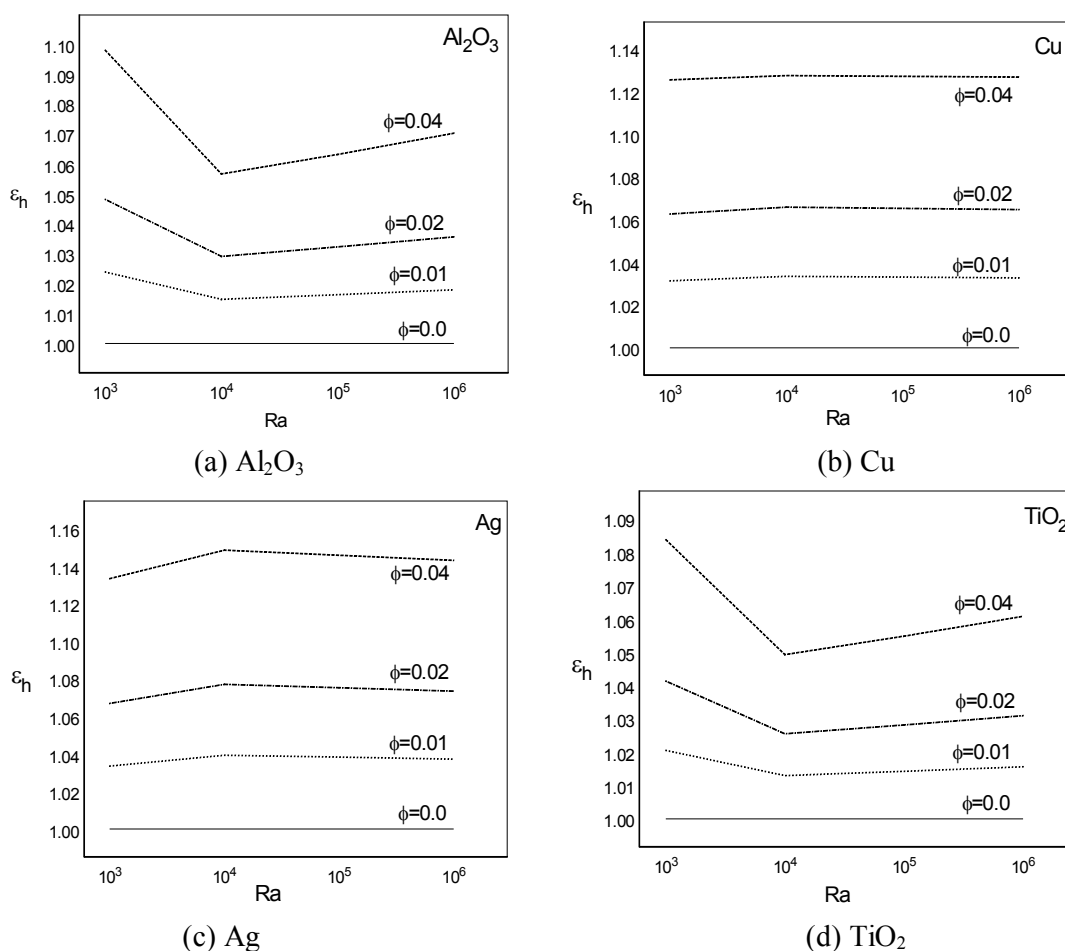


Figure 10. Heat transfer coefficient ratio for different nanofluids

From the simulation results obtained for various parameters involved in this study, the following sets of figures can be enumerated. The average Nusselt number of nanofluids at 1% volume concentration of Al_2O_3 , Cu, Ag and TiO_2 particles increases 2.4%, 3.2%, 3.4% and 2.1% respectively for $\text{Ra}=10^3$ compared with the base fluid. The heat transfer rate of nanofluids with 4% volume concentration of Al_2O_3 , Cu, Ag and TiO_2 particles increases 9.8%, 12.6%, 13.4% and 8.4% respectively for $\text{Ra}=10^3$ compared with the base fluid. The average Nusselt number of nanofluids with 1% volume

concentration of Al₂O₃, Cu, Ag and TiO₂ particles increases 1.8%, 3.3%, 3.7% and 1.6% respectively for Ra=10⁶ compared with the base fluid. Heat transfer rate of nanofluids with 4% volume concentration of Al₂O₃, Cu, Ag and TiO₂ particles increases 7.0%, 12.7%, 14.3% and 6.1% respectively for Ra=10⁶ compared with the base fluid. When increasing the Rayleigh number for a given volume fraction of nanoparticles, the average Nusselt number is constant for Cu nanofluid, while for Ag nanofluid a small amount of variation in the average Nusselt number is found. On the other hand, variation in the average Nusselt number is high for the nanofluids with Al₂O₃ and TiO₂ particles on the same conditions. Therefore, the choice of nanoparticles is very important in the convective heat transfer application.

CONCLUSIONS

The present study numerically examines the heat transfer enhancement of water-based nanofluids containing various nanoparticles in a square cavity with linearly varying wall temperature. Simulation results from a comparative study of four different nanoparticles (Al₂O₃, Cu, Ag and TiO₂) have been presented in detail. The heat transfer capacity of the base fluid can be increased by suspending the nanoparticles in it and the effect is more pronounced as the volume fraction of the particles increases. However, the incremental change in the average Nusselt number is strongly depending on the nanoparticles chosen. The linearly varying wall temperature changes the flow pattern and results in a higher heat transfer rate when compared to the isothermal wall. The heat transfer coefficient ratios of Al₂O₃ and TiO₂ nanofluids are minimum when Ra=10⁴ while they are maximum for Cu and Ag nanofluids. Results clearly show that the type of nanoparticles considered is very important on the convective heat transfer application. A significant difference on the average Nusselt number is found for different nanoparticles.

REFERENCES

1. S. U. S. Choi and J. A. Eastman, "Enhancing thermal conductivity of fluids with nanoparticles", ASME International Mechanical Engineering Congress and Exposition, **1995**, San Francisco, USA.
2. P. E. Phelan, P. Bhattacharya and R. S. Prasher, "Nanofluids for heat transfer applications", *Ann. Rev. Heat Transf.*, **2005**, 14, 255-275.
3. S. Das, S. Choi and H. Patel, "Heat transfer in nanofluids – A review", *Heat Transf. Eng.*, **2006**, 27, 3-19.
4. V. Trisaksri and S. Wongwises, "Critical review of heat transfer characteristics of nanofluids", *Renew. Sustain. Energy Rev.*, **2007**, 11, 512-523.
5. X. Q. Wang and A. S. Mujumdar, "Heat transfer characteristics of nanofluids: A review", *Int. J. Thermal Sci.*, **2007**, 46, 1-19.
6. K. Khanafer, K. Vafai and M. Lightstone, "Buoyancy-driven heat transfer enhancement in a two-dimensional enclosure utilizing nanofluids", *Int. J. Heat Mass Transf.*, **2003**, 46, 3639-3653.
7. R. Y. Jou and S. C. Tzeng, "Numerical research of nature convective heat transfer enhancement filled with nanofluids in rectangular enclosures", *Int. Commun. Heat Mass Transf.*, **2006**, 33, 727-736.

8. D. Wen and Y Ding, "Natural convective heat transfer of suspensions of titanium dioxide nanoparticles (nanofluids)", *IEEE Trans. Nanotechnol.*, **2006**, 5, 220-227.
9. K. S. Hwang, J. H. Lee and S. P. Jang, "Buoyancy driven heat transfer of water-based Al₂O₃ nanofluids in a rectangular cavity", *Int. J. Heat Mass Transf.*, **2007**, 50, 4003-4010.
10. C. J. Ho, M. W. Chen and Z. W. Li, "Numerical simulation of natural convection of nanofluid in a square enclosure: Effects due to uncertainties of viscosity and thermal conductivity", *Int. J. Heat Mass Transf.*, **2008**, 51, 4506-4516.
11. E. Abu-Nada, Z. Masoud and A. Hijazi, "Natural convection heat transfer enhancement in horizontal concentric annuli using nanofluids", *Int. Comm. Heat Mass Transf.*, **2008**, 35, 657-665.
12. H. F. Oztop and E. Abu-Nada, "Numerical study of natural convection in partially heated rectangular enclosures filled with nanofluids", *Int. J. Heat Fluid Flow*, **2008**, 29, 1326-1336.
13. A. K. Santra, S. Sen and N. Chakraborty, "Study of heat transfer augmentation in a differentially heated square cavity using copper-water nanofluid", *Int. J. Thermal Sci.*, **2008**, 47, 1113-1122.
14. B. Ghasemi and S. M. Aminossadati, "Natural convection heat transfer in an inclined enclosure filled with a water-CuO nanofluid", *Numer. Heat Transf. Part A*, **2009**, 55, 807-823.
15. M. A. Hossain and M. Wilson, "Natural convection flow in a fluid-saturated porous medium enclosed by non-isothermal walls with heat generation", *Int. J. Therm. Sci.* **2002**, 41, 447-454.
16. N. H. Saeid and Y. Yaacob, "Natural convection in a square cavity with spatial side-wall temperature variation", *Numer. Heat Transf., Part A*, **2006**, 49, 683-697.
17. M. Sathiyamoorthy, T. Basak, S. Roy and I. Pop, "Steady natural convection flows in a square cavity with linearly heated side wall(s)", *Int. J. Heat Mass Transf.*, **2007**, 50, 766-775.
18. A. A. Dare and M. O. Petinrin, "Modelling of natural convection along isothermal plates and in channels using diffusion velocity method", *Maejo Int. J. Sci. Technol.*, **2010**, 4, 43-52.
19. H. C. Brinkman, "The viscosity of concentrated suspensions and solution", *J. Chem. Phys.*, **1952**, 20, 571-581.
20. S. V. Patankar, "Numerical Heat Transfer and Fluid Flow", Hemisphere, New York, **1980**, pp.79-135.
21. G. D. V. Davis, "Natural convection of air in a square cavity: A bench mark numerical solution", *Int. J. Numer. Meth. Fluids*, **1983**, 3, 249-264.
22. G. V. Hadjisophocleous, A. C. M. Sousa and J. E. S. Venart, "Prediction of transient natural convection in enclosures of arbitrary geometry using a nonorthogonal numerical model", *Numer. Heat Transf., Part A*, **1988**, 13, 373-392.
23. T. Fusegi, J. M. Hyun, K. Kuwahara and B. Farouk, "A numerical study of three-dimensional natural convection in a differentially heated cubical enclosure", *Int. J. Heat Mass Transf.*, **1991**, 34, 1543-1557.
24. G. Barakos, E. Mitsoulis and D. Assimacopoulos, "Natural convection flow in a square cavity revisited: Laminar and turbulent models with wall functions", *Int. J. Numer. Meth. Fluids*, **1994**, 18, 695-719.

Full Paper

Urban ecological characteristics and vascular wall flora on the Anatolian side of Istanbul, Turkey

Volkan Altay^{1*}, İbrahim İ. Özyiğit² and Celal Yarci²

¹ Mustafa Kemal University, Science and Arts Faculty, Department of Biology, 31040, Antakya, Hatay, Turkey

² Marmara University, Science and Arts Faculty, Department of Biology, 34722, Göztepe, Istanbul, Turkey

*Corresponding author, E-mail: valtay@mku.edu.tr ; Tel: +90 326 245 58 66; Fax: + 90 326 245 58 67

Received: 5 May 2010 / Accepted: 16 November 2010 / Published: 27 November 2010

Abstract: The aim of this study is to specify the urban ecologic characteristics of Istanbul and to show their reflection to the vascular wall flora of the Anatolian side, which is a distinctive wall habitat. Plants samples of the urban habitat were collected from the top and vertical surfaces of walls during 2005-2007. A total of 101 taxa (81 species, 13 subspecies and 7 varieties) belonging to 74 genera and 33 families were recorded. It was determined that 80 species were Dicotyledones while 1 was Monocotyledone. The families with the largest number of taxa were Asteraceae (18 species, 22.22%), Poaceae (8 species, 9.87%), Lamiaceae and Brassicaceae (5 species, 6.17%), and Polygonaceae and Scrophulariaceae (4 species, 4.93%). The most common plant species on walls were *Parietaria judaica* L. (Urticaceae), *Stellaria media* (L.) Vill. subsp. *media* (Caryophyllaceae), and *Mercurialis annua* L. (Euphorbiaceae). The percentage of phytogeographical elements among the recorded taxa varied as follows: Euro-Siberian (6 taxa, 7.41%), Mediterranean (11 taxa, 13.58%), E. Mediterranean (2 taxa, 2.47%), Irano-Turanian (1 taxon, 1.23%) and unknown (61 taxa, 75.31%). It was found that 6 taxa (7.41%) were cosmopolitan, 12 (14.82%) were widespread while 1 (1.23%) was endemic. The results were compared with some other European wall floras and some similarities and dissimilarities were noted.

Keywords: vascular wall flora, Istanbul, urban habitat, urban ecology

INTRODUCTION

Istanbul is one of the most populous cities of Eurasia and is the world's 4th largest city proper and 20th largest urban area as well as Turkey's cultural and financial centre. The city is located in the

NW part of Turkey ($41^{\circ} 01.2' N$, $28^{\circ} 58.2' E$) and it extends both on European (Thrace) and Asian (Anatolia) sides of the Bosphorus. It is the only metropolis in the world which is situated on two continents [1-5]. Its neighbours are the Black Sea in the north, Marmara Sea in the south, Kocaeli City in the east, and Tekirdağ City in the west (Figure 1). Istanbul has approximately 5100 km^2 of land area and 12,573,836 population. In its long history, Istanbul served as a capital city of the Roman Empire (AD 330-395), Byzantine Empire (AD 395-1204 and AD1261-1453), Latin Empire (AD 1204-1261), and Ottoman Empire (AD 1453-1922) [3, 6]. In addition to its rich history, high population and productive economy, Istanbul also has a wide variety of ecological features [3].



Figure 1. Districts studied in Istanbul during 2005-2007 (Beykoz, Üsküdar, Kadıköy, Kartal, Ümraniye, Maltepe, Tuzla, Pendik, Adalar and Sultanbeyli)

The main topographical feature of Istanbul is a low plateau at about 100-200 m elevation where there are many hills and a few streams in the city. The geological structure of Istanbul is diverse with Silurian, Devonian, Carboniferous, and Tertiary formations. There are different kinds of rocks including granitic plutons, quartzes, grovacs, clayed schists and radiolarites [2, 7].

In Istanbul, many different types of soils are present while brown forest soil covers the most area. Non-calcareous brown soil is the second and is kind of soil is suitable for plant growth as a result of organic matter. The rendzinas, which cover especially the European side of the city, are also important. In addition, alluvial soil is also present [2, 7].

Istanbul is in a kind of transition zone between less rainy Mediterranean and oceanic climates. In the summer, less precipitation and high temperature are characteristic and the annual mean temperature is 14.5°C for the last two decades. Between May and September the temperature is

generally above 30°C and between November and April it is rarely below 0°C. In the vegetation period, the daily mean temperature is approximately 8°C, which lasts for about 280 days (between 15 March and 20 December) [2-5, 8].

The total precipitation for Istanbul averages 640 mm per year and 40% of the total precipitation falls in winter. December and January are the wettest months. Precipitation in summer is more than the typical Mediterranean situation and is more related to the oceanic climate. The minimal amount of rain falls (about 8%) in July and August. Precipitation is less in spring (about 20-21%) while it increases in autumn (about 28-29%), and snow rarely falls in Istanbul. The rain regime is Winter-Autumn-Spring-Summer (W.A.Sp.Su) and the rain type is “Central Mediterranean Rain Type” [2, 9].

The relative humidity is between 73-77% in the city and these values decrease to 65-68% in the summer despite the effect of the seas. The lower relative humidity, especially in the dry period, forms xerophytic vegetation. The dominant wind in the city is from the NE [8-9].

The wide variety of ecological features in Istanbul have resulted in more Pteridophyta and Angiospermae (2500 species) than those in England (250,000 km² land area, 1850 plant species) and Netherlands (50,000 km² land area, 1600 species) [10]. Istanbul’s rich flora has been studied by many botanists due to its varied climatic and geographic conditions. Many floristic studies in urban and rural areas have been done in Turkey [7, 11-13]. Aksoy [14-15] carried out some studies on the green areas in Istanbul while others have done urban ecological studies, i.e. Şahin [16] in Eminönü and Fatih, Altay et al. [3] in Kartal, Osma et al. [4] in Kadıköy, Mutlu [17] in Üsküdar, and Eskin [18] in Pendik districts.

Buildings and all types of walls are urban features represent a specific environment [19-20]. The colonisation of plants on walls is favoured by the wall ages, the presence of lime mortar, exposure to rain, and such aspects as south and verticality. Most true wall species are only found on vertical walls and as the angle of inclination decreases an ever-widening range of common species colonise [21]. The wall habitat is different from natural habitat and rocks, depending on many different properties related to wall structures. Buildings contain binding materials, which structurally and chemically differ from the original building materials. Usually most of them are cleaned repeatedly; thus, they basically are temporary habitat. Walls are generally isolated, small, and their microclimate is more affected by changes of climatic factors such as temperature, precipitation and irradiation than that of rocks. Wall surfaces resemble each other and have a uniform slope (generally right-angled) and microtopographical characteristic with few microhabitats. Walls are located both in urban and rural areas, so wall flora is influenced by the nearby ruderal and semi-natural vegetation [22].

Wall flora which shows differences from urban and rural flora has attracted many botanists in different countries and cities. Comparison of wall vegetation in southern, western and central Europe was done by Segal [23] and Brandes [24-25]. Carmona et al.[26] in Spain, Hruska [27] in Italy, Gehu [28] in France, Woodell [19] in England, Oberdorfer [29] in Germany, Weretelnik [30] in Poland, Mucina [31] in Austria, Valachovic and Maglocky [32] in Slovakia, Duchoslav [22] in the Czech Republic, and Pavlova and Tonkov [20] in Bulgaria have studied wall flora.

Wall flora studies in Turkey are limited and include those by Gemici et al. [33] in İzmir, Aksoy and Çelik [34] in Kayseri, Yeşilot [35] in Istanbul European side, and Yarcı and Özçelik [36] in Edirne. These studies were mostly on walls of historical buildings.

Our study was carried out in all districts of the Anatolian side of Istanbul, excluding Şile, during 2005-2007 vegetation periods. This study was made on walls of historical buildings as well as those of gardens, houses, hospitals, schools, campuses, train stations and ateliers, and especially on drain walls.

MATERIALS AND METHODS

The wall vascular flora on the Anatolian side of Istanbul was studied. Bryophyta and ornamental plants were not collected. Plant specimens were identified by using the “Flora of Turkey and the East Aegean Islands Volumes I-XI and Supp.” [37] and were deposited in MÜFE Herbarium (Marmara University, Sciences and Arts Faculty Herbarium). The flora is listed alphabetically in the Appendix according to family, genera and species. Life forms [phanerophytes (Ph); chaemaphytes (Ch); hemicryptophytes (H); therophytes (Th); geophytes (G)] and phytogeographical origins [Euro-Siberian (Euro.-Sib.), Irano-Turanian (Ir.-Tur.), Mediterranean (Medit.), East Mediterranean (E. Medit.)] are included and were determined according to the Raunkier system [38-39].

RESULTS AND DISCUSSION

The total number of vascular plants growing spontaneously on walls included 101 taxa with 33 families and 74 genera (81 species, 13 subspecies and 7 varieties). Eighty species were Dicotyledones with one monocotyledon species (Table 1).

Table 1. Summary of collecting

Taxon	Monocotyledones		Dicotyledones		Total Number
	Number	%	Number	%	
Family	1	3.04	32	96.96	33
Genus	1	1.36	73	98.64	74
Species	1	1.24	80	98.76	81

There was only one monocotyledon species, *Asparagus acutifolius* L. (Liliaceae), which consisted of 1.24% of all species, while Dicotyledones were the prevalent group with 98.76% of all species. The following families were represented by the largest number of species: Asteraceae (18 species, 22.22%), Poaceae (8 species, 9.87%), Lamiaceae (5 species, 6.17%), Brassicaceae (5 species, 6.17%), Polygonaceae (4 species, 4.93%) and Scrophulariaceae (4 species, 4.93%) (Table 2). Although Asteraceae was the most common family, it had the lowest species/genus ratio (1.0). The same ratio was also for Brassicaceae, although it was a low-taxa family in this study. This ratio was higher in Polygonaceae (2.0), Scrophulariaceae (1.33), Lamiaceae (1.25) and Poaceae (1.14).

Previous studies noted that Asteraceae species have a species richness compared with other families [3-4, 20, 22, 24, 40-44]. Pavlova and Tonkov [20] also observed that Asteraceae was high in number of species in Central Europe, demonstrating the remarkable success of this family in terms of dispersal and establishment. Davis [37] also mentioned that Asteraceae represents highest number of

species in the flora of Turkey. Other researchers obtained similar results with other families [20, 35-36].

Table 2. Genera and species numbers of the richest families

Family	Genera		Species		Species/Genus ratio
	Number	%	Number	%	
Asteraceae	18	24.32	18	22.22	1
Poaceae	7	9.45	8	9.87	1.14
Lamiaceae	4	5.40	5	6.17	1.25
Brassicaceae	5	6.75	5	6.17	1
Polygonaceae	2	2.70	4	4.93	2
Scrophulariaceae	3	4.05	4	4.93	1.33

In this study, life forms were determined according to the Raunkier system [38] and the largest groups were therophytes (45.72%) and hemicryptophytes (37.00%) (Figure 2). The patterns of these two life forms found on walls were similar to walls in Europe [18, 20-22]. In our study, percentages of other life forms were as follows: chamaephytes (2.46%), geophytes (4.94%) and phanerophytes (9.88%). Therophytes and hemicryptophytes are widespread in areas with a Mediterranean climate [3-4].

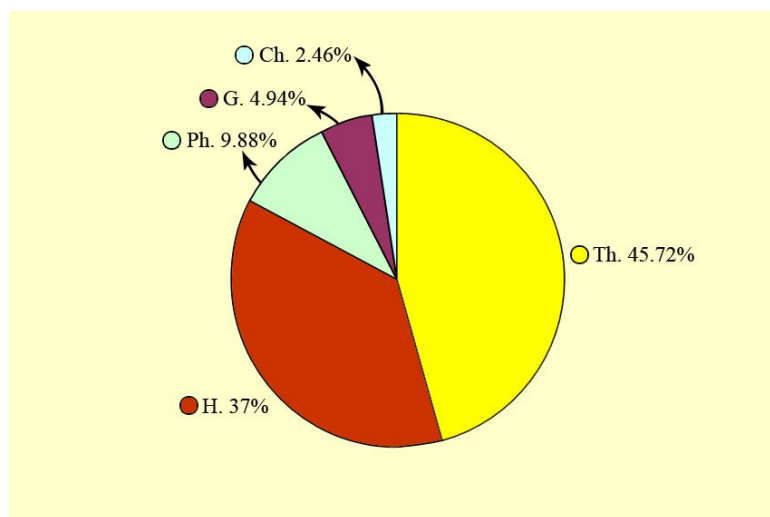


Figure 2. Pie diagram of the prevalence of life forms (H. = hemicryptophytes; Ph. = phanerophytes; G. = geophytes; Ch. = chamaephytes; Th. = therophytes)

The most common phytogeographical elements were Mediterranean (13.58%) and Euro-Siberian elements (7.41%) (Figure 3). This is because Istanbul has a mostly Mediterranean climate.

The northern side of Istanbul is partly affected by the oceanic climate [14]. Our study showed that six taxa (7.41%) were cosmopolitan and 12 taxa (14.82%) were widespread. Only one endemic taxon was found in our study. The most common plant species on walls were: *Parietaria judaica* L. (Urticaceae), *Stellaria media* (L.) Vill. subsp. *media* (Caryophyllaceae) and *Mercurialis annua* L. (Euphorbiaceae). We did not find any pteridophytes although in Central Europe and in the Mediterranean area they are present.

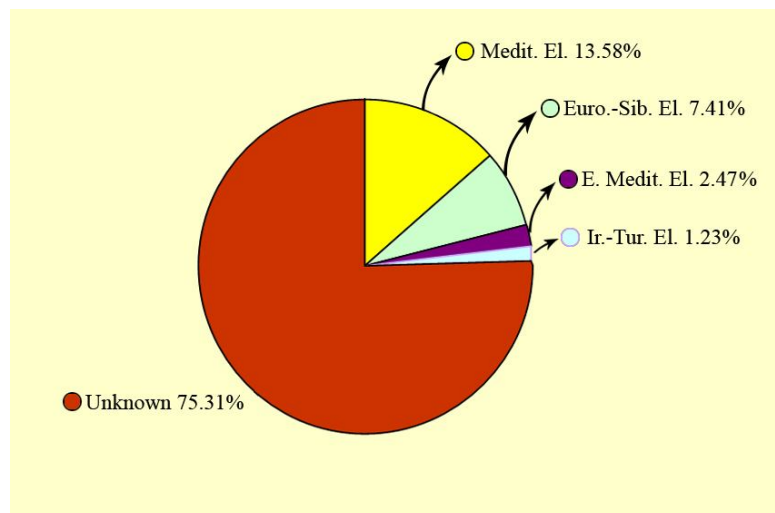


Figure 3. Pie diagram of the phytogeographical origins of the wall flora (Medit. El. = Mediterranean elements, Euro.-Sib. El. = Euro-Siberian elements, E. Medit. El. = East Mediterranean elements, Ir.-Tur. El. = Irano-Turanian elements)

We also found some archaeophyte and neophyte plants. An archaeophyte is not native to the geographical region, but was introduced in "ancient" times rather than during modern times. A neophyte has been recently introduced to the area. Archaeophytes are considered to be those species first introduced prior to 1500 AD while neophytes came after 1500 AD [45-46]. Archaeophyte and neophyte plants are listed in Table 3.

Plants growing on walls reach these habitats by wind (anemochorous), animals (zoochorous), mostly by birds and by stolon fragments (autochorous) [22, 36], and grow there randomly. Deep-rooted plants can be destructive. Although their roots are weak at the beginning of growth, they become stronger in time and cause widening of cracks. Most of these plants absorb little water from the substrate, but absorb it from the air [36]. Although wall plants are often aesthetically appealing, the local municipalities occasionally clean up the walls to prevent damage by the plants. It would be more preferable if the clean-up was more selective by allowing for plant type and degree of damage.

Table 3. Archaeophyte and neophyte plants

Archaeophytes (before 1500 AD)	Neophytes (after 1500 AD)
<i>Lamium purpureum</i> L. (Lamiaceae)	<i>Conyza canadensis</i> (L.) Cronquist (Asteraceae)
<i>Lamium amplexicaule</i> L.	<i>Veronica persica</i> Poiret (Scrophulariaceae)
<i>Euphorbia helioscopia</i> L. (Euphorbiaceae)	<i>Cymbalaria muralis</i> Gaertner
<i>Euphorbia peplus</i> L.	<i>Ailanthus altissima</i> (Miller) Swingle (Simaroubaceae)
<i>Sinapis arvensis</i> L. (Brassicaceae)	<i>Oxalis corniculata</i> L. (Oxalidaceae)
<i>Capsella bursapastoris</i> (L.) Medik.	<i>Diploaxis tenuifolia</i> (L.) DC. (Brassicaceae)
<i>Fumaria officinalis</i> L. (Papaveraceae)	
<i>Stellaria media</i> (L.) Vill. (Caryophyllaceae)	
<i>Cerastium glomeratum</i> Thuill	
<i>Cichorium intybus</i> L. (Asteraceae)	
<i>Solanum nigrum</i> L. (Solanaceae)	
<i>Chenopodium album</i> L. (Chenopodiaceae)	
<i>Setaria viridis</i> (L.) P. Beauv. (Poaceae)	

ACKNOWLEDGEMENTS

We wish to thank Miss Busecan Aksoydan for rearranging the Tables and Figures and Mr. Ahmet Yılmaz for rechecking the language in this document.

REFERENCES

1. The official website of Istanbul metropolis municipality, <http://www.ibb.gov.tr>, access date: March 2010.
2. Ü. Yaşar İ. İ. Özyiğit and M. Serin “Judas tree (*Cercis siliquastrum* L. subsp. *siliquastrum*) as a possible biomonitor for Cr, Fe and Ni in Istanbul (Turkey)” *Rom. Biotech. Lett.*, 2010, 15, 4979-4989.
3. V. Altay, İ. İ. Özyiğit and C. Yarcı “Urban flora and ecological characteristics of the Kartal District (Istanbul): A contribution to urban ecology in Turkey” *Sci. Res. Essays*, 2010, 5, 183-200.
4. E. Osma, İ. İ. Özyiğit, V. Altay and M. Serin “Urban vascular flora and ecological characteristics of Kadıköy district, Istanbul, Turkey” *Maejo Int. J. Sci. Technol.*, 2010, 4, 64-87.
5. S. Kaya and P. J. Curran, “Monitoring urban growth on the European side of the Istanbul Metropolitan area: A case study”, *Int. J. Appl. Earth Obs. Geoinf.*, 2006, 8, 18-25.
6. M. O. Bayrak, “İstanbul Tarihi (History of Istanbul)”, İnkılap Kitabevi, Istanbul, 1996.
7. F. Yaltrık, A. Efe and A. Uzun, “Tarih boyunca İstanbul’un park, bahçe ve koruları egzotik ağaç ve calıları (The inventory of exotic tree and bush species of Istanbul’s parks, gardens and groves)”, No. 4, İstanbul Metropolis Municipality, İsfalt Yayınları, Istanbul, 1997.

8. “The Meteorological Report for 2007 Year of Istanbul”, Prime Ministership, General Directorship for Meteorology, the Directorship for Statistics and Publication, Ankara, **2007**.
9. Y. Akman, “İklim ve Biyoiklim (Climate and Bioclimate)”, Palme Yayın-Dağıtım, Ankara, **1990**.
10. N. Özhatay and M. Keskin, “Ömerli Havzasının İstanbul Doğal Bitkileri (Natural Plants of Ömerli Reservoir, Istanbul)”, Doğal Hayatı Koruma Vakfı Yayınlarından, İstanbul, **2007**.
11. A. Baytop, “Aydos ve Kayışdağ havalisinin çiçekli bitkileri (The flowering plants of Aydos and Kayışdağ environs)”, *Türk Biol. Derg.*, **1962**, 12, 75-111.
12. A. Baytop, “İstanbul Yıldız Parkı’nın florası (The flora of Yıldız Park, Istanbul)”, *İst. Üniv. Ecz. Fak. Mec.*, **1985**, 21, 86-97.
13. N. Özhatay, A. Byfield and S. Atay, “Türkiye’nin Önemli Bitki Alanları (The Important Plant Areas of Turkey)”, Doğal Hayatı Koruma Vakfı Yayınlarından, İstanbul, **2003**, p. 87.
14. Y. Aksoy, “İstanbul’da yeşil alan kullanımı üzerine bir araştırma (A study on the use of green areas in Istanbul)”, *MSc Thesis*, **1994**, Istanbul Technical University, Turkey.
15. Y. Aksoy, “İstanbul kenti yeşil alan durumu irdelenmesi (The evaluation of green areas position in Istanbul)”, *PhD Thesis*, **2001**, Istanbul Technical University, Turkey.
16. N. Şahin, “Eminönü ve Fatih İlçeleri’nin (İstanbul) kentsel ekolojik özellikleri (Urban ecological characteristics of Eminönü and Fatih Towns - Istanbul)”, *MSc Thesis*, **2002**, Marmara University, Turkey.
17. P. Mutlu, “Üsküdar İlçesi’nin (İstanbul) kentsel ekolojik özellikleri (Urban ecological characteristics of Üsküdar Town - Istanbul)”, *MSc Thesis*, **2004**, Marmara University, Turkey.
18. B. Eskin, “Pendik İlçesi (İstanbul) kentsel ekolojisi (Urban ecology of Pendik Town - Istanbul)”, *MSc Thesis*, **2005**, Marmara University, Turkey.
19. S. Woodell, in “Nature in Cities: The Natural Environment in the Design and Development of Urban Green Space” (Ed. I. C. Laurie), John Wiley, Chichester, **1979**, pp. 135-157.
20. D. Pavlova and S. Tonkov, “The wall flora of the Nepet Tepe Architectural Reserve in the city of Plovdiv (Bulgaria)”, *Acta Bot. Croat.*, **2005**, 64, 357-368.
21. O. L. Gilbert, “The Ecology of Urban Habitats”, Chapman and Hall, Cambridge, **1991**, p. 251.
22. M. Duchoslav, “Flora and vegetation of stony walls in East Bohemica (Czech Republic)”, *Preslia, Praha*, **2002**, 74, 1-25.
23. S. Segal, “Ecological Notes on Wall Vegetation”, Junk, The Hague, **1969**.
24. D. Brandes, “Flora und Vegetation von Stadtmauern”, *Tuexenia*, **1992**, 12, 315-319.
25. D. Brandes, “*Asplenietea*- Gesellschaften an sekundären Standorten in Mitteleuropa”, *Ber. d. Reinh.-Tüxen-Ges.*, **1992**, 4, 73-93.
26. E. C. Carmona, M. M. Luque and F. V. Tendero, “The plant communities of the *Asplenietea trichomanis* in the SW Iberian Peninsula”, *Folia Geobot. Phytotax.*, **1997**, 32, 361-376.
27. K. Hruska, “Syntaxonomical study of Italian wall vegetation”, *Vegetatio*, **1987**, 73, 13-20.
28. J. M. Gehu, “Les groupements végétaux du bassin de la Sambre Française”, *Vegetatio*, **1961**, 10, 161-208.
29. E. Oberdorfer, in “Süddeutsche Pflanzengesellschaften” (Ed. E. Oberdorfer), Gustav Fischer Verlag, Jena, **1992**, pp. 23-38.

30. E. Weretelnik, "Flora i zbiorowiska roslin murow niektorych miast i zamkow na dolnnyin Slasku", *Acta Univ. Wratislav. - Pr. Bot. Wroclaw*, **1982**, 25, 63-110.
31. L. Mucina, "Die Pflanzengesellschaften Österreichs" (Ed. G. Grabherr and L. Mucina), Gustav Fischer Verlag, Jena, **1993**, pp. 241-275.
32. M. Valachovic and S. Maglocky, in "Rastlinne spolocenstva Sloveska. I, Pionierska Vegetacia", (Ed. M. Valachovic), Veda, Bratislava, **1995**, pp. 85-106.
33. Y. Gemici, Ö. Seçmen and G. Görk, in "Urban Ecology" (Ed. M. Öztürk), Ege University Press, Izmir, **1995**, pp. 408-413.
34. A. Aksoy and A. Çelik, "Studies on the ecology of plants growing on the historical monuments of Kayseri, Türkiye", Proceedings of the Vth International Symposium, **2000**, Tashkent, Uzbekistan.
35. A. Yeşilot, "İstanbul'da tarihi yapılar üzerinde yetişerek bunları tahrip eden bitkiler (The plants that grow up on historical buildings and destroy them)", *MSc Thesis*, **2000**, Marmara University, Istanbul.
36. C. Yarci and H. Özçelik, "Wall flora of Edirne (Thrace Region)", *Ot Sistematik Botanik Dergisi*, **2002**, 9, 57-66.
37. P. H. Davis (Ed.), "Flora of Turkey and the East Aegean Islands", Vol. 1-11, University Press, Edinburgh, **1965-2000**.
38. J. Braun-Blanquet, "Pflanzensoziologie Grundzüge der Vegetationkunde", Springer-Verlag, Vienna, **1964**.
39. C. Raunkier, "The Life Forms of Plants and Statistical Plant Geography", Oxford University Press, Oxford, **1934**. [Reprinted in "History of Ecology Series" (Ed. F. N. Egerton), Ayer Co., Manchester, 1978.]
40. S. L. Mosyakin and O. G. Yavorska, "The nonnative flora of the Kiev (Kyiv) urban area, Ukraine: A checklist and brief analysis", *Urban Habitats*, **2002**, 1, 45-65. (Electronic version: <http://www.urbanhabitats.org>, access date: September 2009)
41. A. Gonzalvo, F. J. Martinez and M. Boscaiu, "The floristic and vegetation study of an area of interest in Valencia (Spain) proposed as plant micro-reserve", *Notulae Bot. Horti Agrobot. Cluj Napoca*, **2008**, 36, 7-12.
42. C. Yarci, M. Serin and V. Altay, "The segetal vegetation of Kocaeli Province (Turkey)", *Ekoloji*, **2007**, 16, 23-33.
43. J. F. Maxwell, "Vascular flora of the Emerald Pool area, Krabi province, southern Thailand", *Maejo Int. J. Sci. Technol.*, **2009**, 3, 1-25.
44. N. Krigas, E. Lagiou, E. Hanlidou and S. Kokkini, "The vascular flora of the Byzantine walls of Thessaloniki (North Greece)", *Willdenowia*, **1999**, 29, 77-94.
45. H. Schepker and I. Kowarik, "Bekämpfung von Neophyten in Niedersachsen: Ursachen. Umfang, Erfolg", *Neobiota*, **2002**, 1, 343-354.
46. I. Kowarik, "Human agency in biological invasions: Secondary releases foster naturalisation and population expansion of alien plant species", *Biol. Invasions*, **2003**, 5, 293-312.

APPENDIX (Flora List)

(Abbreviations: Ph = phanerophytes; Ch = chaemaphytes; H = hemicryptophytes; Th = therophytes; G = geophytes; Euro.-Sib. = Euro-Siberian; Ir.-Tur. = Irano-Turanian; Medit. = Mediterranean; E. Medit. = East Mediterranean; cos. = cosmopolitan; wid. = widespread; end. = endemic)

ANACARDIACEAE

Pistacia terebinthus L. subsp. *terebinthus* Ph, Medit.

APIACEAE

Conium maculatum L. H

ARALIACEAE

Hedera helix L. Ph

ASTERACEAE

Anthemis cretica L. H

Calendula arvensis L. Th

Carlina corymbosa L. H, Medit.

Centaurea solstitialis L. subsp. *solstitialis* H, wid.

Cichorium intybus L. Ch, wid.

Cirsium creticum (Lam.) d'Urv. subsp. *creticum* H, E. Medit.

Conyza canadensis L. Th

Erigeron acer L. H

Helminthotheca echioides (L.) Holup Th.

Hypochoeris radicata L. H, Euro.- Sib.

Inula viscosa (L.) Ailton H, Medit.

Lactuca saligna L. Th

Pallenis spinosa (L.) Cass. Th, Medit.

Picris strigosa Bieb. H, Ir.- Tur.

Senecio vulgaris L. Th

Sonchus asper (L.) Hill subsp. *glaucescens* (Jordan) Ball H, wid.

Taraxacum officinale Wiggers Ch

Tussilago farfara L. G, Euro.- Sib.

BRASSICACEAE

Capsella bursa-pastoris (L.) Medik. Th, cos.

Diplotaxis tenuifolia (L.) DC. H

Lepidium graminifolium L. H

Neslia apiculata Fisch. Th, wid.

Sinapis arvensis L. Th, wid.

Maejo Int. J. Sci. Technol. **2010**, 4(03), 483-495

CAMPANULACEAE

Campanula lyrata Lam. subsp. *lyrata* H, wid., end.

CARYOPHYLLACEAE

Cerastium glomeratum Thuill Th, cos.

Stellaria media (L.) Vill. subsp. *media* Th

Telephium imperati L. subsp. *orientale* (Boiss.) Nyman H

CHENOPODIACEAE

Chenopodium album L. subsp. *album* var. *album* Th

CONVOLVULACEAE

Convolvulus arvensis L. H, cos.

CUCURBITACEAE

Eballium elaterium (L.) A. Rich. H, Medit.

DIPSACACEAE

Scabiosa columbaria L. subsp. *columbaria* var. *columbaria* H

EUPHORBIACEAE

Euphorbia helioscopia L. Th

E. peplus L. var. *peplus* Th

Mercurialis annua L. Th

FABACEAE

Vicia hybrida L. Th

GERANIACEAE

Geranium purpureum Vill. Th

LAMIACEAE

Ajuga chamaepitys (L.) Schreber H

Calamintha nepeta (L.) Savi H

Lamium amplexicaule L. Th, Wid., Euro.- Sib.

Lamium purpureum L. var. *purpureum* Th, Euro.- Sib.

Micromeria graeca L. subsp. *graeca* H, Medit.

LILIACEAE

Asparagus acutifolius L. G, Medit.

MALVACEAE

Malva sylvestris L. H

MORACEAE

Ficus carica L. subsp. *carica* Ph, wid.

OLEACEAE

Ligustrum vulgare L. Ph, Euro.- Sib.*Phillyrea latifolia* L. Ph, Medit.

OXALIDACEAE

Oxalis corniculata L. Th, cos.

PAPAVERACEAE

Fumaria officinalis L. Th*Glaucium flavum* Crantz H*Papaver dubium* L. Th

PLANTAGINACEAE

Plantago coronopus L. Th, Euro.- Sib.*P. lagopus* L. Th, Medit.

POACEAE

Agrostis capillaris L. var. *capillaris* H*Bromus sterilis* L. Th*Cynodon dactylon* (L.) Pers var. *dactylon* G*Dactylis glomerata* L. subsp. *hispanica* (Roth) Nyman H*Hordeum murinum* L. Th*Poa annua* L. Th*Setaria viridis* (L.) P. Beauv. Th, wid.*Setaria verticillata* (L.) P. Beauv. Th

POLYGONACEAE

Polygonum aviculare L. Th, cos.*Polygonum lapathifolium* L. Th.*Rumex conglomeratus* Murray H*Rumex pulcher* L. H

RESEDACEAE

Reseda lutea L. var. *lutea* H

ROSACEAE

Rubus canescens DC. var. *canescens* Ph, wid.*Sarcopoterium spinosum* (L.) Spach H, E. Medit.

RUBIACEAE

Galium aparine L. Th

SCROPHULARIACEAE

Antirrhinum majus L. subsp. *majus* H*Cymbalaria muralis* Gaerth. Th, Medit.*Veronica cymbalaria* Bodara Th, Medit.*Veronica persica* Poiret Th

SIMAROUBACEAE

Ailanthus altissima (Miller) Swingle Ph

SOLANACEAE

Hyocyamus niger L. Th, wid.*Solanum nigrum* L. subsp. *nigrum* Th, cos.

URTICACEAE

Parietaria judaica L. H, wid.

VALERIANACEAE

Centranthus ruber (L.) DC. G

VITACEAE

Vitis vinifera L. Ph

Full Paper

EEG activity in Muslim prayer: A pilot study

Haider H. Alwasiti^{1,*}, Ishak Aris² and Adznan Jantan³

¹Department of Biomedical Engineering, Institute of Advanced Technology, University Putra Malaysia, 43400 Serdang, Selangor, Malaysia

²Department of Electrical and Electronic Engineering, Faculty of Engineering, University Putra Malaysia, 43400 Serdang, Selangor, Malaysia

³Department of Computer and Communication Engineering, Faculty of Engineering, University Putra Malaysia, 43400 Serdang, Selangor, Malaysia

*Corresponding author, E-mail: hayder@wasiti.net ; Tel: +60173976486

Received: 9 October 2010 / Accepted: 3 December 2010 / Published: 5 December 2010

Abstract: Almost all religions incorporate some form of meditation. Muslim prayer is the meditation of Islam. It is an obligatory prayer for all Muslims that is performed five times a day. Although a large body of literature exists on EEG changes in meditation, to date there has been no research published in a peer-reviewed journal on EEG changes during Muslim prayer. The purpose of this pilot study is to encourage further investigation on this type of meditation. Results of EEG analysis in twenty-five trials of Muslim prayer are reported. Some of the findings are consistent with the majority of the previous meditation studies (alpha rhythm slowing, increased alpha rhythm coherence). However, Muslim prayer does not show an increase in alpha and/or theta power like most of the results of other meditation studies. The possible cause of this discrepancy in meditation-related studies is highlighted and a systematic and standardised roadmap for future Muslim prayer EEG research is proposed.

Keywords: EEG, Muslim prayer, meditation, brainwaves

INTRODUCTION

Electroencephalography (EEG) reflects the action of the brain. It is the electrical activity produced by the firing of the vast number of neurons recorded from the scalp. EEG shows a variety of oscillations due to the summation of the synchronous activity of neurons. Since 1929, when Berger [1] showed that the alpha rhythm tends to decrease in amplitude during mental arithmetic performance, thousands of studies have been published regarding task-related modulation of human EEG. A large number of functional brain activities have been correlated with specific EEG changes. They have been

related, for example, to emotion [2], dyslexia [3], anxiety [4], memory [5], drowsiness [6] and depression [7]. Notwithstanding the vast number of studies in this field, to date there has been apparently no peer-reviewed journal publishing research on EEG changes during Muslim prayer.

Islam obligates all Muslims to pray five times a day. Muslim prayer should be performed with particular genuflections or body movements and the recitation of specific religious phrases. It is one of the most important Islamic acts. Nevertheless, in the Islamic point of view the prayer is not the goal itself. The real goal is the remembrance of God and the training of attention during prayer to focus on God (for example: "...and keep up prayer for my remembrance." [8]). A properly performed prayer will eventually extend the remembrance and the attention to God even when the prayer ends and during the course of everyday-life activities. Individuals praying correctly will feel and remember God at all times. A properly performed prayer from the Islamic point of view will produce a deep calmness and spiritual feelings of closeness to God, with its peak mostly occurring during the prayer ("*Those who have believed and whose hearts are assured by the remembrance of Allah. Unquestionably, by the remembrance of Allah, hearts are assured.*" [9]). According to the rules of Islamic prayer, the value of the prayer is mostly related to the attention of the individual on what he recites and on his focus on God. Without which, the individual does not benefit from the full effect of prayer. Improved focus will yield better results. That is why, from the Islamic point of view, research on the attention and concentration during prayer is of utmost importance.

All types of meditation share common features. It is a way to regulate and control the attention of the mind [10]. Meditation can be divided into two types—concentrative meditation and mindfulness meditation. In fact, there is a whole spectrum in between these two poles depending on the attentional processes involved [11]. This classification will be elaborated upon in the discussion section.

Our main objective is to develop a series of research on the neuroelectric changes during Muslim prayer guided by this pilot study. The lack of previous studies in this field has made us cautious to conduct large-scale research without a preliminary study to check whether neuroelectric changes occur during Muslim prayer. Therefore, it was logical to begin with a pilot study to provide the foundation for designing more comprehensive experiments.

METHODS

Design of Experiment

In order to identify the EEG changes resulting from the spiritual experience and the attention associated with Muslim prayer, it was necessary to compare the recorded EEG during the act of praying with that obtained during another two states by the same participant. The first was the resting state in which the participant was sitting on a chair with his mind wandering freely. This state may be regarded as the baseline for comparison with the EEG changes during prayer.

However, by its very nature Muslim prayer should be performed while maintaining a specific posture for a few seconds up to a few minutes. When the phrase or 'mantra' related to that posture has been completed, a body movement should be made to change to the next posture. There are four different postures in Muslim prayer, viz. standing (1-2 minutes), bowing (a few seconds), prostrating (a few seconds) and sitting (a few seconds up to 1 minute).

Muslim prayer, as mentioned above, should also be performed while reciting certain religious phrases or 'mantra'. This presents a challenge of recording an EEG without muscle artifacts. Artifacts are always present, but EEG researchers are usually keen to decrease them as much as possible. To solve this problem, it was necessary to compare the EEG during prayer with the second state in which the participant was asked to move and speak similarly to how he would during Muslim prayer but without any real concentration (meditation) on God, and the participant was not allowed to use religious phrases in this state. This was done by asking the participant to repeatedly recite names of his first, second and third degree relatives that he could remember. The third state was the real prayer. The participant was asked to concentrate as much as he could on God when reciting the prayer.

In order to identify the EEG changes due to the attention and the spiritual factor of the prayer excluding any neuroelectric changes that occurred as a result of muscular activity of the eyes, body and tongue, we made two comparisons. The first was between the resting-state EEG and the prayer-state EEG (i.e. 'rest to prayer' transition). The second was between the prayer-movement-state EEG and the prayer-state EEG (i.e. 'prayer-movement to prayer' transition).

The EEG changes were not accepted as those resulting from the spiritual and concentrative efforts of the pray-er unless they met two specific criteria: the changes should be significant ($P < 0.05$) and there should be also a significant change in the same EEG feature in the second comparison even though the magnitude of the changes might differ. This is to ensure that the changes were really due to the attention and spiritual effect during prayer. The resting state compared with prayer should register changes due to the pray-er's spiritual state, attention, muscular movements and recitation. The prayer-movement state compared with prayer should reveal changes due to the attention and the spiritual effect of the prayer proper as well as other factors such as voicing their wandering thoughts aloud. Thus, by taking into account the two comparisons, most if not all of the confounding factors should be eliminated.

The other benefit from this methodology is that it will decrease the chance of false positive results occurring due to the well-known statistical multiple comparisons problem (i.e. the multiple t-tests performed on the same data). In our analysis this would be 19 EEG absolute power t-tests + 19 relative power t-tests + 3×171 (combinations of all electrode pairs for amplitude asymmetry + coherence + phase lag) = 551 t-tests for each of the two states compared (i.e. transition). This would yield 27.55 significant false positive results ($P < 0.05$) by chance alone for each transition, which is termed error type I.

Through our method of combining two baselines or control states (i.e. rest and prayer-movement) to be compared with the experimental state (i.e. prayer), the error type I would drastically decrease. The overall (i.e. familywise) chance of error type I appearing in the first and the second transitions combined would be the multiplication of the chance of type-I error in the first and the second transitions, which is $0.05 * 0.05 = 0.0025$ or 0.25%.

Thus, the overall number of significant false positive results by chance alone (if $P < 0.05$ for both transitions) would be reduced from 27.55 to $551 * 0.0025 \sim 1.38$. Even less error type I would result if $P < 0.01$ for both transitions, i.e. well below 1 (~ 0.05).

EEG Recording Protocol

One male Muslim (aged 32, right-handed, no previous mental or chronic physical illness) participated in this pilot study. He was asked to evaluate himself concerning his everyday usual concentration level in his prayer. He chose to place himself in the medium grade, by which he meant that sometimes he would be distracted and his mind would wander and not concentrate on his prayer. Although his concentration was sometimes more or less than this average, this was normally the case for approximately half of his prayer time. Although he was asked to do his best to concentrate on his prayer during our experiments, he was not able to improve his concentration more than he did normally.

The EEG activity for all states was recorded for an average of 2-3 minutes at a time with the eyes closed. In the first state, the participant was asked to sit down on a chair and relax, letting his mind wander freely without any special mental or physical task. This state was identified as the resting state. The EEG of the second state was recorded while the individual was moving as if performing a Muslim prayer but reciting non-religious phrases. This state was referred to as the prayer-movement state. The third state was during the Muslim prayer. The participant was asked to concentrate as much as possible. This state was referred to as the prayer state. All three states were repeated 25 times in the sequence of resting, prayer movement then prayer. EEG recordings were performed at different times during the day. Each 2-3-minute recording of each trial was separated by 30-60 seconds of rest.

Collection of Data

EEG data were recorded from 19 channels according to the International 10-20 electrode system of scalp electrode placement [12] (Figure 1). The EEG data were recorded for offline analysis using a 40-channel Medelec EEG system (Oxford Instruments, Inc., UK) during 5 days randomly chosen in July-August 2010. All EEG recordings were done in the Biomedical Engineering EEG Lab of the University of Malaya. All channels were referenced to A2 (sampling rate = 512 sample/sec). They were remontaged into linked ears montage before offline analysis. The electrodes' impedance was checked before and after each recording and generally all electrodes were maintained at 5-10 kohm. The frequency response of the EEG amplifiers was 0.5-70 Hz without notch filter.

Eight auxiliary channels were used for recording the electromyography (EMG) of the muscles and eye movements, the use of which is mandatory in Muslim prayer. There were 6 bipolar EMG channels: two (right and left) channels were placed at 13 cm below the inion to record the activity of the neck muscles; another two (right and left) were placed at 3-6 cm below and anterior to the ears to record the masseter muscles' activity; one channel was used to record the vertical movements of the tongue (recorded between the nasion and below the chin), and the other was for the horizontal movements of the tongue (recorded between the right cheek and the left cheek). Two electrooculograph (EOG) channels were used to record the vertical and horizontal movements of the eyeballs.

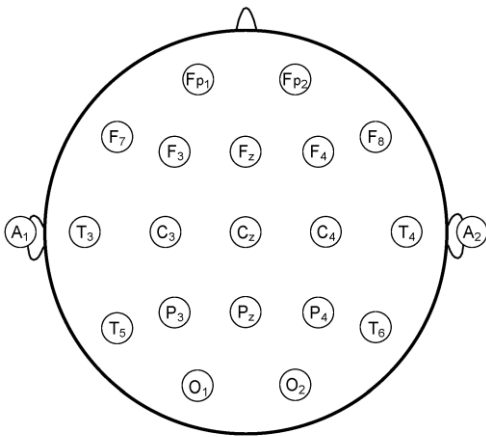


Figure 1. The international 10-20 system of electrode placement

Data Analysis

Offline EEG data were imported into the software ‘NeuroGuide’ (version 2.6.3). Usually, parametric statistical analysis is preferred to the non-parametric one. Parametric statistics has more power: it needs less sample size to draw conclusions with the same degree of confidence. This benefit comes at the cost of a more limiting assumption. It relies on the assumption that the data is sampled from a population with a Gaussian probability distribution (i.e. normally distributed population) [13]. In the real world of data sampling, this assumption will never be met completely. Nevertheless, one should try to make mathematical transformations for the data until the best normality is achieved. If the normality assumption could not be achieved, non-parametric statistics should be used. Previous literature showed that the EEG absolute power and phase in the normal population do not show Gaussian distribution. However, the other features of the EEG (coherence, amplitude asymmetry and relative power) have better normality and do not need any transformation to be used in parametric statistical tests [13]. Thus, the EEG absolute power and phase features were logarithmically transformed to fit the Gaussian distribution.

All the EEG data were revised to exclude any period (i.e. epoch) containing artifacts. This was carried out before the analysis of the EEG signals using the ‘Neuroguide’ software. A minimum amount of EMG artifacts due to tongue movements could not be excluded as they were the very act of Muslim prayer. Hence a low EEG contamination by artifacts was acceptable. It was just for the prominent artifacts that all the EEG for that contaminated epoch was excluded and rejected. This was done by a careful inspection for the whole EEG. After the exclusion of the epochs which were highly artifact-contaminated, the ‘Neuroguide’ software analysis was carried out. The frequency range of the remaining artifacts and the contaminated channels were identified and eliminated from the results before the interpretation of the analysis. This identification was carried out with the aid of topographical EEG analysis (Linked Ears and Laplacian montage) and with the help of the eight auxiliary channels that monitored when and what contamination was aroused from the muscles.

By rejecting the contaminated epochs, on average, sixty seconds of EEG remained from each trial to enter the analysis phase by the ‘Neuroguide’ software. For each trial, the average fast Fourier

transform (FFT) for all the remaining epochs was calculated. Statistical analysis for two-group combinations (prayer trials group – rest trials group, prayer trials group – prayer-movement trials group) was calculated by independent t-tests. The following EEG statistical tests were calculated:

1. Topographical maps for FFT absolute power difference and relative power difference in 14 frequency bands (delta: 1-4 Hz, theta: 4-8 Hz, alpha: 8-12 Hz, beta: 12-25 Hz, high beta: 25-30 Hz, gamma: 30-40 Hz, high gamma: 40-50 Hz, alpha1: 8-10 Hz, alpha2: 10-12 Hz, beta1: 12-15 Hz, beta2: 15-18 Hz, beta3: 18-25 Hz, gamma1: 30-35 Hz, and gamma2: 35-40 Hz). Single Hz frequency bands (1-50 Hz) were also calculated.
2. FFT amplitude asymmetry difference, FFT coherence difference and FFT phase lag difference in 4 bands (delta: 1-4 Hz, theta: 4-8 Hz, alpha: 8-12 Hz, and beta: 12-25 Hz) for all 171 combinations of the 19 EEG scalp channels.

RESULTS

It should be recalled that a change (prayer - rest) was not regarded as acceptable unless the same change was also present in the second control difference (prayer - prayer movement). It was found that the delta band was highly prone to artifacts. This was consistent with the literature in that tongue movements (speaking during prayer) and eye movements produce artifacts mainly in the delta band [14]. This is why this band was excluded from our analysis.

Moreover, EEG during Muslim prayer will definitely be contaminated by EMG. Muscle movements are part of the Muslim prayer and cannot be avoided. EMG artifacts are mostly present in gamma and beta bands. We tried to exclude the contaminated EEG by editing the EEG data (discarding the most likely contaminated epochs) and being more cautious in interpreting changes in these bands by carefully inspecting the topographical distribution of the FFT absolute power gradient in these frequencies.

FFT Absolute and Relative Power Differences

The significant changes for both absolute and relative power differences were the same, so we focused on the FFT absolute power difference. Figure 2 shows the common significant changes in the two transitions, viz. prayer movement to prayer and rest to prayer. Any significant changes that were present in one transition and not in the other are not shown in the figure.

Most of the changes are highly significant ($P < 0.01$) in the alpha2 band (see O1, O2, P3, P4, T5, and T6 electrodes in Figure 2). These electrodes cover the scalp over the occipital, parietal and posterior temporal areas of the brain. We found that in FFT absolute power and relative power analysis, it was important to divide the standard bands (delta, theta, alpha, beta and gamma) into several smaller bandwidths. This was because in certain cases, by averaging a whole frequency band range, there would be some positive changes in specific frequencies and negative changes in others, and each one would cancel the other. For example, in this study we did not find any significant change throughout the alpha band (8-12 Hz), but there was a highly significant EEG power decrease in specific frequencies if considered alone in a smaller bandwidth such as alpha2 (10-12 Hz) or a single (10 Hz) band. The alpha1 band also showed a less significant power increase in P3 and T5. The

changes are listed below with ‘↑’ indicating electrodes with increasing power change from rest and prayer movement to prayer transitions and ‘↓’ for decreasing power change:

Alpha2 band (left hemisphere): ↓ O1, ↓ P3, ↓ T5

Alpha2 band (right hemisphere): ↓ O2, ↓ P4, ↓ T6

Alpha1 band (left hemisphere): ↑ P3, ↑ T5

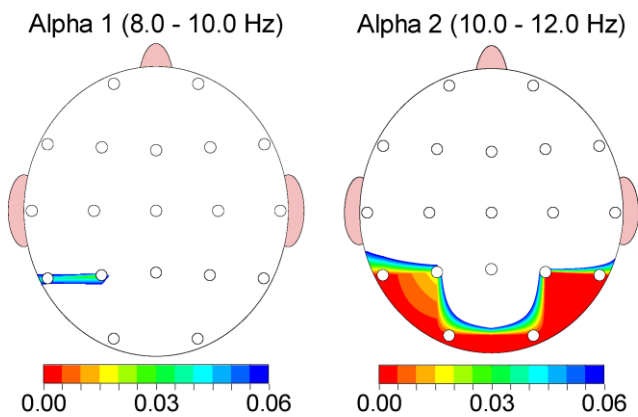


Figure 2. P-values for FFT absolute-power group independent t-test (common significant changes from ‘rest to prayer’ and ‘prayer movement to prayer’ in Alpha1 and Alpha2 bands)

FFT Amplitude Asymmetry Difference

The significant changes for the ‘prayer movement to prayer’ and ‘rest to prayer’ transitions are shown in Figure 3. For a list of significant changes that happened as shown below, the electrode pairs are written in bold font for changes that were common in the two transitions and which were both highly significant ($P < 0.01$). They are written in italic font for changes that were in one case highly significant ($P < 0.01$) and in the other case less significant ($P < 0.05$). The other listed pairs with normal font were less significant in both cases ($P < 0.05$). Electrode pairs that registered significant changes in just one case are not listed or are designated as ‘no significant changes’. (These notations also apply to the next two sections.)

Theta band (left hemisphere): ↓ *FP1-P3*, ↓ *FP1-T5*, ↓ *F3-P3*, ↓ *F3-T5*, ↓ **C3-P3**, ↑ C3-F7, ↓ *C3-T5*, ↑ *P3-O1*, ↑ **P3-F7**, ↑ *P3-T3*, ↓ *O1-T5*, ↓ **F7-T5**, ↓ **T3-T5**

Theta band (right hemisphere): No significant changes

Theta band (homologous pairs): ↑ *P3-P4*, ↑ *T5-T6*

Alpha band (left hemisphere): ↓ *F3-P3*, ↑ *P3-O1*, ↑ **P3-F7**, ↓ *O1-T5*, ↓ *F7-T5*

Alpha band (right hemisphere): ↑ *FP2-O2*, ↑ *F4-O2*, ↑ *P4-O2*

Alpha band (homologous pairs): ↑ **P3-P4**, ↑ **T5-T6**

Beta band (left hemisphere): ↓ *FP1-F3*, ↓ **FP1-F7**

Beta band (right hemisphere): ↑ *F8-T4*

Beta band (homologous pairs): ↑ **P3-P4**

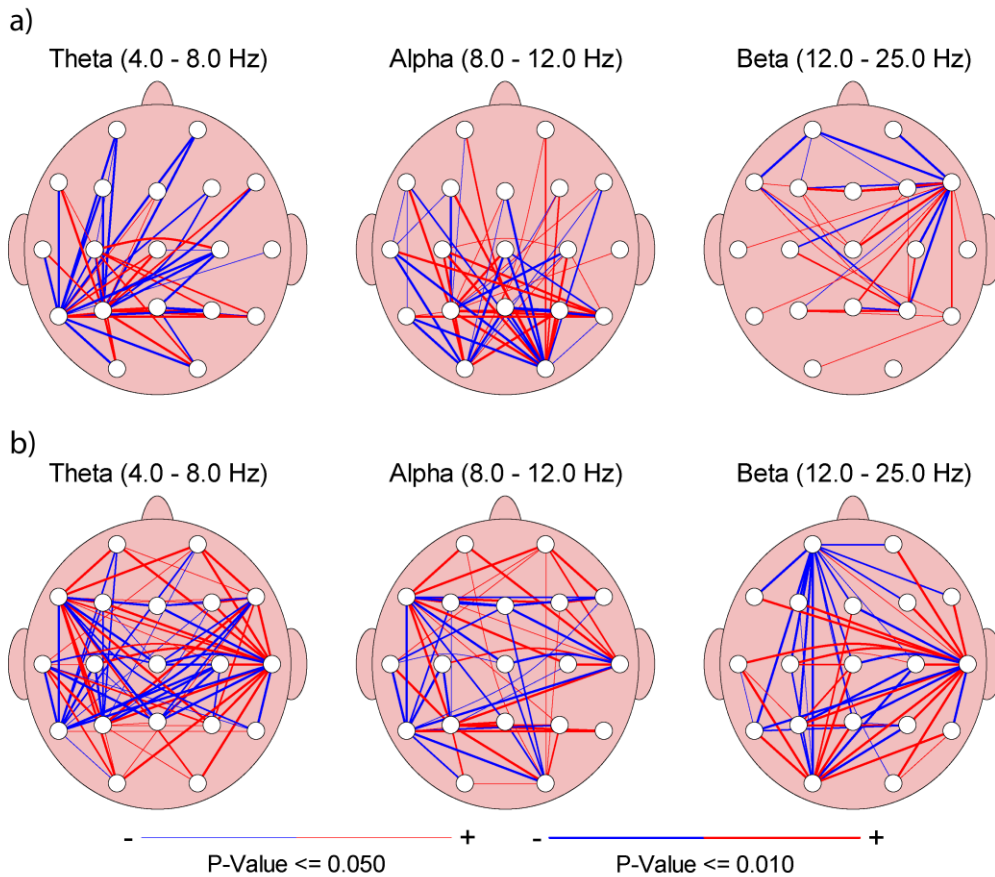


Figure 3. FFT amplitude asymmetry group independent t-test (P-value): a) from prayer movement to prayer, b) from rest to prayer; blue = decreased amplitude asymmetry in prayer compared to rest and prayer movement, red = increased amplitude asymmetry in prayer compared to rest and prayer movement

FFT Coherence Difference

The significant changes from prayer movement to prayer and from rest to prayer are shown in Figure 4. Their list is as follows:

Theta band (left hemisphere, right hemisphere, homologous pairs): No significant changes

Alpha band (left hemisphere): ↓ **F3-O1**, ↑ **C3-P3**, ↑ **C3-O1**, ↑ **T3-T5**, ↓ C3-F7, ↑ **C3-T5**, ↑ **P3-T3**, ↓ **O1-F7**, ↑ **O1-T3**

Alpha band (right hemisphere): ↓ **F4-O2**, ↑ **C4-P4**

Alpha band (homologous pairs): ↓ **O1-O2**

Beta band (left hemisphere): No significant changes

Beta band (right hemisphere): ↑ **F8-T4**

Beta band (homologous pairs): No significant changes

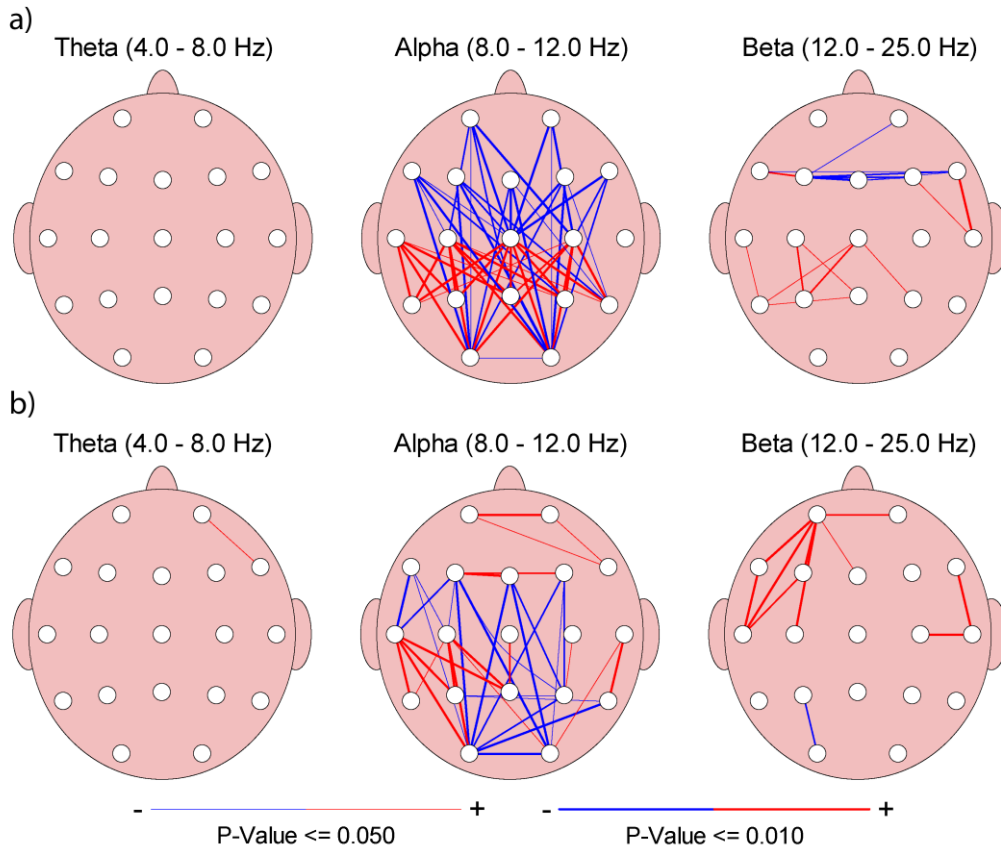


Figure 4. FFT coherence group independent t-test (P-value): a) from prayer movement to prayer, b) from rest to prayer; blue = decreased coherence in prayer compared to rest and prayer movement, red = increased coherence in prayer compared to rest and prayer movement

FFT Phase Lag Difference

The significant changes from prayer movement to prayer and from rest to prayer are shown in Figure 5. Their list is as follows:

Theta band (left hemisphere): \uparrow *FP1-F3*, \downarrow *O1-T3*

Theta band (right hemisphere): No significant changes

Theta band (homologous pairs): No significant changes

Alpha band (left hemisphere): \downarrow *O1-T3*

Alpha band (right hemisphere): \downarrow *T4-T6*

Alpha band (homologous pairs): No significant changes

Beta band (left hemisphere): \downarrow *FP1-C3*

Beta band (right hemisphere): No significant changes

Beta band (homologous pairs): No significant changes

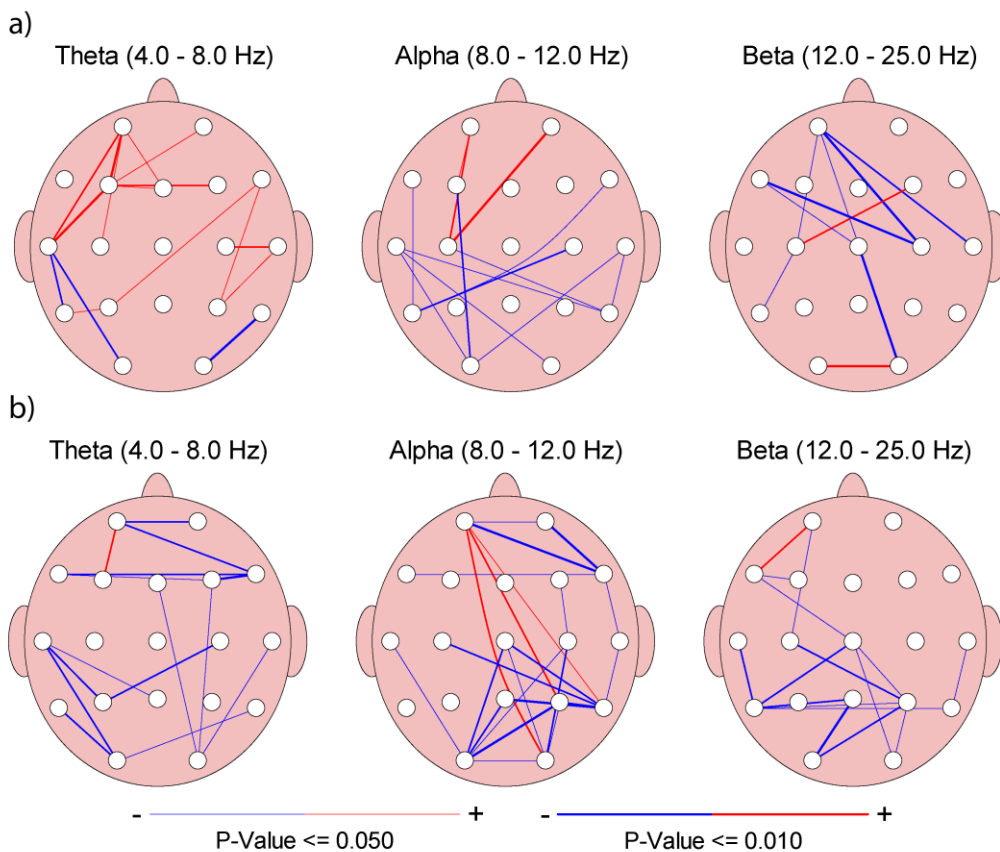


Figure 5. FFT phase lag group independent t-test (P-value): a) from prayer movement to prayer, b) from rest to prayer; blue = decreased phase lag in prayer compared to rest and prayer movement, red = increased phase lag in prayer compared to rest and prayer movement

DISCUSSION

Coherence is a measure of the stability of phase difference between two EEG signals. It is measured with pairs of electrode positions. It provides an indication of the functional coupling of the two brain regions. Coherence is positively related to the number and strength of the connections between neurons (Coherence = $N \cdot S$, where N is the number of connections and S is the strength of connections). The connections can be either intra-cortical connections in gray matter (1-3 mm) or longer connections as ‘U shaped’ white matter fibres (30-60 mm) or long-distance cortico-cortical fibres (> 60 mm) [15]. Normally, the intra-cortical connections and the ‘U shaped’ white matter fibres are more in quantity than the long-distance cortico-cortical fibres in a normal brain. Thus, a short inter-electrode distance (adjacent electrodes) has a higher density of connective fibres, which means less delay (i.e. less phase lag) and more phase stability (i.e. higher coherence).

In previous EEG studies, EEG coherence change was related to several functional cognitive activities, e.g. intelligence [16], memory efficiency [17-18] and arousal level [19]. Increased alpha coherence in meditation was found in many previous studies [e.g. 20-23]. In our study (Figure 6), the coherence changes were highly significant ($P < 0.01$), indicating more connection strength and/or increase in neuronal connections as well as reduced functional differentiation in the affected brain

regions due to the new mental states in prayer. Previous literature showed that there are patients with abnormal mental or neural conditions, in whom EEG coherence are decreased [e.g. 24-28]. Some of those patients were treated with different success rates by training them to increase coherence in multiple neurofeedback sessions [29-35]. The prayer effect on coherence may thus be useful to counterbalance the decrease in coherence in those brain regions. This is a potential research field that has not been attempted before.

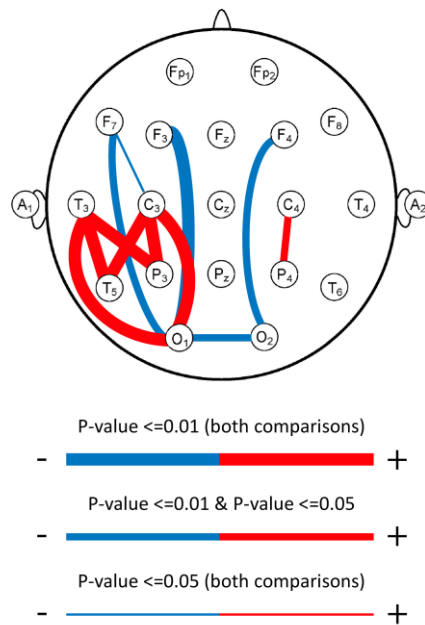


Figure 6. P-values of FFT alpha-band coherence group independent t-test (common changes from rest to prayer and from prayer movement to prayer); blue = decreased coherence in prayer compared to rest and prayer movement, red = increased coherence in prayer compared to rest and prayer movement

The EEG power changes in prayer were further analysed by a single Hz power analysis (Figure 7). The alpha2 band (10-12 Hz) power was decreased in prayer when compared with that in the prayer movement and rest states. The decrease was actually in the 10 Hz power in the occipital and posterior temporal and parietal areas of the brain. Furthermore, there was an increase in the 8 Hz power, mainly in the left posterior temporal and parietal areas.

The majority of previous research findings on EEG changes during meditation indicated increasing theta and/or alpha power [36-37]. However, in this study there was no significant change in the alpha power (8-12 Hz) unless the bandwidth was divided into alpha1 (8-10 Hz) and alpha2 (10-12 Hz) bands or into single Hz bandwidth analysis. This is because the change was not primarily on the power, but rather on shifting of the mean power of the alpha rhythm from 10 Hz to 8 Hz. This change was limited to the alpha bandwidth, hence no net effect on the alpha power as a whole range (8-12 Hz). The slowing alpha rhythm was consistent with some of the previous research findings on the effect of meditation on EEG [36-40].

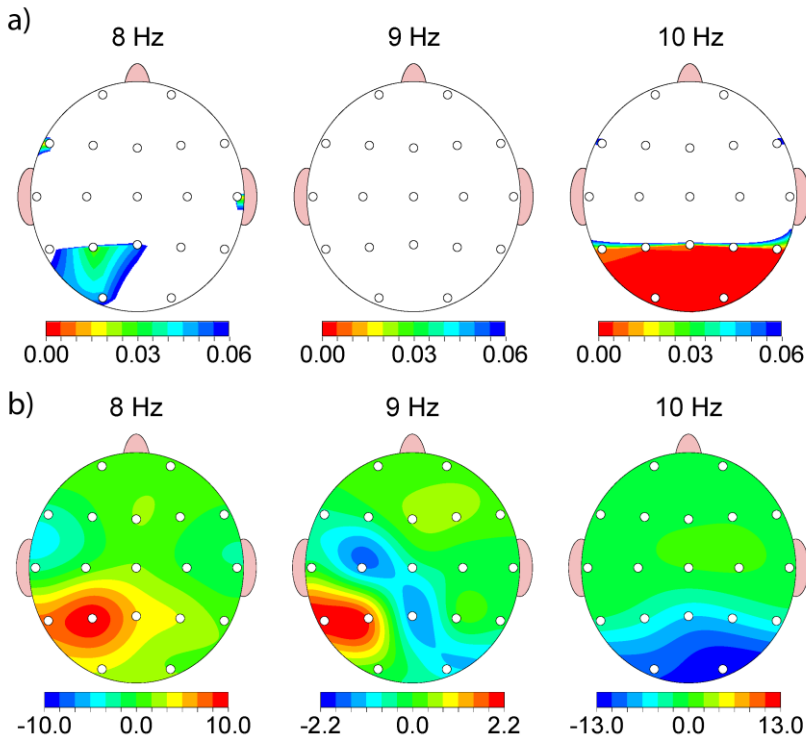


Figure 7. FFT absolute-power group single-Hz frequency analysis for 8-10 Hz (common significant changes from rest to prayer and from prayer movement to prayer): a) independent t-test (P-value), b) absolute power difference (μV^2)

Although considerable research has been done on meditation, most of the findings are dissimilar. We opine that unless there are some standards in categorising the factors that have direct effects on the EEG findings, there will be no consistent results. Although normal EEG changes significantly according to age and gender, no previous trials seem to exist that study a single meditation technique on different age groups or on a specific gender versus the other. Furthermore, the type of meditation determines the mental activity, which has a direct relationship with EEG changes. For example, the two extreme ends of meditative techniques—the yogic concentrative meditation and the Zen mindfulness meditation—cannot give the same EEG findings as the physiological changes in the brain are dependent on the action of the mind. Concentrative meditation involves the concentrative effort of the mind on a single sensory or mental action, whereas mindfulness meditation involves maintaining a passive state of attention and letting thoughts pass in or out of the mind without mentally processing the thoughts. The latter is a neutral observer technique. There are many other meditation techniques that lie between these two extremes. Another factor that has an impact on EEG findings in meditation is the level of experience of the meditator and the duration of his/her training. We cannot expect significant EEG changes in novice meditators who are unable to apply the technique correctly as their mind wandering (in which the default mode network of the brain is activated) will not differ from the resting state.

Muslim prayer is by no means different from other meditation techniques. Future studies concerning the mental and psychological effects on EEG changes should be categorised and

standardised. Although many Muslims have been praying for decades, it does not mean that all of them are performing the prayer in a proper manner. The physiological effect of any mental action on the EEG is dependent on the content of this mental action. Praying for a long time does not guarantee proper concentrative effort. It is the choice and will of the individual praying that really determine the level of concentration in prayer. Although the value of prayer in Islam is on its concentrative strength and on the maintenance of concentration on the phrases, there will be a large proportion of Muslims who usually perform this prayer as a purely physical action without bothering to concentrate. This is because Muslim prayer is obligatory in Islam for all Muslims, and although performing the prayer in this manner may be acceptable, it is the least acceptable in terms of prayer quality. That is why even the time factor for Muslim prayer cannot be relied upon to assess the meditative experience. We propose that there should be a psychological questionnaire developed by experts, similar to other psychological scales (for example the mysticism scale [41]), to assess the level of concentration in Muslim prayer.

In sum, the roadmap for future studies on Muslim prayer should be based on controlling the confounding factors (age, gender, usual prayer concentration level, anxiety level during experiments, etc.) that result in discrepancies. It is hoped that this pilot study will encourage researchers to conduct further studies to analyse the inter-individual variability in EEG changes during Muslim prayer and to investigate the potential therapeutic effect on some abnormal neural and mental conditions. It will also be helpful in the future to study the phase shift and phase lock, which give a more physiologically fundamental measure than coherence. The change in coherence during prayer may be due partly to the very fast phase shifting or short phase lock and this may lead to hypotheses about GABA and/or glutamate excitatory loops as discussed by Buzsaki [42].

ACKNOWLEDGEMENTS

We would like to thank the Ministry of Higher Education of Malaysia for providing the FRGS grant (FRGS/1/10/SP/UPM/02/26) and the staff of the Biomedical Engineering Department of the University of Malaya for providing access to their laboratory and helping us to conduct our experiments.

REFERENCES

1. H. Berger, "On the EEG in humans", *Arch. Psychiatr. Nervenkr.*, **1929**, 87, 527-570.
2. P. C. Petrantonakis and L. J. Hadjileontiadis, "Emotion recognition from EEG using higher order crossings", *IEEE Trans. Info. Technol. Biomed.*, **2010**, 14, 186-197.
3. B. Penolazzi, C. Spironelli, C. Vio and A. Angrilli, "Brain plasticity in developmental dyslexia after phonological treatment: A beta EEG band study", *Behav. Brain Res.*, **2010**, 209, 179-182.
4. D. K. Hannesdóttir, J. Doxie, M. A. Bell, T. H. Ollendick and C. D. Wolfe, "A longitudinal study of emotion regulation and anxiety in middle childhood: Associations with frontal EEG asymmetry in early childhood", *Development. Psychobiol.*, **2010**, 52, 197-204.

5. P. Sauseng, B. Griesmayr, R. Freunberger and W. Klimesch, "Control mechanisms in working memory: A possible function of EEG theta oscillations", *Neurosci. Biobehav. Rev.*, **2010**, 34, 1015-1022.
6. C. W. Chang, L. W. Ko, F. C. Lin, T. P. Su, T. P. Jung, C. T. Lin and J. C. Chiou, "Drowsiness monitoring with EEG-based MEMS biosensing technologies", *GeroPsych*, **2010**, 23, 107-113.
7. A. Steiger and M. Kimura, "Wake and sleep EEG provide biomarkers in depression", *J. Psychi. Res.*, **2010**, 44, 242-252.
8. Holy Quran, "Surat Taha", 20:14.
9. Holy Quran, "Surat Ar-Ra'd", 13:28.
10. A. Lutz, H. A. Slagter, J. D. Dunne and R. J. Davidson, "Attention regulation and monitoring in meditation", *Trends Cognit. Sci.*, **2008**, 12, 163-169.
11. J. Andresen, "Meditation meets behavioural medicine. The story of experimental research on meditation", *J. Conscious. Studies*, **2000**, 7, 17-74.
12. H. H. Jasper, "The ten-twenty electrode system of the International Federation", *Electroencephalogr. Clin. Neurophysiol.*, **1958**, 10, 371-375.
13. R. W. Thatcher, R. A. Walker, C. J. Biver, D. N. North and R. Curtin, "Quantitative EEG normative databases: Validation and clinical correlation", *J. Neurotherapy*, **2003**, 7, 87-121.
14. D. C. Hammond and J. Gunkelman, "The Art of Artifacting", International Society for Neuronal Regulation, Corpus Christi (TX, USA), **2001**, pp. 4-8.
15. R. W. Thatcher, C. J. Biver and D. North, "Spatial-temporal current source correlations and cortical connectivity", *Clin. EEG Neurosci.*, **2007**, 38, 35-48.
16. R. W. Thatcher, D. North and C. Biver, "EEG and intelligence: Relations between EEG coherence, EEG phase delay and power", *Clin. Neurophysiol.*, **2005**, 116, 2129-2141.
17. W. Klimesch, H. Schimke and G. Pfurtscheller, "Alpha frequency, cognitive load and memory performance", *Brain Topogr.*, **1993**, 5, 241-251.
18. P. Sauseng, W. Klimesch, M. Schabus and M. Doppelmayr, "Fronto-parietal EEG coherence in theta and upper alpha reflect central executive functions of working memory", *Int. J. Psychophysiol.*, **2005**, 57, 97-103.
19. J. L. Cantero, M. Atienza, R. M. Salas and C. M. Gómez, "Alpha EEG coherence in different brain states: An electrophysiological index of the arousal level in human subjects", *Neurosci. Lett.*, **1999**, 271, 167-170.
20. J. T. Farrow and J. R. Hebert, "Breath suspension during the Transcendental Meditation technique", *Psychosom. Med.*, **1982**, 44, 133-153.
21. C. Gaylord, D. Orme-Johnson and F. Travis, "The effects of the transcendental meditation technique and progressive muscle relaxation on EEG coherence, stress reactivity, and mental health in black adults", *Int. J. Neurosci.*, **1989**, 46, 77-86.
22. F. Travis, J. Tecce, A. Arenander and R. K. Wallace, "Patterns of EEG coherence, power, and contingent negative variation characterize the integration of transcendental and waking states", *Biol. Psychol.*, **2002**, 61, 293-319.

23. R. Hebert, D. Lehmann, G. Tan, F. Travis and A. Arenander, "Enhanced EEG alpha time-domain phase synchrony during Transcendental Meditation: Implications for cortical integration theory", *Signal Process.*, **2005**, 85, 2213-2232.
24. T. Locatelli, M. Cursi, D. Liberati, M. Franceschi and G. Comi, "EEG coherence in Alzheimer's disease", *Electroencephalogr. Clin. Neurophysiol.*, **1998**, 106, 229-237.
25. L. Leocani and G. Comi, "EEG coherence in pathological conditions", *J. Clin. Neurophysiol.*, **1999**, 16, 548-555.
26. Y. Wada, Y. Nanbu, M. Kikuchi, Y. Koshino, T. Hashimoto and N. Yamaguchi, "Abnormal functional connectivity in Alzheimer's disease: Intrahemispheric EEG coherence during rest and photic stimulation", *Euro. Arch. Psychi. Clin. Neurosci.*, **1998**, 248, 203-208.
27. A. Sritharan, P. Line, A. Sergejew, R. Silberstein, G. Egan and D. Copolov, "EEG coherence measures during auditory hallucinations in schizophrenia", *Psychi. Res.*, **2005**, 136, 189-200.
28. M. Murias, S. J. Webb, J. Greenson and G. Dawson, "Resting state cortical connectivity reflected in EEG coherence in individuals with autism", *Biol. Psychi.*, **2007**, 62, 270-273.
29. M. H. M. Breteler, M. Arns, S. Peters, I. Giepmans and L. Verhoeven, "Improvements in spelling after QEEG-based neurofeedback in dyslexia: A randomized controlled treatment study", *Appl. Psychophysiol. Biofeedb.*, **2010**, 35, 5-11.
30. J. E. Walker and G. P. Kozlowski, "Neurofeedback treatment of epilepsy", *Child Adolesc. Psychi. Clin. North America*, **2005**, 14, 163-176.
31. J. A. Pineda, D. Brang, E. Hecht, L. Edwards, S. Carey, M. Bacon, C. Futagaki, D. Suk, J. Tom, C. Birnbaum and A. Rork, "Positive behavioral and electrophysiological changes following neurofeedback training in children with autism", *Res. Autism Spectr. Disord.*, **2008**, 2, 557-581.
32. R. P. Reddy, J. Rajan, I. Bagavathula and T. Kandavel, "Neurofeedback training to enhance learning and memory in patient with traumatic brain injury: A single case study", *Int. J. Psychosoc. Rehab.*, **2009**, 14, 21-28.
33. T. Sürmeli and A. Ertem, "EEG neurofeedback treatment of patients with Down syndrome", *J. Neurotherapy*, **2007**, 11, 63-68.
34. D. L. Trudeau, T. M. Sokhadze and R. L. Cannon, "Neurofeedback in alcohol and drug dependency", in "Introduction to Quantitative EEG and Neurofeedback: Advanced Theory and Applications", 2nd Edn. (Ed. T. H. Budzynski, H. K. Budzynski, J. R. Evans and A. Abarbanel), Academic Press, Burlington (MA, USA), **2008**, Ch. 10.
35. M. B. Stermán and T. Egner, "Foundation and practice of neurofeedback for the treatment of epilepsy", *Appl. Psychophysiol. Biofeedb.*, **2006**, 31, 21-35.
36. B. R. Cahn and J. Polich, "Meditation states and traits: EEG, ERP, and neuroimaging studies", *Psychol. Bull.*, **2006**, 132, 180-211.
37. J. Fell, N. Axmacher and S. Haupt, "From alpha to gamma: Electrophysiological correlates of meditation-related states of consciousness", *Med. Hypoth.*, **2010**, 75, 218-224.
38. A. Kasamatsu and T. Hirai, "An electroencephalographic study on the Zen meditation (Zazen)", *Psychi. Clin. Neurosci.*, **1966**, 20, 315-336.
39. T. Hirai, "Psychophysiology of Zen", Igaku Shoin Ltd., Tokyo, **1974**, pp. 36-43.

40. B. Taneli and W. Krahne, "EEG changes of transcendental meditation practitioners", *Adv. Biol. Psychi.*, **1987**, 16, 41–71.
41. R. W. Hood Jr, "The construction and preliminary validation of a measure of reported mystical experience", *J. Sci. Study Religion*, **1975**, 14, 29-41.
42. G. Buzsáki, "Rhythms of the Brain", Oxford University Press, New York, **2006**, pp. 464.

Full Paper

Free vibration analysis of symmetrically laminated composite rectangular plates using extended Kantorovich method

Kullasup Phongsrisk*, Prasong Ingsuwan, Wetchayan Rangri and Wiwat Klongpanich

Department of Mechanical Engineering, Faculty of Engineering, Chiang Mai University,
Chiang Mai 50200, Thailand

* Corresponding author, e-mail: phongsrisuk@gmail.com

Received: 11 June 2010 / Accepted: 5 November 2010 / Published: 9 December 2010

Abstract: Free vibration of symmetrically laminated composite rectangular plates with various boundary conditions is analysed by an extended Kantorovich method, in which a separable function to the dynamic-system energy equation is applied in order to reduce the partial differential equations to ordinary differential equations in the direction of x , y coordinates with a constant coefficient. The beam function is used as an initial trial function in the iterative calculation, which is employed to evaluate the natural frequency and force the final solution needed to satisfy the boundary conditions. To verify the accuracy of the present method, the frequency parameters are evaluated in comparison with previous work on the subject. A good agreement proves that the method can be used to evaluate the natural frequencies of unidirectional 0° , unidirectional 90° and cross-ply symmetrically laminated composite rectangular plates.

Keywords: Kantorovich method, free vibration analysis, composite rectangular plates

INTRODUCTION

Composite materials are increasingly being used for rectangular plate structures constructed on mechanical, civil, aerospace and marine engineering projects. Due to their high strength, low weight, good fatigue resistance and good corrosion resistance, their properties meet the requirements of most specific designs. Regarding the bending, buckling or vibrating problem found in rectangular plates, the difficulty involved is in solving the related partial differential equations. The exact method used in doing this is possible when at least a pair of opposite edges is simply supported. Otherwise, an approximate

method such as the Galerkin method, the Rayleigh-Ritz method, the extended Kantorovich method and the finite element method (FEM) is usually employed.

The extended Kantorovich method is used to reduce the partial differential equations to ordinary differential equations in the direction of x, y coordinates. The iterative calculation is used to evaluate the deflection, buckling load or natural frequency and to force the final solution required to satisfy the boundary conditions. The extended Kantorovich method has been reviewed by several researchers. For example, Dalaei and Kerr derived a closed-form approximate solution for a uniformly lateral distributed load [1] and the natural frequency [2] of an orthotropic rectangular clamped plate. An initial trial function which satisfies the boundary conditions along the y coordinate direction was used in the iterative calculation. It was found that the final solution can be obtained from the fourth iteration and that this is independent of an initial trial function. Sakata et al. [3] evaluated the natural frequency of an orthotropic rectangular plate with various boundary conditions. An initial trial function which satisfies the boundary conditions along one direction was used in the iterative calculation. The results showed that the convergence of the final solution is rapid and the particular natural frequency can be obtained separately with a good accuracy while the Rayleigh-Ritz method uses a large number of shape functions if a higher natural frequency is required. Rajalingham et al. [4] improved the convergence of the natural frequency of an isotropic rectangular clamped plate. The shape functions obtained from the extended Kantorovich method were used in the Rayleigh-Ritz method. It was discovered that these shape functions enhance the effectiveness of the Rayleigh-Ritz method. Bercin [5] evaluated the low natural frequency of an orthotropic rectangular clamped plate. An initial trial function such as that used by Dalaei and Kerr [2] was used in the iterative calculation. It was found that the convergence of the solution is very rapid.

Lee et al. [6] derived the free vibration of symmetrically laminated composite rectangular plates with all edges elastically restrained against rotation based on first-order anisotropic shear deformation plate theory. The Timoshenko beam function was used in the iterative calculation as an initial trial function. The results indicated that the extended Kantorovich method can be more effectively and accurately applied to the free vibration of a symmetrically laminated composite with a cross-ply rectangular plate than the Rayleigh-Ritz method, but cannot be applied to the free vibration of a symmetrically laminated composite with an angle-ply rectangular plate. Rajalingham et al. [7] derived a closed-form approximate solution for the natural frequency of an isotropic and clamped plate. As the plate characteristic function was used in the iterative calculation as an initial trial function, the modal parameters were found to be suitable for evaluating a higher natural frequency while the Rayleigh-Ritz method involved a large order matrix eigenvalue problem, plus the finite element method could not provide accurate values for higher natural frequencies. Ungbhakorn and Singhatanadgid [9] evaluated the critical buckling load of symmetrically laminated composite with unidirectional 0° and cross-ply rectangular plates with various boundary conditions. Although an arbitrary function was used in the iterative calculation as an initial trial function, the final solution was automatically forced to satisfy the boundary conditions and the critical buckling load was obtained from the fourth iteration.

The purpose of this study is to evaluate the natural frequencies of symmetrically laminated composite rectangular plates with various boundary conditions using the extended Kantorovich method.

METHODS

Derivation of the Iterative Differential Equations

Hamilton’s principle is a generalisation of the principle of virtual displacement within the dynamics of a system. The principle assumes that the system under consideration is characterised by two energy functions, namely the kinetic energy and the potential energy [8]:

$$\delta \int_{t_1}^{t_2} [K - (V + U)] dt = 0 \tag{1}$$

where K is the kinetic energy and $V+U$ is the potential energy.

The potential energy and the kinetic energy of a symmetrically laminated composite rectangular plate, as shown in Figure 1, can be written as follows.

$$\delta \int_{t_1}^{t_2} \left\{ \frac{1}{2} \int_0^b \int_0^a \left[D_{11} \left(\frac{\partial^2 w}{\partial x^2} \right)^2 + 2D_{12} \left(\frac{\partial^2 w}{\partial x^2} \right) \left(\frac{\partial^2 w}{\partial y^2} \right) + 4D_{16} \left(\frac{\partial^2 w}{\partial x^2} \right) \left(\frac{\partial^2 w}{\partial x \partial y} \right) + D_{22} \left(\frac{\partial^2 w}{\partial y^2} \right)^2 + 4D_{26} \left(\frac{\partial^2 w}{\partial y^2} \right) \left(\frac{\partial^2 w}{\partial x \partial y} \right) + 4D_{66} \left(\frac{\partial^2 w}{\partial x \partial y} \right)^2 \right] dx dy - \frac{1}{2} \int_0^b \int_0^a m(\omega w)^2 dx dy \right\} dt = 0 \tag{2}$$

where D_{ij} is the bending stiffness of the composite plate, w is the lateral deflection, m is mass per unit area of plate and ω is the natural circular frequency.

Assuming the solution is

$$w(x, y) = X(x)Y(y) \tag{3}$$

substitute equation (3) into equation (2):

$$\delta \int_{t_1}^{t_2} \left\{ \frac{1}{2} \int_0^b \int_0^a \left[D_{11} \left(\frac{\partial^2 X}{\partial x^2} Y \right)^2 + 2D_{12} \left(\frac{\partial^2 X}{\partial x^2} Y \right) \left(X \frac{\partial^2 Y}{\partial y^2} \right) + D_{22} \left(X \frac{\partial^2 Y}{\partial y^2} \right)^2 + 4D_{66} \left(\frac{\partial X}{\partial x} \frac{\partial Y}{\partial y} \right)^2 + 4 \left(D_{16} \left(\frac{\partial^2 X}{\partial x^2} Y \right) + D_{26} \left(X \frac{\partial^2 Y}{\partial y^2} \right) \right) \left(\frac{\partial X}{\partial x} \frac{\partial Y}{\partial y} \right) \right] dx dy - \frac{1}{2} \int_0^b \int_0^a [mX^2Y^2\omega^2] dx dy \right\} dt = 0 \tag{4}$$

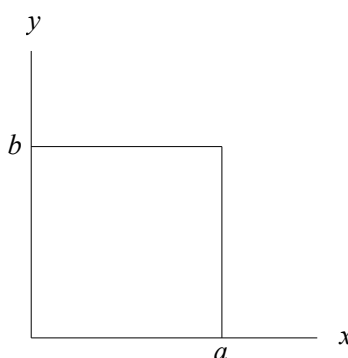


Figure 1. The rectangular plate

If $X(x)$ is defined a priori, equation (4) can be rewritten as

$$\delta \int_{t_1}^{t_2} \left\{ \frac{1}{2} \int_0^b \left[S_{1x} D_{11} Y^2 + 2 S_{2x} D_{12} Y \left(\frac{\partial^2 Y}{\partial y^2} \right) + S_{3x} D_{22} \left(\frac{\partial^2 Y}{\partial y^2} \right)^2 + 4 S_{4x} D_{66} \left(\frac{\partial Y}{\partial y} \right)^2 + 4 S_{5x} D_{16} Y \left(\frac{\partial Y}{\partial y} \right) + 4 S_{6x} D_{26} \left(\frac{\partial Y}{\partial y} \right) \left(\frac{\partial^2 Y}{\partial y^2} \right) \right] dy - \frac{1}{2} \int_0^b S_{3x} m Y^2 \omega^2 dy \right\} dt = 0 \tag{5}$$

where

$$\begin{aligned} S_{1x} &= \int_0^a \left(\frac{\partial^2 X}{\partial x^2} \right)^2 dx, & S_{2x} &= \int_0^a \left(X \frac{\partial^2 X}{\partial x^2} \right) dx \\ S_{3x} &= \int_0^a X^2 dx, & S_{4x} &= \int_0^a \left(\frac{\partial X}{\partial x} \right)^2 dx \\ S_{5x} &= \int_0^a \left(\frac{\partial X}{\partial x} \right) \left(\frac{\partial^2 X}{\partial x^2} \right) dx, & S_{6x} &= \int_0^a X \left(\frac{\partial X}{\partial x} \right) dx \end{aligned}$$

The variational method and integration by parts of equation (5) yield a fourth-order ordinary differential equation as in equation (6) and the boundary conditions along $y = 0$ and $y = b$ as shown in equations (7) and (8) respectively.

$$S_{3x} D_{22} \frac{d^4 Y}{dy^4} + (2 S_{2x} D_{12} - 4 S_{4x} D_{66}) \frac{d^2 Y}{dy^2} + (S_{1x} D_{11} - S_{3x} m \omega^2) Y = 0 \tag{6}$$

$$V_y = S_{3x} D_{22} \frac{d^3 Y}{dy^3} + (S_{2x} D_{12} - 4 S_{4x} D_{66}) \frac{dY}{dy} - 2 S_{5x} D_{16} Y \tag{7}$$

$$M_y = S_{3x} D_{22} \frac{d^2 Y}{dy^2} + 2 S_{6x} D_{26} \frac{dY}{dy} + S_{2x} D_{12} Y \tag{8}$$

Similarly, when $Y(y)$ is defined a priori, a fourth-order ordinary differential equation can be written as equation (9) and the boundary conditions along $x = 0$ and $x = a$ as equations (10) and (11) respectively.

$$S_{3y} D_{11} \frac{d^4 X}{dx^4} + (2 S_{2y} D_{12} - 4 S_{4y} D_{66}) \frac{d^2 X}{dx^2} + (S_{1y} D_{22} - S_{3y} m \omega^2) X = 0 \tag{9}$$

$$V_x = S_{3y} D_{11} \frac{d^3 X}{dx^3} + (S_{2y} D_{12} - 4 S_{4y} D_{66}) \frac{dX}{dx} - 2 S_{5y} D_{26} X \tag{10}$$

$$M_x = S_{3y} D_{11} \frac{d^2 X}{dx^2} + 2 S_{6y} D_{16} \frac{dX}{dx} + S_{2y} D_{12} X \tag{11}$$

where

$$\begin{aligned} S_{1y} &= \int_0^b \left(\frac{\partial^2 Y}{\partial y^2} \right)^2 dy, & S_{2y} &= \int_0^b \left(Y \frac{\partial^2 Y}{\partial y^2} \right) dy \\ S_{3y} &= \int_0^b Y^2 dy, & S_{4y} &= \int_0^b \left(\frac{\partial Y}{\partial y} \right)^2 dy \end{aligned}$$

$$S_{5y} = \int_0^b \left(\frac{\partial Y}{\partial y} \right) \left(\frac{\partial^2 Y}{\partial y^2} \right) dy, \quad S_{6y} = \int_0^b Y \left(\frac{\partial Y}{\partial y} \right) dy$$

Solution of the Iterative Differential Equations

The fourth-order ordinary differential equation (6) can be rewritten in a simple form as

$$\frac{d^4 Y}{dy^4} + \left(\frac{2S_{2x}D_{12} - 4S_{4x}D_{66}}{S_{3x}D_{22}} \right) \frac{d^2 Y}{dy^2} + \left(\frac{S_{1x}D_{11} - S_{3x}m\omega^2}{S_{3x}D_{22}} \right) Y = 0$$

where the form of the general solution is composed of the following four forms:

$$\begin{aligned} Y(y) &= C_{1y} \sin(q_1 y) + C_{2y} \cos(q_1 y) + C_{3y} \sin(q_2 y) + C_{4y} \cos(q_2 y) \\ Y(y) &= C_{1y} \sin(q_1 y) + C_{2y} \cos(q_1 y) + C_{3y} \sinh(q_2 y) + C_{4y} \cosh(q_2 y) \\ Y(y) &= [C_{1y} \sin(q_2 y) + C_{2y} \cos(q_2 y)] \cosh(q_1 y) + [C_{3y} \sin(q_2 y) + C_{4y} \cos(q_2 y)] \sinh(q_1 y) \\ Y(y) &= C_{1y} \sinh(q_1 y) + C_{2y} \cosh(q_1 y) + C_{3y} \sinh(q_2 y) + C_{4y} \cosh(q_2 y) \end{aligned}$$

In this study, considering a case $S_{1x}D_{11} < S_{3x}m\omega^2$, the solution can be written as follows.

$$Y(y) = C_{1y} \sin(q_1 y) + C_{2y} \cos(q_1 y) + C_{3y} \sinh(q_2 y) + C_{4y} \cosh(q_2 y) \tag{12}$$

where q_1 and q_2 are modal parameters in y coordinate direction, and

$$q_1^2 - q_2^2 = \frac{2S_{2x}D_{12} - 4S_{4x}D_{66}}{S_{3x}D_{22}} \tag{13}$$

$$q_1^2 q_2^2 = \frac{S_{3x}m\omega^2 - S_{1x}D_{11}}{S_{3x}D_{22}} \tag{14}$$

Similarly, the fourth-order ordinary differential equation (9) can be rewritten in a simple form as

$$\frac{d^4 X}{dx^4} + \left(\frac{2S_{2y}D_{12} - 4S_{4y}D_{66}}{S_{3y}D_{11}} \right) \frac{d^2 X}{dx^2} + \left(\frac{S_{1y}D_{22} - S_{3y}m\omega^2}{S_{3y}D_{11}} \right) X = 0$$

where the form of the general solution is composed of the following four forms:

$$\begin{aligned} X(x) &= C_{1x} \sin(p_1 x) + C_{2x} \cos(p_1 x) + C_{3x} \sin(p_2 x) + C_{4x} \cos(p_2 x) \\ X(x) &= C_{1x} \sin(p_1 x) + C_{2x} \cos(p_1 x) + C_{3x} \sinh(p_2 x) + C_{4x} \cosh(p_2 x) \\ X(x) &= [C_{1x} \sin(p_2 x) + C_{2x} \cos(p_2 x)] \cosh(p_1 x) + [C_{3x} \sinh(p_2 x) + C_{4x} \cosh(p_2 x)] \sinh(p_1 x) \\ X(x) &= C_{1x} \sinh(p_1 x) + C_{2x} \cosh(p_1 x) + C_{3x} \sinh(p_2 x) + C_{4x} \cosh(p_2 x) \end{aligned}$$

In this study, considering a case $S_{1y}D_{22} < S_{3y}m\omega^2$, the solution can be written as follows.

$$X(x) = C_{1x} \sin(p_1 x) + C_{2x} \cos(p_1 x) + C_{3x} \sinh(p_2 x) + C_{4x} \cosh(p_2 x) \tag{15}$$

where p_1 and p_2 are modal parameters in the x coordinate direction, and

$$p_1^2 - p_2^2 = \frac{2S_{2y}D_{12} - 4S_{4y}D_{66}}{S_{3y}D_{11}} \tag{16}$$

$$p_1^2 p_2^2 = \frac{S_{3y}m\omega^2 - S_{1y}D_{22}}{S_{3y}D_{11}} \tag{17}$$

Iterative Calculation Procedure

The iterative calculation is used to evaluate the natural frequency and to develop a final solution to satisfy the boundary conditions by the following steps.

- (1) The iterative calculation begins by choosing an initial trial function in the x or y coordinate direction using the procedure shown in Figure 2 and choosing the $X_0(x)$ as an initial trial function. S_{1x} through S_{6x} are calculated from $X_0(x)$.
- (2) In the first iteration, substitute the solution equation (12) in the boundary conditions and use q_2 as a function of q_1 , or q_1 as a function of q_2 , from the relationship equation (13). Then find the eigenvalue q_1 or q_2 and the eigenvector $Y_1(y)$.
- (3) In the second iteration, substitute the solution equation (15) in the boundary conditions and use p_2 as a function of p_1 , or p_1 as a function of p_2 , from the relationship equation (16). S_{1y} through S_{6y} are calculated from the eigenvector $Y_1(y)$ obtained from equation (2). Then find the eigenvalue p_1 or p_2 and the eigenvector $X_1(x)$.
- (4) In the third iteration, substitute the solution equation (12) in the boundary conditions and use q_2 as a function of q_1 , or q_1 as a function of q_2 , from the relationship equation (13). S_{1x} through S_{6x} are calculated from $X_1(x)$. Then find the eigenvalue q_1 or q_2 and the eigenvector $Y_2(y)$.
- (5) Compare q_1 and q_2 from equations (4) and (2). If the difference satisfies the specified tolerance level, the last q_1 and q_2 can be taken as the final solution. Otherwise, continue the iterative calculation by repeating steps (2) to (4).
- (6) The natural frequency is calculated from equation (14) or (17).

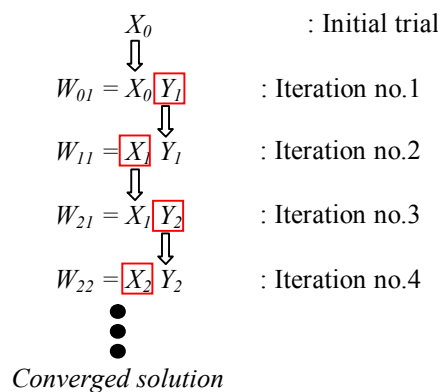


Figure 2. Iteration procedure

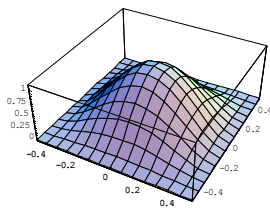
Numerical Verification and Accuracy

For numerical calculation, the present method is applied to a rectangular plate with various aspect ratios b/a , natural frequencies and boundary conditions. The method considers individual plate modes as the product of a separable function in the x, y coordinate directions. The notation for the plate mode (i, j) is a plate mode which is the product of the i^{th} mode for the x coordinate direction and the j^{th} mode for the y coordinate direction. The notation for boundary condition, for example CFCS, is as follows. The first and third letters mean the boundary condition along $x=0$ and $x=a$ respectively, and the second and

fourth letters mean the boundary condition along $y=0$ and $y=b$ respectively. The letters C, S and F mean the clamped, simply supported and free boundary conditions respectively.

The iteration example of the (1, 1) plate mode of an isotropic square plate with CCCC boundary condition is illustrated in Table 1. The (1, 1) plate mode is the product of the first mode of the x and y coordinate directions. The first iteration chooses the first mode of the free vibration of the clamped beam in the x coordinate direction, A , as an initial trial function. S_{1x} through S_{6x} are calculated for the substitution of q_2 as a function of q_1 . The first eigenvalues q_1 and q_2 and the eigenvector in the y coordinate direction are 4.304, 6.567 and B respectively. In the second iteration, the eigenvector in the y coordinate direction from the first iteration is used to determine S_{1y} through S_{6y} for the substitution of p_2 as a function of p_1 . The first eigenvalues p_1 and p_2 and the eigenvector in the x coordinate direction are 4.312, 6.525 and C respectively. The iterative calculation is repeated until the difference of the modal parameter in the x or y coordinate direction satisfies the specified tolerance. The fourth iteration is the end iteration due to the modal parameter in the x coordinate direction of the second and fourth iteration being identified, where $p_1 = 4.312$ and $p_2 = 6.525$. The plate mode shape is the product of the eigenvector in the x and y coordinate directions, $w(x, y) = C D$, as shown in the last column.

Table 1. (1, 1) Plate mode of an isotropic square plate with CCCC boundary condition

Iteration No.	Assumed solution $X(x)$ or $Y(y)$	Solution		
		Eigenvalue	Eigenvector $X(x)$ or $Y(y)$	Mode shape
1	A	$q_1 = 4.304$ $q_2 = 6.567$	B	
2	B	$p_1 = 4.312$ $p_2 = 6.525$	C	
3	C	$q_1 = 4.312$ $q_2 = 6.526$	D	
4	D	$p_1 = 4.312$ $p_2 = 6.525$	C	

Note: $A = \cos(4.730x) + 0.132\cosh(4.730x)$, $B = \cos(4.304y) + 0.041\cosh(6.567y)$
 $C = \cos(4.312x) + 0.042\cosh(6.525x)$, $D = \cos(4.312y) + 0.042\cosh(6.526y)$

For the plate mode shape, the contour representing the lateral deflection is zero and is called the nodal line. The nodal line is defined by the dash line. The nodal lines (i, j) of the (1, 1) through (3, 3) square plate mode with CCCC boundary conditions are illustrated in Figure 3. The nodal lines of the (i, j) plate mode are the i-1 and j-1 lines in the x and y coordinate directions respectively. For example, the nodal lines for the (3, 2) plate mode are 2 and 1 lines in the x and y coordinate directions respectively. The frequency parameter $\omega ab\sqrt{m/D}$ is evaluated by substituting q_1 and q_2 obtained from the third iteration into equation (14), or by substituting p_1 and p_2 obtained from the fourth iteration into equation (17), producing 35.998, as shown in Table 2.

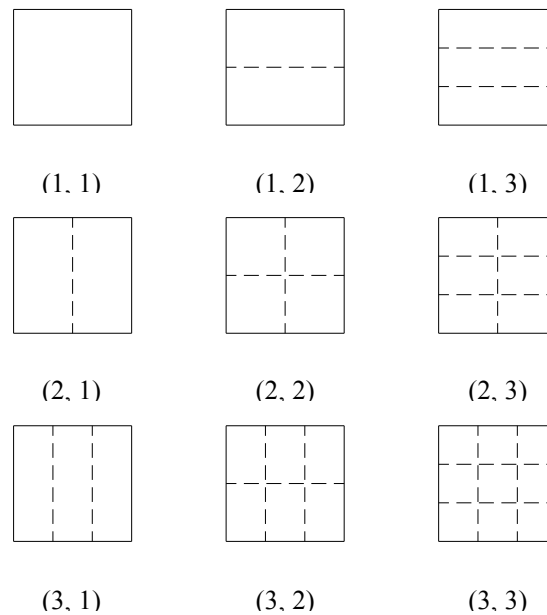


Figure 3. Nodal lines of the mode of square plate with CCCC boundary condition

Table 2. (1, 1) Frequency parameters $\omega ab\sqrt{m/D}$ of an isotropic square plate

Boundary condition	Method				
	Ref [2]	Ref [3]	Ref [4]	Ref [7]	Present
CCCC	35.999	35.999	35.998	35.998	35.998
SSSS	19.739				19.739

The (1, 1) frequency parameters of an isotropic square plate, an orthotropic rectangular plate and the $[0/90]_s$ laminated composite rectangular plate with SSSS boundary condition are evaluated to verify the accuracy of the present method as illustrated in Tables 2-4. In the case of the isotropic square plate, one can consider the bending stiffness of the composite plate as $D_{11} = D_{22} = (D_{12} + D_{66}) = D$, and in the case of the orthotropic rectangular plate, as $D_{11} = D_{22}, (D_{12} + D_{66}) = 0.5D_{11}$. The mechanical properties of the $[0/90]_s$ laminated composite rectangular plate are $G_{12} = 0.5E_2$ and $\nu_{12} = 0.25$.

The natural frequencies of the symmetrically laminated composite rectangular plate are evaluated by the present method and the FEM (ANSYS). In the present method, the natural frequency is obtained by dividing the natural circular frequency from equation (14) or equation (17) with 2π . In the FEM, a mesh size 64 x 64 of an 8-node, 3-D shell element with six degrees of freedom at each node is employed. The convergence of the mesh size of the (1, 1) natural frequencies of the $[0/90]_s$ laminated composite square plate is illustrated in Table 5. The natural frequencies of the unidirectional 0° and cross-ply symmetrically laminated composite rectangular plates are illustrated in Tables 6 and 7 respectively. The mechanical properties of the Kevlar 49 and the plate dimensions are $E_1 = 138$ GPa, $E_2 = 8.96$ GPa, $G_{12} = 7.1$ GPa, $G_{23} = 2.82$ GPa, $\nu_{12} = 0.3$, $\nu_{23} = 0.59$, mass per unit volume = 1600 kg/m³, $a = 1$ m, aspect ratio $b/a = 0.5, 1.0$ and 2.0 , and thickness = 2.5 mm.

Table 3. (1, 1) Frequency parameters $\omega ab \sqrt{m/D_{22}}$ of an orthotropic rectangular plate

Boundary condition	b = 0.5a		b = a		b = 2a	
	Ref [3]	Present	Ref [3]	Present	Ref [3]	Present
CCCC	95.391	95.391	33.917	33.917	23.848	23.848
CCCS	69.687	69.687	29.625	29.625	23.447	23.447
CCSS	67.497	67.497	24.610	24.610	16.874	16.874
CSCS	50.349	50.349	26.809	26.809	23.172	23.172
CSSS	47.325	47.325	21.163	21.163	16.497	16.497
SSSS	45.228	45.228	17.095	17.095	11.307	11.307

Table 4. (1, 1) Frequency parameters $(\omega ab / \pi^2) \sqrt{m/D_{22}}$ of the $[0/90]_s$ laminated composite rectangular plate with SSSS boundary condition

a/b	$E_1 = 10E_2$		$E_1 = 20E_2$		$E_1 = 40E_2$	
	Ref [8]	Present	Ref [8]	Present	Ref [8]	Present
0.5	8.515	8.515	9.355	9.355	9.917	9.917
1.0	2.519	2.519	2.638	2.638	2.721	2.721
1.5	1.531	1.531	1.536	1.536	1.539	1.539
2.0	1.246	1.246	1.229	1.229	1.216	1.216
2.5	1.138	1.138	1.119	1.119	1.105	1.105
3.0	1.087	1.087	1.071	1.071	1.059	1.059

Table 5. Convergence of mesh size of the (1, 1) natural frequencies of the $[0/90]_s$ laminated composite square plate

Boundary condition	Mesh size					
	2x2	4x4	8x8	16x16	32x32	64x64
CCCC	89.087	100.588	101.086	101.504	101.558	101.558
CCCS	86.286	95.144	96.431	96.872	96.927	96.927
CCSS	67.547	71.164	71.726	71.924	71.949	71.949
CFCC	78.816	87.636	89.978	90.526	90.605	90.605
CFCF	78.110	87.030	88.901	89.349	89.405	89.405
CFCS	78.664	87.383	89.556	90.062	90.132	90.132
CFSC	57.985	62.094	63.124	63.374	63.404	63.404
CFSF	57.651	60.838	61.570	61.748	61.771	61.771
CFSS	57.754	61.583	62.498	62.718	62.742	62.742
CSCS	83.499	91.839	93.552	94.004	94.059	94.059
CSSS	63.207	67.047	67.846	68.048	68.072	68.072
FSCS	24.904	25.671	25.971	26.047	26.063	26.063
FSFS	17.935	17.965	17.981	17.986	17.986	17.986
SSFS	19.866	20.534	20.702	20.744	20.752	20.752
SSSS	45.264	47.607	48.044	48.133	48.144	48.144

Table 6. Natural frequencies of the $[0]_4$ laminated composite rectangular plate

(1) Boundary condition CCCC

(i, j)	b = 0.5a		b = a		b = 2a	
	Present	FEM	Present	FEM	Present	FEM
(1, 1)	146.130	145.397	102.081	101.592	96.696	96.295
(1, 2)	302.299	299.966	127.192	126.600	100.315	99.831
(1, 3)	555.059	548.308	178.585	177.714	107.671	107.158
(2, 1)	298.399	295.269	269.499	266.664	265.060	262.274
(2, 2)	423.333	418.502	288.738	285.706	268.635	265.806
(2, 3)	653.828	644.244	327.230	323.824	275.099	272.198
(3, 1)	545.963	536.114	522.745	513.407	518.569	509.310
(3, 2)	647.953	636.133	540.051	530.388	522.185	512.838
(3, 3)	847.768	830.895	572.655	562.375	528.440	518.980

(2) Boundary condition CCCS

(i, j)	b = 0.5a		b = a		b = 2a	
	Present	FEM	Present	FEM	Present	FEM
(1, 1)	127.192	126.462	100.315	99.810	96.608	96.140
(1, 2)	256.654	254.955	120.275	119.661	99.656	99.166
(1, 3)	485.547	480.822	164.861	164.035	106.085	105.561
(2, 1)	288.738	285.501	268.635	265.783	264.972	262.184
(2, 2)	389.848	385.232	285.121	282.037	268.276	265.436
(2, 3)	593.597	585.588	318.92	315.462	274.271	271.335
(3, 1)	540.051	530.183	522.18	512.825	518.516	509.247
(3, 2)	624.615	612.754	537.713	527.981	521.918	512.579
(3, 3)	799.550	783.608	567.276	551.803	527.872	518.375

(3) Boundary condition CCSS

(i, j)	b = 0.5a		b = a		b = 2a	
	Present	FEM	Present	FEM	Present	FEM
(1, 1)	105.833	105.243	72.184	71.920	67.1591	66.965
(1, 2)	245.820	244.214	97.462	97.007	71.280	71.035
(1, 3)	479.172	474.492	148.400	107.666	79.732	79.414
(2, 1)	242.543	240.403	219.274	217.680	215.031	213.535
(2, 2)	354.715	350.935	238.289	236.371	218.841	217.268
(2, 3)	569.048	561.692	276.635	274.196	225.751	224.050
(3, 1)	471.233	464.645	451.405	445.473	447.343	441.525
(3, 2)	563.812	554.870	468.578	462.184	451.129	445.196
(3, 3)	750.246	736.857	501.090	493.857	457.681	451.580

Table 6. (continued)

(4) Boundary condition CFCC

(i, j)	b = 0.5a		b = a		b = 2a	
	Present	FEM	Present	FEM	Present	FEM
(1, 1)	100.644	100.090	96.647	96.161	95.930	95.458
(1, 2)	156.852	155.620	105.935	105.342	97.687	97.197
(1, 3)	311.322	308.453	132.549	131.718	101.911	101.381
(2, 1)	268.865	265.950	264.940	262.115	264.137	261.333
(2, 2)	317.926	313.990	274.476	271.486	266.241	263.402
(2, 3)	447.216	440.793	297.021	293.648	270.708	267.792
(3, 1)	522.206	512.763	518.409	509.081	517.594	508.283
(3, 2)	567.928	557.136	528.024	518.431	519.820	510.460
(3, 3)	680.763	666.671	549.166	539.005	524.408	514.915

(5) Boundary condition CFCF

(i, j)	b = 0.5a		b = a		b = 2a	
	Present	FEM	Present	FEM	Present	FEM
(1, 1)	95.749	95.211	95.743	95.242	95.744	95.261
(1, 2)	106.432	105.693	98.460	97.930	96.407	95.921
(1, 3)	167.132	165.526	109.758	109.042	98.757	98.237
(2, 1)	263.922	260.964	263.921	261.044	263.921	261.085
(2, 2)	278.501	275.256	267.520	264.605	264.787	261.945
(2, 3)	336.718	331.867	280.142	276.937	267.729	264.826
(3, 1)	517.401	507.858	517.385	507.975	517.388	508.023
(3, 2)	533.275	523.320	521.267	511.767	518.302	508.900
(3, 3)	591.097	579.101	534.415	524.491	521.484	511.979

(6) Boundary condition CFCS

(i, j)	b = 0.5a		b = a		b = 2a	
	Present	FEM	Present	FEM	Present	FEM
(1, 1)	98.460	97.919	96.407	95.922	95.902	95.432
(1, 2)	137.590	136.492	103.550	102.962	97.419	96.929
(1, 3)	266.094	263.893	125.300	124.488	101.101	100.568
(2, 1)	267.520	264.602	264.787	261.963	264.119	261.316
(2, 2)	305.380	301.505	272.993	269.991	266.067	263.228
(2, 3)	412.832	406.862	292.648	289.260	270.211	267.288
(3, 1)	521.267	511.810	518.295	508.974	517.591	508.272
(3, 2)	558.869	548.060	526.952	517.356	519.709	510.334
(3, 3)	654.862	641.040	546.097	535.900	524.052	514.554

Table 6. (continued)

(7) Boundary condition CFSC

(i, j)	b = 0.5a		b = a		b = 2a	
	Present	FEM	Present	FEM	Present	FEM
(1, 1)	72.610	72.293	67.215	66.999	66.234	66.049
(1, 2)	139.205	138.057	79.481	79.082	68.618	68.396
(1, 3)	301.769	299.031	111.804	111.093	74.255	73.955
(2, 1)	219.557	217.910	214.998	213.462	214.068	212.567
(2, 2)	275.258	272.268	225.998	224.230	216.493	214.941
(2, 3)	415.360	409.687	251.767	249.520	221.648	219.985
(3, 1)	451.463	445.440	447.247	441.358	446.343	440.490
(3, 2)	501.785	494.174	457.858	451.664	448.810	442.883
(3, 3)	623.742	612.383	481.156	474.313	453.865	447.795

(8) Boundary condition CFSS

(i, j)	b = 0.5a		b = a		b = 2a	
	Present	FEM	Present	FEM	Present	FEM
(1, 1)	65.980	65.727	65.980	65.760	65.980	65.781
(1, 2)	79.834	79.245	69.625	69.352	66.880	66.676
(1, 3)	149.981	148.437	84.179	83.628	70.035	69.771
(2, 1)	213.819	212.153	213.818	212.238	213.819	212.281
(2, 2)	230.45	228.388	217.953	216.323	214.815	213.277
(2, 3)	295.472	291.526	232.396	230.388	218.197	216.576
(3, 1)	446.125	440.018	446.113	440.148	446.116	440.202
(3, 2)	463.589	457.000	450.394	444.340	447.121	441.187
(3, 3)	526.653	517.535	464.876	458.312	448.080	444.572

(9) Boundary condition CFSS

(i, j)	b = 0.5a		b = a		b = 2a	
	Present	FEM	Present	FEM	Present	FEM
(1, 1)	69.625	69.330	66.880	66.666	66.197	66.012
(1, 2)	117.344	116.325	76.345	75.957	68.248	68.025
(1, 3)	255.010	252.805	103.208	102.520	73.162	72.862
(2, 1)	217.523	216.307	214.815	213.281	214.048	212.546
(2, 2)	260.969	258.200	224.245	222.470	216.287	214.734
(2, 3)	378.438	373.259	246.702	244.436	221.051	219.388
(3, 1)	450.394	444.360	447.124	441.237	446.324	440.477
(3, 2)	491.695	484.121	456.672	450.458	448.665	442.740
(3, 3)	595.709	585.020	477.710	470.837	453.468	447.385

Table 6. (continued)

(10) Boundary condition CSCS

(i, j)	b = 0.5a		b = a		b = 2a	
	Present	FEM	Present	FEM	Present	FEM
(1, 1)	114.779	114.051	99.113	98.604	96.485	96.017
(1, 2)	217.513	216.163	114.779	114.149	99.113	98.619
(1, 3)	421.958	418.724	152.854	152.046	104.728	104.194
(2, 1)	282.135	278.869	267.948	265.087	264.225	262.104
(2, 2)	362.621	358.081	282.135	279.016	267.948	265.106
(2, 3)	540.018	533.026	311.768	308.252	273.490	270.560
(3, 1)	535.686	525.759	521.686	512.332	518.448	509.188
(3, 2)	605.709	593.804	535.686	525.915	521.686	512.341
(3, 3)	757.555	742.228	562.335	551.913	527.322	517.827

(11) Boundary condition CSSS

(i, j)	b = 0.5a		b = a		b = 2a	
	Present	FEM	Present	FEM	Present	FEM
(1, 1)	90.654	90.069	70.534	70.266	66.987	66.793
(1, 2)	204.740	203.455	90.655	90.183	70.534	70.285
(1, 3)	414.685	411.499	135.004	134.292	77.942	77.616
(2, 1)	234.777	232.659	218.455	216.855	214.937	213.436
(2, 2)	324.789	321.127	234.777	232.823	218.455	216.876
(2, 3)	513.130	506.817	268.453	265.971	224.838	223.134
(3, 1)	466.287	459.682	450.866	444.915	447.276	441.459
(3, 2)	542.997	534.098	466.287	459.859	450.866	444.928
(3, 3)	705.590	692.887	495.624	488.405	457.077	450.964

(12) Boundary condition FSCS

(i, j)	b = 0.5a		b = a		b = 2a	
	Present	FEM	Present	FEM	Present	FEM
(1, 1)	51.696	51.479	22.408	22.321	16.573	16.543
(1, 2)	178.770	178.132	51.696	51.545	22.408	22.341
(1, 3)	393.258	390.834	104.156	103.887	34.054	33.960
(2, 1)	125.740	124.626	101.457	100.940	96.027	95.612
(2, 2)	240.372	238.154	125.740	124.833	101.457	100.935
(2, 3)	447.414	443.104	171.454	170.131	111.146	110.474
(3, 1)	290.303	287.215	270.198	267.831	265.542	263.160
(3, 2)	386.963	381.572	290.304	287.360	270.198	267.682
(3, 3)	575.454	566.813	328.028	324.248	278.302	275.571

Table 6. (continued)

(13) Boundary condition FSFS

(i, j)	b = 0.5a		b = a		b = 2a	
	Present	FEM	Present	FEM	Present	FEM
(1, 1)	42.969	42.940	10.729	10.733	2.682	2.683
(1, 2)	172.013	171.569	42.969	42.940	10.735	10.733
(1, 3)	387.159	384.950	96.727	96.586	24.162	24.153
(2, 1)	60.005	59.462	23.613	23.393	10.865	10.775
(2, 2)	190.950	189.852	60.005	59.635	23.613	23.446
(2, 3)	406.362	403.381	115.158	114.61	39.690	39.459
(3, 1)	136.407	135.033	105.802	105.32	98.249	97.913
(3, 2)	261.636	258.604	136.407	135.311	105.802	105.292
(3, 3)	473.670	468.161	188.229	186.475	118.489	117.734

(14) Boundary condition SSFS

(i, j)	b = 0.5a		b = a		b = 2a	
	Present	FEM	Present	FEM	Present	FEM
(1, 1)	47.737	47.552	15.001	14.916	5.903	5.864
(1, 2)	176.906	176.283	47.737	47.604	15.001	14.938
(1, 3)	392.079	389.664	101.590	101.328	28.789	28.707
(2, 1)	102.365	101.423	74.511	74.203	68.061	67.895
(2, 2)	224.713	222.705	102.365	101.649	74.511	74.221
(2, 3)	436.568	432.438	152.234	151.105	85.799	85.342
(3, 1)	243.464	241.356	220.832	219.563	215.544	214.333
(3, 2)	348.803	344.303	243.464	241.546	220.832	219.466
(3, 3)	546.216	538.45	285.155	282.340	229.993	228.382

(15) Boundary condition SSSS

(i, j)	b = 0.5a		b = a		b = 2a	
	Present	FEM	Present	FEM	Present	FEM
(1, 1)	73.313	72.782	48.313	48.143	43.585	43.516
(1, 2)	195.924	194.707	73.313	72.905	48.313	48.166
(1, 3)	409.306	406.184	122.783	122.131	57.859	57.613
(2, 1)	193.253	191.815	174.343	173.533	170.246	169.562
(2, 2)	293.255	290.111	193.253	192.000	174.343	173.558
(2, 3)	491.133	485.278	231.440	229.562	181.765	180.816
(3, 1)	402.477	398.250	385.382	381.925	381.416	378.103
(3, 2)	486.526	479.726	402.477	398.449	385.382	381.941
(3, 3)	659.824	648.987	434.818	429.885	392.272	388.619

Table 7. Natural frequencies of the $[0/90]_s$ laminated composite rectangular plate

(1) Boundary condition CCCC

(i, j)	b = 0.5a		b = a		b = 2a	
	Present	FEM	Present	FEM	Present	FEM
(1, 1)	193.481	192.319	102.125	101.558	91.450	90.899
(1, 2)	469.651	464.362	152.510	151.765	97.518	96.953
(1, 3)	898.655	881.793	249.217	247.785	111.734	111.147
(2, 1)	313.322	309.597	256.188	252.850	249.409	246.115
(2, 2)	549.079	541.605	288.967	285.445	254.144	250.807
(2, 3)	959.142	940.036	361.009	356.951	263.753	260.352
(3, 1)	533.285	521.866	493.182	482.191	487.584	476.672
(3, 2)	720.807	706.154	518.596	507.273	491.953	480.954
(3, 3)	1090.160	1064.000	573.029	561.292	500.115	488.978

(2) Boundary condition CCCS

(i, j)	b = 0.5a		b = a		b = 2a	
	Present	FEM	Present	FEM	Present	FEM
(1, 1)	152.510	151.625	97.518	96.927	91.089	90.534
(1, 2)	387.666	384.487	136.904	136.197	95.912	95.336
(1, 3)	778.985	768.074	222.186	221.039	107.889	107.290
(2, 1)	288.967	285.182	254.144	250.773	249.227	245.930
(2, 2)	478.949	473.995	280.300	276.711	253.354	250.015
(2, 3)	846.367	832.686	341.883	337.882	261.669	258.423
(3, 1)	518.596	506.985	491.953	480.927	487.462	476.548
(3, 2)	666.875	652.987	513.249	501.830	491.447	480.437
(3, 3)	990.124	968.900	560.252	548.256	498.895	487.745

(3) Boundary condition CCSS

(i, j)	b = 0.5a		b = a		b = 2a	
	Present	FEM	Present	FEM	Present	FEM
(1, 1)	137.269	136.574	72.242	71.949	63.536	63.310
(1, 2)	381.317	378.238	119.737	119.247	70.075	69.806
(1, 3)	775.394	764.560	211.588	210.591	85.471	85.143
(2, 1)	248.488	246.061	208.084	206.211	202.334	200.563
(2, 2)	453.917	449.041	238.428	236.248	207.152	205.306
(2, 3)	831.045	818.053	307.398	304.631	217.091	215.086
(3, 1)	455.339	447.527	425.601	418.623	419.229	413.743
(3, 2)	616.821	606.346	449.298	441.847	425.031	418.053
(3, 3)	954.976	936.472	501.235	493.040	433.317	426.167

Table 7. (continued)

(4) Boundary condition CFCC

(i, j)	b = 0.5a		b = a		b = 2a	
	Present	FEM	Present	FEM	Present	FEM
(1, 1)	97.635	96.982	91.175	90.605	90.202	89.648
(1, 2)	200.611	199.067	106.120	105.409	92.514	91.935
(1, 3)	475.593	470.517	157.102	156.112	99.276	98.646
(2, 1)	254.611	251.173	249.265	245.944	248.278	244.981
(2, 2)	332.550	327.751	261.871	258.325	250.730	247.387
(2, 3)	568.059	559.489	297.811	293.799	256.467	253.030
(3, 1)	492.296	481.197	487.439	476.489	486.647	475.549
(3, 2)	557.483	544.619	499.170	487.891	488.975	477.976
(3, 3)	751.789	734.541	528.782	561.800	494.415	483.262

(5) Boundary condition CFCF

(i, j)	b = 0.5a		b = a		b = 2a	
	Present	FEM	Present	FEM	Present	FEM
(1, 1)	89.949	89.392	89.974	89.405	89.975	89.416
(1, 2)	101.379	100.501	92.923	92.303	90.699	90.131
(1, 3)	209.883	208.139	109.979	109.134	93.633	93.017
(2, 1)	248.018	244.635	248.018	244.678	248.019	244.703
(2, 2)	263.801	259.951	251.944	248.524	248.972	245.642
(2, 3)	350.810	345.196	267.746	263.932	252.300	248.888
(3, 1)	486.070	475.161	486.216	475.229	486.223	475.262
(3, 2)	503.507	491.831	490.453	479.334	487.231	476.245
(3, 3)	580.894	566.391	505.892	494.201	490.712	479.597

(6) Boundary condition CFCS

(i, j)	b = 0.5a		b = a		b = 2a	
	Present	FEM	Present	FEM	Present	FEM
(1, 1)	92.923	92.288	90.699	90.132	90.150	89.597
(1, 2)	161.439	160.225	100.989	100.292	91.979	91.400
(1, 3)	393.984	390.870	141.452	140.530	97.796	96.866
(2, 1)	251.944	248.513	248.972	245.651	248.245	244.948
(2, 2)	306.302	301.720	258.907	255.360	250.402	247.057
(2, 3)	498.276	491.216	288.384	284.383	255.468	252.031
(3, 1)	490.453	479.348	487.231	476.283	486.449	475.526
(3, 2)	539.019	526.260	497.116	485.824	488.739	477.741
(3, 3)	696.579	680.394	522.430	510.418	493.734	482.570

Table 7. (continued)

(7) Boundary condition CFSC

(i, j)	b = 0.5a		b = a		b = 2a	
	Present	FEM	Present	FEM	Present	FEM
(1, 1)	72.342	71.979	63.653	63.404	62.316	62.100
(1, 2)	188.598	187.222	83.137	82.688	65.468	65.211
(1, 3)	470.997	465.073	142.015	141.225	74.453	74.117
(2, 1)	208.623	206.702	202.383	200.583	201.235	199.472
(2, 2)	296.625	293.078	217.008	214.935	204.075	202.255
(2, 3)	545.876	538.326	258.099	255.479	210.707	208.803
(3, 1)	425.999	418.926	420.594	413.685	419.189	412.651
(3, 2)	497.904	488.802	433.606	426.333	422.293	415.336
(3, 3)	706.154	692.229	466.400	458.186	428.323	421.164

(8) Boundary condition CFSS

(i, j)	b = 0.5a		b = a		b = 2a	
	Present	FEM	Present	FEM	Present	FEM
(1, 1)	62.005	61.757	62.005	61.771	62.005	61.782
(1, 2)	76.702	76.058	65.950	65.645	62.986	62.753
(1, 3)	197.907	196.358	87.702	87.110	66.936	66.636
(2, 1)	200.839	199.086	200.934	199.125	200.935	199.152
(2, 2)	218.906	216.506	205.443	203.547	202.032	200.237
(2, 3)	315.813	311.367	223.598	221.231	205.869	203.979
(3, 1)	419.234	412.221	419.228	412.298	419.241	412.332
(3, 2)	438.236	430.514	423.906	416.841	420.354	413.430
(3, 3)	522.780	512.084	440.948	433.274	421.378	417.137

(9) Boundary condition CFSS

(i, j)	b = 0.5a		b = a		b = 2a	
	Present	FEM	Present	FEM	Present	FEM
(1, 1)	65.950	65.618	62.986	62.742	62.243	62.028
(1, 2)	146.474	145.460	76.576	76.148	64.727	64.472
(1, 3)	387.312	384.362	124.569	123.863	72.096	71.762
(2, 1)	205.443	203.523	202.032	200.234	201.195	199.429
(2, 2)	267.255	263.985	213.507	211.425	203.683	201.862
(2, 3)	473.111	466.783	247.305	244.696	209.555	207.618
(3, 1)	423.906	416.837	420.357	413.452	419.208	412.625
(3, 2)	477.432	468.889	431.274	424.002	422.027	415.070
(3, 3)	647.417	634.742	459.289	451.260	427.532	420.418

Table 7. (continued)

(10) Boundary condition CSCS

(i, j)	b = 0.5a		b = a		b = 2a	
	Present	FEM	Present	FEM	Present	FEM
(1, 1)	124.247	123.437	94.660	94.059	90.835	90.279
(1, 2)	315.594	313.694	124.247	123.545	94.660	94.077
(1, 3)	668.684	662.073	197.927	196.964	104.649	104.037
(2, 1)	273.482	269.661	252.712	249.328	249.079	245.779
(2, 2)	420.358	415.174	273.482	269.842	252.712	249.352
(2, 3)	744.034	734.132	325.479	321.481	260.211	256.764
(3, 1)	508.925	497.250	491.006	479.964	487.354	476.440
(3, 2)	623.666	610.057	508.925	497.450	491.006	479.984
(3, 3)	901.507	883.204	549.377	537.294	497.837	486.660

(11) Boundary condition CSSS

(i, j)	b = 0.5a		b = a		b = 2a	
	Present	FEM	Present	FEM	Present	FEM
(1, 1)	105.089	104.501	68.370	68.072	63.178	62.952
(1, 2)	307.847	306.072	105.089	104.619	68.370	68.095
(1, 3)	664.551	658.038	186.008	185.207	81.370	81.033
(2, 1)	230.460	228.042	206.365	204.488	202.156	200.383
(2, 2)	391.801	387.709	230.460	228.243	206.366	204.515
(2, 3)	726.720	717.624	289.151	286.432	215.090	213.121
(3, 1)	444.409	436.686	424.522	417.518	420.486	413.621
(3, 2)	570.055	560.030	444.409	436.909	424.520	417.540
(3, 3)	863.000	847.658	489.148	480.905	432.105	424.936

(12) Boundary condition FSCS

(i, j)	b = 0.5a		b = a		b = 2a	
	Present	FEM	Present	FEM	Present	FEM
(1, 1)	77.306	77.092	26.144	26.063	16.162	16.131
(1, 2)	292.035	290.730	77.306	77.142	26.144	26.083
(1, 3)	651.767	645.784	166.421	165.958	46.757	46.667
(2, 1)	134.512	133.347	97.272	96.700	90.527	90.061
(2, 2)	331.637	329.028	134.512	133.577	97.272	96.705
(2, 3)	684.864	677.398	212.575	211.179	111.199	110.494
(3, 1)	281.887	278.383	255.083	252.356	249.755	247.033
(3, 2)	441.442	435.532	281.886	278.585	255.083	252.227
(3, 3)	769.934	758.631	341.051	336.930	265.252	262.185

Table 7. (continued)

(13) Boundary condition FSFS

(i, j)	b = 0.5a		b = a		b = 2a	
	Present	FEM	Present	FEM	Present	FEM
(1, 1)	72.036	71.911	18.009	17.986	4.502	4.497
(1, 2)	288.147	286.870	72.036	71.911	18.009	17.986
(1, 3)	648.331	642.336	162.082	161.629	40.521	40.462
(2, 1)	83.270	82.790	27.674	27.480	11.448	11.368
(2, 2)	299.700	298.050	83.270	82.934	27.674	27.533
(2, 3)	659.780	653.365	173.610	172.935	51.282	51.084
(3, 1)	144.436	143.043	101.638	101.141	92.706	92.361
(3, 2)	347.366	344.075	144.436	143.358	101.638	101.129
(3, 3)	702.318	693.893	226.291	224.535	118.408	117.669

(14) Boundary condition SSFS

(i, j)	b = 0.5a		b = a		b = 2a	
	Present	FEM	Present	FEM	Present	FEM
(1, 1)	74.925	74.743	20.817	20.752	6.918	6.887
(1, 2)	290.979	289.694	74.925	74.781	20.817	20.770
(1, 3)	651.105	645.140	164.944	164.497	43.403	43.331
(2, 1)	115.310	114.393	72.463	72.145	64.315	64.140
(2, 2)	321.400	319.050	115.310	114.624	72.463	72.173
(2, 3)	678.360	671.119	198.802	197.654	88.909	88.472
(3, 1)	239.294	236.990	208.880	207.455	202.801	201.444
(3, 2)	411.835	407.033	239.294	237.237	208.880	207.376
(3, 3)	750.287	739.984	304.678	301.741	220.470	218.733

(15) Boundary condition SSSS

(i, j)	b = 0.5a		b = a		b = 2a	
	Present	FEM	Present	FEM	Present	FEM
(1, 1)	92.209	91.729	48.313	48.144	41.282	41.207
(1, 2)	302.581	300.897	92.209	91.846	48.313	48.172
(1, 3)	661.475	655.043	178.202	177.492	64.767	64.550
(2, 1)	193.252	191.688	165.130	164.200	160.189	159.386
(2, 2)	368.837	365.419	193.252	191.910	165.130	164.232
(2, 3)	712.813	704.268	259.070	257.126	175.379	174.334
(3, 1)	385.271	380.406	363.096	359.037	358.611	354.703
(3, 2)	522.682	515.204	385.271	380.653	363.096	359.062
(3, 3)	829.881	816.669	434.817	429.336	371.543	367.306

CONCLUSIONS

The extended Kantorovich method has been employed to analyse the free vibration of a symmetrically laminated composite rectangular plate with various boundary conditions. The frequency parameters of an isotropic square plate, an orthotropic rectangular plate and a cross-ply symmetrically laminated composite rectangular plate were evaluated in order to compare with previously published results on the topic. A good agreement with the results verifies the accuracy of the present method. The natural frequencies of symmetrically laminated composite rectangular plates were also evaluated by the present method and the finite element method. A good agreement with the finite element method verifies that the present method can be used to evaluate the natural frequencies of unidirectional 0° , unidirectional 90° and cross-ply symmetrically laminated composite rectangular plates.

The advantages of the present method are as follows.

- (1) The rectangular plate vibration problem can be resolved by the use of ordinary differential equations.
- (2) Any arbitrary function can be used as an initial trial function in the iterative calculation. An initial trial function which satisfies the boundary conditions will make the convergence of the final solution rapid.
- (3) The final solution converges rapidly; therefore, the final solution can be obtained from the fourth iteration.
- (4) The particular natural frequency can be obtained separately with good accuracy. In the Rayleigh-Ritz method, a larger number of shape functions must be used if a higher natural frequency is required.

However, due to the fact that the present method considers individual modes as a product of separable functions in the x and y coordinate directions, it cannot provide for modes with curved nodal lines.

ACKNOWLEDGEMENT

The Graduate School of Chiang Mai University is acknowledged for the support of the work presented in this paper.

REFERENCES

1. M. Dalaei and A. D. Kerr, "Analysis of clamped rectangular orthotropic plates subjected to a uniform lateral load", *Int. J. Mech. Sci.*, **1995**, 37, 527-535.
2. M. Dalaei and A. D. Kerr, "Natural vibration analysis of clamped rectangular orthotropic plates", *J. Sound Vibr.*, **1996**, 189, 399-406.
3. T. Sakata, K. Takahashi and R. B. Bhat, "Natural frequencies of orthotropic rectangular plates obtained by iterative reduction of the partial differential equation", *J. Sound Vibr.*, **1996**, 189, 89-101.
4. C. Rajalingham, R. B. Bhat and G. D. Xistris, "Vibration of rectangular plates using plate characteristic functions as shape functions in the Rayleigh-Ritz method", *J. Sound Vibr.*, **1996**, 193, 497-509.

5. A. N. Bercin, "Free vibration solution for clamped orthotropic plates using the Kantorovich method", *J. Sound Vibr.*, **1996**, 196, 243-247.
6. J. M. Lee, J. H. Chung and T. Y. Chung, "Free vibration analysis of symmetrically laminated composite rectangular plates", *J. Sound Vibr.*, **1997**, 199, 71-85.
7. C. Rajalingham, R. B. Bhat and G. D. Xistris, "Vibration of rectangular plates by reduction of the plate partial differential equation into simultaneous ordinary differential equations", *J. Sound Vibr.*, **1997**, 203, 169-180.
8. J. N. Reddy, "Mechanics of Laminated Composite Plates and Shells: Theory and Analysis", 2nd Edn., CRC Press, Boca Raton, **2004**.
9. V. Ungbhakorn and P. Singhatanadgid, "Buckling analysis of symmetrically laminated composite plates by the extended Kantorovich method", *Compos. Struct.*, **2006**, 73, 120-128.

Communication

Variation in physical characters and evaluation of genetic diversity in *Acacia caesia* var. *caesia* (L.) Willd. in an environmental gradient in the Western Ghats of Tamil Nadu, India

Palanisamy Sathishkumar, Subramanian Paulsamy* and Anaimalai M. Anandakumar

Post Graduate and Research Department of Botany, Kongunadu Arts and Science College, Coimbatore
- 641 029, India

* Corresponding author, e-mail: paulsami@yahoo.com

Received: 17 April 2010 / Accepted: 1 December 2010 / Published: 17 December 2010

Abstract: A random amplified polymorphic DNA (RAPD) analysis was made to determine the genetic variation between the five populations of the medicinal shrub, *Acacia caesia* var. *caesia* in an environmental gradient. Of the nine random primers tested, one primer, UBC-807 showing polymorphism was used in RAPD analysis. The primer produced 12 scorable DNA fragments in the populations studied, which showed the existence of genetic variation between populations. A dendrogram was constructed based on Jaccard's coefficient to determine the degree of genetic relationship among the five populations and analysed. It showed that the genetic similarity among the populations varied from 55 to 89 %. Further, the genetic polymorphism in the population in a very arid habitat at Chennimalai was higher (70%) than that of other populations, which indicates the plasticity of the genome in a water-stressed environment. Observation of morphological features shows that the population in a very arid habitat had decreased vegetative growth with increased reproductive attributes.

Keywords: *Acacia caesia* var. *caesia*, RAPD analysis, polymorphism, Jaccard's coefficient, morphological variation

INTRODUCTION

Acacia caesia var. *caesia* (L.) Willd. (Leguminosae, Mimosoideae) is a medicinal plant locally used in Coimbatore district of Tamil Nadu, India. The leaves are used for the treatment of bronchitis (asthma), colds and skin problems. It is an armed woody straggling shrub, mainly distributed in tropical regions of India, Sri Lanka and Thailand.

In India it is abundant in the foothills of the Western Ghats [1] in different environmental conditions with distinct morphological variation. The effectiveness of medicinal properties of certain populations of this species inhabiting dry environments is better than that from other habitats [2-3]. In addition to environmental factor, genetic constitution is also known to contribute to this difference in properties in many species [4-6]. To determine the best population for medicinal properties as well as the level of genetic polymorphism in this plant, random amplified polymorphic DNA (RAPD) analysis was undertaken by using UBC-807 RAPD markers.

MATERIALS AND METHODS

Materials

Five different populations of *A. caesia* var. *caesia* were selected in an environmental gradient situated in the Western Ghats of Western Tamil Nadu, viz. at Chennimalai (very arid; 450 m above msl; thorny-scrub jungle), Maruthamalai (arid; 540 m above msl; dry deciduous forest), Palamalai (semi-arid; 620 m above msl; moist deciduous forest), Thadagai Hills (humid; 680 m above msl; moist semi-evergreen forest) and Burliar (very humid; 760 m above msl; moist evergreen forest).

DNA Isolation and Primer Screening

Young tender leaves were collected from 50 individuals at each population and were washed with double distilled water and stored in sealed polythene bags at -70°C in a deep freezer until use. Genomic DNA was isolated from 100 mg of the leaf tissue by using GenElute plant genomic DNA purification kit (Sigma-Aldrich) and following the manufacturer's instructions.

Quality Check and Quantification of Genomic DNA

About 2 μl of the genomic DNA isolated from 100 mg of leaf tissue was subjected to electrophoresis on a 0.8% agarose gel containing 0.5 $\mu\text{g}/\text{ml}$ of ethidium bromide. After electrophoresis, the gel was viewed over a UV transilluminator (UVT-40M, Herolab) and the quality and quantity of the DNA were assessed by using undigested λ DNA as a control. The genomic DNA was diluted to 4ng/ μl and stored at 4°C as a working solution while the stock DNA (undiluted) was stored at -20°C in aliquots.

RAPD Polymerase Chain Reaction (PCR)

The RAPD polymerase chain reaction (PCR) was carried out in 20- μl reaction volume containing genomic DNA (28 ng), *Taq* DNA polymerase (1 unit), 0.5 μM primer 0.2 mM dNTPs, 10 mM Tris-HCl (pH 9.0), 1.5 mM MgCl_2 , 50 mM KCl and 0.01% gelatin. Amplification was carried out in a thermocycler (Eppendorf) with an initial strand separation at 94°C for 4 minutes, followed by 40 cycles of amplification and final extension for 1 minute at 37°C and 1.5 minutes at 72°C . After 40 cycles, there was a final extension step of 5 minutes at 72°C . A negative control without genomic DNA template was used for amplification along with genomic DNA from 5 habitats with primers. This was done to confirm the quality of primer dimers or possible contaminants. Amplification products were

resolved on 1.2% agarose gel in 1 X TBE buffer stained with ethidium bromide (0.5 µg/ml). The gels were photographed using a gel documentation system (Syngene).

Observation on Morphological Characters

To observe morphological variation for plant shoot length, root length, number of lateral roots, stem girth, number of branches, number of leaves, leaf thickness, leaf surface area, number of inflorescences and number of fruits, a hundred mature individuals in each population were randomly selected with three replications.

Molecular Characterisation

Each RAPD band was treated as a unit character and was scored manually as independent binary codes ('1' for presence and '0' for absence). Only distances and well-resolved bands were scored. The bands that had conflicting data between the two readings were eliminated from further analysis. The percentage of polymorphism was calculated as the proportion of polymorphic bands to the total number of bands. The 1/0 matrix was prepared and the data were used to generate genetic similarity (GS) based on Jaccard's coefficient of similarity: $GS(ij) = a/a+b+c$, where $GS(ij)$ is the measure of genetic similarity between individuals i and j , a is the number of polymorphic bands that are shared by i and j , b is the number of bands present in i and absent in j , and c is the number of bands present in j and absent in i . To examine the genetic relationship among populations, a dendrogram was generated from distance values using the unweighted pair-group method of arithmetic averages (UPGMA), using the multivariate statistic package (MVSP) software version 3.13n [7].

RESULTS AND DISCUSSION

DNA extracted from the five populations was examined for their PCR-RAPD patterns. Out of 9 primers screened, one was selected based on robustness of amplification, reproducibility and scorability of banding pattern and used for diversity analysis in all five populations. The UBC-807 AGAGAGAGAGAGAGAGT primer generated 12 amplification products and out of them 7 bands had 58.3% polymorphism (Figure 1). The number of polymorphic bands ranged from 4 to 7 across the populations analysed and a total number of 12 polymorphic bands were formed in the five populations. The percentage of polymorphism obtained in the populations varied. In Chennimalai there was 70% polymorphism followed by 62% in Maruthamalai, 60% in Burliar, 55% in Palamalai and 50% in Thadagai Hills (Tables 1-2).

The Jaccard's coefficient of genetic similarity matrix [8] prepared on the basis of RAPD data showed that it varied from 0.55 to 0.89 among the clusters—Maruthamalai to Burliar through Thadagai Hills, and Palamalai and Chennimalai (Figure 2). It showed that abiotic environmental factors influenced genetic differentiation within and between populations [4]. Also important to note is the chance of sharing a common gene pool between all populations studied except Chennimalai population which has a higher percentage of polymorphism. Populations at Chennimalai and Burliar, which are at two extremes in the environmental gradient, generally showed high degrees of polymorphism, which may be explained due to the different environments. The lower levels of polymorphism in the other populations

is due to the expansion within the range of variation. The genetic diversity evidence from the RAPD analysis clearly indicates the interaction between a major abiotic factor, i.e. climate, and other minor abiotic factors in shaping the genome to survive in other environments.

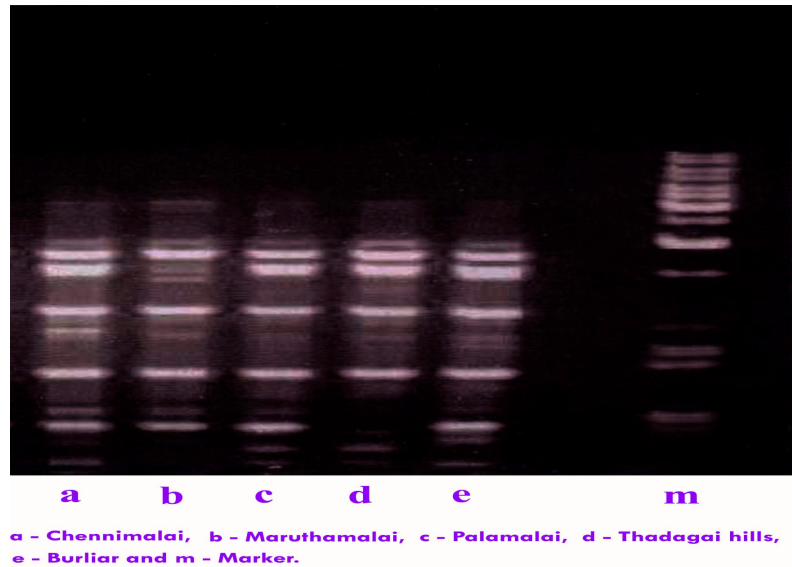


Figure 1. Amplification products obtained from DNA of the five different populations of *A. caesia* with UBC-807 AGAGAGAGAGAGAGT primer

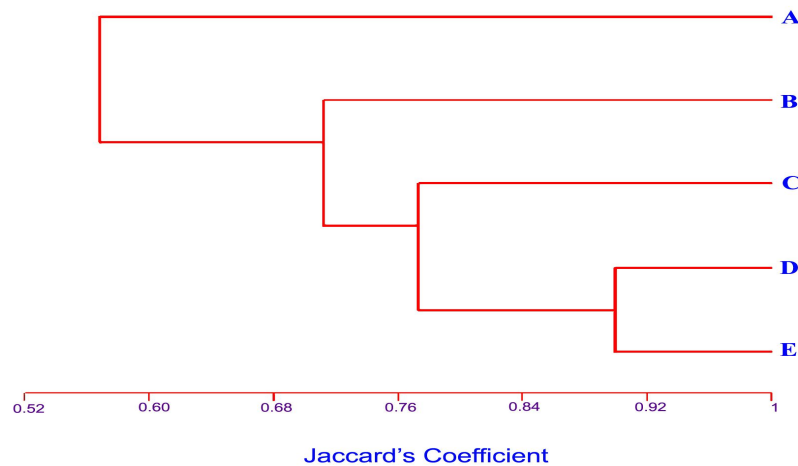
Table 1. Matrix coded for bands obtained in RAPD analysis in *Acacia caesia*

Population	Band											
	1	2	3	4	5	6	7	8	9	10	11	12
Chennimalai	1	1	1	0	1	1	1	1	1	1	0	1
Maruthamalai	1	1	1	0	1	1	0	1	0	0	1	1
Palamalai	1	1	1	0	1	0	0	1	1	1	1	1
Thadagai Hills	1	1	0	1	1	1	0	1	1	1	0	0
Burliar	1	1	1	0	1	1	0	1	1	1	1	1

Note: 1 - Presence of band; 0 - Absence of band

Table 2. Polymorphic and non-polymorphic bands for UBC-807 AGAGAGAGAGA GAGAGT primer in *A. caesia* populations

Population	Total no. of bands	Polymorphic bands	Percentage of polymorphism
Chennimalai	10	7	70
Maruthamalai	8	5	62
Palamalai	9	5	55
Thadagai hills	8	4	50
Burliar	10	6	60



A, B, C, D and E are the populations of *Acacia caesia* in Maruthamalai, Thadagai hills, Burliar, Palamalai and Chennimalai respectively.

Figure 2. Dendrogram for the five populations of *A. caesia* developed from RAPD data using unweighted pair-group method of arithmetic averages (UPGMA)

It is known that vegetative traits of this plant, e.g. shoot length, root length, number of lateral roots, stem girth, number of branches, number of leaves, leaf thickness and leaf surface area, generally increase with more humid conditions (Table 3). Reproductive attributes such as the number of inflorescences and number of fruits per plant are more in arid condition at Chennimalai and Maruthamalai. It indicates that the suppression of vegetative growth in arid places concomitantly enhanced the reproductive ability of the species. This feature was observed by Patricia et al. [9] for *Grevillea barklyana* and by Chandler and Bartels [10] for many wild plants.

Sathishkumar et al. [2] reported that the medicinal value was significantly higher in the population of *A. caesia* in the very arid habitat at Chennimalai. The high degree of polymorphism (70%), higher expression of reproductive characters and greater medicinal value at Chennimalai indicates the best area for cultivation of this species. Pharmacognostical studies are needed to confirm this observation.

Table 3. Morphological and reproductive features of *A. caesia* studied at the five sites

Character	Study area*				
	Chennimalai (very arid)	Maruthamalai (arid)	Palamalai (semi-arid)	Thadagai Hills (humid)	Burliar (very humid)
Shoot length (cm)	228.84 ^a ± 5.38	244.16 ^b ± 4.02	243.02 ^b ± 8.49	249.70 ^c ± 6.36	250.36 ^c ± 4.02
Root length (cm)	149.38 ^a ± 4.57	151.70 ^a ± 2.46	150.74 ^a ± 5.27	159.08 ^b ± 2.36	159.60 ^b ± 2.46
No. of lateral roots/ plant	78.90 ^a ± 1.83	80.70 ^a ± 2.94	82.18 ^b ± 2.85	85.78 ^c ± 2.94	86.50 ^c ± 2.94
Stem girth (cm) / plant	3.90 ^a ± 0.57	4.17 ^b ± 0.65	4.14 ^b ± 0.29	4.86 ^b ± 0.68	4.79 ^b ± 0.65
No. of branches /plant	14.52 ^a ± 1.88	18.08 ^b ± 3.16	17.78 ^b ± 4.08	23.14 ^c ± 3.16	23.80 ^c ± 3.11
No. of leaves / plant	2594.94 ^a ± 0.20	3175.06 ^b ± 10.83	3198.86 ^b ± 9.60	3302.24 ^b ± 10.83	3314.24 ^b ± 12.42
Leaf thickness (mm)	0.33 ^a ± 0.02	0.35 ^a ± 0.03	0.34 ^a ± 0.02	0.38 ^a ± 0.01	0.38 ^a ± 0.01
Leaf surface area (cm ²)	18.15 ^a ± 0.64	17.05 ^a ± 0.33	17.03 ^a ± 1.71	20.17 ^b ± 0.33	20.19 ^b ± 0.33
No. of inflorescences/plant	135.10 ^a ± 1.67	133.58 ^a ± 3.46	133.28 ^a ± 2.33	132.20 ^a ± 3.46	131.70 ^a ± 4.34
No. of fruits /plant	92.04 ^a ± 2.50	89.88 ^b ± 4.36	89.42 ^b ± 3.07	86.12 ^c ± 4.36	85.02 ^c ± 4.41

Note: In horizontal rows, means followed by different letters are significant to each other at 5% level according to DMRT.

* Chennimalai – 450m above msl, thorny scrub jungle, hard stony soil; Maruthamalai – 540m above msl, dry deciduous forest, gravel with shallow soil; Palamalai – 620 m above msl, moist deciduous forest, coarse sand with gravels; Thadagai Hills – 680 m above msl, moist semi-evergreen forest, sandy loam and shallow soil; Burliar – 760 m above msl, moist evergreen forest, humus soil with shallow nature

REFERENCES

1. K. M. Matthew, "The Flora of the Tamilnadu Carnatic", Vol. 13, The Rapinat Herbarium, St. Joseph's College, Tiruchirapalli, Tamil Nadu (India), **1995**.
2. P. Sathishkumar, S. Paulsamy, A. M. Ananda kumar and P. Senthilkumar, "Effect of habitat variation on the content of certain secondary metabolites of medicinal importance in the leaves of the plant, *Acacia caesia* (L.) Willd.", *Adv. Plant Sci.*, **2009**, 22, 451-453.
3. A. M. Anandakumar, S. Paulsamy, P. Sathishkumar and P. Senthilkumar, "Preliminary phytochemical studies for the quantification of secondary metabolites of medicinal importance in the plant, *Acalypha fruticosa* Forssk.", *J. Appl. Nat. Sci.*, **2009**, 1, 41-43.
4. Y. B. Linhart and M. C. Grant, "Evolutionary significance of local genetic differentiation in plants", *Annu. Rev. Ecol. Syst.*, **1996**, 27, 237-277.
5. S. Via and R. Lande, "Genotype-environment interactions and the evolution of phenotypic plasticity", *Evolution*, **1985**, 39, 505-522.

6. S. Via and R. Lande, "Evolution of genetic variability in a spatially heterogeneous environment: Effects of genotype-environment interaction", *Genet. Res.*, **1987**, 49, 147-156.
7. MultiVariate Statistical Package, Kovach Computing Services, UK, <http://www.kovcomp.co.uk/mvsp/>
8. P. Jaccard, "Étude comparative de la distribution florale dans une portion des Alpes et des Jura", *Bulletin de la Societe Vaudoise des Sciences Naturelles*, **1901**, 37, 547-579.
9. P. M. Hogbin, D. J. Ayre and R. J. Whelan, "Genetic variation and reproductive success of road verge populations of the rare shrub *Grevillea barklyana* (Proteaceae)", *Heredity*, **1998**, 80, 180-186.
10. J. W. Chandler and D. Bartels, "Drought: avoidance and adaptation", in "Encyclopedia of Water Science", 2nd Edition (Ed. S. W. Trimble, B. A. Stewart and T. A. Howell), Taylor and Francis Group, London, **2008**, p. 224.

Communication

Antilisterial effects of ethanolic extracts of some edible Thai plants on refrigerated cooked pork

Siriporn Stonsaovapak* and Soithong Saiyudthong

Institute of Food Research and Product Development, Kasetsart University, Bangkok 10900, Thailand

* Corresponding author, e-mail: ifrsps@ku.ac.th

Received: 26 May 2010 / Accepted: 3 December 2010 / Published: 21 December 2010

Abstract: *Listeria monocytogenes* is a major foodborne pathogen responsible for the disease listeriosis. Effective methods for reducing *L. monocytogenes* in foods would reduce the likelihood of foodborne outbreaks of listeriosis and decrease economic losses to the food industry. Crude ethanolic extracts from 50 edible Thai plants were screened for inhibitory effects on isolated strains and type strains of *L. monocytogenes* by the well assay technique. Ethanolic extracts of *Micromelum minutum*, *Artocarpus heterophyllus*, *Piper retrofractum* and *Cucurbita moschata*, which showed listerial growth inhibition, were applied to cooked pork to determine their antimicrobial activities against *L. monocytogenes*. Pork was cooked to an internal temperature of 85°C, allowed to cool to 8°C and then treated by surface application with the plant extracts. Low (10^2 cfu g⁻¹) or high (10^5 cfu g⁻¹) population of *L. monocytogenes* were applied and samples were stored at 4°C for up to 7 days. *M. minutum* and *A. heterophyllus* extracts were most effective in inhibiting the growth of the pathogen. These results suggested that some edible Thai plant extracts might be useful as antimicrobials in cooked, ready-to-eat pork.

Keywords: antilisterial activity, edible Thai plants, *Listeria Monocytogenes*, *Micromelum minutum*, *Artocarpus heterophyllus*

INTRODUCTION

Listeria monocytogenes is a gram-positive foodborne pathogen which has been involved in several outbreaks in the past two decades. This psychrotrophic bacterium is able to grow at a wide temperature range from 2.5°C to 44°C [1] and is widespread. It has been isolated from various foods including poultry, meat, milk, milk products, seafoods and vegetables. The bacterium causes listeriosis, a severe foodborne illness with a mortality rate as high as 30-40% [2].

Refrigerated, ready-to-eat foods have become increasingly popular in recent years because of their convenience. Unfortunately, this type of food may have a potential microbiological safety problem. Most ready-to-eat foods receive little or no final heat treatment before being consumed because they are assumed to be, and are often labelled as, fully cooked. The addition of antimicrobial ingredients in combination with refrigeration may compensate for the lack of a terminal heating step and provide protection in addition to low temperature alone. However, consumers are sometimes suspicious of food additives and prefer additive-free foods. Thus, the challenge of ensuring the safety of refrigerated, ready-to-eat foods and at the same time satisfying consumer preference is an important issue for the food industry.

Herbs and spices are widely used components in food preparation and are classified as GRAS (generally recognised as safe) products. The use of such naturally occurring plant products may provide an additional barrier to the growth of foodborne pathogens as well as satisfy both the consumers and the regulatory agencies. Testing of natural products for their antilisterial properties and their potential use as natural preservatives in food has been performed [3-6]. In Thailand, many plants are utilised as food and medicine. Some of these plants have been demonstrated to exhibit antilisterial activity [7]. However, most studies on the antilisterial activity of plant extracts have been conducted in vitro—little information exists regarding the practical use of such antimicrobial extracts in real foods. The objective of this study is to determine the potential use of some edible Thai plant extracts in inhibiting the growth of *L. monocytogenes* on refrigerated cooked pork. The use of extracts rather than purified compounds in this experiment was designed to take advantage of all active compounds present in the extracts.

MATERIALS AND METHODS

Test Organisms and Preparation of Inocula

Cultures of *L. monocytogenes* isolated from food samples, namely raw meat, vegetables and ready-to-eat food (KUS-1, KUS-2 and KUS-3) [8], were used in this study. A reference culture (IFRPD 2068) was kindly supplied by A. D. Hitchins, U.S. Food and Drug Administration, Washington, D.C. Cultures were maintained on tryptic soy agar supplemented with 0.6% yeast extract (TSAYE; Merck) and stored at 4°C until use by subculturing.

L. monocytogenes was activated by culturing in TSAYE broth at 35°C at least twice in 24-hour period prior to use in the experiment. The culture was then centrifuged (c. 2000 g, 10 minutes) and the pellet was resuspended in 0.1 M potassium phosphate buffer (pH 7.0). The final inocula were prepared by serial dilution in the buffer such that the final population was about 10^2 or 10^5 cfu g⁻¹ of pork.

Plant Extracts and Sample Preparation

Edible Thai plants used in this study are shown in Table 1. They were dried and ground before extracting with 95% ethyl alcohol for 48 hours. The final volume of each extract solution was adjusted to a concentration of 100 mg extract/ml and was then sterilised by a Millipore membrane (0.45 µm).

Fresh pork was purchased from a local retail supermarket and transported under refrigeration (2-7°C) to the laboratory. It was cooked to an internal temperature of 85°C, then cut into 25-g pieces with a sanitised knife, placed in sterile Petri dishes and immediately stored at 4°C before use.

Table 1. Edible Thai plants tested for antilisterial activity

Common name	Scientific name	Part extracted
Buabok	<i>Centella asiatica</i>	Leaf
Buab	<i>Cucurbitaceae</i> sp.	Fruit
Chamuang	<i>Garcinia cowa</i>	Leaf
Cha-om	<i>Acacia pennata</i>	Leaf
Chaphlu	<i>Piper sarmentosum</i>	Leaf
Dipli	<i>Piper retrofractum</i>	Fruit
Dok Pheka	<i>Oroxylum indicum</i>	Flower
Fakthong	<i>Cucurbita moschata</i>	Leaf
Hang Plachon	<i>Emilia sonchifolia</i>	Leaf
Horapha	<i>Ocimum basilicum</i>	Leaf
Hua Plee	<i>Musa sapientum</i>	Flower
Kaphrao	<i>Ocimum tenuiflorum</i>	Leaf
Khanun	<i>Artocarpus heterophyllus</i>	Fruit
Krachai	<i>Boesenbergia pandurata</i>	Rhizome
Krachiap Daeng	<i>Hibiscus sabdariffa</i>	Leaf
Krathin	<i>Leucaena leucocephala</i>	Leaf
Lepkhрут	<i>Polyscias fruticosa</i>	Leaf
Makham	<i>Tamarindus indica</i>	Leaf
Mamuang	<i>Mangifera indica</i>	Leaf
Mamuang Himmajaan	<i>Anacardium occidentale</i>	Leaf
Mapring	<i>Bouea oppositifolia</i>	Leaf
Maenglak	<i>Ocimum americanum</i>	Leaf
Manthet	<i>Ipomoea batatas</i>	Leaf
Mara	<i>Momordica charantia</i>	Leaf
Mui	<i>Micromelum minutum</i>	Leaf
Phak Bung	<i>Ipomoea aquatica</i>	Leaf
Phak Chee	<i>Coriandrum sativum</i>	Leaf
Phak Chee Farang	<i>Eryngium foetidum</i>	Leaf
Phak Chee Lao	<i>Anethum graveolens</i>	Leaf
Phak Chiangda	<i>Gymnema inodorum</i>	Leaf
Phak Keehuud	<i>Raphanus sativus</i>	Fruit
Phak Khana	<i>Brassica alboglabra</i>	Leaf
Phak Khom	<i>Amaranthus lividus</i>	Leaf
Phak Krachet	<i>Neptunia oleracea</i>	Leaf
Phak Kutkhao	<i>Diplazium esculentum</i>	Leaf
Phak Mae	<i>Momordica subangulata</i>	Leaf
Phak Paem	<i>Eleutherococcus trifoliatus</i>	Leaf
Phak Plang	<i>Basella alba</i>	Leaf
Phak Sian	<i>Cleome gynandra</i>	Leaf

Table 1. (Continued)

Common name	Scientific name	Part extracted
Phak Tamlueng	<i>Coccinia grandis</i>	Leaf
Phak Tang-o	<i>Chrysanthemum coronarium</i>	Leaf
Phak Wan	<i>Melientha suavis</i>	Leaf
Phak Wan Ban	<i>Sauropus androgynus</i>	Leaf
Phlu	<i>Piper betle</i>	Leaf
Phrik Khinuu	<i>Capsicum frutescens</i>	Leaf
Phrik Thai	<i>Piper nigrum</i>	Fruit
Sadao	<i>Azadirachta indica</i>	Flower
Takhrai	<i>Cymbopogon citratus</i>	Stem
Thammang	<i>Litsea petiolata</i>	Leaf
Thua Fakyao	<i>Vigna unguiculata</i>	Fruit

Sensitivity Testing and Minimum Inhibitory Concentrations

Sensitivity testing was done by well assay technique using TSA (tryptic soy agar; Merck) incubated at 35°C for 24 hours [9]. The well diameter was 4 mm. Minimum inhibitory concentrations (MIC) were determined according to the method of Richards et al [10].

Treatment of Pork Samples

The plant extract (1.0 ml) was uniformly deposited on the pork sample using a pipette and then spread with a sterile bent glass rod. Controls consisted of pork to which 95% ethanol (1.0 ml) was similarly applied, or pork that was untreated. The treated pork samples were kept in a biological safety cabinet for 15 minutes to allow alcohol to evaporate before being inoculated with the test bacteria. The samples were then inoculated with either low (10^2 cfu g⁻¹) or high (10^5 cfu g⁻¹) population of the reference culture of *L. monocytogenes* (IFRPD 2068). Inoculated pork samples were left to stand undisturbed for 30 minutes to allow residual moisture to be absorbed. They were then separately placed into polyethylene sampling bags and incubated at 4°C. Analysis of *L. monocytogenes* population was conducted after 0, 3, 5 and 7 days of storage.

Microbiological Analysis

On each sampling day, the incubated samples were removed for enumeration of *L. monocytogenes*. Phosphate buffer (225 ml) was added to each sampling bag and the contents were macerated with a Stomacher for 2 minutes. The resulting slurry was serially (1:10) diluted, and 0.1 ml of the diluted slurry was spread-plated in duplicate onto Oxford agar and Palcam agar plates (Merck). They were then incubated at 35°C for 48 hours.

RESULTS AND DISCUSSION

Of the 50 edible plant extracts tested, those of *Micromelum minutum* (Mui), *Artocarpus heterophyllus* (Khanun), *Piper retrofractum* (Dipli) and *Cucurbita moschata* (Fakthong) demonstrated

the greatest inhibitory effect on the four strains of *L. monocytogenes* and were chosen for further study. As shown in Table 2, *M. minutum* showed potent growth inhibition against *L. monocytogenes* with a clear-zone diameter ranging from 20.89 ± 0.53 mm to 27.29 ± 0.21 mm (mean inhibitory zone of 23.60 mm). Application of *A. heterophyllum* resulted in zones of inhibition ranging from 19.93 ± 0.21 to 24.39 ± 0.83 mm (mean inhibitory zone of 21.89 mm). It is noteworthy that the potent antilisterial activity of these four species (*M. minutum*, *A. heterophyllum*, *P. retrofractum* and *C. moschata*) has not been reported before.

Table 2. Antilisterial activity of four most potent plant extracts

Plant	Diameter of inhibition zone (mm) \pm SD ^a			
	<i>L. monocytogenes</i> strain			
	IFRPD 2068	KUS-1	KUS-2	KUS-3
Mui (<i>Micromelum minutum</i>)	21.50 ± 0.05	27.29 ± 0.21	24.76 ± 0.75	20.89 ± 0.53
Khanun (<i>Artocarpus heterophyllum</i>)	22.48 ± 0.03	24.39 ± 0.83	19.93 ± 0.21	20.75 ± 0.47
Dipli (<i>Piper retrofractum</i>)	18.20 ± 0.80	21.25 ± 1.10	19.09 ± 0.71	18.44 ± 0.97
Fakthong (<i>Cucurbita moschata</i>)	14.25 ± 0.03	11.33 ± 0.66	14.76 ± 1.14	16.10 ± 0.80

^aMean value of four determinations, each from a different plate

MIC assays were also performed to determine the lowest concentrations of the plant extracts that produced an inhibitory effect. *M. minutum* and *A. heterophyllum* were most inhibitory to the four strains of *L. monocytogenes*, with MIC of 625 μ g/ml. The extracts of *P. retrofractum* and *C. moschata* were also effective, with MIC of 1250 and 2500 μ g/ml (Table 3).

Table 3. MIC against *L. monocytogenes* of four most potent plant extracts

Plant	MIC (μ g/ml)			
	<i>L. monocytogenes</i> strain			
	IFRPD 2068	KUS-1	KUS-2	KUS-3
Mui (<i>Micromelum minutum</i>)	625	625	625	625
Khanun (<i>Artocarpus heterophyllum</i>)	625	625	625	625
Dipli (<i>Piper retrofractum</i>)	1250	1250	1250	2500
Fakthong (<i>Cucurbita moschata</i>)	2500	1250	2500	1250

M. minutum, which showed the highest activity in the antilisterial screening, is a shrub belonging to the Rutaceae family. It is consumed mainly in the southern part of Thailand as a fresh vegetable served with certain dishes such as rice noodles with hot curry. *M. minutum* has also been used as a folk medicine for fever and giddiness [11]. The medicinal principles of *M. minutum* have not yet been elucidated thoroughly although many bioactive compounds such as coumarins, a flavanone, a quinolone alkaloid and carbazole alkaloids have previously been isolated [11-12].

A. heterophyllum is a tree belonging to the Moraceae family and produces a fruit which is eaten when it is still unripe by boiling with salt. Thais also eat it as a fresh fruit with chili paste, or sometimes

add it to curry. The methanolic extract of *A. heterophyllus* fruit exhibits a broad-spectrum antibacterial activity [13].

At the storage temperature of 4°C, typically the temperature at which consumers store cooked food, little or no growth of the test strain of listeria was observed in control samples when both low (Table 4a) and high (Table 4b) populations of inocula were applied. However, listeria population on cooked pork with high inoculum which was treated with either *M. minutum* or *A. heterophyllus* extracts was at least 2 to 3 magnitudes of logarithmic scale less than that on control samples. This difference persisted throughout the storage period (7 days) (Table 4b). When samples were inoculated with a low level of inoculum (c. 10^2 cfu g⁻¹), *M. minutum* and *A. heterophyllus* extracts were also the most effective in controlling *L. monocytogenes* during storage of pork at 4°C. After 5 days and 7 days of storage, *L. monocytogenes* could not be detected in samples treated with *M. minutum* and *A. heterophyllus* respectively (Table 4a). Samples treated with *P. retrofractum* also suppressed the growth of *L. monocytogenes* although not as effectively as *M. minutum* and *A. heterophyllus* extracts.

Table 4. Population (\log_{10} cfu g⁻¹ \pm SD) of *L. monocytogenes* (IFRPD 2068 strain) on cooked pork with (a) low inoculum (c. 10^5 cfu g⁻¹) and (b) high inoculum (c. 10^2 cfu g⁻¹) at 4 °C

(a)

Treatment	Time (days)			
	0	3	5	7
None	1.90 \pm 0.02	1.85 \pm 0.08	2.64 \pm 0.11	2.07 \pm 0.23
95% ethanol	1.84 \pm 0.06	1.90 \pm 0.06	2.03 \pm 0.08	2.15 \pm 0.09
Mui (<i>Micromelum minutum</i>)	1.05 \pm 0.01	1.21 \pm 0.03	ND ^a	ND
Khanun (<i>Artocarpus heterophyllus</i>)	1.03 \pm 0.01	1.37 \pm 0.03	1.23 \pm 0.10	ND
Di pli (<i>Piper retrofractum</i>)	1.62 \pm 0.02	1.71 \pm 0.08	2.69 \pm 0.08	2.08 \pm 0.47
Fak thong (<i>Cucurbita moschata</i>)	1.93 \pm 0.04	2.05 \pm 0.03	2.79 \pm 0.10	2.26 \pm 0.32

^a ND = not detected

(b)

Treatment	Time (days)			
	0	3	5	7
None	4.65 \pm 0.02	4.91 \pm 0.04	4.63 \pm 0.06	5.03 \pm 0.10
95% ethanol	4.35 \pm 0.01	4.75 \pm 0.06	4.94 \pm 0.11	5.00 \pm 0.11
Mui (<i>Micromelum minutum</i>)	4.08 \pm 0.03	2.03 \pm 0.06	2.29 \pm 0.08	1.78 \pm 0.28
Khanun (<i>Artocarpus heterophyllus</i>)	4.78 \pm 0.01	2.71 \pm 0.03	2.41 \pm 0.08	1.80 \pm 0.34
Di pli (<i>Piper retrofractum</i>)	4.61 \pm 0.06	4.12 \pm 0.05	3.57 \pm 0.14	2.64 \pm 0.25
Fak thong (<i>Cucurbita moschata</i>)	4.57 \pm 0.03	4.51 \pm 0.07	4.24 \pm 0.19	4.81 \pm 0.21

ACKNOWLEDGEMENTS

The authors would like to acknowledge Dr. Gassinee Trakoontivakorn of the Institute of Food Research and Product Development for providing dried edible plant extracts, and Kasetsart University Research and Development Institute for funding this study.

REFERENCES

1. H. P. R. Seeliger, "Listeriosis", Hafner Publishing, New York, **1961**, pp.61-62.
2. A. R. Datta, "*Listeria monocytogenes*", in "International Handbook of Foodborne Pathogens" (Ed. M. D. Miliotis and J. W. Bier), Marcel Dekker, New York, **2003**, pp.105-121.
3. R. J. Owen and E. A. Palombo, "Anti-listerial activity of ethanolic extracts of medicinal plants, *Eremophila alternifolia* and *Eremophila duttonii*, in food homogenates and milk", *Food Control*, **2007**, *18*, 387-390.
4. M. K. M. Nair, P. Vasudevan and K. Venkitanarayanan, "Antibacterial effect of black seed oil on *Listeria monocytogenes*", *Food Control*, **2005**, *16*, 395-398.
5. A. Smith-Palmer, J. Stewart and L. Fyfe, "The potential application of plant essential oils as natural food preservatives in soft cheese", *Food Microbiol.*, **2001**, *18*, 463-470.
6. K. V. Menon and S. R. Garg, "Inhibitory effect of clove oil on *Listeria monocytogenes* in meat and cheese", *Food Microbiol.*, **2001**, *18*, 647-650.
7. S. Stonsaovapak, P. Charoenthamavat, M. Boonyaratanakornkit and P. Chimanage, "Sensitivity of *Listeria monocytogenes* to native Thai spices", Proceedings of the XII International Symposium on Problems of Listeriosis, **1995**, Perth, Western Australia, pp.129-134.
8. S. Stonsaovapak and M. Boonyaratanakornkit, "Prevalence and antimicrobial resistance of *Listeria* species in food products in Bangkok, Thailand", *J. Food Saf.*, **2010**, *30*, 154-161.
9. K-T. Chung, W. R. Thomasson and C. D. Wu-Yuan, "Growth inhibition of selected food-borne bacteria, particularly *Listeria monocytogenes*, by plant extracts", *J. Appl. Bacteriol.*, **1990**, *69*, 498-503.
10. R. M. E. Richards, D. K. L. Xing and T. P. King, "Activity of p-aminobenzoic acid compared with other organic acids against selected bacteria", *J. Appl. Bacteriol.*, **1995**, *78*, 209-215.
11. C. Ito, T. Otsuka, N. Ruangrunsi and H. Furukawa, "Chemical constituents of *Micromelum minutum*: Isolation and structural elucidation of new coumarins", *Chem. Pharm. Bull.*, **2000**, *48*, 334-338.
12. M. Rahmani, R. A. Susidarti, H. B. M. Ismail, M. A. Sukari, T. Y. Y. Hin, G. E. C. Lian, A. M. Ali, J. Kulip and P. G. Waterman, "Coumarins from Malaysian *Micromelum minutum*", *Phytochem.*, **2003**, *64*, 873-877.
13. M. R. Khan, A. D. Omoloso and M. Kihara, "Antibacterial activity of *Artocarpus heterophyllus*", *Fitoterapia*, **2003**, *74*, 501-505.

Report

Botanical notes

James F. Maxwell*

CMU Herbarium, Biology Department, Faculty of Science, Chiang Mai University, Chiang Mai 50200, Thailand

* E-mail: scopplrn@chiangmai.ac.th

Received: 1 October 2010 / Accepted: 29 December 2010 / Published: 31 December 2010

Abstract: *Indigofera caudata* Dunn (Leguminosae, Papilionoideae) is noted as a new record for Thailand. Two new combinations in *Hedyotis* from *Oldenlandia* (Rubiaceae) are made, viz. *Hedyotis krewanhensis* (Pierre ex Pit.) Maxw. and *Hedyotis chevalieri* (Pit.) Maxw.

Keywords: *Indigofera caudata* Dunn, *Oldenlandia krewanhensis* Pierre ex Pit., *Oldenlandia chevalieri* Pit., *Hedyotis krewanhensis* (Pierre ex Pit.) Maxw., *Hedyotis chevalieri* (Pit.) Maxw.

***Indigofera caudata* Dunn; Leguminosae, Papilionoideae; New Record for Thailand**

Craib [1] in the initial listing of Thai *Indigofera* included 22 species. de Kort & Thijsse [2] indicated that *Indigofera caudata* Dunn is known from Yunnan, China (type) and Laos. Thuan et al. [3] also included this species and noted that the material they examined was from Xieng Khouang Province, Laos at 1500 m elevation.

The QBG specimen Srisanga, Watthana, and La-Ongsri 865 from Doi Phu Kha National Park, Nan province is this species. It is distinguished by being a shrub with imparipinnate leaves having 3-4 opposite pairs of lanceolate leaflets, 3-6 x 2-2.5 cm, with mucronate tips and simple hairs underneath; 4-angled, brown-hirsute branches with similar indumentum on the axillary, spike-like racemes which are twice as long as the leaves; and wings obviously shorter than the standard and keel—all of which are white. The specimen was collected in flower at 1670 m elevation on 4 July 1999 in primary, evergreen, seasonal, hardwood (*sic.* hill evergreen) forest.

Indigofera longicaudata Thuan [3], from southern Vietnam, seems to be morphologically closely related, but has elliptic leaflets, shorter inflorescences, apparently different indumentum and red petals.

***Hedyotis* (Rubiaceae)**

Fukuoka [4] included 43 species in his revision of this genus for Thailand. Another 13 species were excluded due to insufficient material. In recent years, *Hedyotis bahaii* Maxw. has been newly described [5] while *Hedyotis kamputensis* (Pit.) Wangs. & Chant. [6], *Hedyotis ternatus* (Pierre ex Pit.) Maxw., and *Hedyotis linoides* (Griff.) Kurz [7] have been added. It is expected that more species of *Hedyotis* will be added to the Thai flora as more collections from the areas bordering Laos and Cambodia are collected and studied.

Pitard [8] included *Hedyotis* in *Oldenlandia* in which 8 sections were distinguished based mainly on the capsules, especially the mode of dehiscence. He included 71 species in his treatment for Indochina, most of which are now included in *Hedyotis*. Two of these species have been examined from CMU Herbarium material and are now transferred to *Hedyotis*.

1. *Hedyotis krewanhensis* (Pierre ex Pit.) Maxw. (Rubiaceae), *comb. nov.* (Figure 1)

Oldenlandia krewanhensis Pierre ex Pit., Flore Générale de L'Indo-Chine III (1922) 142 [8]

Pitard [8] included this species in *Oldenlandia* Sect. *Euoldenlandia* which has membranous, 2-valved, smooth capsules with longitudinal dehiscence and regular corollas. This species, an annual herb, has terminal and upper axillary, multiflorous cymes with all the flowers in several dense capitula. The calyces and capsules are hispidulous, the latter being *c.* 2 mm diameter.

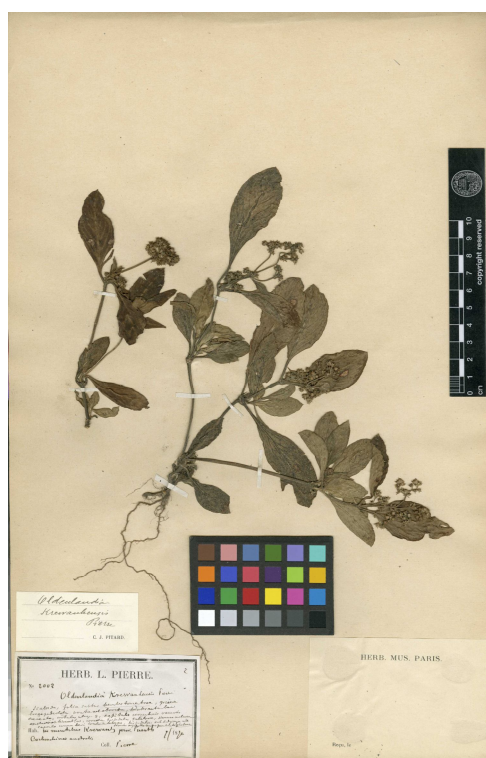


Figure 1. One of the five syntypes of *Hedyotis krewanhensis* (Pierre ex Pit.) Maxw. in the Paris Herbarium (P). It was collected by Pierre from Mt. Krewanh, Cambodia, in July 1870.

I have made two collections of this species, both from islands in the Mekong River, Kratie province, Sambour district, Cambodia, viz. Maxwell 06-814 (capsules, Sahng Gawng Island, 13 November 2006) and 07-469 (flowers and capsules, Svan Island, 1 August 2007). Both collections were from degraded, fire damaged, deciduous, seasonal, hardwood forest with bamboo and nearby beach at *c.* 30 m elevation on metamorphic sandstone bedrock. The species was also observed in deciduous dipterocarp forest on other islands.

Pitard [8] noted that this species had been collected at Steung Treng, which is *c.* 20 km north of where I found it. Type material was from Mt. Krewanh, Pursat province, Cambodia, while the other specimens noted were from SW Vietnam.

There are at least five specimens of this species in the Paris Herbarium (P) collected and named by Pierre. Pierre 2002 (2 sheets) was from Mt. Krewanh and was collected in July 1870. There were three sheets of Pierre 2006, all from SW Vietnam. Two of them were from Tri-huyen, Hoa Bin province (April 1873). The other was from Lake Day, Chaudok, An Giang province (December 1867). Pierre *sn* was from Bé à Ti-tinh River, Song Be province, collected in February 1866 and was annotated by Pitard as *Oldenlandia krewanhensis*.

2. *Hedyotis chevalieri* (Pit.) Maxw., *comb. nov.* (Figure 2)

Oldenlandia chevalieri Pit., Flora Générale de L'Indo-Chine III (1922); 125-126 and Fig. 13 # 14 (p.115) [8]

This species was included in sect. *Diplophragma* by Pitard [8] in his revision of *Oldenlandia* for Indochina. In this section, it has dehiscent capsules in which the summits are not conspicuous, i.e. not concealed by the calyx lobes. *Hedyotis chevalieri* is easily recognised by being an annual herb up to 20 cm tall with dense whitish to brown indumentum on the quadrangular stems; peduncled, axillary, capitate, multi-flowered inflorescences; lobed stipules; globose, pubescent capsules 2 mm diameter with many seeds; and pubescent fruiting calyx lobes which are ovate-lanceolate, acute at the tip and *c.* 3 mm long.

The specimen examined was collected by J. Lawinheung, #17, from Huay Nahn village, Muang Wahng district, Wieng Chan province, Laos. It was found in a shaded place in primary, evergreen, seasonal, hardwood forest at 250 m elevation in fruit on 31 December 2001. The CMU specimen was distributed from the herbarium at the Biology Department, National University of Laos. The corolla is noted to be yellow and the leaf blades dark green above and dark purple underneath.

The type material was collected by the French botanist Auguste Chevalier (1873-1956) from Nghe Tinh (Nghe-an) province, Vietnam. This specimen, Chevalier 32442, in the Paris Herbarium (P) was collected on 10 May 1914.



Figure 2. Chevalier 32442, holotype of *Hedyotis chevalieri* (Pit.) Maxw., in the Paris Herbarium (P). It was collected in Nghe Tinh (Nghe-an) province, north Vietnam on 10 May 1914.

Acknowledgements

I am indebted to Aurelien Morin (P) for sending me photographs of both species of *Hedyotis* discussed here. World Wildlife Fund Cambodia is thanked for sponsoring my three, very productive trips to Kratie province, Cambodia. Martin van de Bult commented on and typed the draft on a computer. His energetic, dedicated, proactive, participatory work for the alleviation of professional boredom is gratefully acknowledged. Dr. Le Quang Bao is thanked for clarifying some locations in Vietnam.

References

1. W. G. Craib, "Florae Siamensis Enumeratio", Vol. I, Siam society, Bangkok, **1928**, pp.377-383.
2. I. de Kort and G. Thijssen, "A revision of the genus *Indigofera* (Leguminosae, Papilionoideae) in Southeast Asia", *Blumea*, **1984**, 30, 105-143.
3. N. V. Thuan, P. dy Phon and C. Niyomdahm, "Légumineuses, Papilionoidées", *Flore Cambodge Laos Vietnam*, **1987**, 23, 65-78.
4. N. Fukuoka, "Contributions to the flora of Southeast Asia III, *Hedyotis* (Rubiaceae) of Thailand", *Tonan Ajia Kenyu* (The Southeast Asian Studies), **1970**, 8, 305-336.
5. J. F. Maxwell, "Notes on Thai *Hedyotis* (Rubiaceae)", *Nat. Hist. Bull. Siam Soc.*, **2002**, 50, 3-6.

6. K. Wangsawit and P. Chantaranothai, "A new combination in *Hedyotis* (Rubiaceae)", *Thai Forest Bull.*, **2002**, 30, 69-71.
7. J. F. Maxwell, "*Hedyotis linoides* (Griff.) Kurz (Rubiaceae)—new record for Thailand", *Nat. Hist. Bull. Siam Soc.*, **2004**, 52, 113-114.
8. J. Pitard, "Rubiacées, *Oldenlandia*", in "Flore Générale de L'Indo-Chine", Vol. III (Ed. O. Lecomte), Masson, Paris, **1922**, pp.92-142.

© 2010 by Maejo University, San Sai, Chiang Mai, 50290 Thailand. Reproduction is permitted for noncommercial purposes.